Dynamics in strongly correlated quantum gases

Dissertation

Dominik Muth

Vom Fachbereich Physik der Technischen Universität Kaiserslautern
zur Verleihung des akademischen Grades „Doktor der Naturwissenschaften“
genehmigte Dissertation

Betreuer: Prof. Dr. Michael Fleischhauer

Zweitgutachter: Jun.-Prof. Dr. Jesko Sirker

Datum der wissenschaftlichen Aussprache: 25. April 2012

D 386

Abstract

The experimental realization of ultra-cold atoms in optical lattices and other confining optical potentials has led to a new and versatile quantum optical approach to many-body physics. Experimental techniques now exist for cooling and trapping atomic gases in various potentials including effectively one-dimensional geometries. In contrast to typical solid state systems, cold atoms stand out due to tunability of interactions, the absence of impurities and the much larger length scales that permit single site addressability. It is possible to implement models in an almost perfect way, which have been developed in theoretical solid state physics only as an idealization, such as the Hubbard and Bose-Hubbard models, the Lieb-Liniger model of a 1D interacting Bose gas, and several spin-lattice models. In a certain sense, ultra cold gases form a versatile quantum simulator. In particular they offer the possibility to study non-equilibrium physics and dynamical evolution.

The present thesis contributes to the theoretical understanding of strongly interacting ultra-cold gases. The focus is on one-dimensional systems because quantum effects are most pronounced in 1D and there are some exactly solvable models. The dynamical behavior, as well as the ground state properties of interacting many particle systems is investigated using numerical techniques based on matrix-product state approaches.

We develop a discretization method for one-dimensional Bose- and Fermi-gases with contact interactions, which is necessary for the numerical treatment of the continuous problem. The ground state of those bosons and fermions is calculated for a harmonic confinement, for the whole range between the weakly and the strongly interacting limit. The resulting density and momentum profiles, as well as the two-particle correlation functions should be observable in present experiments. For the problem of Rydberg-polaritons which are subject to van der Waals-interaction interactions, we present the first calculation of the Luttinger-parameter, confirming that the correlations become much stronger than for any local interaction, and significantly improving previous approximate approaches. For a gas with van der Waals-interaction on the lattice, we give the first non-perturbative phase diagram, which features a fractal structure of Mott-insulating regions.

A subject of current interest is the relaxation dynamics in closed quantum systems and the influence of integrability on the ensemble describing a possible thermal final state. Here, the relaxation after a quench from the free boson ground state to repulsive interaction is investigated, showing that local correlations equilibrate on a certain, short timescale, to a value reminiscent of a thermal Gibbs state. Due to numerical limitations and finite size effects, it can not be decided here whether the small discrepancy from the grand-canonical value can be attributed to integrability. The propagation of non-local correlations shows a finite speed, leading to an effective light cone. In the case of attractive interactions, metastable exited states (Super Tonks gas) form, as recently shown in experiments. Here a quench from the Tonks gas to strong attractive interactions is simulated, and the signature of this metastable state and of the strongly bound pair states becomes apparent in the oscillations of the two-body correlations, which do not relax on the timescale accessible. We can ascribe this lack of thermalization to the proximity of the quenched system to a many-body eigenstate, and the small number of different states that contribute to the correlation amplitude, which renders dephasing ineffective.

An experimental method to probe cold gases with unmatched spatial and temporal resolution using scanning electron microscopy has been developed in the group of H. Ott. The quasi one-dimensional regime can be reached where the Rubidium atoms are well

described by the Lieb-Liniger model in the intermediate interaction range. As part of a joint experimental-theoretical project, we present the first numerical calculation of the normal ordered two-particle correlation function between two different times for the ground state, which is in spite of formal similarity different from the dynamical structure factor available from the exact Bethe ansatz solution. The time dependent correlation function measured in the experiment is in good agreement with the calculations, showing appreciable antibunching at short intervals due to the repulsive interactions.

Recent progress in single-site addressability and manipulation in lattice systems, motivates the investigation of relaxation dynamics in the Bose-Hubbard model in the strongly interacting regime. A method to prepare exceptionally pure Mott insulators is introduced. Single defects are removed from a finite size Mott insulator formed by repulsively bound dimers, by evaporating through the boundaries. The scattering between different defect types mediates the redistribution of momenta, which is required to bring all defects into the momentum range where the cluster boundaries are penetrable. This proposal works for essentially any initial configuration with an unbiased initial momentum distribution, confirmed numerically using an effective theory, where only the position of the defects are dynamical variables, and the dimers only contribute a static background.

The full quantum-dynamical simulations of many body systems, which are globally out of equilibrium, e.g., after a quench, are limited by the linear growth of entanglement entropy with time, making classical simulation exponentially hard. Going to the Heisenberg picture, instead of evolving the complicated many body state, only a simple operator of interest is evolved. We show that then logarithmic scaling of the entropy is observed, if only the operator itself is a conserved density. Integrability, as conjectured in the literature, is not necessary. This result is hopefully useful in extending the numerical method to longer timescales. Finally different methods of exploiting particle number conservation in matrix product operators, found, e.g., in the Heisenberg picture formulation of the numerical algorithm, are discussed. While conservation laws are implemented routinely to increase the efficiency matrix product state calculations, in the case of matrix product operators, we show that this can be done on two different levels, and a careful choice has to be made depending on the problem. The reduction of the number of parameters by the symmetry constrained is under certain circumstances, i.e. a large filling fraction in the case of particle number conservation, overcompensated by the additional entanglement introduced.

Zusammenfassung

Die experimentelle Realisierung ultrakalter Atome in optischen Gittern hat einen neuen und vielseitigen Zugang zur Vielteilchenphysik eröffnet. Es existieren experimentelle Methoden zum Kühlen und Fangen atomarer Gase in verschiedenen Potentialen, einschließlich effektiv eindimensionaler Geometrien. Kalte Atome zeichnen sich gegenüber typischen Festkörpersystemen dadurch aus, dass sie veränderbaren Wechselwirkungen unterliegen, frei von Störstellen sind und Zugriff auf einzelne Gitterplätze zulassen. Es ist möglich Modelle in fast perfekter Weise zu implementieren, so etwa das Hubbard- und das Bose-Hubbard-Model, das Lieb-Liniger-Model eines 1D wechselwirkenden Bose-Gases und verschiedene Spin-Gitter-Systeme. In gewissem Sinne stellen ultrakalte Quantengase einen vielseitigen Quantensimulator dar. Speziell bieten sie die Möglichkeit zum Studium von Nicht-Gleichgewichts-Physik und Zeitevolution.

Die vorliegende Dissertation trägt zum theoretischen Verständnis stark wechselwirkender ultrakalter Gase bei. Der Schwerpunkt liegt auf 1D Systemen, weil Quanteneffekte dort am stärksten zu Tage treten und außerdem exakt lösbare Vielteilchenmodelle existieren. Das dynamische Verhalten, sowie die Grundzustandseigenschaften wechselwirkender Vielteilchensysteme werden mit numerischen Methoden, welche auf dem Matrix-Produkt-Ansatz aufbauen, untersucht.

Es wird eine Diskretisierungsmethode für eindimensionale Bose- und Fermi-Gase mit Kontaktwechselwirkung entwickelt, welche notwendig ist für die numerische Behandlung kontinuierlicher Probleme. Der Grundzustand wird für einen harmonischen Einschluss berechnet, vom schwach bis zum stark wechselwirkenden Grenzfall. Die resultierenden Dichte und Impulsverteilungen, sowie die Zwei-Teilchen-Korrelationsfunktionen sollten in aktuellen Experimenten beobachtbar sein. Für das Problem wechselwirkender Rydberg-Polaritonen mit van der Waals-Wechselwirkungen, wird die erste Berechnung des Luttinger-Parameters vorgestellt, welche zum einen bestätigt, dass sich Korrelationen ausprägen, die stärker sind als für jede lokale Wechselwirkung, und zum anderen eine deutliche Verbesserung gegenüber existierenden approximativen Ansätzen darstellt. Für ein Gas mit van der Waals-Wechselwirkungen im Gitter, wird das erste nicht-störungstheoretische Phasendiagramm gezeigt, welches eine fraktale Struktur Mott-isolierender Bereiche aufweist.

Ein Thema dem momentan viel Aufmerksamkeit zuteil wird, ist der Vorgang der Relaxation in geschlossenen Quantensystemen und der Einfluss der Integrabilität auf einen möglichen thermischen Endzustand. Wir untersuchen hier die Relaxation nach einem Quench vom Grundzustand freier Bosonen hin zu repulsiver Wechselwirkung, wobei gezeigt wird, dass lokale Korrelationen auf einer bestimmten, kurzen Zeitskala einem stationären Wert zustreben, der im Wesentlichen dem eines thermischen Gibbs-Zustandes entspricht. Aufgrund numerischer Limitierungen und Effekten durch die endliche Systemgröße, kann hier nicht abschließend geklärt werden, ob auftretende kleine Abweichungen vom großkanonischen Wert auf die Integrabilität des Modells zurückgeführt werden können. Die Ausbreitung nicht-lokaler Korrelationen weist eine endliche Geschwindigkeit auf, die zu einem effektiven Lichtkegel führt. Im Falle attraktiver Wechselwirkung bilden sich metastabile, angeregte Zustände (das Super-Tonks-Gas), wie kürzlich in Experimenten gezeigt wurde. Hier wird ein Quench vom Tonks-Gas hin zu stark attraktiven Wechselwirkungen simuliert. Die Signatur dieses metastabilen Zustandes und der stark gebundenen Paare wird deutlich in der Oszillation der zwei-Teilchen Korrelationen, welche auf den Zeitskalen die hier zugänglich sind nicht relaxieren. Dieses Fehlen von Thermalisierung können wir der Nähe des Zustandes

zu einem Vielteilchen-Eigenzustand zuschreiben, sowie der geringen Anzahl an verschiedenen Zuständen, welche zur Korrelationsamplitude beitragen, wodurch eine Dephasierung ineffektiv wird.

Eine experimentelle Methode zur Untersuchung kalter Gase mit unerreichter Orts- und Zeitauflösung mittels Rasterelektronenmikroskopie wurde in der Gruppe von H. Ott entwickelt. Das quasi eindimensionale Regime, in dem die Rubidiumatome gut durch das Lieb-Liniger Modell im Bereich mittlerer Wechselwirkungen beschrieben werden, kann erreicht werden. In einem gemeinsamen Projekt liefern wir die erste Berechung der normal- und zeitgeordneten zwei-Teilchen Korrelationsfunktion im Grundzustand, welche sich trotz formaler Ähnlichkeit vom dynamischen Strukturfaktor unterscheidet, welcher aus der exakten Bethe-Ansatz-Lösung bekannt ist. Die im Experiment gemessene Korrelationsfunktion befindet sich in guter Übereinstimmung mit der Berechnung, wobei sie deutliches Antibunching bei kleinen Zeitabständen aufgrund der Abstoßung zeigt.

Der aktuelle Fortschritt in der gitterplatzgenauen Auflösung und Manipulation hat die Untersuchen der Relaxationsdynamik im Bose-Hubbard-Model im stark wechselwirkenden Regime motiviert. Eine Methode zur Präparation eines außergewöhnlich reinen Mott-Isolators wird vorgestellt. Einzelne Defekte werden aus einem Mott-Isolator endlicher Größe, welcher aus repulsiv gebundenen Paaren besteht, entfernt, in dem sie durch den Rand evaporieren. Die Streuung zwischen verschiedenen Typen von Defekten vermittelt die Umverteilung von Impulsen, welche notwendig ist, um alle Defekte in den Impulsbereich zu bringen, wo die Ränder durchdrungen werden können. Der Ansatz wird bestätigt durch numerische Simulationen mit einer effektiven Theorie, in der nur die Position der Defekte als dynamische Variablen auftreten, während die Dimere nur einen statischen Hintergrund bilden.

Die volle quantenmechanische Simulation von Vielteilchensystemen wird limitiert durch das lineare Anwachsen der Verschränkungsentropie mit der Zeit, wodurch klassische Simulationen exponentiell aufwendig werden. Beim Übergang ins Heisenberg-Bild wird anstelle eines komplizierten Vielteilchenzustandes nur ein einfacher Operator an dem man interessiert ist evolviert. Hier wir gezeigt, dass man in diesem Fall logarithmisches Anwachsen der Entropie beobachtet, falls der Operator selbst eine erhaltene Dichte darstellt. Integrabilität, wie in der Literatur vermutet, ist nicht notwendig. Es ist zu hoffen, dass dieses Ergebnis dazu beiträgt, die numerische Methode auf längere Zeitskalen auszuweiten. Zuletzt werden Methoden besprochen, die Teilchenzahlerhaltung in Matrix-Produkt-Operatoren, wie sie etwa in der Heisenberg-Bild-Formulierung des numerischen Algorithmus auftreten, zu berücksichtigen. Während Erhaltungssätze routinemäßig implementiert werden um die Effizienz von Rechnungen mit Matrix-Produkt-Zuständen zu erhöhen, zeigen wir im Fall von Matrix-Produkt-Operatoren, dass dies auf zwei verschiedene Ebenen geschehen kann, und eine sorgfältige Wahl in Abhängigkeit vom gegebene Problem getroffen werden muss. Die Reduktion in der Zahl der Parameter durch die Symmetrieeinschränkung wird unter bestimmten Voraussetzungen, speziell bei einer hohen Anzahl an Teilchen je Gitterplatz im Falle der Teilchenzahlerhaltung, überkompensiert durch die Erzeugung zusätzlicher Verschränkung.

Contents

I Introduction **9**

1 Ultracold atoms in optical lattices **10**
- 1.1 Bose-Hubbard model . . . 12
  - 1.1.1 Grandcanonical phase diagram . . . 12
  - 1.1.2 Repulsively bound pairs . . . 15
- 1.2 Lieb-Liniger model . . . 16
  - 1.2.1 Tonks-Girardeau gas . . . 17
  - 1.2.2 Bethe ansatz . . . 18
  - 1.2.3 Finite temperature . . . 22
  - 1.2.4 Attractive interactions . . . 23
- 1.3 Bose–Fermi mapping for general contact interactions . . . 24
- 1.4 Luttinger liquid theory . . . 26
- 1.5 Thermalization dynamics in closed quantum systems . . . 28

2 Matrix product state algorithms **32**
- 2.1 Matrix product states . . . 33
- 2.2 Imposing conservation laws . . . 35
- 2.3 Density matrix renormalization group (DMRG) . . . 36
- 2.4 Time evolving block decimation (TEBD) . . . 38

II Ground state properties of quantum gases **41**

3 Discretized models of 1D quantum gases **42**
- 3.1 Discretization . . . 43
- 3.2 Bosonic mapping . . . 43
- 3.3 Fermionic mapping . . . 45
- 3.4 Jordan-Wigner mapping . . . 46
- 3.5 The interacting Fermi gas in a harmonic trap . . . 48

4 DMRG for models with long range interactions **54**
- 4.1 Polynomially decaying interactions . . . 55
- 4.2 Luttinger parameter . . . 56

4.3 Phase diagram on the lattice 58

III Dynamics in strongly correlated quantum gases 64

5 Fermionization dynamics of a strongly interacting 1D Bose gas 65
5.1 Local relaxation 68
5.2 Non-local dynamics 72
5.3 Experimental observation 74

6 Dynamics of pair correlations in the attractive Lieb-Liniger gas 76
6.1 Numerical simulation of the full many-body case 77
6.2 The two particle case 80

7 Time dependent correlations 86
7.1 TEBD numerics 90
7.2 Adaptions to the experimental situation 91
7.2.1 Finite beam width 91
7.2.2 Varying Tonks parameter 93
7.2.3 More than two detection events 93
7.2.4 Local depletion 94
7.2.5 Average over multiple systems 95
7.3 Comparison to experimental data 97
7.4 Dependence on particle statistics 98

8 Dynamics and evaporation of defects in Mott clusters 101
8.1 Clusters of repulsively bound dimers 101
8.1.1 Hole and particle defects 102
8.2 Single defect model in the strong-interaction limit 103
8.3 Momentum redistribution between the defects 104
8.3.1 Two classical particles 105
8.3.2 Two quantum particles: Numerical simulations 106
8.4 Many-body numerical simulations 107
8.4.1 Many defect effective theory in the strong-interaction limit . . 107
8.4.2 Initial states 108
8.4.3 Numerical results 109
8.5 Two species Bose-Hubbard model 113
8.5.1 Fermionic Hubbard model 115

IV t-DMRG in the Heisenberg picture 118

9 Matrix product operators 119

10 Integrable and non-integrable models in the Heisenberg picture 121
10.1 Integrable models equivalent to free fermions 122
10.2 Non-integrable models 126

11 Particle number conservation in MPO 131
11.1 Unprojected operators 132
11.2 Projected operators 134
11.3 Preparing the projector onto the subspace of a fixed particle number 136
11.4 Examples 138

Appendices 146

A Free bosons quenched in a periodic system 147
A.1 Explicit calculation for three particles 148

B Transmission of a particle through a domain wall 152

C Two particle Hamiltonian in momentum space 153

D Effective theory for monomers and trimers 154

E MPS representation of single particle states 156

F Two particle correlations in a non interacting 1D Fermi gas 159

References 160

Part I
Introduction

1 Ultracold atoms in optical lattices

Advanced cooling techniques for atomic or molecular gases are giving us access to physical phenomena which were not observable directly before. Most prominently, many body phenomena known from solid state physics can be observed in very clean systems, undisturbed by other effects, with tunable parameters and high resolution. The first milestone on that way was the observation of Bose-Einstein condensation in cold atomic gases [AEM+95, BSTH95, DMA+95], made possible by the development of advanced cooling techniques, most importantly optical Doppler cooling and evaporative cooling of trapped atoms. By bringing additional standingwave laser fields into the gas, it became possible to resemble the periodic structure that is the basis of many effects in solid state physics. A well known example is the observation of a strongly correlated Mott-insulating phase in such an optical lattice, first reported by Greiner et al. [GME+02].

Triggered by the recent successes in the experimental realization of strongly interacting atomic quantum gases in one spatial dimensional (1D) [KWW04, PWM+04, GSM+05, HLF+07, HGM+09] there is an increasing interest in the theoretical description of these systems beyond the mean field level, taking into account strong correlation and taking into account the specifics of trapped, finite size, quantum gases.

If an atomic gas is sufficiently cooled, all electronic degrees of freedom are frozen out, such that the atoms will all be in an electronic eigenstate. In the experiment the atoms have to be optically pumped into a specific hyper-fine state. In this case, the atoms can then be treated as identical particles. For neutral atoms, the only relevant interaction is then the collision of two particles. For bosons, low energy collisions are dominated by s-wave scattering, such that the only parameter in the interaction is the s-wave scattering length $a_{3\mathrm{D}}$. The Hamiltonian then reads

$$\begin{aligned}\hat{H} &= \int \mathrm{d}^3\vec{x}\Big\{\hat{\Psi}^\dagger(\vec{x})\left[-\frac{\hbar^2}{2m}\left(\partial_x^2+\partial_y^2+\partial_z^2\right)+V_{\text{external}}(\vec{x})\right]\hat{\Psi}(\vec{x})+\\ &\quad+\frac{g_{3\mathrm{D}}}{2}\hat{\Psi}^\dagger(\vec{x})\hat{\Psi}^\dagger(\vec{x})\hat{\Psi}(\vec{x})\hat{\Psi}(\vec{x})\Big\},\end{aligned} \tag{1}$$

with $\hat{\Psi}^\dagger(\vec{x})$ creating a bosonic atom at position $\vec{x}$. Here and throughout this thesis we set $\hbar$ and the mass m of the atoms equal to 1. The operators fulfill the usual bosonic commutation relations

$$\left[\hat{\Psi}(\vec{x}),\hat{\Psi}^\dagger(\vec{x}')\right]=\delta(\vec{x}-\vec{x}'),\quad \left[\hat{\Psi}(\vec{x}),\hat{\Psi}(\vec{x}')\right]=\left[\hat{\Psi}^\dagger(\vec{x}),\hat{\Psi}^\dagger(\vec{x}')\right]=0. \tag{2}$$

The bare interaction strength is $g_{3D} = 4\pi a_{3D}$, and the external potential $V_{\text{external}}(\vec{x})$ accounts for an overall trap.

The scattering length can be varied by using Feshbach resonances [KGJ06]: Its amplitude can become very large, if the energy of the two colliding atoms is close to resonance with a state of a molecule consisting of these atoms. Although the formation of a molecule is strictly forbidden in the absence of a third particle or some other means of energy dissipation, virtual transitions lead to a large phase shift and therefore scattering length. The atomic and molecular levels can be adjusted by an external static magnetic field, such that a_{3D} can be tuned to very large or small, positive or negative values. Longer range interactions can also be realized using ions which are subject to coulomb interaction, polar molecules which interact via dipole-dipole interaction, or atoms in Rydberg states which typically experience van der Waals interactions.

Quantum particles in lattice potentials, e.g. electrons in crystals, have been studied since the early days of quantum theory [AM76, FW71]. With the development of artificial (optical) lattice potentials for cold neutral atoms [BDZ08], bosonic lattice models are recently attracting increased interest [LSA+07]. If a standing wave laser field is imposed on the atoms, the atoms experience a spatially varying single particle potential

$$\hat{H}_{\text{lattice}} = \int \mathrm{d}^3\vec{x}\; V_{\text{lattice}}(\vec{x})\; \hat{\Psi}^\dagger(\vec{x})\hat{\Psi}(\vec{x}). \tag{3}$$

It is the AC-Stark effect which is responsible for this potential and its strength V_{lattice} is directly proportional to the light intensity. For two counter-propagating laser beams in x-direction it is proportional to $\sin^2(2\pi x/\lambda)$. The wavelength λ of the laser is thus twice the lattice constant. Larger lattice constants can be achieved by taking an angle smaller than π between the beams. A three-dimensional lattice can be created by using three pairs of counter-propagating lasers. The atoms seek intensity minima in blue detuned optical lattices, which have therefore the advantage of minimizing the inelastic scattering of light from the atoms. On the other hand atoms are attracted to the intensity maxima in red detuned lattices. This has the advantage of giving rise to an additional overall trapping potential, because the atoms avoid the outer regions, where the laser is not focused as strongly as in the center.

Instead of the Bloch basis, commonly used for the treatment of periodic potentials, one can use the Wannier basis, which provides localized basis functions

$$w^{(\nu)}(\vec{x}-\vec{n}) = \int \mathrm{d}^3\vec{k}\; e^{i\vec{k}\vec{n}}\; b^{(\nu)}_{\vec{k}}(\vec{x}), \tag{4}$$

where $b^{(\nu)}_{\vec{k}}(\vec{x})$ is the Bloch wave function in the νth band, and $\vec{n}$ is a real lattice vector.

It is a reasonable assumption, that all atoms are in the lowest Bloch band $\nu = 1$, if the temperature is small compared to the recoil energy

$$E_\mathrm{r} = \frac{\hbar^2 (2\pi)^2}{2m\lambda^2}, \tag{5}$$

which gives the order of magnitude for the distance between the lowest and the first excited band. We introduce creators and annihilators on the lattice in the lowest Bloch band by

$$\hat{b}^\dagger_{\vec{n}} = \int \mathrm{d}^3\vec{x}\; w^{(1)}(\vec{x} - \vec{n}) \hat{\Psi}^\dagger(\vec{x}). \tag{6}$$

They fulfill the usual bosonic (or equivalently harmonic oscillator) commutation relations

$$\left[\hat{b}_{\vec{j}}, \hat{b}^\dagger_{\vec{j}'}\right] = \delta_{\vec{j},\vec{j}'}, \quad \left[\hat{b}_{\vec{j}}, \hat{b}_{\vec{j}'}\right] = \left[\hat{b}^\dagger_{\vec{j}}, \hat{b}^\dagger_{\vec{j}'}\right] = 0 \tag{7}$$

Neglecting all other bands, the field operator can in good approximation be expressed by

$$\hat{\Psi}^\dagger(\vec{x}) = \sum_{\vec{n}} \hat{b}^\dagger_{\vec{n}} w^{(1)}(\vec{x} - \vec{n}). \tag{8}$$

Inserting this into (1) yields

$$\hat{H} = \sum_{\vec{i},\vec{i}'} \left\{ -J_{\vec{i},\vec{i}'} \hat{b}^\dagger_{\vec{i}} \hat{b}_{\vec{i}'} + \sum_{\vec{j},\vec{j}'} U_{\vec{i},\vec{i}',\vec{j},\vec{j}'} \hat{b}^\dagger_{\vec{j}} \hat{b}^\dagger_{\vec{i}} \hat{b}_{\vec{i}'} \hat{b}_{\vec{j}'} \right\}. \tag{9}$$

The single particle matrix reads

$$J_{\vec{i},\vec{i}'} = -\int \mathrm{d}^3\vec{x}\; w^{(1)\,*}(\vec{x} - \vec{i}) \left[-\frac{1}{2}\left(\partial_x^2 + \partial_y^2 + \partial_z^2\right) + V(\vec{x}) + V_\mathrm{lattice}(\vec{x}) \right] w^{(1)}(\vec{x} - \vec{i}'), \tag{10}$$

and the two particle matrix is given by

$$U_{\vec{i},\vec{i}',\vec{j},\vec{j}'} = g_\mathrm{3D} \int \mathrm{d}^3\vec{x}\; w^{(1)\,*}(\vec{x} - \vec{i})\; w^{(1)\,*}(\vec{x} - \vec{j}) w^{(1)}(\vec{x} - \vec{j}') w^{(1)}(\vec{x} - \vec{i}'). \tag{11}$$

1.1 Bose-Hubbard model

1.1.1 Grandcanonical phase diagram

If the lattice potential is several recoil energies deep, the Wannier functions will be strongly localized. In this limit, it is a good approximation to keep only up to nearest neighbor terms in the single particle Hamiltonian, and only local terms in the interaction [JBC+98]. The result is named the Bose-Hubbard model. It's

Figure 1: Illustration of the Bose-Hubbard model in one dimension, Eq. (13).

Hamiltonian has the form

$$\hat{H} = -J \sum_{\langle \vec{j}, \vec{j}' \rangle} \hat{b}^\dagger_{\vec{j}} \hat{b}_{\vec{j}'} + \frac{U}{2} \sum_{\vec{j}} \hat{b}^\dagger_{\vec{j}} \hat{b}^\dagger_{\vec{j}} \hat{b}_{\vec{j}} \hat{b}_{\vec{j}} + \sum_{\vec{j}} V(\vec{j}) \hat{b}^\dagger_{\vec{j}} \hat{b}_{\vec{j}}, \tag{12}$$

where J is the particle hopping rate between adjacent lattice sites (here assumed to be isotropic), the first sum being over all pairs of nearest neighbors, U is the contact interaction between the particles on the same lattice site, and $V(\vec{j})$ accounts for a possibly present slowly varying external potential. In one dimension, Eq. (12) is usually written in the form

$$\hat{H} = -J \sum_j (\hat{b}^\dagger_j \hat{b}_{j+1} + \text{H.a.}) + \frac{U}{2} \sum_j \hat{b}^\dagger_j \hat{b}^\dagger_j \hat{b}_j \hat{b}_j + \sum_j V(j) \hat{b}^\dagger_j \hat{b}_j. \tag{13}$$

See Fig. 1 for an illustration.

The Bose-Hubbard model (BHM) [FWGF89] is an important example for a lattice model, because it is the most simple interacting lattice model for bosons, which features a quantum phase transition from a superfluid regime, to the Mott-insulating regions that exist for integer fillings of n particles per lattice site. The relevant parameter in the model is the ratio J/U. U can be changed in comparison to J either by tuning the bare interaction strength using Feshbach resonances [KGJ06], or by changing the lattice depth, because a deeper lattice results in more localized Wannier functions and smaller J/U (10), (11). At fixed integer filling, for $J = 0$ the ground state will have exactly n particles per lattice site, which minimizes the interaction energy. For small J/U, the hopping term is also not relevant. It leads to small quantum fluctuations, where a single particle moves, thus breaking up the filling with exactly n particles and creating particle and hole defects. Those are however exponentially suppressed. But if J becomes comparable to U it can become favorable to have free defects, as they can absorb a kinetic energy of the order of $2JnD$, where D is the dimension, by delocalizing. As the particle hole gap is vanishing, there is a phase transition from the Mott-insulator to a compressible phase. For finite temperature this phase is expected to be a Bose glass phase [FWGF89], while at $T = 0$ the transition is directly to a superfluid phase. At incommensurate filling, the system is always in a compressible phase. The behavior of the system becomes most

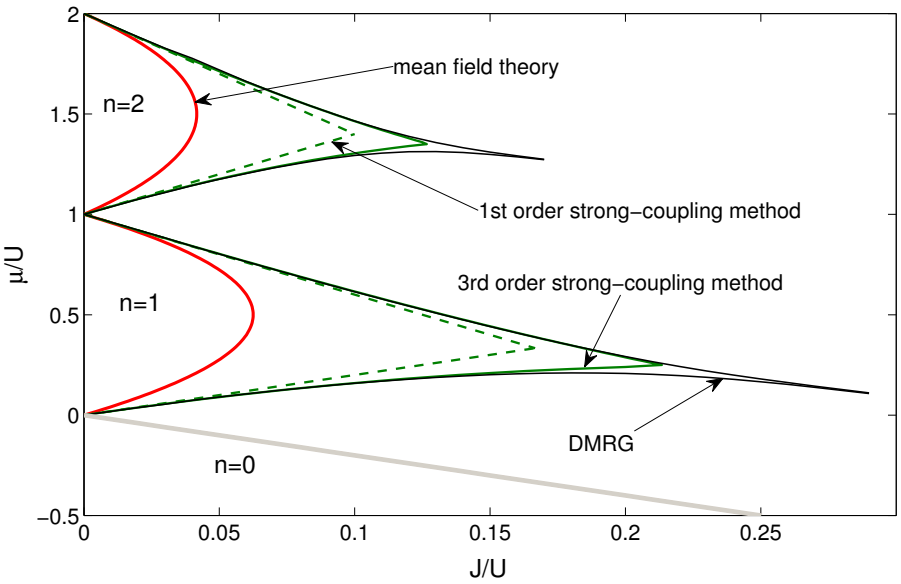

Figure 2: Phase diagram of the Bose Hubbard model in one dimension at zero temperature, calculated using different methods. Shown are the two Mott lobes with filling $n = 1$ and $n = 2$ only. Mean field data are taken from [vOvdSS01]. The first order strong coupling (perturbation theory in J/U) curves are given by $\mu_n^+(J) = nU - 2(n+1)J$, $\mu_n^-(J) = (n-1)U + 2nJ$. The third order strong coupling expansion can be found in [FM96]. Details on the numerically exact (DMRG) data can be found in [Mut08]. – Figure taken from [Mut08].

apparent in the grand canonical phase diagram, introducing the chemical potential as a parameter

$$\mu = \left(\frac{\partial \langle \hat{H} \rangle}{\partial \rho} \right)_S , \tag{14}$$

with $\rho = \langle \hat{b}_j^\dagger \hat{b}_j \rangle$ beeing the density, which is the same for every site j, and S the entropy, which vanishes at zero temperature. At $J = 0$, the density takes only integer values, except at integer values n of μ, where we have $n < \rho < n + 1$. For finite J/U the particle hole gap of the Mott insulator at filling n, i.e., $\mu_n^+ - \mu_n^-$ with $\mu_n^\pm = \lim_{\rho \to n^\pm} \{\mu(\rho)\}$ becomes smaller and finite regions with a phase of finite compressibility open between the commensurable regions. For increasing J/U the Mott lobes decrease in μ direction, until the gap vanishes and the above described phase transition at commensurate filling takes place. The exact shape of the phase diagram can be found only numerically, see Fig. 2 for $T = 0$ and $D = 1$. Using cold atoms, the Mott-superfluid transition has been first observed by Greiner et al. [GME+02].

1.1.2 Repulsively bound pairs

A remarkable phenomenon in the BHM is that pairs of strongly interacting bosons, i. e., in the case $|U| \gg J$ can form tightly bound "dimers" both for attractive and repulsive interactions [WTL+06, PM07, VP08, PSAF07]. In free space, or in the presence of some means of energy dissipation, the repulsive interaction inevitably leads to pair dissociation. In a deep lattice however, the kinetic energy of each particle is restricted to the width of a given Bloch band, usually the lowest. Consequently, two co-localized particles in a dissipation-free lattice remain tightly bound together as a dimer when their interaction energy U exceeds the kinetic energy of free particles $\sim J$ within the Bloch band.

Considering a lattice that contains only dimers, created by the creation operator $\hat{c}_j^\dagger = \hat{a}_j^\dagger \hat{a}_j^\dagger$ when applied to the vacuum, a simple effective Hamiltonian can be constructed. We therefore start from a lattice that contains only zero particles (empty) or two particles (a pair) on each site. Adiabatically eliminating all states with odd number of particles per site in second order, then leads to an effective Hamiltonian for the dimers [PSAF07] that contains only terms with energies on the characteristic scale of $J^2/U \ll J$:

$$\hat{H} = -\tilde{J} \sum_j (\hat{c}_j^\dagger \hat{c}_{j+1} + \text{H.a.}) + \tilde{B} \sum_j \hat{c}_j^\dagger \hat{c}_{j+1}^\dagger \hat{c}_{j+1} \hat{c}_j. \tag{15}$$

$\tilde{J} = -2J^2/U$ is the effective dimer hopping rate, associated with a second order process where one single particle of a given pair virtually hops to a neighboring site (the coupling is $\sqrt{2}J$ due to bosonic statistics, and the intermediate state is off-resonant by $-U$), and then the other constituent particle of the same pair follows. $\tilde{B} = -16J^2/U$ is:

- the effective nearest neighbor interaction, generated by the process of one partner in either pair hopping onto the neighboring pair (with a coupling by the hopping of $\sqrt{6}J$, creating a trimer with energy U higher than for the single dimers), $-12J^2/U$,

- subtracting the self energy of the two neighborless dimers, generated by a constituent particle hopping to the free neighboring site (again with coupling strength $\sqrt{2}J$ to the intermediate state with energy lower by U), $4J^2/U$.

Because more than a single dimer on a given site shall be forbidden, the dimer creation

and annihilation operators satisfy the hard-core boson commutation relations

$$i \neq j: \qquad [\hat{c}_i, \hat{c}_j] = [\hat{c}_i, \hat{c}_j^\dagger] = 0, \tag{16a}$$

$$i = j: \qquad \{\hat{c}_j, \hat{c}_j\} = 0, \ \{\hat{c}_j, \hat{c}_j^\dagger\} = 1. \tag{16b}$$

We see that eliminating unpaired particles, we have transformed bosons with strong (of order U) local repulsion to hard core bosons with nearest neighbor attraction of order J^2/U, which is however stronger than the hopping term by a factor of 8. This pairs form stable clusters, and we will show in section 8 how this feature can be used to dynamically create pure clusters of dimers. Note that for attractively bound pairs one arrives at nearest neighbor repulsion for the pairs along the same lines [SBE+09]. Since hard core bosons on a lattice are equivalent to a spin-1/2 chain in one dimension, see section 3.4, this makes the creation of antiferromagnetic order possible, if the gas can be cooled below J^2/U.

1.2 Lieb-Liniger model

An optical lattice can be applied in two directions only. The atoms experience a strong lattice potential in y and z direction, while in x direction there will be only the shallow potential of the external trap. Thus the optical lattice divides the gas into many long and parallel, cigar shaped subsystems or "tubes". A similar geometry can be created using a magnetic micro trap on an atom chip [HLF+07], which has the advantage of having only a single, isolated tube or only small number (usually two) of tubes such that coupling between them can be studied with better control. At low temperatures the transverse motion of the atoms in the tube is frozen out: only the transverse ground state is occupied. The remaining longitudinal degree of freedom constitutes an effective one-dimensional system.

A Bose gas in one spatial dimension is described by the Hamiltonian

$$\hat{H} = \int \mathrm{d}x \left[\hat{\Psi}^\dagger(x) \left(-\frac{1}{2}\partial_x^2 \right) \hat{\Psi}(x) + \frac{g}{2} \hat{\Psi}^{\dagger\,2}(x) \hat{\Psi}^2(x) + \hat{\Psi}^\dagger(x) V(x) \hat{\Psi}(x) \right]. \tag{17}$$

Here $\hat{\Psi}(x)$ is again the field operator of the Bose gas in second quantization, $V(x)$ some possible trap potential, and g the strength of the local particle-particle interaction. For small interactions, g is directly proportional to the underlying three-dimensional interaction strength $g_{3\mathrm{D}}$ and the strength of the transverse confinement (measured by the corresponding harmonic oscillator length $a_\perp$). If however $a_{1\mathrm{D}}$ becomes comparable to $a_\perp$, there is a confinement induced resonance [Ols98], at which

the effective one-dimensional local interaction strength diverges

$$g = -\frac{2}{a_{1\mathrm{D}}} = \frac{g_{3\mathrm{D}}}{\pi a_\perp^2}\left(1 - C\frac{a_{3\mathrm{D}}}{a_\perp}\right)^{-1}. \tag{18}$$

In the homogeneous case, the physics of (17) is given by only one parameter, which is the ratio between the interaction strength and the particle density $\rho = \langle\hat{\Psi}^\dagger(x)\hat{\Psi}(x)\rangle$, called the Tonks parameter

$$\gamma = g/\rho. \tag{19}$$

It gives also a measure for the ratio between the average interaction energy, which is $\sim g\rho^2$, and the average kinetic energy, which scales as $\rho^{3/d} = \rho^3$ in $d = 1$ dimension. This shows that in the one-dimensional case, the effects of a zero-range interaction are more relevant at low densities, in contrast to the higher dimensional case.

1.2.1 Tonks-Girardeau gas

An interesting feature of the Lieb-Liniger model is that it is an interacting many body model but still exactly solvable in the homogeneous case. This is a very rare case. Before we discuss the nature of the full solution for finite γ in the next section, let us take a look at the limit of impenetrable or hard core bosons, $\gamma \to \infty$, called the Tonks-Girardeau gas [KWW04, PWM+04]. Girardeau [Gir60] showed, that this problem is equivalent to that of free fermions. To see this, we construct the eigenfunctions of the Hamiltonian in first quantization. Given N particles, the wave function $\phi(x_1, \ldots, x_N)$ must vanish whenever $x_i = x_j$ if $i \neq j$. Everywhere else, the wave function must fulfill the equation of free particles

$$\left(\sum_{j=1}^{N} \partial_j^2\right)\phi(x_1, \ldots, x_N) = E\phi(x_1, \ldots, x_N). \tag{20}$$

Both conditions can be trivially solved using a Slater determinant of single particle eigenstates. We get all eigenvalues by using all combinations of mutually different single particle eigenstates. However the resulting wave function will be totally anti-symmetric (fermionic), such that we have to symmetrize it. The complete information about a state is in fact contained in the principal sector $R_1 : x_1 < x_2 < \cdots < x_N$. The wave function in all other sectors is simply given by sorting the particle positions. In second quantization, the symmetrization of the Slater determinant can be elegantly accounted for by introducing fermionic field operators

$$\hat{\Upsilon}(x) = \exp\left(i\pi\int_{-\infty}^{x} \mathrm{d}y\hat{\rho}(y)\right)\hat{\Psi}(x), \tag{21}$$

$$\left\{\hat{\Upsilon}(x), \hat{\Upsilon}^\dagger(x')\right\} = \delta(x-x'), \ \left\{\hat{\Upsilon}(x), \hat{\Upsilon}(x')\right\} = \left\{\hat{\Upsilon}^\dagger(x), \hat{\Upsilon}^\dagger(x')\right\} = 0. \tag{22}$$

$\hat{\rho}(x) = \hat{\Upsilon}^\dagger(x)\hat{\Upsilon}(x) = \hat{\Psi}^\dagger(x)\hat{\Psi}(x)$ is the density operator. Any eigenstate of the Tonks gas can then be written

$$|k_1, \ldots, k_N\rangle = \hat{\Upsilon}^\dagger_{k_1} \cdots \hat{\Upsilon}^\dagger_{k_N}|0\rangle, \tag{23}$$

where the set of quantum numbers $\{k_1, \ldots, k_N\}$ is mutually different and

$$\hat{\Upsilon}^\dagger_k = \int \mathrm{d}x \phi^*_k(x)\hat{\Upsilon}^\dagger(x) \tag{24}$$

creates a (fermionic) particle in the single particle eigenstate k described by the wave function $\phi_k(x)$ (e.g. plain waves for periodic boundary conditions or harmonic oscillator eigenfunctions for a harmonic longitudinal confinement).

We see now, that hard core bosons and free fermions have exactly the same spectrum. Some properties of the eigenstates are also the same, e.g. the local density $\hat{\rho}(x)$ and therefore all density-density correlators, even at different times. However other observables behave totally different. The simplest examples are non local single particle correlations:

$$\hat{\Psi}^\dagger(x)\hat{\Psi}(y) \neq \hat{\Upsilon}^\dagger(x)\hat{\Upsilon}(y), \tag{25}$$

because the phase factors in (21) do not cancel if $x \neq y$. The same is true for non equal time single particle correlations:

$$\hat{\Psi}^\dagger(x,t)\hat{\Psi}(x,t') \neq \hat{\Upsilon}^\dagger(x,t)\hat{\Upsilon}(x,t') \quad \text{for } t \neq t', \tag{26}$$

because the phase factor in (21) is not a conserved quantity. The particle number in arbitrary single particle basis states is also sensitive to the statistics: The density in momentum space

$$\hat{\rho}^{\mathrm{F}}_k = \hat{\Upsilon}^\dagger_k\hat{\Upsilon}_k \neq \hat{\Psi}^\dagger_k\hat{\Psi}_k = \hat{\rho}^{\mathrm{B}}_k, \tag{27}$$

where $\hat{\Psi}^\dagger_k = \int \mathrm{d}x \phi^*_k(x)\hat{\Psi}^\dagger(x)$ creates a Boson in state $|k\rangle$, is a well known example and shown in Fig. 3. The number of bosons in the single particle ground state is much larger than one, because there is no Pauli principle for the bosons. We will come back to this Bose-Fermi mapping in section 1.3.

1.2.2 Bethe ansatz

The interacting case (finite $\gamma > 0$) can also be solved exactly. This was first done by Lieb and Liniger [LL63] using an idea first utilized by Bethe [Bet31] long before. Bethe diagonalized what is called in modern literature the spin-1/2 XXZ chain. Spin

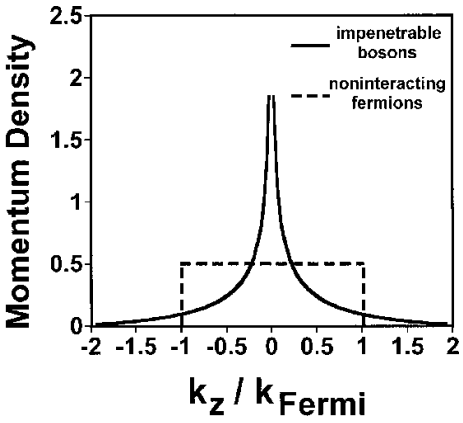

Figure 3: Momentum distribution for a system of hard core bosons at zero temperature in the thermodynamic limit. Corresponding distribution for an ideal Fermi gas is shown for comparison. The Fermi momentum in one dimension is $k_{\text{Fermi}} = \pi\rho$. – Taken from [Ols98].

chains are typical systems where exactly solvable models can be constructed, using the more general algebraic Bethe ansatz [KBI93, Mos08]. The spin-1/2 XXZ chain will turn out to be the discretized version of the Bose-Fermi mapped (21) Lieb-Liniger gas, see section 3. The one-dimensional nature of the problem is critical to the complete solvability. Because any eigenfunction of the Lieb-Liniger model must be totally symmetric (bosonic), it is always sufficient to work in the principal sector R_1. The δ-interaction leads to $N-1$ boundary conditions

$$(\partial_j - \partial_{j+1})\,\phi(x_1,\ldots,x_N)|_{x_j=x_{j+1}} = g\,\phi(x_1,\ldots,x_N)|_{x_j=x_{j+1}}\,. \tag{28}$$

A last boundary condition is imposed by the physical boundary condition, which we will assume to be periodic of length L. Then

$$\partial_x\,\phi(x,x_2,\ldots,x_N)|_{x=0} = \partial_x\,\phi(x_2,\ldots,x_N,x)|_{x=L}\,. \tag{29}$$

Inside R_1 we still have the free equation (20), which is trivially fulfilled if we make a generalized plain wave ansatz, requiring $k_1 < k_2 < \cdots < k_N$ for uniqueness,

$$\phi(x_1,\ldots,x_N) = \sum_P a(P) P \exp\left(i\sum_j k_j x_j\right). \tag{30}$$

The outer sum is over all permutations P of the rapidities $\{k_1,\ldots,k_N\}$. Outside R_1 the wave function is fixed by symmetry, not by (30). Because we are in one dimension, we now have the same number N of boundary conditions as we have independent

variables. Lieb and Liniger [LL63] showed, that the contact conditions (28) require

$$a(Q) = -a(P)\exp(i\theta_{ij}) \tag{31}$$

whenever $P^{-1}Q$ exchanges only k_i with k_j, and

$$\theta_{ij} = -2\tan^{-1}\left(\frac{k_i - k_j}{g}\right). \tag{32}$$

The periodic boundary condition then fixes the allowed sets of ks via

$$(-1)^{N-1}e^{-ik_jL} = e^{i\sum_{s=1}^{1} N\theta_{sj}}. \tag{33}$$

Division of successive equations results in the set of $N-1$ Bethe equations for the differences

$$\delta_j := \frac{k_{j+1} - k_j}{L} = \sum_{s=1}^{N}(\theta_{sj} - \theta_{sj+1}) + 2\pi n_j. \tag{34}$$

The solution of this system defines all θ_{ij} and thus k_1. Note that k_1 is only defined up to a multiple of $\frac{2\pi}{L}$, because giving all particles an additional momentum of $m\frac{2\pi}{L}$ for an integer m trivially results again in a solution. The quantum numbers n_j and m completely define the eigenstate of a system. We must have $n_j \geq 1$ in order to have $\delta_j > 0$. The ground state has $n_j = 1$ for all j and m such that the total momentum $|P| = \left|\sum_j k_k\right| \leq \frac{2\pi L}{N}$.

We can get a feeling for the solution by looking at the limit $g \to \infty$. Then $\theta = 0$ and $\delta_j = 2\pi n_j$ and (31) is solved by $a(P) = (-1)^P$ resulting in the usual Slater determinant for free fermions in R_1. The ground state is just the filled Fermi sea. For finite interactions, the n_j still define the occupation inside a Fermi sea, but the resulting momenta k_j are no longer equally spaced. Elementary excitations are still characterized as holes in the Fermi sea ($n_j = 2$ for $1 < j < n-1$) or particles outside ($n_1 > 1$ or $n_{N-1} > 1$).

We remark, that although the Bethe equations can be solved for large particle numbers N, the resulting wave function is still hard to evaluate. Nonlocal correlation functions can only be extracted with considerable numerical efforts [CC06].

In contrast to this, thermodynamic properties and certain local correlations are easily accessible directly in the thermodynamic limit

$$N, L \;\to\; \infty, \quad \rho = \frac{N}{L} \;=\; \text{const.} \tag{35}$$

At $T = 0$ this can be done [LL63] by Taylor expanding $\theta_{sj} - \theta_{sj+1}$ (because k_j will

approach k_{j+1} in the thermodynamic limit) in (34). All k_j will lie between $-K = k_1$ and $K = k_N$. Defining the density of rapidities as

$$g(x = k_j/K) = \rho(k_j) = \frac{1}{L(k_{j+1} - k_j)}, \tag{36}$$

(34) becomes the integral equation

$$2\pi g(y) = 1 + 2\lambda \int_{-1}^{1} \frac{g(x)\mathrm{d}x}{\lambda^2 + (x-y)^2}, \tag{37}$$

which can be solved numerically using iteration. The normalization condition

$$\int_{-K}^{K} \rho(k)\mathrm{d}k = \rho \tag{38}$$

can be used afterwards to get

$$\lambda := \frac{g}{K} = \gamma \int_{-1}^{1} g(x)\mathrm{d}x \tag{39}$$

as a function of γ. The total energy of the system is

$$E = \sum_j k_j^2 = L \int_{-1}^{1} g(x)(Kx)^2 K\mathrm{d}x = N\rho^2 e(\gamma) \tag{40}$$

where $e(\gamma) = \frac{\gamma^3}{\lambda^3} \int_{-1}^{1} g(x)x^2\mathrm{d}x$. The equation of state reads ($T = 0$ means that E is also the free energy)

$$\mu = \partial_N E = g^2 \underbrace{\frac{3e(\gamma) - \gamma e'(\gamma)}{\gamma^2}}_{=:f(\gamma)}. \tag{41}$$

All the thermodynamics is contained within $e(\gamma)$ (or $f(\gamma)$) [LL63, DLO01a], tabulated in [DLO01b]. E.g., the density as a function of interaction and chemical potential reads

$$\rho = \frac{g}{f^{-1}\left(\frac{\mu}{g^2}\right)}. \tag{42}$$

This equation is useful, e.g., to calculate density profiles for inhomogeneous systems in local density approximation (LDA): Given an inhomogeneous system, where the interaction strength $g(x)$ or the local potential $V(x) = -\mu(x)$ are varying slowly on the scale of the interparticle distance $1/\rho$, it is true in good approximation, that the local density distribution $\rho(x)$ is still given by (42) everywhere, with the now x-

dependent parameters. The reason for this is, that many particles around the point x effectively experience the same parameter values, and in equilibrium the system is locally close to a homogeneous system in the thermodynamic limit. The LDA works for other short range interactions, higher order local or short range correlations and finite temperatures as well, but it fails in the limit of free bosons, because every particle can then be delocalized over a distance much larger then $1/\rho$.

Local two body correlations can easily be calculated [LL63] using the Hellmann-Feynman theorem [Hel33, Fey39], which essentially states the easily proven fact that

$$\langle\Psi_g|\hat{H}_{\text{i.a.}}|\Psi_g\rangle = \partial_g\left(\langle\Psi_g|\hat{H}_{\text{free}} + g\hat{H}_{\text{i.a.}}|\Psi_g\rangle\right) = \partial_g E_g, \tag{43}$$

Where $|\Psi_g\rangle$ is a certain eigenstate with energy E_g of the Hamiltonian $\hat{H}_{\text{free}} + g\hat{H}_{\text{i.a.}}$, depending on the interaction strength g. Using the ground state energy (40) and $\hat{H}_{\text{i.a.}} = \int \mathrm{d}x\langle\hat{\Psi}^\dagger(x)^2\hat{\Psi}(x)^2\rangle$ thus yields

$$g^{(2)} = \frac{\langle\hat{\Psi}^\dagger(x)^2\hat{\Psi}(x)^2\rangle}{\rho^2} = \frac{1}{L\rho^2}\partial_g E = e'(\gamma). \tag{44}$$

Nonlocal [OD03] correlation functions can only be calculated perturbatively, or using general numerical techniques, which don't rely on integrability, as we will do [MF10, MFS10, MSF10] in this thesis, sections 3, 5, and 6. The same is true for three body correlations, but besides perturbative expansions [GS03], exact methods are developing [CSZ06a, CSZ06b, KMT09, KCI12].

1.2.3 Finite temperature

Yang and Yang [YY69] found similar integral equations, that describe the thermodynamics of the Lieb-Liniger model at nonzero temperature. This involves introducing the density $\rho_{\text{h}}(k)$ of (rapidity) holes (there are ν holes between the rapidities k_j and k_{j+1} for $n_j = 1 + \nu$) in addition to the density of rapidities $\rho(k)$. Both densities are no longer confined to a finite range of k values, and in addition to the equation for the total energy

$$E = \sum_j k_j^2 = L\int_{-\infty}^{\infty}\rho(k)k^2\mathrm{d}k \tag{45}$$

the entropy of the system is

$$S = L\int_{-\infty}^{\infty}\Big[\big(\rho(k)+\rho_{\text{h}}(k)\big)\ln\big(\rho(k)+\rho_{\text{h}}(k)\big) - \rho_{\text{h}}(k)\ln\rho_{\text{h}}(k) - \rho(k)\ln\rho(k)\Big]\mathrm{d}k. \tag{46}$$

The equilibrium condition, that the free energy $F = E - TS$ is minimal, leads to integral equations similar to (37). Once the free energy and the local density is found numerically, we have again

$$F = N\rho^2 e\Big(\gamma, \frac{T}{2g^2}\Big). \tag{47}$$

The equation of state then reads

$$\mu = \left(\frac{\partial F}{\partial N}\right)_T = g^2 f(\gamma, \frac{T}{2g^2}), \tag{48}$$

and (42) can be used in the same way, e.g., for calculating density profiles in local density approximations for systems which are globally in thermal equilibrium. Again the Hellmann-Feynman theorem can be used to calculate the local two-body correlations [KGDS03].

1.2.4 Attractive interactions

So far we have considered the repulsive case $g > 0$. In the attractive case, the problem can still be solved by the coordinate Bethe ansatz. However, there are additional difficulties, which become apparent already when studying the $N = 2$ particle case [LL63, MF10]. Complex rapidities become admissible, and the δ_j can be imaginary. In the two particle case, the ground state is the one where two particles form a bound pair. This pair is strongly localized in the strongly interacting regime $|\gamma| \gg 1$: The distance between the particles[1] is of order $1/\gamma$, and the binding energy correspondingly $\sim \gamma^2$. The ground state of the many-particle system [McG64] has energy $\sim N^2$ and is therefore thermodynamically unstable.

However there exist solutions with all real rapidities. These are the gas like states, that do not contain any bound particles, i.e., their energy remains finite if adiabatically taking the limit $\gamma \to -\infty$. The lowest lying such state is called the super Tonks-Girardeau gas state [ABCG05, CGYH10]. For small $|\gamma|$ it is adiabatically connected to an excited state of the free bosonic system, and in the limit of large $|\gamma|$ it becomes identical to the Tonks-Girardeau state [TZS08]. For finite interaction strength it shows some peculiarities, such as stronger correlations, see Fig. 22, and lower compressibility [ABCG05] than the Tonks-Gas, i.e., than free fermions. Although it is a highly excited state, the super Tonks-Girardeau gas can be prepared in experiment [HGM+09] by a sudden quench from the attractive to the repulsive regime, using a fast sweep through the confinement induced resonance (18). We will investigate the dynamics of this process [MF10] in section 6.

[1] This expression can of course only be valid as long as $1/\gamma$ is still large compared too the range r_0 of the true inter-particle potential.

1.3 Bose–Fermi mapping for 1D quantum gases with general contact interactions

The Bose-Fermi mapping used in section 1.2.1 can also be used to map bosons to fermions and vice versa which have finite strength local interactions [YG05]. We consider bosonic or fermionic quantum gases, that are fully described by their two particle Hamiltonian, i.e., the Hamiltonian is a sum of the form

$$H = -\frac{1}{2}\sum_j \partial_{x_j}^2 + \sum_{i<j} W(x_i - x_j), \tag{49}$$

and additionally require that the true interaction potential $W(x_i - x_j)$ can be approximated by a local pseudo-potential, i.e. it vanishes for $x_i \neq x_j$. Since we are in one dimension, this leads to the exact integrability of these models in the case of translation invariance [LL63] using coordinate Bethe ansatz [Bet31, Gau83].

To see the connection between the bosonic and the fermionic case, it is sufficient to consider the relative wave function $\phi(x = x_1 - x_2)$ of just *two* particles. The Hamiltonian then reads

$$H = -\partial_x^2 + W(x) \tag{50}$$

where we have dropped the term corresponding to the freely evolving center of mass.

The continuous two-particle case has been analyzed by Cheon and Shigehara [CS98, CS99]. The local pseudo-potential W is fully described by a boundary condition on ϕ at $x = 0$: Since ϕ fulfills the free Schrödinger equation away from 0, it must have a discontinuity at the origin as an effect of the interaction. Thus we see that

$$\partial_x^2\phi(x) = \begin{cases} \phi''(x) & x \neq 0 \\ \delta(x)\left[\phi'(0^+) - \phi'(0^-)\right] + & \\ \quad + \delta'(x)\left[\phi(0^+) - \phi(0^-)\right] & x = 0. \end{cases} \tag{51}$$

In the case of distinguishable or spinful [GO04] particles both singular terms contribute. Otherwise, due to symmetry, the term proportional to the delta function δ can only be nonzero for bosons, while the δ' term exists only for fermions. That means, we have for bosons

$$\partial_x^2\phi(x) = \begin{cases} \phi''(x) & x \neq 0 \\ 2\delta(x)\phi'(0) & x = 0. \end{cases} \tag{52}$$

and for fermions

$$\partial_x^2\phi(x) = \begin{cases} \phi''(x) & x \neq 0 \\ 2\delta'(x)\phi(0) & x = 0. \end{cases} \tag{53}$$

In order to get proper eigenstates (i.e. without any singular contribution), the pseudo-potential W acting on the wave-function must absorb the singular contributions from the kinetic energy. Thus the only possible form of a local pseudo-potential for bosons is $W_B\phi = g_\mathrm{B}\delta(x)\phi(0)$, while that for fermions reads $W_F\phi = -g_\mathrm{F}\delta'(x)\phi'(0)$. Note that ϕ (ϕ') is continuous at 0 for bosons (fermions). These two possibilities represent the well known cases, where the particle interact either by s-wave scattering only or by p-wave scattering only, and the interaction strength corresponds to the scattering length, respectively scattering volume, which are the only free parameters left.

Since all wave functions must have the respective symmetry, we can restrict ourselves in the following to the primary sector R_1, which means $x > 0$ in relative coordinates. We will write $\phi(0)$ for $\lim_{x\to 0^+}\phi(x)$ and $\phi'(0)$ for $\lim_{x\to 0^+}\phi'(x)$. The above shows that W imposes a boundary condition on every proper wave function:

$$\begin{aligned} \phi'(0) &= \tfrac{g_\mathrm{B}}{2}\phi(0) \qquad \text{bosons,} \\ \phi'(0) &= -\tfrac{2}{g_\mathrm{F}}\phi(0) \qquad \text{fermions.} \end{aligned} \tag{54}$$

Eqs. (51) and (54) reveal a one-to-one mapping between the two cases, i.e., every solution for the bosonic problem yields a solution for the fermionic problem with

$$g_\mathrm{B} = -4/g_\mathrm{F} \tag{55}$$

by symmetrizing the wave function and vice versa. Any solution to the Lieb-Liniger model (possibly extended by an external potential or inhomogeneous interaction strength) is at the same time a solution of a fermionic model, obtained by the mapping (21). The attractive interactions map to repulsive interactions, and weak interactions map to strong interactions. The fermionic counterpart of the Tonks-Girardeau gas, which is the bosonic system corresponding to free fermions, is named the fermionic Tonks-Girardeau gas [Gir60, GM06, MG06]. It is the fermionic system corresponding to free bosons, i.e., $g_\mathrm{F} \to -\infty$. It can be treated analytically, e.g., the momentum distribution is known for arbitrary particle numbers [BEG05].

It should be remarked, that boundary conditions of the form (54) are the only ones that are equivalent to a local potential [Seb86, CS98]. While boundary conditions involving higher order derivatives can be taken into account to describe experimental realizations using cold gases in quasi 1D traps [ILGG10], they necessarily require finite range potentials and cannot be described fully by local pseudo-potentials.

1.4 Luttinger liquid theory

The low energy physics of gap-less, one-dimensional many-body systems can be universally described [Gia03] by a so-called Luttinger liquid

$$\hat{H} = \frac{1}{2\pi} \int \mathrm{d}x \left\{ uK \left[\pi \hat{\Pi}(x) \right]^2 + \frac{u}{K} \left[\partial_x \hat{\phi} \right]^2 \right\}. \tag{56}$$

Here $\hat{\phi}$ and $\hat{\Pi}$ are conjugate fields

$$\left[\hat{\phi}(x), \hat{\Pi}(y) \right] = i\delta(x-y). \tag{57}$$

Phenomenologically, $\partial_x \hat{\phi}$ is the operator of density fluctuations, and $\hat{\Pi}$ measures phase fluctuations. u is the characteristic velocity of the system, and K is a number, referred to as the Luttinger parameter.

An example where this Hamiltonian is exact can be constructed from the problem of free fermions: The ground state at finite density is the state where all single particle states are filled up to the Fermi energy. Around the Fermi energy, the dispersion relation is to good approximation linear. Due to this linearity, there is a well defined dispersion relation for low energy particle-hole excitations, which correspond to the excitation of a fermion from $k < k_\mathrm{F}$ to $k' > k_\mathrm{F}$. Thus there are well defined elementary excitations. Mathematical rigor additionally requires to regard left ($\hat{c}_\mathrm{L}^\dagger$) and right ($\hat{c}_\mathrm{R}^\dagger$) moving fermions (around $-k_\mathrm{F}$ and $+k_\mathrm{F}$ respectively) as distinguishable particles, each filling up an infinitely deep Fermi see, which does not change the physics at low energies. The resulting model is the Tomonaga-Luttinger model. It can be expressed in terms of it's elementary excitations, which are bosonic, because they are quadratic in the fermions:

$$\hat{b}_k^\dagger = \left(\frac{2\pi}{L|k|} \right) \left[\theta(-k) \hat{\rho}_\mathrm{L}^\dagger(k) + \theta(k) \hat{\rho}_\mathrm{R}^\dagger(k) \right], \tag{58}$$

with $\hat{\rho}_r^\dagger(k) = \sum_{k'} \hat{c}^\dagger(k'+k)\hat{c}(k')$ and θ the Heaviside step function. This transformation is referred to bosonization. The Hamiltonian becomes exactly (56), with $\hat{\phi}$ and $\hat{\Pi}$ linear expressions in the bosonic operators [Gia03]. Such a procedure can only work in one dimension. In higher dimensions there is e.g., no well defined dispersion relation for elementary excitations, because $\vec{k'} - \vec{k}$ does not have to be perpendicular to the Fermi surface.

For the Tomonaga-Luttinger model we have $u = \pi\rho = v_\mathrm{F}$, the Fermi velocity, and $K = 1$. The most important observation is, that an interaction between the particles does not introduce additional terms in the Hamiltonian (56). Interactions only renormalize K and u, as long as there does not occur a phase transition. The

Hamiltonian remains quadratic, and the interaction system is still described by the physics of free bosons. Many properties of the system can be calculated with u and K as parameters, e.g. the compressibility

$$\frac{1}{\chi} = \rho^2 \frac{\partial \mu}{\partial \rho} \tag{59}$$

satisfies

$$\frac{K}{u} = \pi \rho^2 \chi, \tag{60}$$

a relation used in section 4. Using a high energy cutoff, $\alpha \ll 1/\rho$, the two-point density-density correlation at large distances,$|r| \gg \alpha$, is given by [Gia03]

$$\langle \hat{\rho}(r)\hat{\rho}(0)\rangle = \frac{1}{2\pi^2}\left[K\frac{y_\alpha^2 - x^2}{(y_\alpha^2 + x^2)^2)} + \frac{1}{\alpha^2}\cos(2\pi\rho x)\left(\frac{\alpha}{|r|}\right)^{2K}\right], \tag{61}$$

with the space-time point $r = (x, u\tau)$ and $y_\alpha = u\tau + \alpha \mathrm{sign}(\tau)$. The correlation function shows a power law behavior. There is neither a typical correlation length, nor true log range order, which would mean finite correlations in the limit of large distance. This shows, that the system is always in a critical state, at the verge of a phase transition to an ordered state. This reflects the competition between the interactions on one hand, which have such a strong effect in one dimension that perturbation theory exhibits divergencies [Gia03], and the impossibility of true long range order in one dimension due to quantum fluctuations on the other hand. The slower the diagonal correlations (61) decay, the faster does the off-diagonal pair correlation function [Gia03]

$$\lim_{a\to 0}\left\langle \hat{\Psi}^\dagger(r)\hat{\Psi}^\dagger(r+a)\hat{\Psi}(a)\hat{\Psi}(0)\right\rangle \sim \frac{1}{(\pi\alpha)^2}\left(\frac{\alpha}{|r|}\right)^{1/(2K)}. \tag{62}$$

It also decays as a power law, such that true superfluid order is just as impossible as true long range density-density order. Note that at $K = 1/2$ the exponents for both types of order are the same, and there is a crossover between dominating diagonal and dominating off-diagonal order.

Many one-dimensional systems are actually described by a Luttinger Liquid in the low energy regime. Examples include the Lieb-Liniger model, the Hubbard and Bose-Hubbard models away from the Mott-insulating phases, and also spin chain models. In the cases with a spin degree of freedom (or with more than one species), there is a pair of conjugate fields for both spin and charge, which enter the Hamiltonian in general with different Luttinger parameters. Then there exist independent elementary charge and spin excitations, a fact known as spin-charge separation, because they usually separate due to their different velocity. This shows that any excitation of

a bare particle, which carries both spin and charge, breaks up into more than one collective type of excitation. This is another characteristic of one-dimensional physics.

A general problem is the determination of u and K from a given microscopic Hamiltonian. To determine both requires two equations. One can, e.g., be the compressibility relation (59). For Galileanly invariant models [Hal81], the second equation required is

$$uK = \pi\rho. \tag{63}$$

For the Lieb-Liniger model, this is enough to determine $u(\gamma)$ and $K(\gamma)$ using Bethe ansatz [Zvo10]. The Tonks gas (and free fermions) have $K = 1$, while K goes continuously to ∞ as the repulsion between the bosons goes to zero (or the fermions become increasingly attracting). To reach stronger correlations in the sense of (61), i.e. $K < 1$, requires to go to attractive interactions [Büc11] in the sense of the unstable super-Tonks Girardeau gas, or to use interactions that act over a nonzero distance. The latter can be, e.g., dipolar interactions, discussed in section 4, or the hard rod potential [ABCG05] which results in similar properties as the super Tonks-Girardeau gas.

1.5 Thermalization dynamics in closed quantum systems

Quantum mechanics is known to go beyond the laws of classical physics, e.g., by allowing for tunneling through barriers, by the uncertainty principle, by matterwave interference, by creating nonclassical correlations through entanglement and more recently also by seemingly allowing quantum computers to solve problems otherwise believed to be effectively unsolvable. Although quantum mechanics is supposed to be the more general theory and the old physics should be contained in it as the classical limit, this connection usually requires detailed analysis. A specific problem, where the quantum and the classical formalism work quite differently, is the relaxation of a closed system, which is initially far from equilibrium. It has attracted much attention recently, as first experiments on relaxation dynamics using cold atoms in optical potentials have been reported [KWW06, HLF+07, CDEO08, CFM+08, MS09, CWBD11, TCF+11]. They all consider an initial non-equilibrium state generated by a quench, i.e., by a sudden change in a parameter of the system, e.g., in the external confinement or the interaction strength.

In classical mechanics the thermalization of a system initially out of equilibrium is attributed to its chaotic behavior resulting from nonlinear equations of motion. A typical example is an interacting gas initially confined to some volume and released into a larger volume. After the release, the atoms will move on the energy shell in phase space ergodically, i.e., with no preference for any region. As a consequence,

after averaging over a certain time interval, all observables attain the same values as averaged over the energy shell, i.e., in the microcanonical ensemble. This generic mechanism does however not work for integrable systems. The presence of a number of conserved quantities equal to the number of degrees of freedom, confines the evolution to an invariant torus, fixed by the initial conditions. The statistical approach of describing the system by few macroscopic quantities fails, because the memory of the initial conditions persists.

The concept of thermalization via classical chaos fails when the system is described quantum mechanically. Quantum dynamics is always linear and there is always a number of trivial conserved quantities as large as the dimension of the Hilbert space. These are the projectors onto the eigenstates of the system. This is the case also for systems which exhibit chaotic dynamics classically.

Thermalization in quantum mechanical systems can be ascribed to the eigenstate thermalization hypothesis (ETH). It states that if $\hat{O}$ is an observable that acts only on a small subsystem (such as the local density) then, if $|\Psi_E\rangle$ is an eigenstate with not too small energy E, the expectation value $\langle\Psi_E|\hat{O}|\Psi_E\rangle$ is independent of the precise value of E. That means, all states with similar energy yield the same expectation value, which must therefore be an almost smooth function of E. Therefore $\langle\Psi_E|\hat{O}|\Psi_E\rangle$ takes the same value as in the microcanonical ensemble, and the details of the initial state does not matter.

The ETH rules out a possible survival of the initial conditions in any $\hat{O}$ due to the trivial conserved quantities. The initial state of the system can be expanded in energy eigenstates,

$$|\Psi_0\rangle = \sum_n c_n |n\rangle, \tag{64}$$

with complex amplitudes c_n. The Projectors $\hat{P}_n|n\rangle\langle n|$ commute with the Hamiltonian and the occupation numbers $c_n^* c_n$ are constant in time. We have

$$\langle\Psi_t|\hat{O}|\Psi_t\rangle = \sum_{n,m} c_m^* c_n \exp\left[(E_m - E_n)t\right] O_{nm} \tag{65}$$

with $O_{nm} = \langle\Psi_n|\hat{O}|\Psi_m\rangle$ the matrix elements of the observable. Due to dephasing, after a certain time the contribution of the off-diagonal part can be expected to cancel out. The expectation value then approaches

$$\langle\hat{O}\rangle_{\mathrm{d}} = \mathrm{Tr}\left[\hat{\rho}_{\mathrm{d}}\hat{O}\right], \tag{66}$$

with $\hat{\rho}_{\mathrm{d}} = \sum_n c_n^* c_n \hat{P}_n$ the density operator of the diagonal ensemble. After a quench, such as the release of a gas into a larger container, the amplitudes c_n are peaked

around an average energy $\bar{E} = \langle \hat{H} \rangle$, i.e., c_n vanishes unless $E_n \approx \bar{E}$. Due to the ETH, the diagonal ensemble gives the same expectation values for $\hat{O}$ as the microcanonical ensemble, independent of which eigenstates exactly are occupied. The fact, that there are in generally many states with $E_m \approx \bar{E}$ but negligible c_m does not matter.

This thermalization mechanism shows that the role of conserved quantities in quantum mechanics is quite different. Although the diagonal ensemble contains a lot of information about the initial state, the equilibrium expectation value of $\hat{O}$ are just that of the microcanonical ensemble due to the ETH.

The results are quite different if the model in question is quantum integrable. We call a quantum system integrable if it possesses an infinite number of conserved quantities (not just the Hamiltonian or possibly a total particle number) which are the integral over conserved local densities, i.e. operators defined on a subsystem of finite extent. Well known examples of such conserved densities are the Hamiltonian density and the particle density. For Bethe integrable systems, an infinite series of conserved densities can be constructed [GM96, ZNP97, CSZ06b]. In essence, solutions via Bethe ansatz yield a nontrivial transformation to a system of free particles [Gau83, KBI93, BPG08]. In a prominent experiment [KWW06] it has been shown, that cold atoms, in a regime that is well described by the integrable Lieb-Liniger model, do not thermalize as expected from thermodynamics. This result has triggered much attention. Even if an integrable system relaxes to a steady state, this steady state is in general not well described by the microcanonical ensemble [RMO06, Caz06, RDYO07, RDO08]. It is however described by the diagonal ensemble, which can not count as a statistical description,because it contains an exponentially large number of parameters.

Instead of using the conventional ensembles of statistical mechanics, it has been proposed [RMO06], to describe integrable systems using as generalized Gibbs ensemble (GGE). Such an ensemble fixes not only the usual thermodynamical parameters, but also the nontrivial conserved quantities $\hat{I}_m$:

$$\hat{\rho}_{\mathrm{g}} = \mathcal{Z}_{\mathrm{g}}^{-1} \exp\left(-\sum_n \lambda_m \hat{I}_n\right), \quad \mathcal{Z}_{\mathrm{g}} = \mathrm{Tr}\left[\exp\left(-\sum_n \lambda_m \hat{I}_n\right)\right] \tag{67}$$

The Lagrange parameters λ_m are fixed by requiring that the expectation values of the initial state match that of the GGE for all $\hat{I}_m$: $\mathrm{Tr}\left[\hat{\rho}_{\mathrm{d}} \hat{I}_m\right] = \mathrm{Tr}\left[\hat{\rho}_{\mathrm{init}} \hat{I}_m\right]$. It has been demonstrated for various models [RMO06, Caz06, RDYO07, KE08, RDO08, Rig09] both analytically and numerically, that the GGE does in general describe the long term asymptotics of an integrable system, while the microcanonical ensemble does not[2]. As to why this is the case, is still an open question, especially because the

[2] Alternatively, a generalized microscopic ensemble [CCR11] also works.

GGE is not uniquely defined [KE08]. For example is has been shown, that for hard core bosons on a one-dimensional lattice [RDYO07] it is sufficient to take for $\hat{I}_m$ the occupation numbers of the eigenstates of the corresponding Jordan-Wigner fermions, which are conserved separately. This is an infinite number in the thermodynamic limit, but scales only linearly in the particle number, not exponentially as the Hilbert space dimension. Finite products of occupation numbers $\hat{I}_{m_1}\hat{I}_{m_1}\cdots\hat{I}_{m_r}$, which are trivially also conserved and independent, are not taken into account. It has been demonstrated by Kollar et al. [KE08] that whether a GGE does agree with long time dynamics does depend on the choice of $\hat{I}_m$. (The diagonal ensemble is a special case of a GGE, where the projectors on the eigenstates are chosen for the $\hat{I}_m$.) Consequently, the subject requires further investigation, and new inside can, e.g., be given by numerical simulations.

Most studies of specific models have been done either for non-interacting particles [CDEO08] or systems that can directly be mapped to free systems such as hard-core bosons [RDYO07], the Luttinger model [Caz06], or the $1/r$ fermionic Hubbard model [KE08]. Other models require numerical treatment. While exact diagonalization gives accurate results for small systems [RDO08, Rou09], large system sizes are preferable, in order to justify a possible statistical treatment in the first place and also to overcome the artifacts that make different standard statistical ensembles different, although they typically yield identical results in the thermodynamic limit. Simulations on larger system sizes using exact numerical simulations [FCM+08, BPG+09, ES12] usually suffer from the fact, that large enough times to determine the relaxed expectation values are hard to reach. However one DMRG study on the non-integrable tilted Ising model [BCH11] has shown, that even without integrability, the final steady state can be different from thermal predictions. In this thesis we will add two important examples to the discussion. To this end we will numerically simulate an interaction quench in the continuous Lieb-Liniger gas. Although it is integrable, the mapping to free particles is not trivial and to our knowledge only a few conserved densities are known explicitly. We have access to long enough time scales to observe local (but not global) relaxation and compare to thermal descriptions in section 5. In a quench to attractive interactions, we observe coherent dynamics only, and no relaxation at all, which can be easily understood from the specific quench we implement, see section 6.

2 Matrix product state algorithms

In the present section we give an introduction to the numerical methods used in this thesis. Our goal is to describe quantum many-body systems exactly, including those where there is no analytic solution available. What that means is, that we want to use an algorithm, that generates results with arbitrary precision, given that the system is small enough (or the time over which it is evolved is short enough in the case of dynamical simulations) for the available computational resources, or given that the resources are increased sufficiently for the given problem (the scaling being exponentially in the worst case, as we will see). An algorithm known to satisfy this requirement is exact diagonalization, which however scales unfavorably with system size, because of the exponentially increasing dimension of the Hilbert space. We therefore employ matrix product state (MPS) algorithms, which aim at capturing the relevant part of the Hilbert space in terms of entanglement. They are trivially equivalent to exact diagonalization[3] if the dimension χ of the matrices used approaches the full Hilbert space dimension. A different approach that also yields potentially exact results are various quantum Monte Carlo methods, which where not used here. While being able to give an insight into the physics of specific systems, methods such as different variants of mean-field theory or finite order perturbation theory usually do not give numerically exact results.

Variational MPS methods have been used for more than half a century [KW41] to describe the transfer matrix of two-dimensional classical models in statistical mechanics, which are equivalent to one-dimensional quantum systems. For references see, e.g., the work of Baxter [Bax78] and references therein. Later on the density-matrix renormalization group (DMRG) method [Whi92] has been developed independently and proved very successful in describing low-energy eigenstates of one-dimensional quantum lattice systems which are typically only moderately entangled. In the last decade DMRG has been extended to real-time evolution [Vid03, Vid04, DKSV04, WF04] (t-DMRG). These and various other extensions all rely on the MPS framework to capture the relevant part of the Hilbert space in terms of the largest singular values [McC07, Sch11].

[3] In fact we checked the validity of all our implementations against exact diagonalization for small systems.

2.1 Matrix product states

MPS are an efficient way of specifying the state

$$|\Psi\rangle = \sum_{\vec{j}} c_{\vec{j}} |\vec{j}\rangle \tag{68}$$

(assumed here to be normalized) of a one-dimensional lattice system. Here $\vec{j}$ is a vectors of occupation numbers (or whatever other quantities are required to uniquely define the state of a single site) for every lattice site, thus corresponding to a Fock state. The number of parameters $c_{\vec{j}}$ is exponentially large in the system size. An MPS reduces this number by parametrizing the state in terms of finite size matrices A, which we will assume here to be all square and of dimension $\chi \times \chi$:

$$|\Psi\rangle = \sum_{\vec{j}} c_{\vec{j}} |\vec{j}\rangle = \sum_{\vec{j}} \mathrm{Tr}\left[\prod_m A^{[m],j_m}\right] |\vec{j}\rangle \tag{69}$$

$$= \mathrm{Tr}\left[\bigotimes_m \left(\sum_j A^{[m],j} |j\rangle_m\right)\right] \tag{70}$$

While the product $\prod$ in (69) denotes the usual matrix product, $\bigotimes$ in (70) denotes matrix product between A matrices and at the same time the direct product of the states of each lattice site. "Tr" here means taking the trace over the auxiliary space, i.e., the one where the matrices A act, only. The trace is required only for systems with periodic boundary conditions[VPC04, PWE10], while for finite systems comprising L sites the matrices belonging to the first site ($A^{[1],j}$) and those belonging to the last site ($A^{[L],j}$) can all be chosen to be row respectively column vectors instead of matrices. Equation (70) shows that an MPS is a generalization of the notion of a usual product state, to which it reduces if all $A^{[m],j}$ are complex numbers, i.e., $\chi = 1$.

Obviously the matrices A are not uniquely defined by (69). If the system is not subject to periodic boundary conditions, there is however a unique canonical[PGVWC07] form of the MPS (In this context the word "canonical" refers to the orthogonality and normalization properties which we do not find in an MPS in its general form (70) and is not to be mixed up with canonical in the sense of working at a fixed particle number, section 11.2.):

$$|\Psi\rangle = \sum_{\vec{j}} \Gamma^{[1]j_1} \lambda^{[1]} \dots \lambda^{[m-1]} \Gamma^{[m]j_m} \lambda^{[m]} \dots \lambda^{[L-1]} \Gamma^{[L]j_L} |\vec{j}\rangle \tag{71}$$

The $\lambda^{[m]}$ matrices are diagonal and contain the singular values from a Schmidt de-

composition of a bi-partition of the system into the sub-chain A comprising sites 1 to m and the sub-chain B comprising sites $m+1$ to L (in descending order for uniqueness):

$$|\Psi\rangle = \sum_{\alpha=1}^{\chi} \lambda_{\alpha}^{[m]} |\alpha\rangle_{\mathrm{A}} \otimes |\alpha\rangle_{\mathrm{B}} \tag{72}$$

$\{|\alpha\rangle_{\mathrm{A}}\}$ and $\{|\alpha\rangle_{\mathrm{B}}\}$ respectively form an orthonormal set, the reduced bases. Orthogonality for all possible bi-partitions means that the matrices are both left orthogonal

$$\sum_{j} \lambda^{[m-1]\,\dagger}\, \Gamma^{[m]j_m\,\dagger}\, \Gamma^{[m]j_m} \lambda^{[m-1]} = \mathbf{1}, \tag{73}$$

and right orthogonal

$$\sum_{j} \Gamma^{[m]j_m} \lambda^{[m]}\, \lambda^{[m]\,\dagger}\, \Gamma^{[m]j_m\,\dagger} = \mathbf{1}, \tag{74}$$

From this representation the constraint of MPS becomes apparent: The maximum number of nonzero singular values is χ. For a general state, this number can be the smaller of Hilbert space dimensions of A and B. At the heart of DMRG lies the discarding of all but the χ largest eigenvalues of the reduced density matrix of any of the two subsystems, which is equivalent to approximating the state by an MPS with dimension χ. Roughly speaking, this approximation is only good, if the entanglement entropy

$$S^{[m]} = -\sum_{\alpha=1}^{\chi} {\lambda_{\alpha}^{[m]}}^2 \log_2 \left({\lambda_{\alpha}^{[m]}}^2 \right) \tag{75}$$

between A and B is small. Rigorous results on the approximability in terms of entanglement entropies can be found in [SWVC08b]. Low lying eigenstates of 1D systems with short-range interaction can be approximated well [VC06], as S grows only logarithmically with system size. In real-time evolution however, S grows in general linear in time [CC05]. While t-DMRG is still a very useful method to calculate the short time entanglement dynamics, as was done by us in [UMF10], this limits the timescales accessible, at least in the Schrödinger picture. The situation may be different in the Heisenberg picture, as we will see in section 10.

The matrix product ansatz presented here is naturally adapted to systems with open boundary conditions, as the lattice sites are numbered by a single index and nearest neighbors are coupled by the matrices $\lambda^{[m]}$. MPSs can be used to represent states of systems with different geometry, e.g., by covering a 2D plane with a chain of tensors. However the Ansatz does not reflect the actual physical connectivity. As a consequence the matrix dimension required to reach a given accuracy quickly grows, e.g. for periodic boundary conditions [Whi93] as compared to open bound-

ary conditions. There exist generalizations to other geometries: Periodic boundary conditions can be tackled by coupling the first and the last site also via a λ tensor [VPC04, PWE10]. Projected entangled pair states (PEPS) [VC04], tree tensor networks [SDV06], and the multi–scale entanglement renormalization ansatz (MERA) [Vid07b, Vid10] are adaptions to higher dimensions, and will not be discussed in the present thesis. These methods suffer from a much higher computational complexity in using the ansatz in variational methods as compared to DMRG.

2.2 Imposing conservation laws

Conservation laws resulting from global symmetries can be taken into account explicitly in the construction of MPSs [Sch05, McC07, SZV10, BCOT11]. This reduces the number of degrees of freedom such that approximations with higher matrix dimensions can be calculated using the same amount of computation time and memory. In addition arithmetical errors of the type that would lead out of the symmetry sector of the initial state are impossible.

Implementing abelian symmetries is particularly easy [Sch05]. When calculating low lying eigenstates with a given accuracy, the gain in CPU time and memory is typically of an order of magnitude or more. In dynamical simulations, abelian symmetries allow for calculations on longer timescales[DCJZ05].

If the state $|\Psi\rangle$ is an eigenstate of the total particle number in the whole system with eigenvalue N, then the Schmidt vectors $|\alpha\rangle_{\mathrm{A}}$ and $|\alpha\rangle_{\mathrm{B}}$ also have to be eigenstates of the total particle number in there respective subsystems, their eigenvalues $N_{\mathrm{A}}(\alpha)$ and $N_{\mathrm{B}}(\alpha)$ adding up to N but maybe different for different values of α.

The Schmidt decomposition at two neighboring bonds reads

$$|\Psi\rangle = \sum_{\alpha,\beta=1}^{\chi} \sum_{j} \lambda_{\alpha}^{[m-1]} \Gamma_{\alpha,\beta}^{[m]j} \lambda_{\beta}^{[m]} \; |j\rangle_m \otimes |\alpha\rangle_{\mathrm{A}} \otimes |\beta\rangle_{\mathrm{B}}. \tag{76}$$

Here A comprising sites 1 to $m-1$. If the state has a certain symmetry, this restricts the number of allowed states $|j\rangle_m$ for given $|\alpha\rangle_{\mathrm{A}}$ and $|\beta\rangle_{\mathrm{B}}$. In the case of particle number conservation we have $j = N - N_{\mathrm{A}}(\alpha) - N_{\mathrm{B}}(\alpha)$. When implementing this scheme, we can therefore leave out the physical dimension of the tensor $\Gamma_{\alpha,\beta}^{[m]j}$ completely (if there is no further local degree of freedom besides occupation number). This is one point where the conservation law makes the algorithm more efficient in terms of memory. The tensor $\Gamma_{\alpha,\beta}^{[m]j}$ is said to be symmetric. For a more mathematical description in terms of group theory see, e.g., [McC07, BCOT11] and references therein. It should be noted at this point, that applying particle number conservation in this way to MPS for infinite size systems [Vid07a] requires the average filling to

be a multiple of one over the size of the unit cell[McC08], thus in general requiring large unit cells to approximate generic filling.

The typical algorithms used with MPS, namely DMRG to find low lying eigenstates and the time evolving block decimation (TEBD) to calculate the real or imaginary time evolution of a given state, conserve this structure of the MPS. In this way we gain access to the canonical ensemble, while without using the symmetry, one automatically allows for any particle number. This results in a much larger number of free parameters. For calculating eigenstates, the average particle number has to be fixed by setting the corresponding chemical potential, which is not known a priori. In time evolution arithmetical errors can lead out of the symmetry sector of the initial state.

A generalization to the case of more than one species, where the actual number of particles in each class is separately conserved., is straight forward. We note that the case of non abelian symmetries [MG02, SZV10, Sch11] is more involved and will not be discussed here.

2.3 Density matrix renormalization group (DMRG)

The original idea of the numerical renormalization group (NRG) algorithm is to calculate the lowest lying states of a small system that can be treated exactly and use them as a basis for a system that is larger by some lattice sites. One has good reason to assume that iterating this process yields the ground state in the thermodynamic limit. However in practice, the algorithm suffers from the fact, that for the small system artificial boundary conditions have to be introduced, which strongly decrease the overlap of the lowest lying states with those of the larger system. This problem is circumvented by DMRG. Instead of using the lowest energy eigenstates, one resorts to the largest eigenvalues of the reduced density matrix, when the system is coupled to an environment. The environment is typically a copy of the system. Then the system can again be grown iteratively, keeping the largest eigenvalues in each step, which is called the *infinite size algorithm*. The numerical precision can however largely be improved by terminating at a given system size, and then *sweeping* the boundary between system and environment from one end of the lattice to the other until the ground state energy converges (*finite size algorithm*).

It can be shown, that keeping only the χ largest eigenvalues of the reduced density matrix is equivalent to requiring the state to be representable by an MPS of matrix dimension less than χ. In general on can expect the finite size algorithm to converge to the best MPS approximation for the matrix dimension given. However there is no guarantee, that DMRG does not get stuck in an excited state, or at least remain

very close to one for many sweeps. Such behavior is naturally observed if the system shows phase separation. In the following we will resort to the modern formulation of DMRG in terms of MPS. The infinite size algorithm will not further be discussed, because it is conceptually much easier, to start with finite size sweeps right away, converging to the ground state independently of the initial state. At least for short range interactions, the time evolving block decimation, section 2.4 gives also access to quantities in the thermodynamic limit.

An MPS represents any state in terms of $\mathcal{O}(N\chi^2)$ variables. We want to find the MPS with lowest energy, which is a variational problem. However MPSs do not form a vector space (the sum of two MPS requires an MPS of double matrix dimension to be represented exactly), and thus we have a nonlinear optimization problem. The finite size DMRG algorithm turns this into a series of linear optimization problems, which can be solved efficiently. This is one of the key points, why DMRG is a successful technique. In every step of a finite size sweep, one optimizes two adjacent sites,

$$|\Psi\rangle = \sum_{\alpha,\beta,\gamma=1}^{\chi} \sum_{i,j=0}^{d-1} \lambda_\alpha^{[m-1]} \Gamma_{\alpha,\beta}^{[m]i} \lambda_\beta^{[m]} \Gamma_{\beta,\gamma}^{[m+1]j} \lambda_\gamma^{[m+1]} \; |i\rangle_m |j\rangle_{m+1} \otimes |\alpha\rangle_{\mathrm{A}} \otimes |\gamma\rangle_{\mathrm{B}}. \tag{77}$$

In this basis, the state corresponds to a $\chi^2 d^2$ dimensional vector with elements $\sum_{\beta=1}^{\chi} \lambda_\alpha^{[m-1]} \Gamma_{\alpha,\beta}^{[m]i} \lambda_\beta^{[m]} \Gamma_{\beta,\gamma}^{[m+1]j} \lambda_\gamma^{[m+1]}$. The Hamilton operator is then a matrix of dimension $\chi^2 d^2 \times \chi^2 d^2$. It's extreme eigenvalues[4] can be computed using iterative methods, e.g. the Lanczos method, an implementation of which is available as part of the ARPACK package [LSY98]. The size of the Hamiltonian matrix forbids explicit construction due to memory limitations. Iterative eigenvalue solvers however require only that the Hamiltonian can be applied to an arbitrary input state. Therefore we observe that any operator that acts on the local sites m and $m+1$ only, or only either in A or B, can be stored explicitly, eventually using sparse matrix representations. Typical Hamiltonian terms, like a density density interaction $\hat{a}_r^\dagger \hat{a}_r \hat{a}_s^\dagger \hat{a}_s$ can thus be applied to any state, no matter if r respectively s are in A, $[m, m+1]$, or B.

For an efficient implementation it is critical to group operators in the Hamiltonian as much as possible. The Hamiltonian can always be decomposed as

$$\begin{aligned} \hat{H} &= \hat{H}_{\mathrm{A}} + \hat{H}_{\bullet\bullet} + \hat{H}_{\mathrm{B}} && \text{(78a)} \\ &+ \hat{H}_{\mathrm{A}\bullet\bullet} + \hat{H}_{\bullet\bullet\mathrm{B}} + \hat{H}_{\mathrm{AB}} + \hat{H}_{\mathrm{A}\bullet\bullet\mathrm{B}}, && \text{(78b)} \end{aligned}$$

where $\hat{H}_{\mathrm{A}}$ acts on subsystem A only, $\hat{H}_{\bullet\bullet}$ acts on sites $[m, m+1]$ only, $\hat{H}_{\mathrm{A}\bullet\bullet}$ couples A

[4] In the periodic MPS ansatz [VPC04, PWE10] one has to solve a generalized eigenvalue problem, because the orthogonality constraints (73) and (74) can not be fulfilled.

with $[m, m+1]$, etc. The first step is to always have those terms in the Hamiltonian summed up in the basis (77) which form $\hat{H}_{\mathrm{A}}$ respectively $\hat{H}_{\mathrm{B}}$. For local Hamiltonians, where the terms in (78b) contain only a finite number of summands each, this results in a complexity per step which is totally independent of the lattice size L[5]. For long range couplings more grouping is necessary. For a long range density–density interaction, as used in section 4, we group [Xia96]

$$\hat{H}_{\mathrm{AB}} = \sum_{i\in\mathrm{A}}\sum_{j\in\mathrm{B}} V(j-i)\hat{n}_i\hat{n}_j = \sum_{i\in\mathrm{A}} \hat{n}_i\hat{\bar{n}}_i^{\mathrm{B}}, \tag{79}$$

where for $i \notin \mathrm{B}$ we define $\hat{\bar{n}}_i^{\mathrm{B}} = \sum_{j\in\mathrm{B}} V(j-i)\hat{n}_j$. Thus we have at most $\mathcal{O}(L)$ summands in each term of (78b). Thus the complexity is reduced from the naive $\mathcal{O}(L^2)$ found on the right hand side of (79).[6]

After the ground state has been found, it is decomposed back into the form (77) using a singular value decomposition. As only the χ largest singular values can be kept, right orthogonality (74) is not fulfilled for site $m+1$ and likewise left orthogonality (73) is void for site m. This has however no further consequence if the next optimization is carried out either using sites $[m-1, m]$ or $[m+1, m+2]$, which should therefore be the case in any implementation. When going one site to the right (left) one has to update all operators that act on A and m (B and $m+1$) which will together form the new A (B) and reload all operators acting on the new B (A) with site $m+2$ ($m-1$) removed which have not changed since the last right (left) sweep[7].

2.4 Time evolving block decimation (TEBD)

Vidal [Vid03] observed, that it is a particularly easy operation to apply an operator $\hat{U}$ to an MPS that acts on two neighboring sites only. After applying such an operator

[5] Of course the number of steps per sweep is still of order L and the number of sweeps required for convergence in general grows with L also.

[6] In the case of general two body interactions, which have to be tackled e.g. in momentum space DMRG [Xia96, NJGN02] or in the form of Haldane's pseudo potential in quantum Hall physics [FRNDS08, ZSH11] similar grouping is required. The number of summands to represent $\sum_{ijkl} V(i,j,k,l)\hat{a}_i^\dagger\hat{a}_j^\dagger\hat{a}_k\hat{a}_l$ at a given step in the sweep can be reduced from the naive $\mathcal{O}(L^4)$ to $\mathcal{O}(L^2)$.

[7] This can be done very elegantly if the Hamiltonian is given as a MPO (section 3 of [McC07]) [CDV08, Sch11]. Although that clarifies the algorithm and allows for a quite general implementation (taking the Hamiltonian as an arbitrary input), it requires exponentially decaying interactions and would therefore be of limited use in this work.

($U^{ij}_{i'j'} = 0$ if $i + j \neq i' + j'$),

$$\hat{U}|\Psi\rangle = \sum_{\alpha,\beta=1}^{\chi} \sum_{i,j} \sum_{i',j'} U^{ij}_{i'j'} \cdot \lambda^{[m-1]}_{\alpha} \Gamma^{[m]i'}_{\alpha,\beta} \lambda^{[m]}_{\beta} \Gamma^{[m]j'}_{\beta,\gamma} \lambda^{[m]}_{\gamma} \times \\ \times \quad |i\rangle_m \otimes |j\rangle_{m+1} \otimes |\alpha\rangle_{\mathrm{A}} \otimes |\gamma\rangle_{\mathrm{B}}, \tag{80}$$

here B comprising sites $m+2$ to L, the singular value decomposition of the tensor

$$T^{i\alpha}_{j\gamma} = \sum_{i',j',\beta} U^{ij}_{i'j'} \Gamma^{[m]i'}_{\alpha,\beta} \lambda^{[m]}_{\beta} \Gamma^{[m]j'}_{\beta,\gamma} \tag{81}$$

has to be calculated, to bring the MPS back to it's canonical form[8]. This allows e.g. the application of arbitrary sequences of logical quantum gates (in the case when the local degrees of freedom represent qubits), with the severe restriction that the entanglement in the chain remains small.

This can be used to simulate time evolution [Vid04] with local Hamiltonians by using a Suzuki-Trotter decomposition[Suz76]: We can write the Hamiltonian as a sum

$$\hat{H} = \sum_m \hat{H}_m, \tag{82}$$

where $\hat{H}_m$ couples sites m and $m+1$ only. A second order Suzuki-Trotter decomposition then reads

$$\left(e^{-\frac{i}{2}\hat{H}_1\Delta t} e^{-\frac{i}{2}\hat{H}_2\Delta t} \cdots e^{-\frac{i}{2}\hat{H}_L\Delta t}\right)\left(e^{-\frac{i}{2}\hat{H}_L\Delta t} e^{-\frac{i}{2}\hat{H}_{L-1}\Delta t} \cdots e^{-\frac{i}{2}\hat{H}_1\Delta t}\right) = e^{-i\hat{H}\Delta t + \mathcal{O}(\Delta t^3)} \tag{83}$$

With this formula one can evolve an initial state for a time $t = n\Delta t$ given that Δt is chosen small enough, all intermediate states can be approximated well by MPSs and the number n of steps is not too large such that arithmetical errors remain small. The Hamiltonian can also be time dependent itself. The Suzuki-Trotter decomposition approximates the full propagator by a series of local unitary operators $\hat{U}_m = e^{-\frac{i}{2}\hat{H}_m\Delta t}$. Higher order decompositions, allowing for larger time steps Δt can be constructed, and tend to be rather lengthy. In practice a fourth order method ($\mathcal{Z}^1_4$ in [SS99]), which reduces the error to $\mathcal{O}(\Delta t^5)$ turned out to be a good choice and is used throughout this work.

The only nontrivial (i.e., not conserving the MPS structure automatically) opera-

[8] If the total particle number is conserved, T will be composed of blocks, each having a fixed value of $N_{\mathrm{A}}(\alpha) + i$ (and correspondingly $j + N_{\mathrm{B}}(\alpha) = N - N_{\mathrm{A}}(\alpha) - i$). Typically these blocks are much smaller each then the size of T itself, and can moreover be decomposed in parallel, such that the symmetry again gives a big advantage when operating on MPS.

tion required to perform calculations, e.g. using the TEBD scheme, is acting with an operator on two neighboring sites. After each such two-site operation of a Trotter step the evolved state $|\Psi_j\rangle = \hat{U}_{m,m+1}(\Delta t)|\Psi_{j-1}\rangle$ has to be projected to the new reduced basis of dimension χ. The resulting truncated state $|\mathrm{RG}(\Psi_j)\rangle$ (which is normalized before the next unitary is applied) has norm $\nu_j = \sqrt{\langle \mathrm{RG}(\Psi_j)|\mathrm{RG}(\Psi_j)\rangle}$ which fulfills $0 \leq 1-\nu_j \ll 1$. The accumulated cut-off error is defined as $1-\prod_j \nu_j$ which is approximately the sum of the single step cut-off errors, $1-\nu_j$, as long as it is much smaller than unity. The accumulated cutoff error is a useful indicator for the accuracy of the MPS approximation. If it becomes comparable to unity, the successive truncations have degraded the state too much, and the evolution leads to wrong results.

The origin of the cut-off error is of course the entanglement generated, most accurately measured be the distribution of the Schmidt coefficients $\lambda^{[m]}$. However, the exact distribution of those can in general not be calculated using a finite matrix dimension. A DMRG calculation will only give an approximate result for this distribution, from which one can however estimate the fidelity of the result, i.e., the overlap with the true ground state. For time evolution the cut-off error gives a more direct measure for this fidelity, assuming that the initial state is exact.

The TEBD algorithm has be adapted to DMRG language [DKSV04, WF04], providing mathematically equivalent methods. Those are usually termed "adaptive time-dependent DMRG" (t-DMRG). This is to contrast them to earlier approaches to include time-dependence in DMRG, which use a fixed basis as in (77), see e.g. [CM02, LXW03, SW06], and are therefore much more restricted to short times. There also exist other methods to calculate time dependence using MPSs and approximate algorithms different from the Suzuki-Trotter decomposition[GR06, SW06], some of which are also capable of treating non-local interactions. In the present work, TEBD has however proved very reliable and can easily be adapted to different problems, as long as the Hamiltonian involved is local.

Part II
Ground state properties of quantum gases

3 Discretized vs. continuous models of 1D quantum gases with local interactions[9]

As we have seen in the introduction, model Hamiltonians describing homogeneous 1D quantum gases with contact interaction are often integrable by means of Bethe Ansatz [Bet31, LL63, KBI93, Gau83]. In practice, however, only a small number of quantities can actually be obtained from Bethe Ansatz or explicit calculations are restricted to a small number of particles, and only properties associated with low energy or long wavelength excitations can be described by bosonization techniques [Gia03]. For more general problems one has to rely on numerical techniques such as DMRG or TEBD. Both work on lattice models and thus in order to apply them to continuous systems requires a proper mapping between the true continuum model and a lattice approximation. In fact any numerical technique describing a continuous system relies on some sort of discretization. In the present section, we will give a detailed derivation of a proper discretization of the one-dimensional Bose-gas with contact interactions (s-wave scattering), and equally of the corresponding (see section 1.3) model of spin-polarized fermions with local interactions (p-wave scattering). The problem is nontrivial, because the interaction potential $W(x)$ has a singular support, which has to be properly accounted for when mapped to the lattice, which has only finite resolution. For longer range interaction, the solution is more straight forward, see e.g. (109) in the next section.

We consider massive bosonic or fermionic particles with contact interactions. Only two types of contact interaction potentials are allowed for identical, non relativistic particles, representing either bosons with s-wave interactions or fermions with p-wave interactions. Both systems are dual and can be mapped onto each other by the well-known boson-fermion mapping, see section 1.3. A proper discretization of 1D bosons with s-wave interaction is straight forward and has been used quite successfully to calculate ground-state [SF07], finite temperature [SPF05], as well as dynamical problems, see section 5 for trapped 1D gases. For p-wave interacting fermions a similar, straight forward discretization fails however, as can be seen when comparing numerical results using such a model with those obtained from the bosonic Hamiltonian after the boson-fermion mapping. Using a general approach to quantum gases in 1D with contact interaction [Sch09] we here derive a proper mapping between a continuous model and a lattice approximation. We show in particular that p-wave interacting fermions are mapped to the critical spin 1/2 XXZ model. By virtue of the boson-fermion mapping the same can be done for s-wave interacting bosons, thus maintaining integrability in the map between continuous and discretized mod-

[9] This section is based on the publication [MFS10].

els. As an application we calculate the real-space and momentum-space densities of the ground state of a p-wave interacting Fermi gas in a harmonic trap, as well as local and non-local two particle correlations in real space. To prove the validity of the discretized fermion model we compare the numerical results with those obtained from the dual bosonic model as well as with Bethe ansatz solutions when available.

3.1 Discretization

The treatment of continuous gases in one dimension using numerical techniques requires a proper discretization. That is we approximate the two-particle wave function $\phi(x) \in L^2(\mathbb{R})$ by a complex number $\phi_j \in \ell^2(\mathbb{Z})$, where the integer index j describes the discretized relative coordinate $x = x_1 - x_2$. We interpret $|\phi_j^2|$ as the probability to find the two particles between $(j - \frac{1}{2})\Delta x$ and $(j + \frac{1}{2})\Delta x$. In order to apply numerical methods such as DMRG or TEBD efficiently, it is favorable to have local or at most nearest neighbor interactions in the lattice approximation of the continuous model. It will turn out, that the above systems can all be discretized using such nearest neighbor interactions only.

We start with the kinetic term, that can be approximated by

$$\partial_x^2 \phi \mapsto \frac{\phi_{j-1} - 2\phi_j + \phi_{j+1}}{\Delta x^2}. \tag{84}$$

In what follows, we will derive two distinct discretizations: first for the bosons, where we allow for double occupied lattice sites and can therefore use on-site interactions to reproduce the boundary conditions (54), and then for fermions, where double occupation is forbidden by the Pauli principle and interactions between neighbors are necessary in the lattice model. Note however, that both descriptions are equivalent due to the Bose-Fermi mapping in the continuum limit.

3.2 Bosonic mapping

In the lattice approximation the kinetic-energy term, Eq. (51) reads

$$\partial_x^2 \phi(x) = \begin{cases} \frac{\phi_{j-1} - 2\phi_j + \phi_{j+1}}{\Delta x^2} & j > 0 \\ \frac{2(\phi_1 - \phi_0)}{\Delta x^2} & j = 0 \end{cases} \tag{85}$$

Thus assuming a local contact interaction only, we find for the bosons

$$(H\phi)_j = \begin{cases} -\frac{\phi_{j-1} - 2\phi_j + \phi_{j+1}}{\Delta x^2} & j > 0 \\ U\phi_0 - \frac{2\phi_1 - 2\phi_0}{\Delta x^2} & j = 0 \end{cases}. \tag{86}$$

In order to determine the value of U, we assume, that it can be expressed as a series in Δx and evaluate the stationary Schrödinger equation $(H\phi)_j - E\phi_j = 0$ at $j = 0$. Reexpressing ϕ_1 in terms of $\phi(0)$ by means of the discretized version of the contact condition (54)

$$\phi_1 = \phi(0) + \Delta x \underbrace{\phi'(0)}_{=\frac{g_B}{2}\phi(0)} + \frac{\Delta x^2}{2} \underbrace{\phi''(0)}_{=-E\phi(0)} + \ldots, \tag{87}$$

we arrive at

$$\begin{aligned} 0 &= (H\phi)_{j=0} - E\phi_{j=0} \\ &= U\phi(0) + \frac{2\phi(0)}{\Delta x^2} - E\phi(0) - \frac{2}{\Delta x^2} \times \\ &\times \left(\phi(0) + \Delta x \frac{g_B}{2}\phi(0) - \frac{1}{2}\Delta x^2 E\phi(0) + \mathcal{O}(\Delta x^3)\right). \end{aligned} \tag{88}$$

Equating orders gives

$$U = \frac{g_B}{\Delta x} + \mathcal{O}(\Delta x). \tag{89}$$

The constant term vanishes, since $-\partial_x^2\phi = E\phi$ for any eigenstate. The higher orders $\mathcal{O}(\Delta x)$ contain E and would thus not be independent on the eigenvalue. This is perfectly consistent, since discretizations will only work as long as the lattice spacing is much smaller than all relevant (wave) lengths in the system. Thus the lowest order in (89) is already optimal. There are no higher order corrections possible for a general state.

We can now easily write down the corresponding *many* particle Hamiltonian for the case of indistinguishable bosons in *absolute* coordinates, represented by an integer index i and in second quantization:

$$H = \sum_i \left[-J(a_i^\dagger a_{i+1} + h.a.) + \frac{U}{2} a_i^\dagger a_i^\dagger a_i a_i + V_i a_i^\dagger a_i\right]. \tag{90}$$

Here a_i is the bosonic annihilator at site i and V_i introduces an additional external potential in the obvious way. So not surprisingly we have arrived at the Bose-Hubbard Hamiltonian as a lattice approximation to 1D bosons with s-wave interaction. Since Δx must be smaller than all relevant length scales, we are in the low-filling and weak-interaction limits $U \ll J = \frac{1}{2\Delta x^2}$ [10]. This does of course not imply that the corresponding Lieb-Liniger gas is in the weakly interacting regime. This result might seem trivial, since we can also directly get it by substituting the field operator in

[10] In the case of ground state calculations as done in section 3.5 we actually achieve good results even before J exceeds U. However for non equilibrium dynamics [MSF10] it can become crucial that the bandwidth proportional to J is large compared to the pairing energy U.

the continuous model: $\Psi(j\Delta x) \mapsto \frac{a_j}{\sqrt{\Delta x}}$ [SF07]. However, this simple and naive discretization does not work in the fermionic case we are going to discuss now.

3.3 Fermionic mapping

For fermions the kinetic-energy term, Eq. (51) reads in lattice approximation

$$\partial_x^2\phi(x) = \begin{cases} \frac{\phi_{j-1}-2\phi_j+\phi_{j+1}}{\Delta x^2} & j>1 \\ \frac{\phi_2-2\phi_1}{\Delta x^2} & j=1 \\ 0 & j=0 \end{cases} \tag{91}$$

Due to the anti-symmetry of the wave-function ϕ_0 must vanish, i.e. the simplest way interactions come into the lattice model is for nearest neighbors. Thus we write for the Hamiltonian

$$(H\phi)_j = \begin{cases} -\frac{\phi_{j-1}-2\phi_j+\phi_{j+1}}{\Delta x^2} & j>1 \\ B\phi_1 - \frac{\phi_2-2\phi_1}{\Delta x^2} & j=1 \\ 0 & j=0 \end{cases} \tag{92}$$

To obtain the value of B we proceed as in the case of bosons. As will be seen later on it is most convenient to expand B in a series in the following way:

$$\frac{1}{B} = \Delta x^2 \left(B^{(2)} + \Delta x B^{(3)} + \mathcal{O}(\Delta x^2)\right). \tag{93}$$

Now the stationary Schrödinger equation for $j=1$ yields

$$\begin{aligned} 0 = 1 - \frac{2}{g_{\mathrm{F}}}\Delta x - \frac{\Delta x^2}{2}E + \mathcal{O}(\Delta x^3) + \\ + \left(B^{(2)} + \Delta x B^{(3)} + \Delta x^2 B^{(4)} + \mathcal{O}(\Delta x^2)\right)\left[1 + \mathcal{O}(\Delta x^3)\right]. \end{aligned} \tag{94}$$

Equating orders results in

$$B^{(2)} = -1, \quad B^{(3)} = \frac{2}{g_{\mathrm{F}}}, \quad B^{(4)} = \frac{1}{2}E. \tag{95}$$

Note that his time the interaction appears only in the *second* lowest order, which can not be described by a simple substitution formula. The next higher order contained in $\mathcal{O}(\Delta x^2)$ does not vanish, but depends again on the energy as expected. If we had chosen a straightforward expansion of B instead of (93), the next order after the one that introduces the interaction would have contained again the interaction parameter:

$$B = -\frac{1}{\Delta x^2} - \frac{2}{g_F \Delta x} - \frac{4}{g_F^2} + \frac{E}{2} + \mathcal{O}(\Delta x). \tag{96}$$

Neglecting this term would therefore introduce a larger error than in the chosen expansion (93). In fact the low energy scattering properties would be reproduced only to one order less. For the bosons this problem did not occur (89). From (93) we read that the optimal result in the fermionic case is

$$B = -\frac{1}{\Delta x^2}\left(\frac{1}{1-\frac{2\Delta x}{g_{\mathrm{F}}}}\right). \tag{97}$$

The corresponding many-body Hamiltonian for indistinguishable fermions reads

$$H = \sum_i \left[-J(c_i^\dagger c_{i+1} + h.a.) + B c_i^\dagger c_i c_{i+1}^\dagger c_{i+1} + V_i c_i^\dagger c_i^\dagger\right], \tag{98}$$

where now c_i is a fermionic annihilator at site i. Eq. (98) describes spin polarized lattice fermions with hopping J and nearest-neighbor interaction B. In contrast to the bosonic case, Eq. (95), where the correct discretized model could be obtained from the continuum Hamiltonian just by setting $\Psi(x) \to a_i/\sqrt{\Delta x}$, we now see from (98) and (97) that a similar naive and straight-forward discretization fails in the case of p-wave interacting fermions.

3.4 Jordan-Wigner mapping

The failure of a naive discretization of the fermionic Hamiltonian becomes transparent if we map this model to that of a spin lattice: Using the Jordan-Wigner transformation

$$\sigma_i^+ = \exp\Big\{i\pi \sum_{l<i} c_l^\dagger c_l\Big\}\, c_i^\dagger, \qquad \sigma_i^z = 2c_i^\dagger c_i - 1 \tag{99}$$

where $\sigma_i^\pm = \sigma_i^x \pm i\sigma_i^y$, (98) can be mapped to the spin-1/2 XXZ model in an external magnetic field

$$\begin{aligned} H &= \sum_i \Big\{ -\frac{1}{4\Delta x^2}\big(\sigma_i^x\sigma_{i+1}^x + \sigma_i^y\sigma_{i+1}^y + \\ &+ \Delta(\sigma_i^z+1)(\sigma_{i+1}^z+1)\big) + V_i\sigma_i^z\Big\}, \end{aligned} \tag{100}$$

where the anisotropy parameter defining the XXZ model is $\Delta = -1/[1-\frac{2\Delta x}{g_{\mathrm{F}}}]$.

There is an easy way to see that these mappings are quite physical by considering the ground states: The repulsive Bose gas ($g_{\mathrm{B}} > 0$) maps to the repulsive ($U > 0$) Bose-Hubbard model in the super fluid, low filling regime, which has an obviously gas like ground state. The same is true for the corresponding attractively interacting ($g_{\mathrm{F}} < 0$) Fermi gas, which maps to the ferromagnetic XXZ model which, due to the

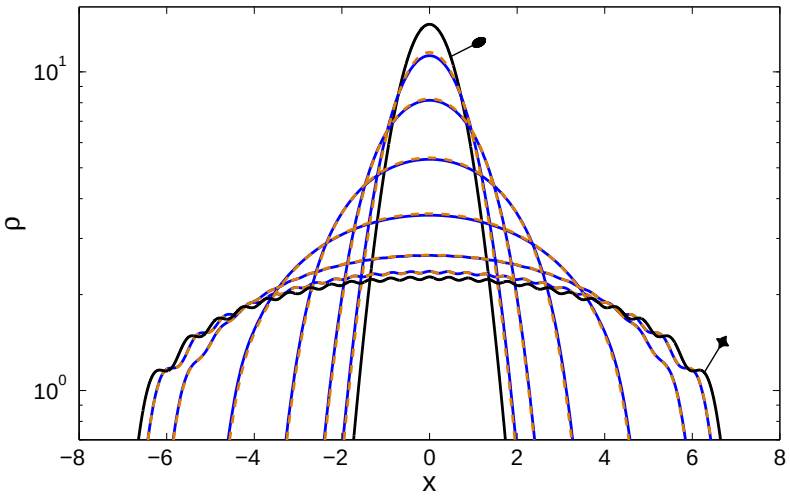

Figure 4: Local density distribution of the interacting Fermi or Bose gas. The (orange) dashed lines show results obtained by Bose-Fermi mapping and solving the Bose Hubbard lattice model, the (blue) continuous lines correspond to the XXZ discretization. The interaction strength g_F is $-51.2, -12.8, -3.2, -0.8, -0.2, -0.05$ from the narrow to the broad distributions. The solid black lines show the limiting cases of free fermions (broad, star-marked) and infinitely strong interacting fermions (narrow, ellipse-marked, corresponds to free bosons). The calculations are done for $\Delta x = \frac{1}{64}$. One recognizes perfect agreement between the fermionic and bosonic discretization approaches. Note that both fermions and bosons with corresponding interaction show the same local density, since the quantity is invariant under the Bose-Fermi-mapping.

specific form of the interaction parameter in the discretized fermion model, Eq. (97), is always in the critical regime close to the transition point ($\Delta \xrightarrow{\Delta x \to 0} -1^+$). A naive discretization would have lead to an anisotropy parameter that could cross the border to the gapped phase, which is clearly unphysical.

In the attractive Bose gas, bound states emerge, that lead to a collapse of the ground state as it is of course also true in the Bose Hubbard model for $U < 0$. On the fermionic side, this collapse can be also observed, as for $\Delta < -1$ the XXZ model has a ferromagnetically ordered ground state, which leads to phase separation in the case of fixed magnetization.

Note that we call the Fermi gas repulsively interacting if $g_\mathrm{F} > 0$, although B is negative in this case as well, and although there exist bound states, who's binding energy actually diverges as $g_\mathrm{F} \to 0^+$, as is immediately clear from the Bose Fermi mapping in the continuous case.

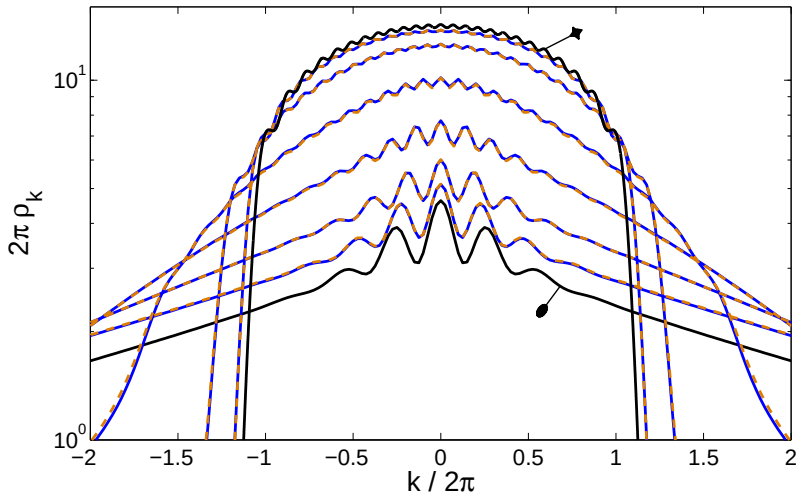

Figure 5: Momentum distribution of the interacting Fermi gas. Dashed (orange) lines show results via the Bose Hubbard discretization, solid (blue) lines correspond to XXZ discretization. The interaction strength g_{F} is $-51.2, -12.8, -3.2, -0.8, -0.2, -0.05$ from the broad to the narrow distributions. Solid (black) lines show the limiting cases of free fermions (narrow, star-marked) and infinitely strong interacting fermions (broad, ellipse-marked, calculated from the formula given in [BEG05]). The calculations are done for $\Delta x = \frac{1}{64}$. Again there is perfect agreement between bosonic and fermionic discretization.

3.5 The interacting Fermi gas in a harmonic trap

We now apply our method to the interacting Fermi gas in a harmonic trap,

$$H = -\frac{1}{2}\sum_{i=1}^{N}\partial_{x_i}^2 - \frac{g_{\mathrm{F}}}{2}\sum_{j<i}\delta'(x_j - x_i)\left(\partial_{x_j} - \partial_{x_i}\right)\big|_{x_j = x_{i+}} + \sum_{i=1}^{N}\frac{1}{2}x_i^2. \tag{101}$$

We here choose the trap length to set the length scale. The choice of an harmonic potential is arbitrary. We can include any other potential as well, the only crucial thing is, that the potential should not have structures that remain unresolved within the chosen discretization length Δx. One can also consider a homogeneous but finite system, which then corresponds to an infinite box potential. By (55) the Tonks parameter in the corresponding Lieb-Liniger model is

$$\gamma = \frac{4}{-g_{\mathrm{F}}\rho}, \tag{102}$$

where the local density ρ can be read of the resulting ground state, Fig. 4.

For $g_{\mathrm{F}} = -\infty$ we have the fermionic Tonks-Girardeau gas, section 1.3. Since it

maps to free bosons under the Bose Fermi mapping, it can be treated analytically, e.g., the momentum distribution is known for arbitrary particle numbers [BEG05]. The momentum distribution is of special experimental relevance, since it is equivalent to the density distribution measured in a time-of-flight experiment. However for intermediate interaction strength numerical calculations are required, which we are now able to do.

First we note, that we have two options to discretize the model. Direct discretization will yield the XXZ Hamiltonian, while a Bose Fermi mapping will result in the Bose Hubbard Hamiltonian. Both methods of course have to produce exactly the same results in the continuum limit.

Fig. 4 shows the spatial density distribution in the ground state for $N = 25$ particles, i.e.,

$$\rho(x) = \int \mathrm{d}x_2 \ldots \mathrm{d}x_N \, |\phi(x, x_2, \ldots, x_N)|^2 \,, \tag{103}$$

which is approximated by the discretized system as the diagonal elements of $\langle a_i^\dagger a_j \rangle$. The ground state of the discretized system is calculated using a TEBD code and an imaginary time evolution, which has already been applied successfully to calculate the phase diagram of a disordered Bose Hubbard model [MMF08]. The interaction strength is varied all the way from the free fermion regime to the regime of the fermionic Tonks-Girardeau gas. The density distribution changes accordingly from the profile of the free fermions, showing characteristic Friedel oscillations, to a narrow Gaussian peak for the fermionic Tonks-Girardeau gas. Note that the Bose Fermi mapping does not affect the local density, so the curves are the same for the corresponding bosonic system. I.e. the density distribution in the fermionic Tonks-Girardeau regime is identical to that of a condensate of non-interacting bosons. The curves obtained from the bosonic and fermionic lattice models are virtually indistinguishable which shows that both approaches are consistent.

The corresponding momentum distribution for the fermions,

$$\rho_k(k) = \int \mathrm{d}k_2 \ldots \mathrm{d}k_N \, |\phi(k, k_2, \ldots, k_N)|^2 \,, \tag{104}$$

which is quite different from that of the bosons, is shown in Fig. 5. It was obtained from the discretized wave function as the diagonal elements of the Fourier transform of $\langle a_i^\dagger a_j \rangle$. Again perfect agreement between the bosonic and fermionic lattice approximations can be seen. In accordance with physical intuition invoking the uncertainty relation and Pauli principle, the momentum distribution broadens as the real space distribution narrows. While for the free particles, real and momentum space description coincide for the harmonic oscillator trapping potential, the Friedel oscillations

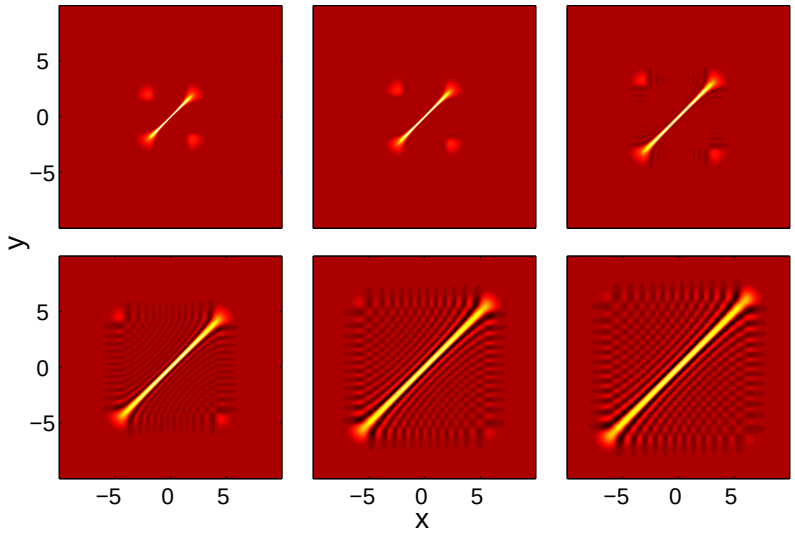

Figure 6: Single particle density matrix of the interacting Fermi gas calculated using XXZ discretization. Light regions are positive, dark regions negative. The interaction strength g_{F} is $-51.2, -12.8$, and -3.2 (upper row) and $-0.8, -0.2$, and -0.05 (lower row). Remember that the cloud size is independent of the particle number towards the fermionic Tonks limit (because there is condensation in the bosonic picture) while it grow as $\sqrt{N}$ for free fermions.

are deformed gradually towards the result for the fermionic Tonks-Girardeau gas calculated e.g. by Bender et al. [BEG05]. The oscillations that remain in this limit are effects from the finite number of particles. They vanish as $1/N$ as can be seen from a Taylor expansion in $1/N$ of the expressions given in [BEG05] for the Fermi-Tonks case.

In Fig. 6 we have plotted the complete single particle density matrix

$$\rho(x, y) = \int \mathrm{d}x_2 \ldots \mathrm{d}x_N \phi^*(x, x_2, \ldots)\phi(y, x_2, \ldots) \tag{105}$$

for different interaction strength, starting from the Fermi-Tonks limit to the case of free fermions. One clearly recognizes two small off-diagonal peaks for larger interaction strength. The weight of these peaks, which are responsible for the oscillations in the momentum distribution, Fig. 5, to the remaining part near the diagonal is $\frac{1}{N}$, as can bee seen from analyzing the limiting case numerically, which can be done for much larger N also. The sign of the peaks is positive only if N is odd and negative for even N, so the momentum distributions in Fig. 5 would show a local minimum at $k = 0$ for all interaction strength if N was chosen even instead of 25.

On first glance it may seem surprising that a mapping of a continuous, Bethe-

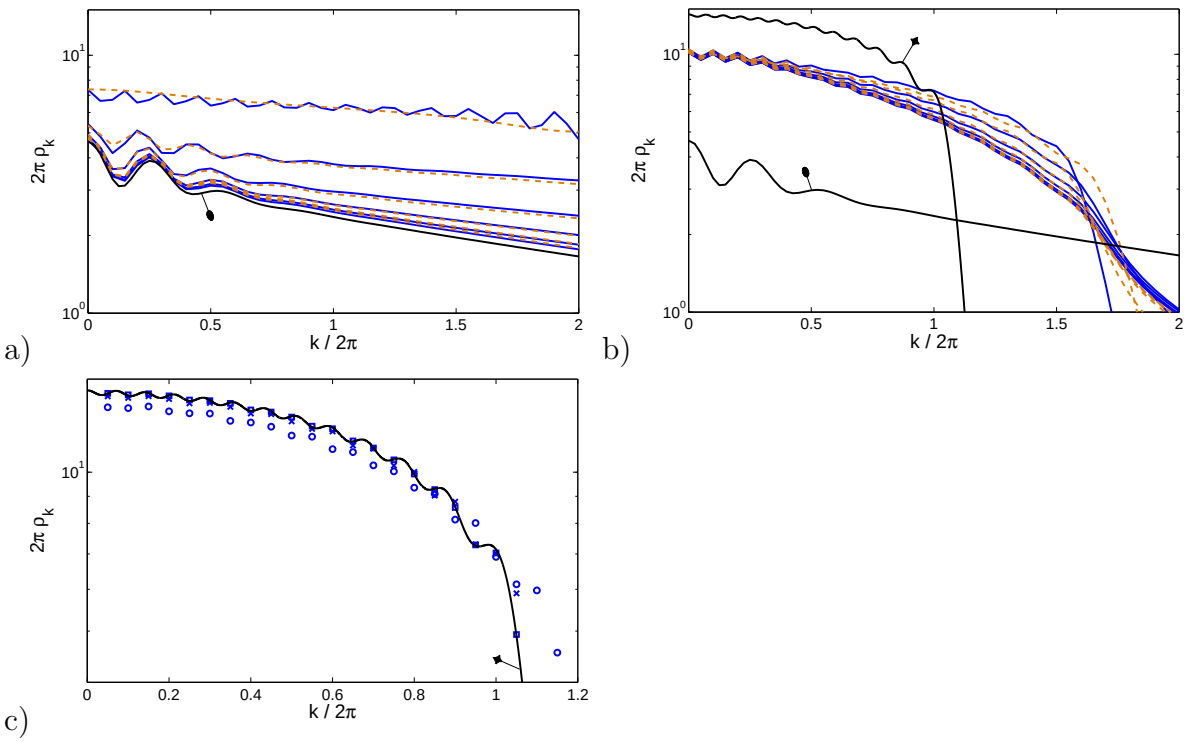

Figure 7: momentum space distribution of the Fermi gas showing convergence of the method with discretization for a) the Fermi Tonks limit, b) $g_{\mathrm{F}} = -0.8$, and c) the free fermionic case. Again in a) and b) dashed (orange) lines show results via the Bose Hubbard discretization, solid (blue) lines correspond to XXZ discretization. a) Results are shown for $\Delta x = \frac{1}{4}, \frac{1}{8}, \frac{1}{16}, \frac{1}{32}, \frac{1}{64}, \frac{1}{128}$. As the grid gets finer, both discretization formulas converge to the exact result (black line, ellipse-marked). b) The same discretizations are used as in a) and we again observe convergence of both formulas towards a common limit, which is in this case not known analytically. The black lines are those showing up in a) and c) respectively and are for orientation. c) Note that in this case there is no sense in distinguishing the two formulas, since implementing $U = \infty$ always means excluding double occupation of sites by bosons which is immediately equivalent to simulating free fermions. We here only show $\Delta x = \frac{1}{4}$ (circles), $\frac{1}{8}$ (crosses), $\frac{1}{128}$ (squares) to avoid confusion since the lines converge quite quickly. Although the squares sit perfectly on top of the exact result (black line, star-marked) they are not spaced densely enough to resolve the Friedel oscillations. This would require a lattice that extends across a region in space much larger than N oscillator length where we have chosen to restrict the calculation to 20 oscillator length to speed it up.

Ansatz integrable Hamiltonian such as the Lieb-Liniger model to the non-integrable Bose-Hubbard model should produce accurate results. However, since the Lieb Liniger gas is dual to p-wave interacting fermions its lattice approximation is equivalent to the spin 1/2 XXZ model, which is again Bethe-Ansatz integrable. Furthermore

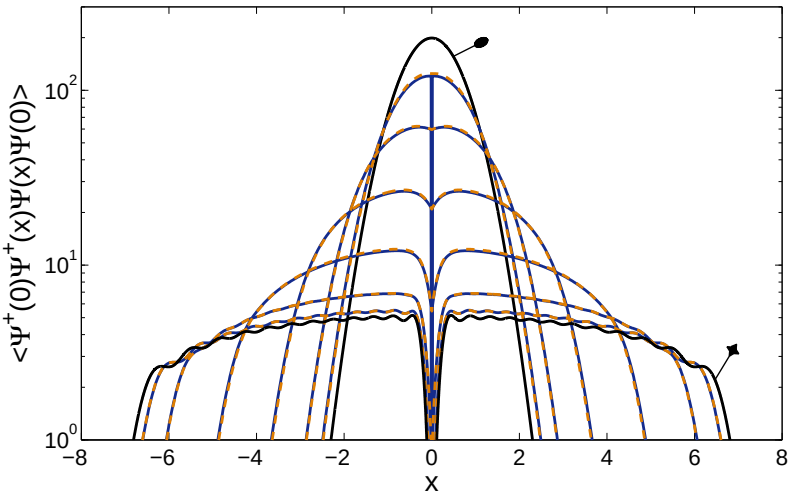

Figure 8: Density-density correlations of the interacting Fermi or Bose gas. The (orange) dashed lines show results obtained by Bose-Fermi mapping and solving the Bose Hubbard lattice model, the (blue) continuous lines correspond to the XXZ discretization. The interaction strength g_{F} is $-51.2, -12.8, -3.2, -0.8, -0.2, -0.05$ from the narrow to the broad distributions. The solid black lines show the limiting cases of free fermions (broad) and infinitely strong interacting fermions (narrow, corresponds to free bosons). The calculations are done for $\Delta x = \frac{1}{64}$. One recognizes perfect agreement between the fermionic and bosonic discretization approaches apart from $x = 0$ (see text). Note that both fermions and bosons with corresponding interaction show the same density-density correlations, since the quantity is invariant under the Bose-Fermi-mapping.

full recovery of the properties of the continuous model can of course only be expected in the limit $\Delta x \to 0$. In Fig. 7 we have shown the momentum distribution of p-wave interacting fermions for decreasing discretization length Δx for three different values of the interaction strength. One clearly recognizes convergence of the results as $\Delta x \to 0$. In the two analytically tractable cases of a free fermion gas and the Fermi-Tonks gas the curves approach quickly the exact ones.

As a final application we calculate the real-space two-particle correlations in a trap. The corresponding results are shown in Fig. 8. Again the (blue) solid lines are obtained from the fermionic lattice model and the dashed (orange) lines from the dual bosonic model. Due to Pauli exclusion $g^{(2)}(0) = 0$ and there is a pronounced dip in the $g^{(2)}$ near the origin for non interacting or weakly attractive fermions, while we see again Friedel oscillations for larger inter particle distances. In the dual bosonic case the dip is enforced by a strong repulsive interaction. As the fermionic attraction is increased, the depth of this dip is decreased. There is a smooth transition to the perfect Gaussian shape expected for free bosons when approaching the case of

strongly interacting fermions.

Outside the point where the particle positions coincide both discretization formulas give the same result. There is a discontinuity maintaining $g^{(2)}(0) = 0$ for the fermions, enforced by the symmetry of the wave functions. It should be noted that this singular jump is not reproduced in the dual bosonic model. This is because the duality mapping of the discretized models is only valid for two particles at different lattice sites and the dual bosonic model can only be used to calculate multi-particle correlations of fermions at pairwise different locations.

Both discretization formulas presented here have the nice property of approximating two-particle interactions in the continuum by two-particle interactions on a lattice. Interestingly, only the fermionic lattice model preserves the property of being integrable. However, it is known, that the q-Boson lattice model [BBP93, BIK98] also has the Lieb-Liniger model as a continuum limit and is integrable. But when written in terms of ordinary particles, the simple hopping of the nonlinear q-Bosons becomes a non-polynomial expression, thus involving n-particle interactions for arbitrary n, locally and on nearest neighbor sites. Nevertheless, simulations using DMRG schemes should be possible and it might be interesting to compare the results to those given here.

Finally we note that using the discretization formulas (89) and (95) one can of course also calculate other many body properties like off diagonal order [Yan62, MG06] using DMRG. The method was also used to calculate out-of equilibrium dynamics for bosonic gases in the repulsive [MSF10] as well as attractive regime [MF10], as we will discuss in part III of this thesis. A generalization to higher dimensions is not immediately evident and requires a separate discussion.

The method presented in this section is not limited to problems including only one species of particles. We can as well describe fermions with spin-degrees of freedom, mixtures of bosons and fermions or even a gas with Boltzmann statistics. Whenever two distinguishable particles interact, both terms in (51) can contribute, i.e., one ends up with a s-wave as well as a p-wave contribution to the interaction. Following similar lines as in this section one can then easily derive a corresponding Hamiltonian in second quantization.

4 DMRG for models with long range interactions

As discussed in the introduction, we can only expect DMRG to give accurate results for low lying states and at the same time be more efficient than brute force diagonalization, if we work with a one-dimensional system that features only short range interactions. From the viewpoint of DMRG, two dimensional systems are a paradigm for longer range interactions, because the lattice sites have to be ordered in some way, necessarily introducing interactions over many sites, even if they are nearest neighbor only if viewed as a two-dimensional system. In two dimensions, it is a well known fact [LP94, CP00], that the truncation error decreases only very slowly with the bond dimension if one uses straight forward DMRG, i.e., sorting the lattice sites in a one-dimensional order. The same is true in the case of true long range interactions, falling of only like the inverse inter-particle distance or slower, in one dimension. An example here naturally generated by interacting particles in two dimensions which are confined to the lowest Landau level. As a basis one naturally chooses the angular momentum eigenstates in z-direction, such that the non-interacting case is solved trivially. The basis has only one parameter and can be interpreted as belonging to a one-dimensional system. The interactions (although local or short range in position space) in this basis lead to a Haldane pseudo potential, a general two-particle interaction which falls of very slowly with the difference in the z-component of the angular momentum. Calculating the low energy spectrum of this model is of great interest to understand fractional quantum Hall physics. There has been slight progress using DMRG for this problem and interacting fermions [FRNDS08, LH08, ZSH11], which motivated us to apply DMRG to the same problem in the case of bosons. However we have not been able to calculate ground states for systems significantly larger than those treatable using exact diagonalization[11]. The reason for this is the strong entanglement in the system, which manifests itself in a linear growth of entanglement entropy with system size [LBH10].

We can however apply DMRG effectively to one-dimensional systems with moderate long range interactions, i.e., with an interaction potential that decays faster then $1/r$. In this section, we will apply DMRG to the model of bosons in one dimension with interactions that decay according to such a power law. The low-energy excitations of this system can be described by an effective Luttinger liquid model, and specifically we will calculate the Luttinger parameter K, which is the key quantity of this model, in the continuous system. The many-body ground state in the one-dimensional case is correlated more strongly than it is possible for any local in-

[11] For details on the bosonic case and results from exact diagonalization see [Gruon] and references therein.

teraction, i.e., with a Luttinger parameter $K \ll 1$. For the system on a lattice, we calculate the full phase diagram numerically. A fractal structure emerges with Mott-insulating phases at any rational filling fraction, similar to the case of dipolar interactions [BPCS09].

Specifically, we perform numerical calculations for van der Waals interactions. Physically they are realized by an ensemble of Rydberg atoms which are optically excited near resonance [WLPB08]. Starting from a fully quantized model of the optical excitation one can show that Rydberg excitations always possess a finite kinetic energy mediated by photon exchange even if the motion of the atoms can be disregarded. The kinetic energy competes with the repulsive van der Waals interaction [Lau12, OLMFon].

4.1 Polynomially decaying interactions

We are interested in the ground state properties of a one-dimensional Bose gas with power law density-density interactions:

$$\hat{H} = \int \mathrm{d}x\, \hat{\Psi}^\dagger(x) \left(-\frac{1}{2}\partial_x^2\right) \hat{\Psi}(x) + \frac{1}{8\pi} \int \mathrm{d}x \mathrm{d}x'\, \hat{\Psi}^\dagger(x)\hat{\Psi}^\dagger(x') \frac{C_\beta}{|a_\mathrm{B}|^\beta + |x-x'|^\beta} \hat{\Psi}(x')\hat{\Psi}(x). \tag{106}$$

Here $\beta = 3$ corresponds to dipolar interactions and $\beta = 6$ describes van der Waals interactions. a_B is a screening length, which is physically always present, because the power law can not hold at arbitrary short inter-particle distances. With (106) the potential becomes flat at $x \lesssim a_\mathrm{B}$. If a_B is small compared to the inter-particle distance, it is negligible and the only free parameter is a dimensionless interaction strength defined by

$$\Theta = \frac{\rho^{\beta-2} C_\beta}{2\pi}. \tag{107}$$

It gives the interaction energy at the average inter-particle distance compared to the Fermi energy

$$E_\mathrm{F} = \pi^2 \rho^2 / 2. \tag{108}$$

The generalization of the Fermi energy to the bosonic system is justified, because given that both Θ and a_B are not too large, the kinetic energy per particle approaches that of free fermions (see below), which is of the order E_F.

In order to make use of DMRG, we have to use a discretization of the continuous model. In contrast to the contact interactions discussed in the introduction, this is

straight forward for an interaction over a distance. We may simply replace

$$\begin{aligned} \hat{\Psi}(j\Delta x) &\longmapsto \frac{\hat{a}_j}{\sqrt{\Delta x}} \\ \int \mathrm{d}x &\longmapsto \Delta x \sum_j . \end{aligned} \tag{109}$$

This leads directly to a lattice Hamiltonian of the form (117), additionally accounting for nonzero a_B if required. The continuous model is well approximated given that Δx is both smaller than the average inter-particle distance and the characteristic length scale on which the structure of the interaction potential can be resolved. The latter is anyway infinite for a power-law interaction potential. The parameters of the discretized model satisfy

$$J/c_\beta = 2n^{\beta-2}/\Theta \tag{110}$$

with $n = \rho\Delta x$ the average number of particles per lattice site (and $J = 1/2\Delta x^2$ see section 3).

4.2 Luttinger parameter

To determine the Luttinger parameters K and u, we make use of the fact [Gia03] that their ratio

$$\frac{K}{u} = \pi\rho^2\chi \tag{111}$$

is determined by the compressibility

$$\frac{1}{\chi} = \rho^2\frac{\partial\mu}{\partial\rho}. \tag{112}$$

The second equation required is

$$uK = \pi\rho, \tag{113}$$

which is true for any Galileanly invariant model [Hal81].

To test the numerical procedure, we first calculate the Luttinger parameter for the repulsive Lieb-Liniger gas. For strong local interactions, the Luttinger parameter can be found via the compressibility from Lieb and Linigers' original solution in the thermodynamic limit [LL63]. For strong interactions (large γ) it can be approximated as [Zvo10]

$$\frac{1}{K} = 1 - \frac{4}{\gamma} + \frac{12}{\gamma^2} + \cdots , \tag{114}$$

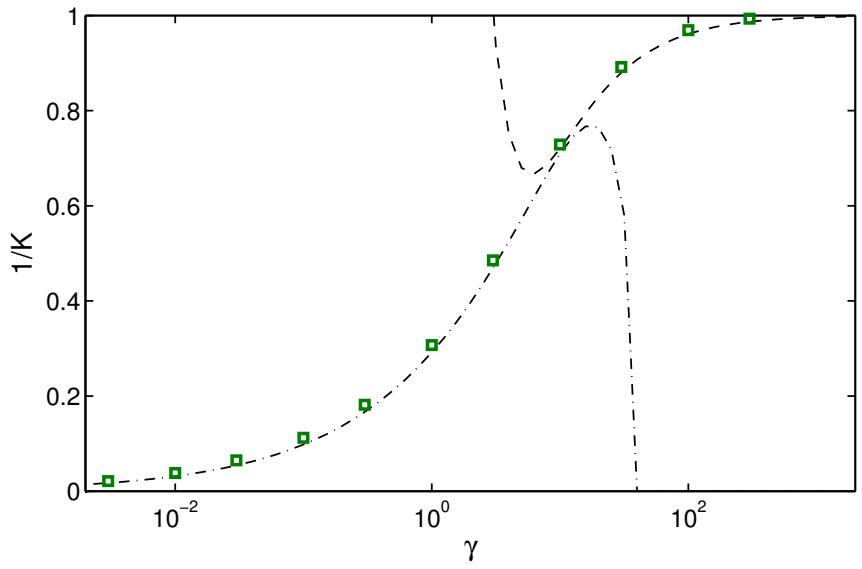

Figure 9: Inverse Luttinger parameter as a function of interaction strength for local interactions. Dashed and dot-dashed lines show analytical approximations (114) and (115) respectively. Squares show results from DMRG calculations using 10 particles on 100 lattice sites with open boundary conditions and matrix dimension $\chi = 16$.

while for weak interactions one has approximately [Lee71a, Lee71b, Zvo10]

$$\frac{1}{K} \approx \frac{1}{\pi}\sqrt{\gamma - \frac{1}{2\pi}\gamma^{3/2}}. \tag{115}$$

Each of this formulas is correct within 1% in $1/K$ for γ larger respectively smaller than 10. A comparison to our DMRG results is shown in Fig. 9. The agreement is astonishingly good, even for bond dimensions as small as 16. Differences when doubling the system size are not visible, such that finite size effects are also negligible. This confirms the validity of our numerical procedure, which we will now apply to longer range interactions.

For the repulsive long range interactions (106), in the absence of screening i.e. $a_B = 0$, an approximate analytical interpolation formula for the Luttinger parameter was given in [DPZ10]

$$K = \frac{1}{\sqrt{1 + \frac{\beta(\beta+1)\zeta(\beta)\Theta}{2\pi^2}}}, \tag{116}$$

where ζ is the Riemann zeta function. For small Θ, the Luttinger parameter is one, because the interaction, no matter how small C_β, has a singularity at zero inter-particle distance, such that the wave function has to vanish there and the system

becomes again equivalent to free fermions. For strong interactions, the correlations become even stronger and K decreases as $\Theta^{-1/2}$.

Our DMRG calculations, Fig. 10, qualitatively reproduce this result. The asymptotics are also reproduced in the limit of strong and weak interaction. However the quantitative difference increases in the intermediate regime for higher β and in the van der Waals case is as large as 45% around $\Theta = 0.25$. For comparison, we have also used periodic boundary conditions, which reduce the finite size effect at the expense of having to use a larger bond dimension χ.

Introducing a finite screening $a_\mathrm{B} > 0$ has the following effect: At large Θ, nothing changes, because of the strong repulsive interactions, the particles do not come close enough to be effected by the finite a_B. For weaker interaction strength, the screening allows the particles to be at the same position. Consequently, for some Θ the Luttinger parameter becomes larger than one and goes to infinity as the interaction vanishes and the system becomes that of free bosons.

The increased correlations can also be seen in the density profile, if open boundary conditions are used, Fig. 11. The upper panel shows, that in the unscreened case the limit of free fermions is approached, which happens more quickly for dipolar than for van der Waals interactions. If the interaction is screened, the Friedel oscillations are strongly reduced as $K \gg 1$ [Caz04]. For strong interactions, the particles order into fixed positions. Quantum fluctuations become more and more suppressed, such that the compressibility can be calculated by assuming that the particles behave classically and localize at their average inter-particle distance $1/\rho$. Then a classical calculation of the compressibility immediately gives the $K \sim \Theta^{-1/2}$ behavior. For open boundary conditions, the repulsion also forces the outermost particles to the boundary, because they miss a neighbor. This has the effect, that actually the density and therefore Θ is overestimated by assuming $\rho = N/L$. This finite size effect, which shifts the curves for open boundary conditions slightly upwards for larger Θ in Fig. 10, can be eliminated by using periodic boundary conditions, also shown in Fig. 10.

4.3 Phase diagram on the lattice[12]

The equivalent of (106) on a lattice reads

$$\hat{H} = \sum_j \left[-J \left(\hat{a}_j^\dagger \hat{a}_{j+1} + \text{H.a.} \right) + c_\beta \sum_{j' \neq j} \frac{\hat{a}_j^\dagger \hat{a}_j \hat{a}_{j'}^\dagger \hat{a}_{j'}}{|j - j'|^\beta} \right] . \tag{117}$$

[12] This section is part of the basis for a publication in preparation [LMFon].

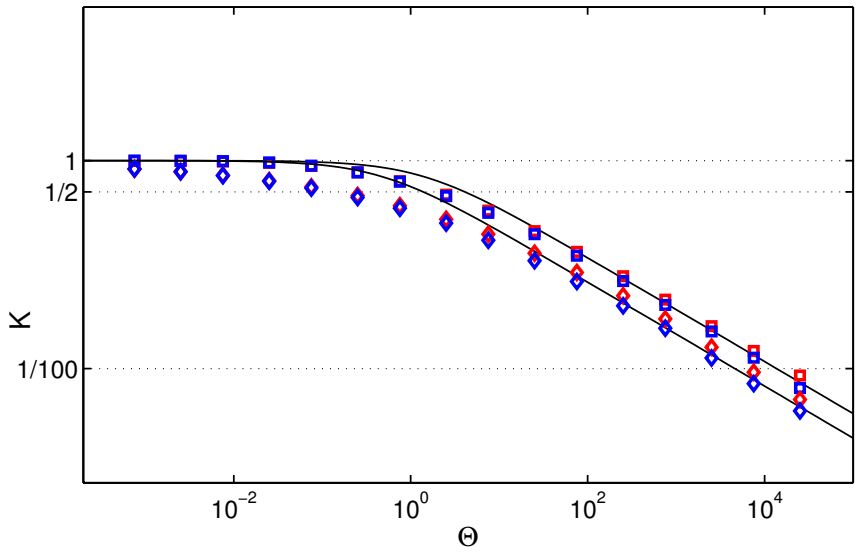

a)

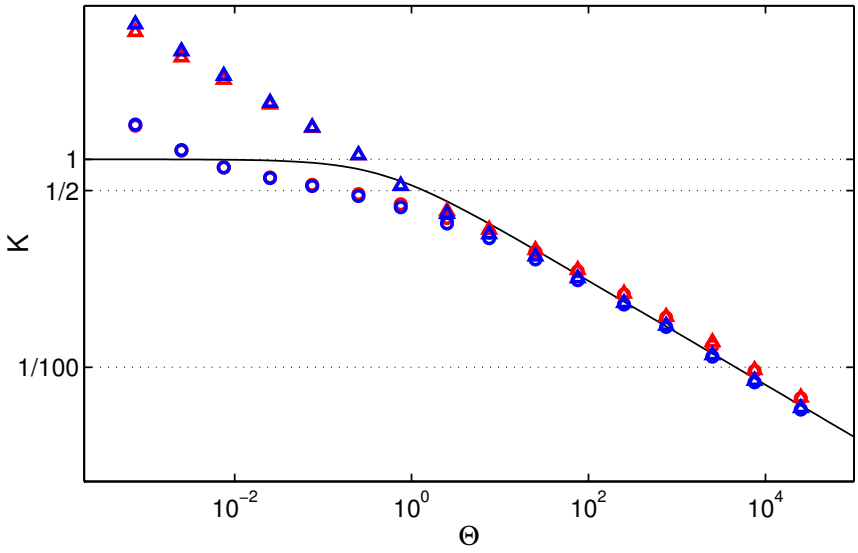

b)

Figure 10: Luttinger parameter K as a function of interaction strength. a) Unscreened long range interactions (106). The upper (lower) line shows the analytical approximation (116) for $\beta = 3$ ($\beta = 6$). Squares (diamonds) show results from DMRG calculations with open {red, using 20 particles on 200 lattice sites} and periodic {blue, using 10 particles on 100 lattice sites} boundary conditions and matrix dimension $\chi = 16$ respectively $\chi = 32$. Quantum Monte Carlo results for the $\beta = 3$ case can be found in [COPC07, CDPO$^+$08]. b) Screened long range interaction with exponent $\beta = 6$. $a_B = 1/2\rho$ (triangles) and $a_B = 1/5\rho$ (circles), with numerical parameters as in b. Continuous line shows (116) for comparison.

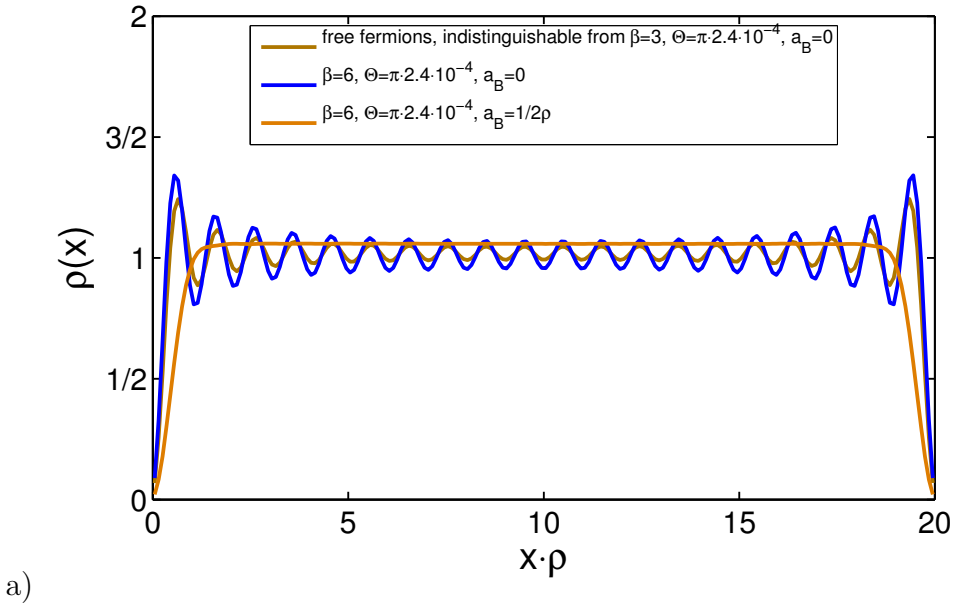

a)

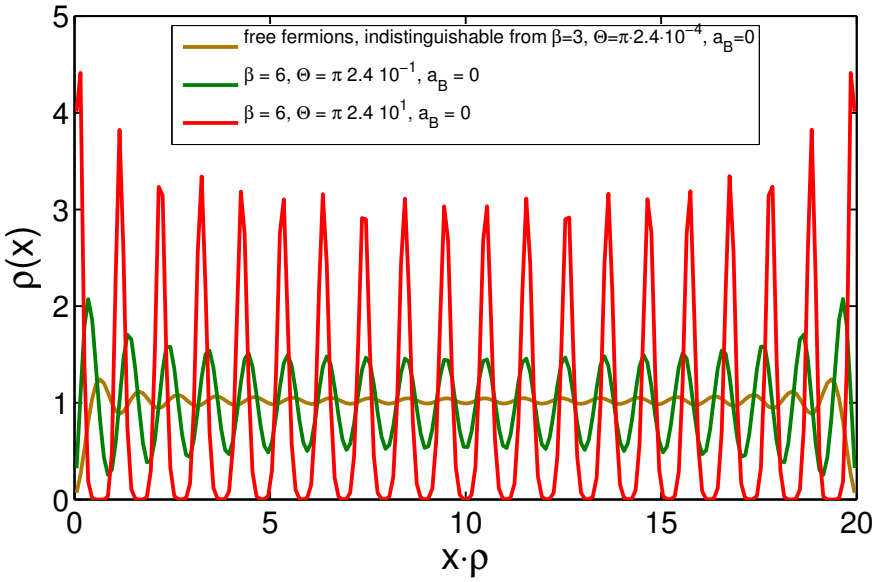

b)

Figure 11: Density profiles for open boundary conditions using 20 particles on 200 lattice sites and matrix dimension $\chi = 16$. a) screened and unscreened weak van der Waals interaction b) stronger van der Waals interaction. Free fermions are shown for comparison.

Such a model can be realized by imposing an additional deep optical lattice onto the gas that contains the Rydberg atoms [Lau12].

In the classical limit of strong interaction, $J/c_\beta \to 0$, the ground state is well known – in fact for arbitrary positive, convex interaction potential, that decay faster than the Coulomb case [PU78, Hub78]: The inter-particle distance between nearest

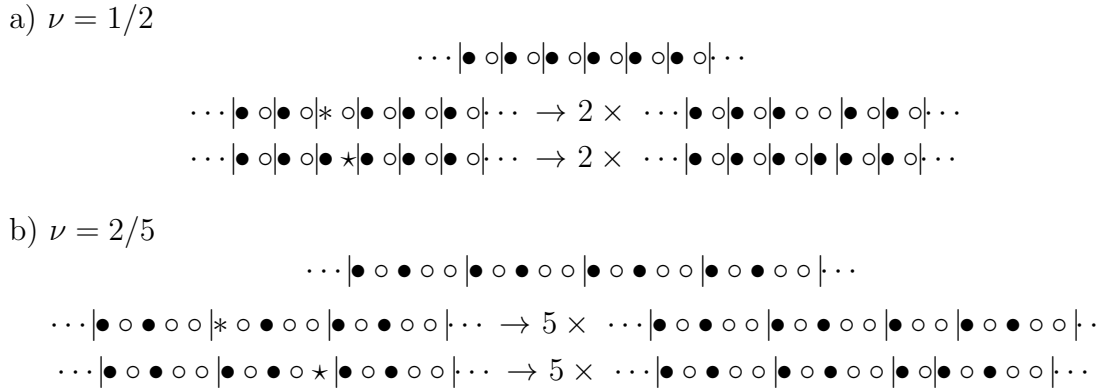

Figure 12: Removing (asterisk, middle row) or adding (star, lower row) single particles in a fractionally filled insulating phase (upper row) creates multiple, fractionally charged defects.

neighbors takes at most two values in this ground state, which differ only by one lattice site. For any rational filling fraction ν, the interaction energy is minimized by a regular distribution of the particles. This is illustrated in the upper rows in Fig. 12 for two different filling fractions. An incompressible state emerges for every rational filling fraction, such that the equation of state, $\rho(\mu)$, becomes a devils staircase [BB82]: The particle hole gap is of the order of c_β times the size of the unit cell (in lattice sites) to the power of $-\beta$. The extension of each incompressible phase for $J = 0$ is of the order of $(q-1)^{-\beta}$ with $\nu = p/q$ the reduced filling fraction. At $J = 0$ the lattice is completely filled ($\nu = 1$), as soon as $\mu \geq 2\sum_{j=1}^{\infty} \frac{1}{j^\beta} = 2\zeta(\beta)$. Adding (removing) a single particle to (from) an incompressible state, generates q defects. Those defects consist of an additional pair of neighboring atoms with the smaller (larger) separation. In lowest order perturbation theory in J/c_β these particles move freely with hopping amplitude J in-between the regular unit cells and carry a fractional charge each, illustrated in the lower rows of Fig. 12. The quantum fluctuations break up the insulator as soon as the kinetic energy of the q defects can compensate the energy required to add or remove a particle from the system, i.e. as soon as J/q becomes of the order $(q-1)^{-\beta}$. Because the gap becomes rapidly smaller with increasing q, also does the extension of the incompressible phase in J/c_β-direction. Adding a particle to a state with filling $1/q$, we create q defects (with inter-particle distance $q-1$) raising the interaction energy by $q/(q-1)^\beta$[13]. (These points are marked on the y-axis of the phase diagram for the van der Waals interaction case shown in Fig. 13 and give a good rule of thumb for the position of the phases with filling $1/\nu$.)

The phase diagram for dipolar interactions has been calculated approximatively

[13] Taking only interactions between neighboring atoms into account for the sake of simplicity.

using strong coupling expansion, i.e. higher order perturbation theory in J/c_β, in [BPCS09] and for the van der Waals case in [Lau12]. Here we consider the van der Waals case using DMRG for long range interactions, which gives correct results also for large J. The resulting phase diagram is shown in figure Fig. 13. It agrees well with the strong coupling expansion for small J/c_β, and shows the pronounced tips of the insulating lobes known from the Bose-Hubbard model, cf. Fig. 2. Because of the large difference in size of the incompressible phases for different q, we use logarithmical scaling respectively magnifications of selected regions to resolve them visually. The phase boundaries are accurately calculated for unit-cell sizes up to $q = 7$. This is rather demanding, given that an additional particle added to (removed from) a system with filling fraction p/q adds q defects to the system, each of the size $p-q$ (p). Therefore the size L of the system must be large compared to q^2 in order for all those defects to separate and well approximate the situation in the thermodynamic limit where the defects do not interact with each other at all. For $q = 1, 2, 3, 4$, and 5 a finite size extrapolation could be applied using the data available for the different system sizes. Even then the critical point can not be accurately determined because the gap closes too slowly. (The curves in Fig. 13 end at arbitrary points.)

In conclusion, we have successfully applied DMRG to bosons with van der Waals interactions in one-dimension, describing systems of Rydberg excitations that receive much attention because of the strong correlations implied by the van der Waals-interaction potential. We carried out the first exact numerical calculation of the Luttinger-parameter as a function of interaction strength and screening length in the continuous system, confirming that the correlations become much stronger than for any local interaction, and significantly improving previous approximate approaches. Specifically, K decreases much below $1/2$, such that a regime is entered where the diagonal correlations (61) dominate over the off-diagonal ones (62). In the lattice case, we give the first non-perturbative calculation of the full phase diagram at zero temperature in the μ–J/c_β plain.

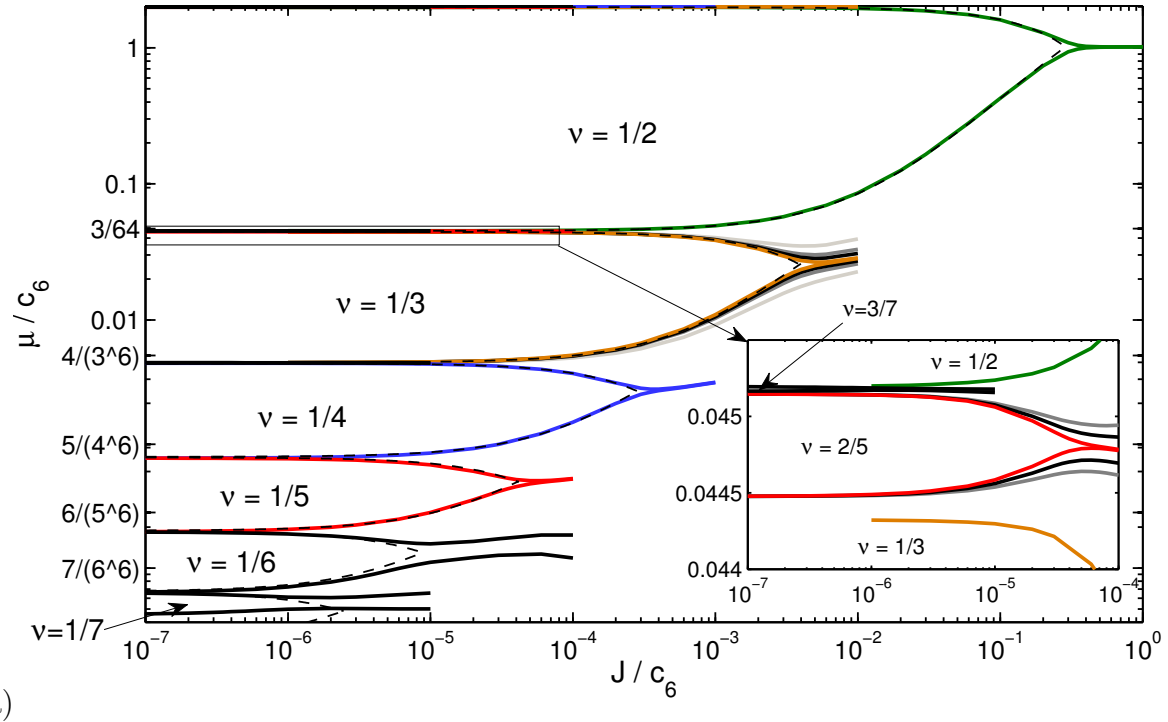

a)

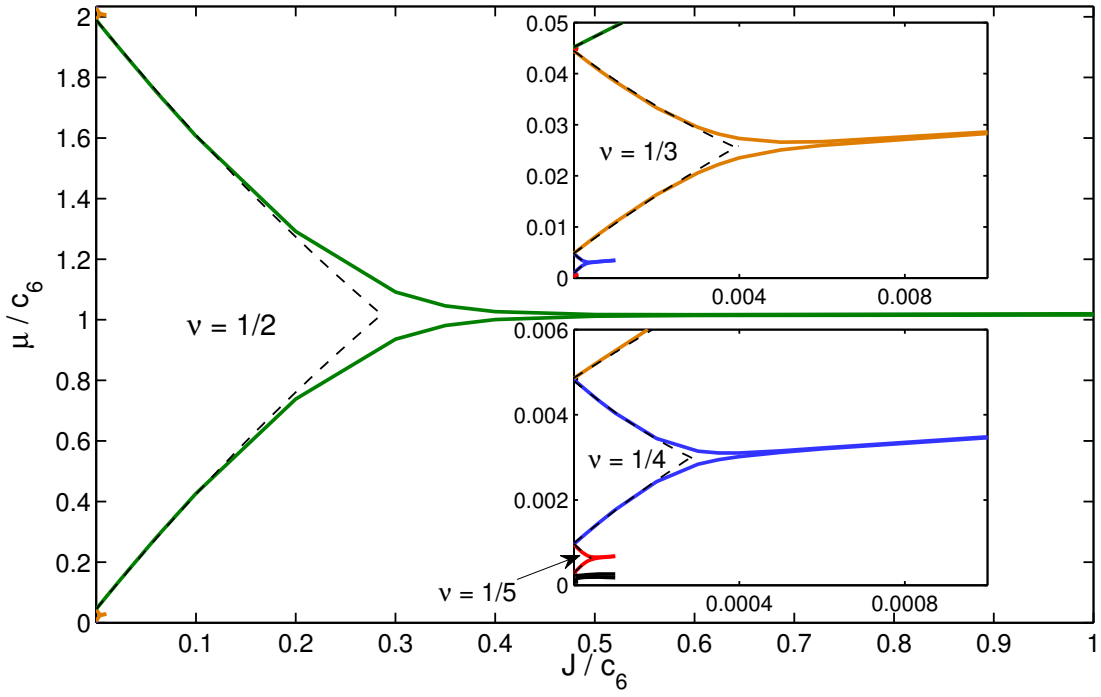

b)

Figure 13: Phase diagram of hard core bosons with van der Waals interactions on the lattice. Colored lines are infinite size extrapolations from ≈ 24 ($\nu = 1/2$ and $\nu = 1/3$ only), ≈ 60, and ≈ 120 sites DMRG calculations using open boundary conditions. For $\nu = 1/6$ ($\nu = 1/7, 3/7$) data are shown from ≈ 120 (≈ 140) site calculations without extrapolation, because these phases can not be resolved in smaller systems. Dashed lines show the second order strong coupling expansion from [Lau12] for comparison. a) Double logarithmic plot. The inset shows a closeup of the marked region (using a linear μ axis). Additionally the finite size results are shown for the $\nu = 1/3$ and $\nu = 2/5$ phases to illustrate the extrapolation. b) Linear plot with two closeups.

Part III
Dynamics in strongly correlated quantum gases

5 Fermionization dynamics of a strongly interacting 1D Bose gas after an interaction quench[14]

In the present section we analyze the dynamics of a 1D Bose gas with s-wave scattering interactions, described by the Lieb-Liniger (LL) model, after a sudden quench of the interaction strength from zero to a finite value, covering the full range from weak to strong interactions. Performing numerical simulations using TEBD, we show that local quantities, in particular the local two-particle correlation $g^{(2)}(0,0,t)$, attain a steady state expectation value on a short time scale determined only by the Tonks parameter γ and the particle density ρ. This shows that although non-local quantities such as the momentum distribution do not approach a steady state over long times [MS09], there is an equilibration in a local sense. Furthermore the asymptotic values of $g^{(2)}(x,x)$ are very close to those obtained from a thermal Gibbs ensemble [YY69], with temperature and chemical potential determined by the initial conditions and the amplitude of the interaction quench. Thus it is possible to define local temperature and chemical potential and the influence of constants of motion other than total energy and particle number is very small, if present at all. Non-local quantities such as the density-density correlation approach a steady-state distribution on a larger time scale by way of correlation waves propagating out of the sample.

Specifically we consider here a system initially prepared in the non-interacting ground state of (17), where the interaction strength is zero. We study the dynamics after an interaction quench to positive g numerically by means of the TEBD algorithm. This requires the use of a discretized version of the Lieb-Liniger model. As seen in section 3, one possible discretization leads to the (non-integrable) Bose-Hubbard model (13), see also [SF07]. Then $J = 1/(2\Delta x^2)$ and $U = g/\Delta x$ with Δx being the lattice constant of the discretization grid. The appropriateness of discretized lattice models to describe continuous interacting Bose or Fermi gases in the limit $\Delta x \to 0$ has been discussed and verified in [SF07, MFS10], see section 3. Because the Lieb-Liniger model can be mapped to the integrable spin 1/2 XXZ model, for some data sets we used both models to verify that in the considered limit the non-integrability of the Bose-Hubbard model has no influence on the results.

In the non-interacting ground state, all particles occupy the same single particle state, i.e. they are in a coherent superposition. Such a state can be expressed in terms of MPS, see appendix E, such that we can exactly put it as initial state into the TEBD algorithm. The initial state is an eigenstate of the total particle number, and as such any local density matrix (tracing out all sites but one) has only diagonal elements. In the course of interactions non-diagonal elements are not created. Thus

[14] This section is based on the publication [MSF10].

the reduced local density matrix is entirely determined by the number distribution. Two quantities of interest are its first and second moments, i.e. the density ϱ and the local two-particle correlation $g^{(2)}(x,x,t)$, where

$$g^{(2)}(x,y,t) = \frac{\langle \hat{\Psi}^\dagger(x)\hat{\Psi}^\dagger(y)\hat{\Psi}(y)\hat{\Psi}(x)\rangle}{\rho(x)\rho(y)}. \tag{118}$$

We are here concerned with the dynamical evolution of the equal time two-particle correlation at two possibly different positions. The time dependence enters via the dynamical evolution of the state of the system. This has to be contrasted to the two-particle time-ordered correlations for different times in a steady state, which we will be the subject of section 7. In principle also moments of higher-order than $g^{(2)}(x,y,t)$ are nonzero. They will, however, not be considered here.

It turns out, that for the simulation of dynamics the necessary grid sizes are much smaller than for equilibrium simulations [SF07, MFS10], see section 3. Empirically we found that in order to minimize lattice artifacts resulting into numerical errors, the average number of particles per lattice site $\langle \hat{n}\rangle = \rho\,\Delta x$ should be small compared to $1/\gamma$, where $\gamma = g/\rho(x=0)$ is given with respect to the density at the center of the cloud. We can explain this by the requirement that the interaction energy of a two-particle collision in the lattice, i.e., $g/\Delta x = U$ should be smaller than the bandwidth of the lowest Bloch band, which is $2/\Delta x^2 = 4J$, in order not to see lattice artifacts. To accommodate the requirement of a very small $\langle \hat{n}\rangle$ at the center of the cloud we use space dependent grid sizes such that the average boson number per site was constant for the center part of the particle distribution. Nevertheless to approximate the continuous model sufficiently well, very fine grids are needed leading to rather large lattice sizes of up to $L = 2880$ sites, which requires appreciable numerical resources. In order to illustrate the effects of discretization we have plotted in Fig. 14a the local two-particle correlation (see following section) for $\gamma = 200/9$ and increasing lattice sizes L, corresponding to finer grids. One clearly recognizes oscillation artifacts which only slowly disappear with increasing L.

The convergence of the TEBD scheme was checked by varying the bond dimension χ of the matrix product state (MPS) and calculating the truncation error in the state norm accumulated during the time evolution. In Fig. 14b the accumulated truncation error is plotted for $\gamma = 200/9$ and increasing values of χ from 25 to 200. One recognizes that for the maximum value of $\chi = 200$ which we were able to use, the truncation error is below the level of 10^{-3} for the time scale of interest. This value is larger then the accuracy typically reached in ground state calculations. However we are not at the point where the cut-off explodes, which typically happens in dynamical simulations at some point. Finally the matrix dimension required to achieve a given

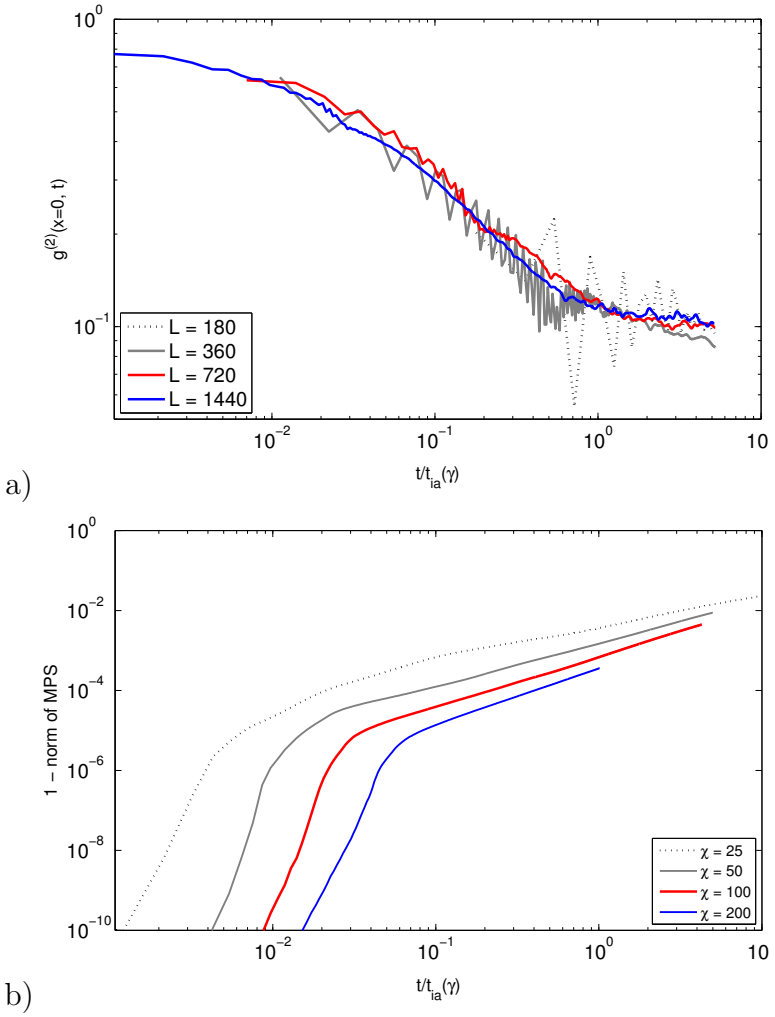

Figure 14: a) Time evolution of normalized local two-particle correlation $g^{(2)}(0,0,t)$ (see section 5.1) for $N = 9$ particles and $\gamma = 200/9$ for increasing lattice length, corresponding to finer grid sizes. One clearly recognizes oscillations which are lattice artifacts and which only disappear for the largest lattice sizes. *b)* Accumulated truncation error of the norm of the MPS in the dynamical TEBD algorithm for $\gamma = 200/9$ and increasing bond dimension χ.

accuracy does not depend on the discretization length, i.e. the number of lattice sites used. It is rather the number of particles which determines the entanglement produced and therefore the complexity of the calculations. Thus the restriction to a moderate particle number allows us to work on lattices large compared to other applications of the algorithm.

5.1 Local relaxation

In order to be able to perform numerical simulations with a fixed number of particles (up to 18, which corresponds to the experiments in references [PWM+04, HGM+09]) we have to work with a finite size system, because the extension of TEBD to infinite systems does not allow for the inclusion of a conservation law. Therefore we assumed an initial weak harmonic trapping potential $V(x) = \frac{1}{2}\omega^2 x^2$. Initially the Bose gas is in the canonical ground state ($T = 0$) of non-interacting bosons in the trap, for which the matrix product representation is analytically known, since it is a product of single particle states, see appendix E. At $t = 0$ we suddenly switch the interaction strength from zero to a finite value $g > 0$. At the same time the trap, the only purpose of which is the preparation of an appropriate initial state, is switched off. On the time scales we are interested in, the density distribution does not change, so that the presence of a trap would be of no relevance. This also allows to apply the results of the present analysis to a homogeneous gas in the sense of a local density approximation.

The initial state has a Gaussian density distribution $\rho(x) = N\sqrt{\frac{\omega}{\pi}}e^{-\omega x^2}$ with $l_{\mathrm{osc}} = \frac{1}{\sqrt{\omega}}$ being the oscillator length. Fig. 15 shows the time evolution of $g^{(2)}(0,0,t)$ with time normalized to the characteristic time scale t_{ia}, defined below, for different values of γ. One recognizes after an initial phase a power-law decay with an exponent that is monotonous in the interaction parameter. At times close to t_{ia} a steady state value is attained indicating that a local equilibrium is reached. That means that although globally a Lieb-Liniger gas does not thermalize [KWW06], local quantities do. The time scale t_{ia} of the local dynamics can be estimated from the discrete Hamiltonian. The repulsive interaction $U\hat{n}(\hat{n}-1)$ causes particle number fluctuations to be driven out of a given lattice site. This happens in the following way: Initially all components of the state vector have the same phase and tunneling has no effect[15]. However, due to the interaction, components with different particle number attain a differential phase shift and are subsequently coupled to states in adjacent lattice sites by tunneling with rate J. Since in the limit $\Delta x \to 0$ we have $J \gg U$, the maximum rate of this process is limited by the average interaction energy per particle $U\langle\hat{n}\rangle$. Thus we have

$$t_{\mathrm{ia}} = \frac{1}{U\langle\hat{n}\rangle} = \frac{1}{g\rho} = \frac{1}{\gamma\rho^2}. \tag{119}$$

Note that already for moderate interaction strength this time is much shorter than

[15] That is because the initial state is an eigenstate of the tunneling alone, because it is the non-interacting ground state.

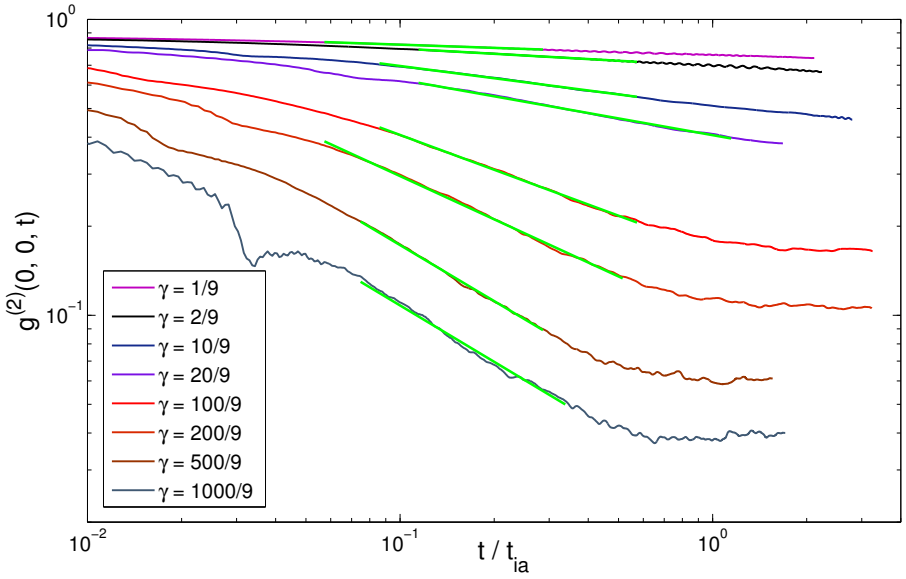

Figure 15: Time evolution of the normalized local two-particle correlation $g^{(2)}(0,0,t)$ after a sudden switch on of interactions at $t = 0$ obtained from a numerical TEBD simulation for 9 particles initially prepared in the non-interacting ground state of a harmonic trap. An intermediate power-law decay with an exponent that is monotonous in γ is apparent. The lattice size was up to $L = 2880$ for the strongest interactions corresponding to a lattice spacing of $\Delta x/l_{\rm osc} \approx 6.15 \cdot 10^{-4}$ at the trap center.

for example the oscillation time $t_{\rm osc}$ in the trap:

$$t_{\rm ia} = \frac{\pi l_{\rm osc}^2}{\gamma N^2} = t_{\rm osc}\,\frac{\pi}{\gamma N^2} \ll t_{\rm osc} \quad \text{if} \quad \gamma \gg \frac{\pi}{N^2}. \tag{120}$$

Accordingly, the density distribution does not change for times of the order $t_{\rm ia}$ as seen in Fig. 16.

Note furthermore that although the characteristic time of the expansion of the gas after switching off the trap becomes much shorter for larger interactions, it will be large compared to $t_{\rm ia}$. This is because energy transferred to the particles will be of the order $\gamma\rho^2/2$ and therefore, after it has been converted into kinetic energy, their characteristic speed $v_{\rm c}$ will be of the order $\sqrt{\gamma}\cdot\rho$ only. Requiring $v_{\rm c}\cdot t_{\rm ia} \ll l_{\rm osc}$ again yields the same mild requirement $\gamma \gg \pi/\gamma N^2$. Accordingly we found numerically that the density profile did not change on the timescale $t_{\rm ia}$ even for the largest values of γ used. Whether or not the thermalized local correlation will adiabatically follow the density evolution after longer times, i.e. when the expansion of the cloud sets in, cannot be concluded from our simulations. We would however expect such a behavior.

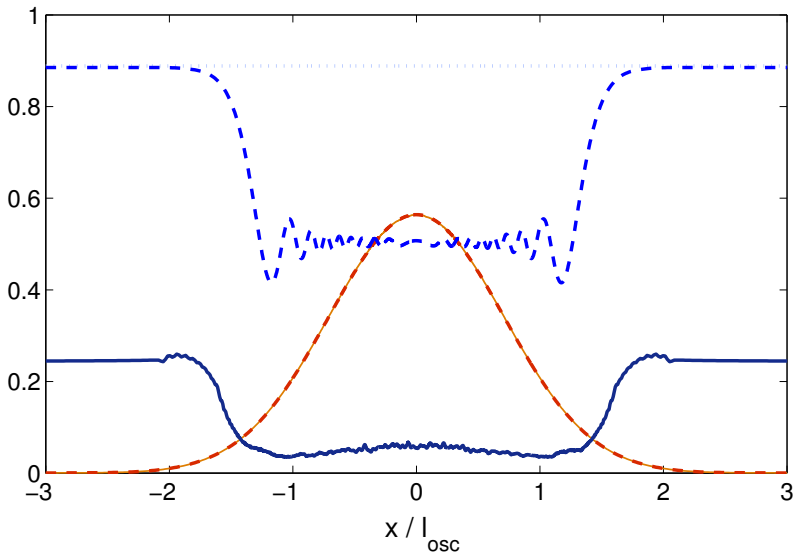

Figure 16: Local density and two-particle correlation function for $\gamma = 500/9$. The normalized local density distribution $\rho(x)/N$ at $t = t_{\mathrm{ia}}$ (orange contniuous) has not changed visibly from $t = 0$ (red dashed), while the normalized local two-particle correlation $g^{(2)}(x, x, t)$ (shown for $t = 0$ [pale blue dotted], $t = 10^{-2} t_{\mathrm{ia}}$ [bright blue dashed], and $t = t_{\mathrm{ia}}$ [dark blue continuous]) relaxes. The data set is the same as shown used Fig. 15

The fluctuations in the plots are artifacts of the discretization, which leads to an oscillatory behavior of $g^{(2)}$ on top of the continuous-system time evolution. These artifacts, which are most pronounced for larger interactions, could not be eliminated completely even for the smallest grid sizes used. As a result the asymptotic values of $g^{(2)}(0, 0, t)$ can only be given with a certain error.

In Fig. 17 we have plotted the exponents obtained from a fit to the curves in Fig. 15 which, for intermediate times, follows a power law

$$g^{(2)}(0, 0, t) \sim \left(\frac{t}{t_{\mathrm{int}}} \right)^{\alpha - 1} . \tag{121}$$

The exponent is a monotonous function of the interaction strength and slowly approaches the limit -1 for $\gamma \to \infty$, i.e., for a Tonks-Girardeau gas [CGM+08].

We now want to analyze the local state of the system after it has become stationary. In particular we will show that the local steady-state can be well described by the usual finite-temperature Gibbs state for homogeneous systems. To this end we calculate the expected asymptotic value $g^{(2)}_{\mathrm{YY}}(0, 0)$ from the thermodynamic Bethe Ansatz, section 1.2.3. The system is initially prepared in its non-interacting ground state, so we have $g^{(2)}_{\mathrm{init}}(0, 0) = 1 - 1/N$, which in the thermodynamic limit $N \to \infty$

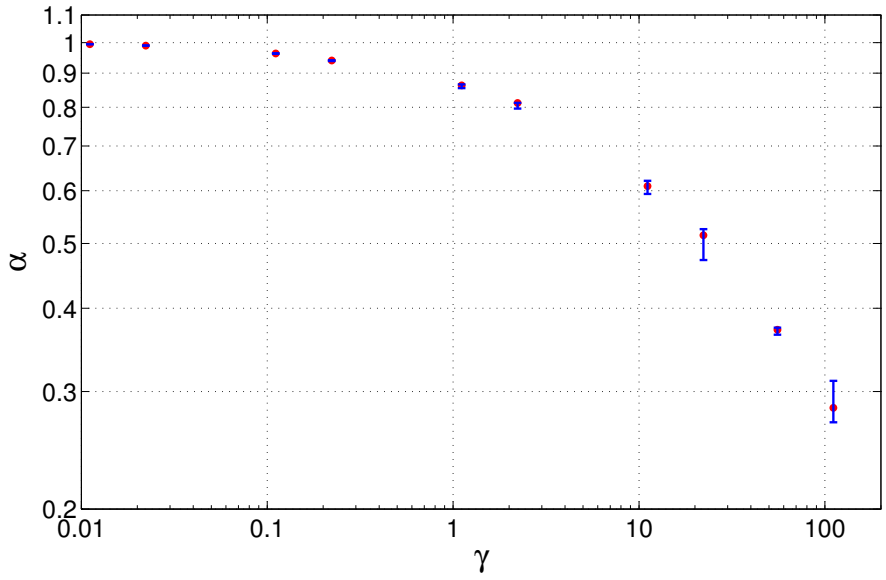

Figure 17: Exponents $\alpha-1$ of the intermediate power-law decay of $g^2(0,0,t)$ in Fig. 15 as function of γ. Error-bars indicate systematic fitting error.

approaches unity, as should be the case for free bosons. The energy of this state with respect to the non-interacting Hamiltonian is 0. At time $t = 0$ the interaction is switched to a finite strength $g > 0$ and the expectation value of the interaction energy immediately after the quench is given by

$$E_{\mathrm{ia}} = \int \mathrm{d}x \, \frac{g}{2} \langle \hat{\Psi}^{\dagger\,2}(x) \hat{\Psi}^2(x) \rangle = \int \mathrm{d}x \, \frac{\gamma}{2} g^{(2)}(x,x) \rho^3(x). \tag{122}$$

Since in a homogeneous system there is no x-dependence the energy per particle is

$$\left. \frac{E}{N} \right|_{t=0+} = \left. \frac{E_{\mathrm{ia}}}{N} \right|_{t=0+} = \gamma T_{\mathrm{c}}. \tag{123}$$

Here we have introduced the quantum degeneracy temperature T_{c} in one dimension

$$T_{\mathrm{c}} = \rho^2/2. \tag{124}$$

One recognizes that the system is in a highly excited non-equilibrium state after the quench if $\gamma \gtrsim 1$. Using the energy per particle, the density ρ and the Tonks parameter γ as input parameter, we can extract a temperature T of a corresponding thermal Gibbs state by inverting the Yang-Yang equations of the thermodynamic Bethe Ansatz as described in section 1.2.3. With the help of the Hellmann-Feynman theorem we can then obtain the value $g^{(2)}_{\mathrm{YY}}(0,0)$ corresponding to the Gibbs state

at temperature T [KGDS03]. For $\gamma \gg 1$ we see that the energy per particle (123) becomes large compared to T_c. We are thus in the high temperature regime where $E/N \approx T/2$ and therefore $\tau = T/T_c \approx 2\gamma$. In this limit $1 \ll \tau \ll \gamma^2$, one obtains the asymptotic solution [KGDS03]

$$g^{(2)}_{\mathrm{YY}}(0,0) = \frac{2\tau}{\gamma^2} = \frac{4}{\gamma}. \tag{125}$$

In Fig. 18 we have plotted the values of $g^{(2)}_{\mathrm{YY}}(0,0)$ from the thermal Gibbs state in the thermodynamic limit as function of the interaction strength γ (solid line). It indeed approaches (125) for large γ. Also shown are the steady-state values obtained from the numerical simulation in Fig. 15. The error bar indicates uncertainties which are here due to discretization artifacts and error estimates obtained from comparing simulations with MPS bond dimensions $\chi = 100$ and 200. It is available only for one parameter set, since the variation of the discretization length and the bond dimension is numerically expensive. However we expect it to be of about the same relative size for all data points. One recognizes that $g^{(2)}(0,0,t)$ attains in the long-time limit values which are close to that of the thermal Gibbs state. One should note that the steady-state values for the largest values of γ ($\gamma = 500/9$ and 18 bosons as well as $\gamma = 1000/9$ and 9 bosons) are slightly overestimated in the simulation due to the remaining grid artifacts since here $\langle\hat{n}\rangle\gamma \approx 0.73$ is no longer small compared to unity. Also shown is the asymptotic local temperature of the gas in units of the degeneracy temperature. For large values of γ, $T \approx \gamma T_c \gg T_c$, i.e., after relaxation the gas is in a state with large local temperature. Specifically, in the steady state after the quench $g^{(2)}(0,0)$ scales as $1/\gamma$ in contrast to the $1/\gamma^2$ behavior at low temperatures [LL63]. In this sense the non-adiabaticity of the quench prevents the system from showing complete fermionization, which is found at large γ in the ground state.

5.2 Non-local dynamics

We now discuss the dynamics of non-local quantities. Specifically we consider the non-local two-particle correlation $g^{(2)}(0,x;t)$. In Fig. 19 we have plotted $g^{(2)}(0,x,t)$ for different times after the interaction quench. One recognizes that while the local correlations attain a steady-state value on a short time scale, the non-local evolution happens much slower. Switching on the particle-particle repulsion leads to a fast reduction of the probability to find two particles at the same position. Associated with this is a correlation flow to larger distances leading to expanding correlation waves. For very short times the propagation velocity of correlation waves is faster than the Fermi velocity $v_F = \pi\rho$. But at the largest time shown in Fig. 19 corresponding

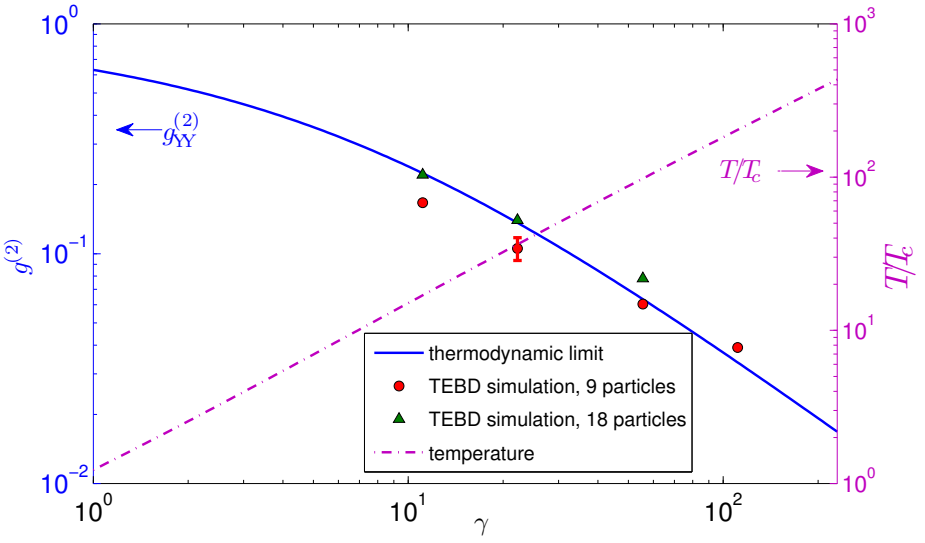

Figure 18: Steady-state values of $g^{(2)}(0,0)$ (left scale) for different values of the interaction parameter γ after the interaction quench obtained from TEBD simulations using 9 (red circles, corresponding to Fig. 15) and 18 (green triangles) bosons. Solid line: value from thermal Gibbs state in the thermodynamic limit; dot dashed line: temperature (right scale) corresponding to the given energy per particle in the thermodynamic limit. The error bar reflects discretization error estimated by comparing steady-state values for $L = 720$ and $L = 1440$ lattice sites as well as error resulting from finite MPS matrix dimension obtained from comparing results for bond dimension $\chi = 100$ and 200.

to $t = 0.01 t_{\mathrm{osc}}$, the maximum of the correlation wave has traveled a distance of approximately $\Delta x = 0.12 l_{\mathrm{osc}}$ which is consistent with the speed of sound which for large values of γ approaches

$$v_s = v_F \left(1 - \frac{4}{\gamma}\right). \tag{126}$$

The buildup of a maximum that behaves like a wave front can be understood as follows: In a homogeneous system the integral over space of $g^{(2)}(0,x,t)$ is a constant with respect to time due to particle number conservation, because $\langle \hat{\Psi}^\dagger(x)\hat{\Psi}^\dagger(0)\hat{\Psi}(0)\hat{\Psi}(x)\rangle$ is proportional to the joint probability distribution to find a particle at position x given that there is one particle at the origin.

Given that the quench can not change $g^{(2)}(0,x,t)$ significantly outside the light cone given by the Fermi velocity, the reduction of the probability to find two particles close together must be accompanied by an increase at finite distance.

Fig. 19 is also consistent with the assertion that the non-local correlation function approaches at least for smaller distances in the large-time limit that of the thermal Gibbs state with temperature and density given by the initial conditions and the

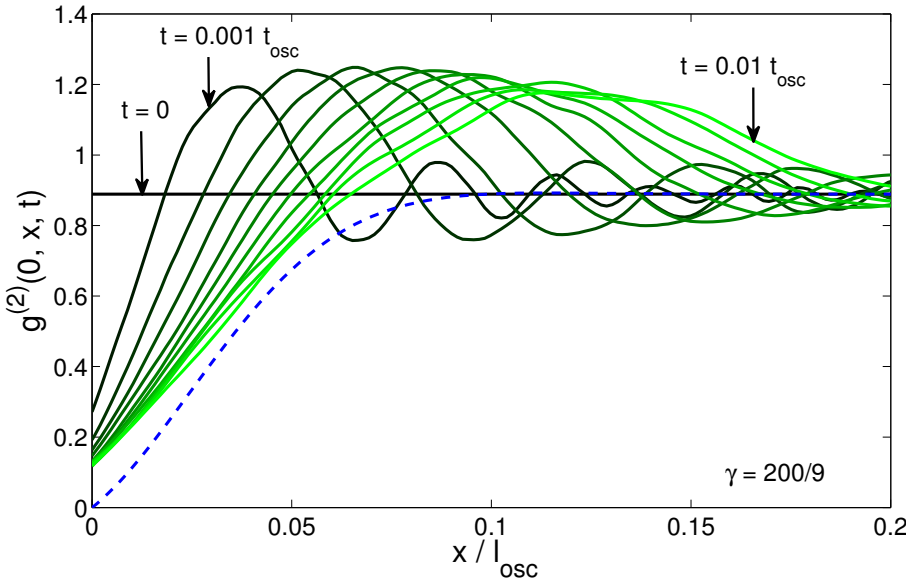

Figure 19: Time evolution of non-local density-density correlations $g^{(2)}(0,x,t)$ for $\gamma = 200/9$. $x = 0$ denotes the center of the cloud. One recognizes the formation of expanding correlation waves. The dashed blue line shows the approximation (127) to the non-local correlation in a thermal Gibbs state from [DSG+09] multiplied by $g^{(2)}(0,0,t=0) = 8/9$ to account for the final particle number ($N = 9$) used in the simulation.

Tonks parameter γ. For comparison we have plotted an approximation to the finite-temperature non-local $g^{(2)}$ from reference [DSG+09] which holds in the regime $1 \ll \tau \ll \gamma^2$

$$g_{\mathrm{T}}^{(2)}(0,x) = 1 - \left[1 - 4\sqrt{\frac{\pi\tau}{\gamma^2}}\left(\frac{x}{\lambda_T}\right)\right] \mathrm{e}^{-2\pi(x/\lambda_T)^2}. \tag{127}$$

Here $\lambda_T = \sqrt{4\pi/\tau\rho^2}$ is the thermal de Broglie wave length.

5.3 Experimental observation

In the following we discuss the possibility to test the local relaxation in an experiment. For this we make use of the fact that by energy conservation the interaction energy lost by the decrease of $g^{(2)}(0,0)$ must be gained as kinetic energy

$$E_{\mathrm{kin}}(t) = E_{\mathrm{ia}}(t=0) - E_{\mathrm{ia}}(t) \tag{128}$$

and the kinetic energy therefore directly gives the value of $g^{(2)}(0,0,t)$ in the homogeneous case:

$$E_{\mathrm{kin}}(t) = \int dx\, \frac{g}{2}\Big(1 - g^{(2)}(0,0,t)\Big)\rho^2. \tag{129}$$

If the interaction is turned on at $t = 0$ and turned off abruptly at some time $t = t_1 > 0$ only the kinetic energy remains in the system and can be used to measure $g^{(2)}(0, 0, t_1)$:

$$g^{(2)}(0, 0, t_1) = 1 - \frac{2}{\gamma\rho^2}\frac{E_{\text{kin}}^{\text{final}}}{N}. \tag{130}$$

The kinetic energy can be extracted from the momentum distribution which is routinely measured in time-of-flight experiments. In an experimental setup, the gas must be confined e.g. by an harmonic trapping potential. So the initial non-interacting state has a Gaussian density distribution. It is also a good assumption, that the correlations decay locally as in the homogeneous system corresponding to the local density provided the density $\rho(x)$ remains constant over the time scale of interest. This is indeed the case, if $t_{\text{int}} = 1/(\gamma\varrho^2) \ll l_{\text{osc}}/v_s \approx l_{\text{osc}}/\pi\varrho(0)$. This means, that the Tonks parameter must be large compared to $\frac{\pi^{3/2}}{N}$, which is of course the case we are interested in. We note that the region in the wings of the density distribution which does not fulfill this constraint gives a negligible contribution to the total interaction energy. Of course measuring the kinetic energy in the trap gives only an average of $\frac{g^{(2)}(x,x)}{\rho^2(x)}$ over the trap, but one can account for this by a weighted average over different simulation parameters.

In summary, in this section we have numerically analyzed the dynamics of a 1D Bose gas (LL-model), after an interaction quench from zero to a finite value. Although globally the 1D Bose gas does not thermalize, we have shown that local quantities attain a steady-state value on a time scale $t_{\text{ia}} = (\gamma\rho^2)^{-1}$. Within the achievable accuracy these values are consistent with the assumption that local quantities relax to a thermal Gibbs state with local temperature determined by the initial energy and chemical potential. Non-local quantities such as the density-density correlation relax on a much longer time scale set by the velocity of sound by means of correlation waves propagating out of the sample. The observation that certain quantities like energy density (which is connected to the local $g^{(2)}$) relax to thermal values locally on much shorter timescales than required for global equilibration is known as prethermalization [BBW04] in the literature. The value of the local observables attained in the steady state after t_{ia} might be only preliminary. Globally the steady state after t_{ia} can not be the final one, which is reached after two-body (and all higher) correlations have propagated throughout the system and a global equilibrium is reached. The role of integrability for the expectation value of the local $g^{(2)}$ might be different between the preliminary and the truly relaxed state.

6 Dynamics of pair correlations in the attractive Lieb-Liniger gas[16]

In dynamical setups, attractively and repulsively interacting gases are equally well accessible. A recent milestone in this direction is the creation of the super Tonks-Girardeau gas [ABCG05, CGYH10] by Haller et al. [HGM+09], realized by a rapid sweep through a confinement induced resonance [Ols98] from the strongly repulsive to the strongly attractive side. We here analyze the dynamics of this quench process by numerical simulations employing the TEBD algorithm as applied to the Lieb-Liniger gas in the repulsive regime (see previous section) and a number of lattice models [GKSS05, SK05, FCM+08].

The dynamics of a 1D, trapped Bose gas with local interactions is governed by the Lieb-Liniger Hamiltonian (17) introduced in section 1.2, with the additional potential $V(x) = \frac{m}{2}\omega^2 x^2$ here again describing a harmonic trap.

The spectrum of (17) is quite different depending on the sign of γ, however the positive- and negative-γ spectra agree in the limits of weak *as well as* strong interactions [TZS08]. This can be understood from the problem of two particles with $V = 0$ and periodic boundary conditions: The center panel of Fig. 20 shows the lowest lying states with vanishing center-of-mass momentum. The non interacting ground state (left and right outside of the figure at $E = 0$) has a constant relative wave function. For finite interactions, the wave function must obey the contact conditions (28). It develops a peak at zero inter particle distance when an attractive interaction ($\gamma < 0$) is turned on and eventually forms a closely bound pair with binding energy $\sim \gamma^2$ (see below). On the repulsive side ($\gamma > 0$) a dip-like kink emerges with increasing interaction, which eventually makes the wave function vanish at coinciding particle positions – this is the famous fermionized Tonks-Girardeau gas. When approaching the strong interaction regime from the attractive side, the *first excited state* adiabatically connects to exactly the same fermionized state (also shown in Fig. 20) – the super Tonks-Girardeau gas. This matching continues for higher excited states and can be generalized to many particles, where the bound states can be classified by the number of dimers, trimers, etc. [MS98].

Fig. 20 indicates, that a quench from the Tonks-Girardeau regime to the strongly attractive regime will put the gas to good approximation in the super Tonks-Girardeau state. Experiments have successfully demonstrated this, while the difference between Tonks-Girardeau and super Tonks-Girardeau can be detected by their different compressibility [ABCG05].

[16] This section is based on the publication [MF10].

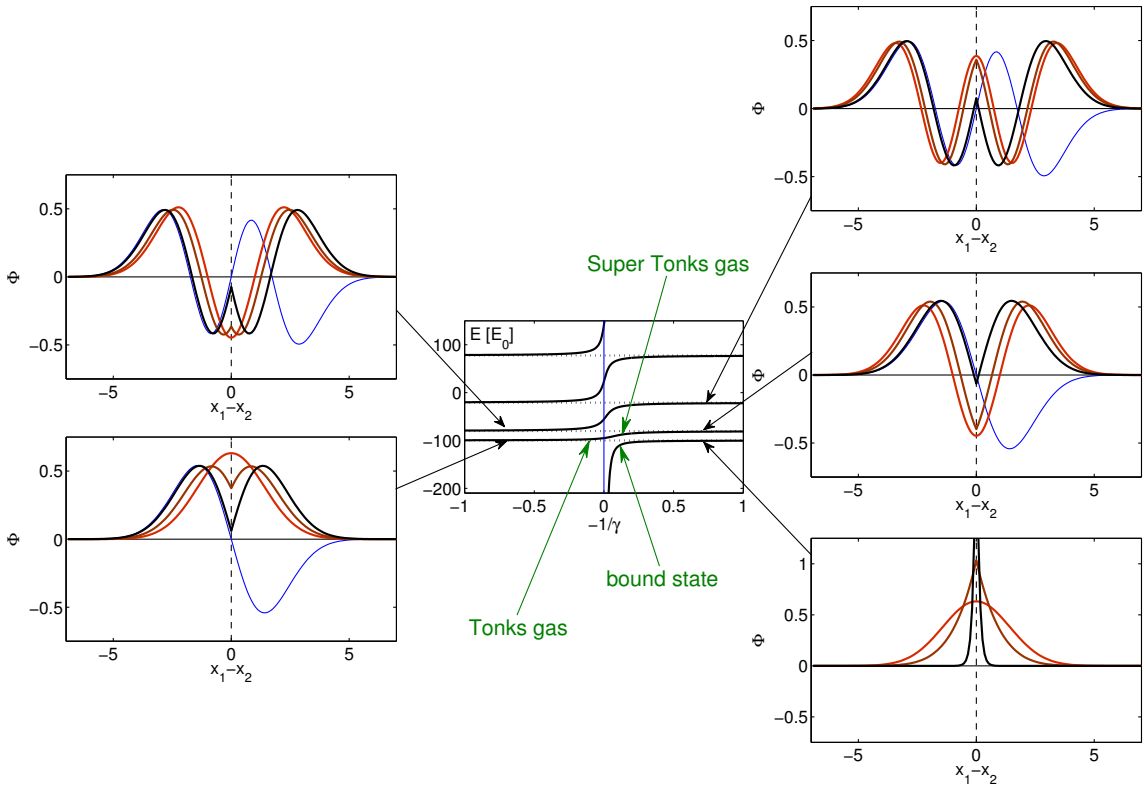

Figure 20: The spectrum of the Lieb-Liniger Hamiltonian for two particles with vanishing total momentum on a ring of length L as a function of inverse interaction strength is shown in the center. The energy unit is $E_0 = 4\pi^2\hbar^2/(L^2 m)$. One recognizes equivalence of the spectra at vanishing ($|\gamma| \to 0$) as well as for infinitely strong interactions ($|\gamma| \to \infty$). The outer panels illustrate the continuous change of the relative part of the two-particle wave functions as the interaction strength is tuned, for simplicity in a harmonic trap (with the trap length set to 1). The free boson ground state (red curve in lowest panels on both sides) approaches (brown curves: intermediate, black curves: strong interactions) the Tonks gas for repulsive, and a tightly bound state for attractive interactions, as the interaction strength is increased, i.e., towards the center of the center panel. For higher states, the nth bosonic eigenstate approaches adiabatically the nth respectively $(n-1)$th fermionic eigenstate (blue curves) up to normalization for repulsive respectively attractive interactions.

6.1 Numerical simulation of the full many-body case

We here consider a gas of N particles, confined by a harmonic trap, initially in the ground state for $\gamma = +\infty$, i.e. starting from the Tonks-Girardeau gas. At $t = 0$ the interactions are switched to the strongly attractive side $\gamma \ll -1$. In simulations we use values of γ between -6 and -145. The trap plays a minor role, since interactions give the relevant time scale.

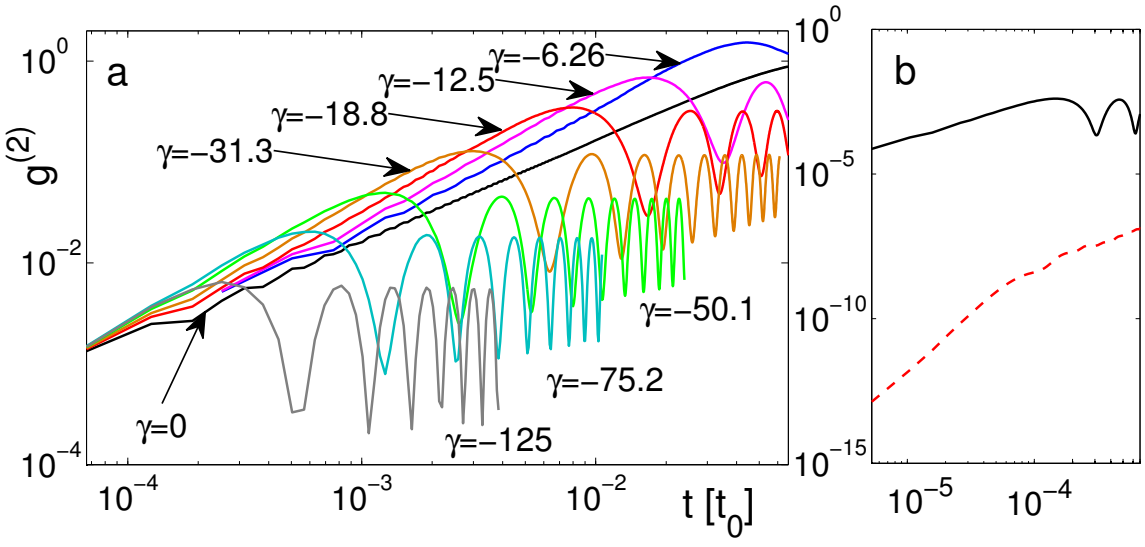

Figure 21: *left:* Time evolution of the local two particle density density correlation in a system of $N = 18$ particles calculated via TEBD (colored lines). gray line: two particle case with periodic boundary conditions and $\gamma = 0$. *right:* Time evolution of local three-particle correlation $g^{(3)}$ (red dashed) at the trap center and $g^{(2)}$ (black) for comparison at $\gamma = -145$. (The artifacts for very short times are due to the finite time steps used by the numerical algorithm.)

We simulate the full many-body dynamics using TEBD as in the preceding section. Again the continuous model is discretized, resulting in the sparsely filled Bose-Hubbard model. To prepare the initial state, we use imaginary time evolution, because the exact ground state can not be easily expressed as a matrix-product-state, as was the case for the ground state of free bosons. The lattice is finite, but comprises all of the gas (which does not change its density distribution on the time scale in question, much the same as in section 5). The dynamics is simulated using a fourth order trotter decomposition [SS99]. While time dependent simulations are generally limited to short times due to the linear growth of entanglement entropy [BHV06, EO06], this it not crucial here. Although we also observe such a linear growth, the increase is slow and we can go much beyond the time scale of interactions, which was the limit in section 5, for as much as $N = 18$ particles on a 1280 sites lattice using rather small matrices of dimension 100 in the algorithm. This can be accounted to the fact, that the initial state is actually very close to an eigenstate of the Hamiltonian after the quench, as we will discuss in detail below.

Fig. 21a shows the local two-particle correlation $g^{(2)}(t) = g^{(2)}(x_1 = 0, x_2 = 0, t)$, where

$$g^{(2)}(x_1, x_2, t) = \frac{\langle \hat{\Psi}^\dagger(x_2)\hat{\Psi}^\dagger(x_1)\hat{\Psi}(x_1)\hat{\Psi}(x_2)\rangle}{\rho(x_1)\rho(x_2)}, \tag{131}$$

as a function of time for various values of the interaction strength. The correlation function first grows as a power law $\sim \left(t/t_0\right)^\alpha$. The time unit in the plots is $t_0 = 4m/(\hbar\rho^2) = 2\pi^2\hbar/E_\mathrm{F}$. By a linear fit to the numerical data, we find α growing from 1 in the free case to a value of about 4/3 in the strongly attractive case. We see that $g^{(2)}$ rises up to a finite value much smaller than 1 for reasonably strong interaction. This reflects the fact, that most of the gas ends up in the fermionized super Tonks-Girardeau state. For longer times and stronger interactions, we observe however a rather peculiar oscillatory behavior with large modulation depth. The oscillation frequency coincides with the binding energy of a *pair* of particles in the McGuire state $\omega_2 \simeq \gamma^2\hbar\rho^2/4m = \gamma^2/t_0$ [McG64]. Thus the dynamics seems to be strongly affected by the contribution of bound pairs. Moreover, there is no sign of a relaxation, as observed in the repulsive case above. In Fig. 21b the local three-particle correlation $g^{(3)}(t) = g^{(3)}(x_1 = 0, x_2 = 0, x_3 = 0, t)$ is plotted, where

$$g^{(3)}(x_1, x_2, x_3, t) = \frac{\langle\hat\Psi^\dagger(x_3)\hat\Psi^\dagger(x_2)\hat\Psi^\dagger(x_1)\hat\Psi(x_1)\hat\Psi(x_2)\hat\Psi(x_3)\rangle}{\rho(x_1)\rho(x_2)\rho(x_3)}. \tag{132}$$

One recognizes that $g^{(3)}$ remains extremely small, showing that higher-order cluster states are not populated in the interaction quench. This agrees well with the finding in [GA10] where the overlap of the Tonks-Girardeau wave function with the McGuire cluster state was calculated.

Fig. 22 shows the dynamical evolution of the density-density correlations, where we fix one position at the center of the cloud. The initial state shows the typical feature of fermionization, i.e. $g^{(2)}(0,0)$ is zero and $g^{(2)}(0,x)$ rises to one (no correlation) on a length scale proportional to the average inter-particle distance. In the limit $\gamma \to -\infty$ the correlations do not show much resolvable dynamics because the initial Tonks-Girardeau gas is close to the super Tonks-Girardeau state. However for moderate interaction strength, we see $g^{(2)}(0,x)$ rising sharply around zero distance. This clearly shows transitions to states other than the super Tonks-Girardeau state. One finds that the characteristic length scale of the peak at the origin is given by a_1D. This gives further indication of a finite admixture of the $N = 2$ cluster state. Since $\int \mathrm{d}x\langle\hat\Psi^\dagger(x)\hat\Psi^\dagger(0)\hat\Psi(0)\hat\Psi(x)\rangle = \rho(0)(N-1)$, as discussed in the previous section, the integral over $g^{(2)}(0,x)$ must be constant in time, as long as the density is homogeneous. The increase at $x_1 - x_2 = 0$ must therefore be accompanied by a decrease at larger distances as seen in the correlation waves building up in Fig. 22.

The insert of Fig. 22 shows another interesting feature: Apart from small distances, where oscillations continue, the correlations become quickly stationary (at least over several oscillation periods) and can be well approximated for intermediate distances by $g^{(2)}$ of a Tonks-Girardeau gas shifted by a_1D and renormalized by a

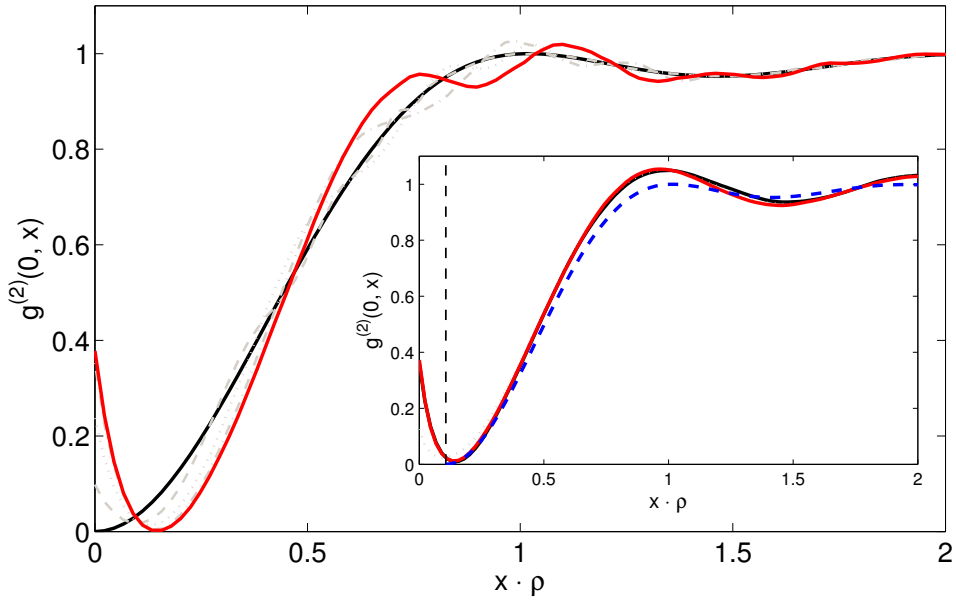

Figure 22: Time evolution of the non-local density-density correlation function for interaction strength $\gamma = -18.7931$ calculated for $N = 18$ particles using TEBD. Curves are shown for 0 (black), 1/4 (dotted), and 1/2 (red, maximum value at $x = 0$) oscillation periods of the local correlation. *insert*: $g^{(2)}$ at times of 3.5 (black), 4 (dotted), and 4.5 (red) periods. The vertical dashed line indicates $x = a_{1D}$. The blue dashed line shows $g^{(2)}$ for a Tonks-Girardeau gas shifted by a_{1D} and renormalized.

factor $(1 - \gamma^{-1})$ (dashed, blue line). This can be explained as follows: As shown by Girardeau and Astrakharchik [GA10] the wave function of the two-particle problem with finite attractive interactions has a node at some distance $x = a$ and for distances not smaller than this coincides with the Tonks-Girardeau wave function apart from normalization. For large $|\gamma|$ one finds $a \approx a_{1D}$. Furthermore, the renormalized and shifted Tonks-Girardeau correlation curve agrees very well with $g^{(2)}(0, x)$ for a system of hard rods with excluded volume $a \approx a_{1D}$, which was recently calculated using quantum Monte Carlo as well as bosonization techniques in [MABC08]. The fact that the TEBD results show slightly more pronounced oscillations than the shifted Tonks-Girardeau or hard-rod curve is due to the small excitation of higher gas like states.

6.2 The two particle case

We will show now that the two-particle correlations in the trapped gas can be very well reproduced by a system containing only $N = 2$ particles. This is due to the fact that for strong interactions, eigenstates are expected to be well approximated by pair

product states of the Jastrow-Bijl type [GA10]

$$\Phi(x_1,\ldots,x_N) = \left[\prod_{i<j}\phi(x_i-x_j)\right]\prod_{j=1}^{N}\exp\left(-\frac{x_j^2}{2l_{\mathrm{osc}}^2}\right), \tag{133}$$

with $l_{\mathrm{osc}}^2 = \hbar/(m\omega)$, and $\phi(x_i - x_j)$ is a two-particle wave-function. The two-particle solution will provide insight into the nature and the size of the oscillations observed in the numerical simulations. For the actual calculations we impose periodic boundary conditions, which is reasonable for the comparison to the trapped gas, since the trapped gas is homogeneous in good approximation over some inter-particle distances. The periodic boundary conditions problem gives analytical expressions and allows to extract the scaling with γ in the strongly interacting regime. This problem has been solved for attractive interactions in the original paper by Lieb and Liniger [LL63]. We will use their solution in the following.

The Hamiltonian for the two particle problem reads in first quantization

$$\hat{H} = -\frac{\hbar^2}{2m}\left(\partial_1^2+\partial_2^2\right) + g\delta(x_1-x_2). \tag{134}$$

All eigenstates of the LL model can be constructed from coordinate Bethe ansatz [YY69]. In the primary sector R_1 ($0 \le x_1 \le x_2 \le L$), the solution is $\phi(y = x_1 - x_2) = 2Ae^{i\frac{\delta}{4}}\cos\left[\frac{\delta}{2}(\frac{y}{L}-\frac{1}{2})\right]$. A is a normalization constant, and δ is related to the scattering phase shift $\Theta = -2\tan^{-1}[(k_2-k_1)L/2\gamma]$ via $\Theta = \delta/2 - \pi$. Note that $e^{i\frac{\delta}{4}}$ is not a simple phase factor as δ will be imaginary for the bound state.

We will now calculate asymptotic expressions for the bound state ϕ_{b}, where $\gamma \to -\infty$, as well as Tonks-Girardeau and super Tonks-Girardeau states $\phi_{\pm}$, where $\gamma \to \pm\infty$. For the bound state ϕ_{b} we need to find an imaginary solution of the Bethe equations (34). Substituting $\delta = i\tilde{\delta}$ we find in the strongly interacting limit $\tilde{\delta} = (-2\gamma)$. With this we calculate the normalization of the wave function, yielding $A_{\mathrm{b}} \to \sqrt{\tilde{\delta}/2}/L$. Thus the wave function at coinciding particle positions reads

$$\phi_{\mathrm{b}}(x_1-x_2=0) = 2A_{\mathrm{b}}e^{-\frac{\tilde{\delta}}{4}}\cosh\frac{\tilde{\delta}}{4} \xrightarrow{\gamma\to-\infty} -\frac{\sqrt{-\gamma}}{L}. \tag{135}$$

Due to bosonic statistics the local two-particle correlation is given in terms of the wave function as $g^{(2)}(0,0) = 2|\phi(0)|^2/\rho(0)^2$. As the density ρ is $2/L$ everywhere, this results in $g_{\mathrm{b}}^{(2)}(0,0) \to \tilde{\delta}/4 = -\gamma/2$.

We denote the lowest lying gas like states $\phi_{\pm}$ for $\gamma \to \pm\infty$. From the Bethe equation we see that a real solution δ will be close to 2π. Expanding the tangent around its singularity at $\pi/2$ we get $\delta = 2\pi\left(1-\frac{2}{\gamma}\right)$. For the normalization this

means $A_\pm \to 1/L\sqrt{2}$, such that the wave function at coinciding particle positions becomes

$$\phi_\pm(x_1 - x_2 = 0) = 2A_\pm e^{\frac{i\delta}{4}} \cos\frac{\delta}{4} \xrightarrow{\gamma\to-\infty} i\sqrt{2}\frac{\pi}{\gamma L}. \tag{136}$$

The local two-particle correlation is in this case $g_\pm^{(2)}(0,0) = \pi^2/\gamma^2$. The γ^{-2} scaling is well known [KGDS03] and is the same as in the many particle case.

The overlap between the initial Tonks-Girardeau gas state $\phi_0 = \lim_{\gamma\to\infty}\phi_+$ and the bound state for finite γ can easily be calculated. In the strongly interacting regime one finds $\varepsilon \equiv \langle\phi_0|\phi_b\rangle \to -2\sqrt{2}\pi\gamma^{-3/2}$.

We now want to calculate the dynamics of the local correlation in the two particle case. This can be done in different ways. Here we used again discretization combined now with exact diagonalization to find the exact solution shown in Fig. 23 as a black solid curve. From the above calculations we can derive simple approximations which are very good in the strongly interacting regime. We can decompose the initial state $|\phi_0\rangle$ according to

$$|\phi_0\rangle = \varepsilon|\phi_\mathrm{b}\rangle + \Big(|\phi_0\rangle - \varepsilon|\phi_\mathrm{b}\rangle\Big) = \varepsilon|\phi_\mathrm{b}\rangle + |\bar{\phi}_0\rangle. \tag{137}$$

Note that for large $|\gamma|$, $|\bar{\phi}_0\rangle$ is approximately normalized. Since the initial state is the Tonks-Girardeau gas with $\phi_0(x_1 - x_2 = 0) = 0$ one finds from (137) and (135) that for $t = 0$ the wave function at coinciding particle positions is given by

$$\bar{\phi}_0(x_1 - x_2 = 0, t = 0) \xrightarrow{\gamma\to-\infty} i2\sqrt{2}\frac{\pi}{\gamma L}. \tag{138}$$

Note the factor of 2 as compared to Eq. (136) which is physically due to the very small admixture of the bound state. $\bar{\phi}_0$ is not an eigenstate, but is composed out of low lying gas like states, that have an energy spread much smaller than the pair binding energy. For small times one can ignore the energy differences and thus the time dependence of $\bar{\phi}_0$. This results in

$$g^{(2)}(t) \xrightarrow{\gamma\to-\infty} 8\frac{\pi^2}{\gamma^2}\Big[1 - \cos(\omega_2 t)\Big]. \tag{139}$$

This expression describes the initial increase of $g^{(2)}$ as observed in the many-particle calculation (and in the exact solution of the $N = 2$ case) very well. It does predict, however, oscillations with maximum modulation depth, which is not true for the exact solution. The reason for this is that $\bar{\phi}_0$ contains in addition to the dominant, lowest gas-like state (i.e. the super Tonks-Girardeau state) ϕ_- also small admixtures of higher lying gas states which oscillate in time all with slightly different frequencies.

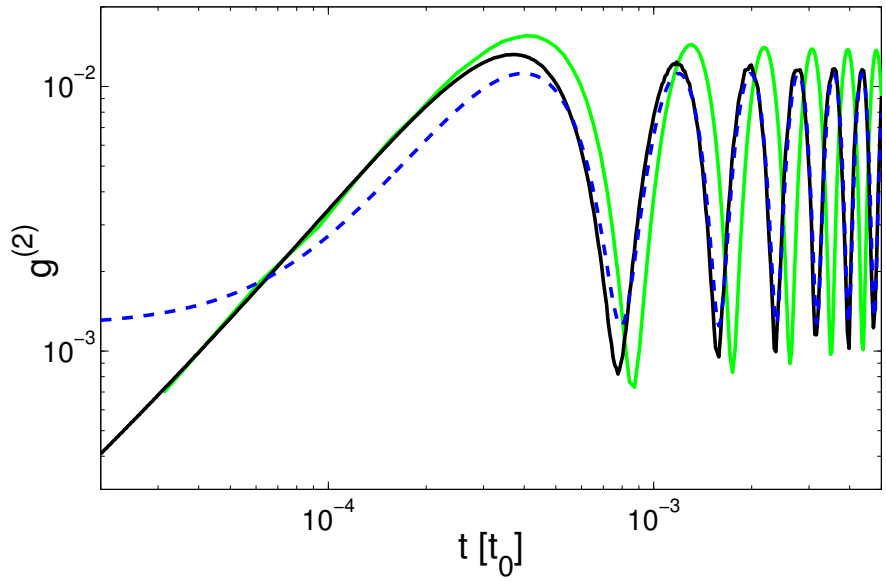

Figure 23: Comparison of the many body results with the results from the two particle system with periodic boundary conditions in the case $\gamma = -89.0355$. The thick black line corresponds to the two particle case, the thin green one shows the $N = 9$ particle case (calculated via TEBD), and the blue dashed one is the beating approximation (140).

For larger times these oscillations lead to an effective dephasing in the interference part of $g^{(2)}$. On the other hand the direct contribution of these excited gas states to $g^{(2)}$ is negligible. An approximation which is much better suited to describe the large time behavior is $|\phi_0\rangle \approx \varepsilon|\phi_\mathrm{b}\rangle + |\phi_-\rangle$. Comparing (136) and (138) shows, that we have only changed a factor of 2 such that

$$g^{(2)}(t) \xrightarrow{\gamma\to-\infty} \left\{5 - 4\cos\left[\left(\omega_2 + \pi^2/t_0\right) t\right]\right\} \frac{\pi^2}{\gamma^2}, \tag{140}$$

where we used that the super Tonks-Girardeau gas energy is $\hbar\pi^2/t_0$ for strong interaction, giving a minor correction to the frequency. On short timescales this expression is invalid, but for $t > t_0/\gamma^2$ it becomes a much better approximation than (139) and is shown in Fig. 23. It is interesting to note that $g^{(2)}$ scales as $1/\gamma^2$, while the pair fraction, i.e. the probability to find particles in a paired state, $\eta = |\epsilon|^2 = 8\pi^2/|\gamma|^3$ scales as $|\gamma|^{-3}$ and is thus more difficult to observe for large $|\gamma|$.

In summary we have shown in this section by numerical TEBD simulations that an interaction quench of a 1D Bose gas from strong repulsive to strong attractive interactions puts the gas predominantly into the lowest gas-like excited state, the super Tonks-Girardeau gas. There is however a small coherent admixture of two-

particle bound states that results in a large amplitude oscillation of the local density-density correlation with a frequency corresponding to the energy difference between super Tonks-Girardeau gas and bound pair state. At the same time higher-order correlations remain extremely small showing that more deeply bound, multi-particle cluster states are not formed in the quench. Analytical calculations of the $N = 2$ case where shown to reproduce the results of the many-particle simulations with high accuracy. This indicates that the many-body state can be well approximated by a Jastrow-Bijl type pair product wave function, where each term is a coherent superposition of a gas-like state with a very small component of a two-particle bound state. The peculiar oscillations of $g^{(2)}$ show furthermore that despite their small weight, the two-particle cluster states are accessible to experimental probes. For strong interactions, the bound pairs are highly co-localized. Since in all physical realizations of the LL model, the true inter particle potential is of finite range, details of the potential will show up in the binding energy. In this way, the two particle correlation dynamics can be used to measure details of the underlying true potential.

In contrast to the quench presented in the preceding section, we do not observe local relaxation here. One possible interpretation is, that the diagonal ensemble (66) contains very few states that contribute to the local $g^{(2)}$, namely the super-Tonks gas and the states that contain bound pairs. Therefore the decoherence, which must be assumed when using the diagonal ensemble, never happens, but coherent oscillations are observed instead. Furthermore it is rather obvious, that the eigenstate thermalization hypothesis must not necessarily hold here, because the spectrum of the attractive Lieb-Liniger gas is rather peculiar. Above the various deeply bound dimers and aggregations of larger particle numbers [TZS08], there are the gas-like states starting at the super-Tonks gas, which have in the strongly interacting limit the same spectrum as free fermions. Therefore the spectrum looks as if the system was close to its ground state and we can not expect the eigenstate thermalization hypothesis to work. Fortunately, the fact that we are working close to an eigenstate turns out to be favorable for the application of the TEBD algorithm, because there is only moderate entanglement produced. The calculations give another example, that the TEBD algorithm is suitable for the simulation of dynamical processes in strongly interacting, continuous quantum gases.

In order to assess whether the effect predicted is accessible in current experiments let us compare the beat frequency $\omega_2 = \gamma^2\hbar\rho^2/4m$ to the transverse trap frequency $\omega_\perp$. Introducing the longitudinal trap frequency $\omega_\parallel$ one finds $\omega_2 = \gamma^2 N\omega_\parallel/4$. For $\gamma \approx 10$ and 10 particles per tube this gives $\omega_2 \approx 250\omega_\parallel$. For the experiment of [HGM+09] this corresponds to about 3kHz which is only a factor of 4 smaller than $\omega_\perp$. Using larger laser beam diameters this factor can be increased however to one

order of magnitude, such that the 1D approximation remains valid[17]. Furthermore our numerics showed that the oscillations with a single dominant frequency ω_2 prevail even for values of γ as low as -1, which would result in a reduction of ω_2 by two orders of magnitude.

[17] E. Haller, private communication

7 Time dependent correlations[18]

The goal of the present section is the exact numerical calculation of the time dependent two-particle correlation function in the Lieb-Liniger model. Such a quantity is now available in experiments via analyzing the temporal correlations in detection events originating from a single position in the cold atomic gas. Explicitly, the quantity of interest is the time and normal ordered two-particle correlation function

$$g^{(2)}(\xi = x - x_0, \tau = t - t_0) = \frac{\langle \hat{\Psi}^\dagger_{t_0}(x_0)\hat{\Psi}^\dagger_t(x)\hat{\Psi}_t(x)\hat{\Psi}_{t_0}(x_0)\rangle}{\langle \hat{\Psi}^\dagger_{t_0}(x_0)\hat{\Psi}_{t_0}(x_0)\rangle\langle \hat{\Psi}^\dagger_t(x)\hat{\Psi}_t(x)\rangle}. \tag{141}$$

Due to repulsive interactions, its value is smaller then 1 for small ξ and τ and approaches the value 1 (no correlation), for $\xi \gg 1/\rho$ or $\tau \gg 2/\rho^2\pi^2 = 1/\omega_{\mathrm{F}}$ (the latter is because the typical energy scale of the system is given by the Fermi energy at not too small γ). Although similar to the two particle correlation function of the preceding sections, this is not a dynamically evolving quantity in the sense that the system as a whole would be out of equilibrium. (The combination of operators at different times does not allow to swap the time-dependence to the state here. The index of the field operators gives the time in the Heisenberg picture.) The expectation values are rather taken in a steady state. (We will restrict the discussion to a low temperature ensemble below quantum criticality, respectively the ground state itself). The dependence on only the differences ξ and τ assumes a homogeneous system in the thermodynamic limit. Correspondingly the densities entering the denominator for normalization are equal to the constant density ρ.

Recent technological developments [WLG+09, BGP+09, BPT+10, SWE+10, WES+11] allow for detection and manipulation of cold atoms with a spatial resolution of a single lattice site, or respectively well below the average particle distance in the continuous case. A method using an ionizing electron beam in a scanning electron microscope setup has been pioneered in the group of H. Ott [GUHO06, WGL+09]. The scheme is depicted in Fig. 24 (left): The trapped ^{87}Rb gas can be cooled to form a Bose-Einstein condensate. An electron beam is focused on the cloud, which ionizes atoms at a well controlled position. The ions are pulled out of the cloud by an electric field and detected by a channeltron detector. Due to the high sensitivity of the detector, one has single atom efficiency. By scanning the beam over the cloud, particle positions can be resolved with uncertainty much below the average inter-particle distance. Complementary, by focusing the beam on a fixed position, the point of ionization in time can be reconstructed from the arrival time at the detector [GWE+11]. In [GWE+11],

[18] Results of this section are available together with measurements from a recent cold atoms experiment in the preprint[GML+12].

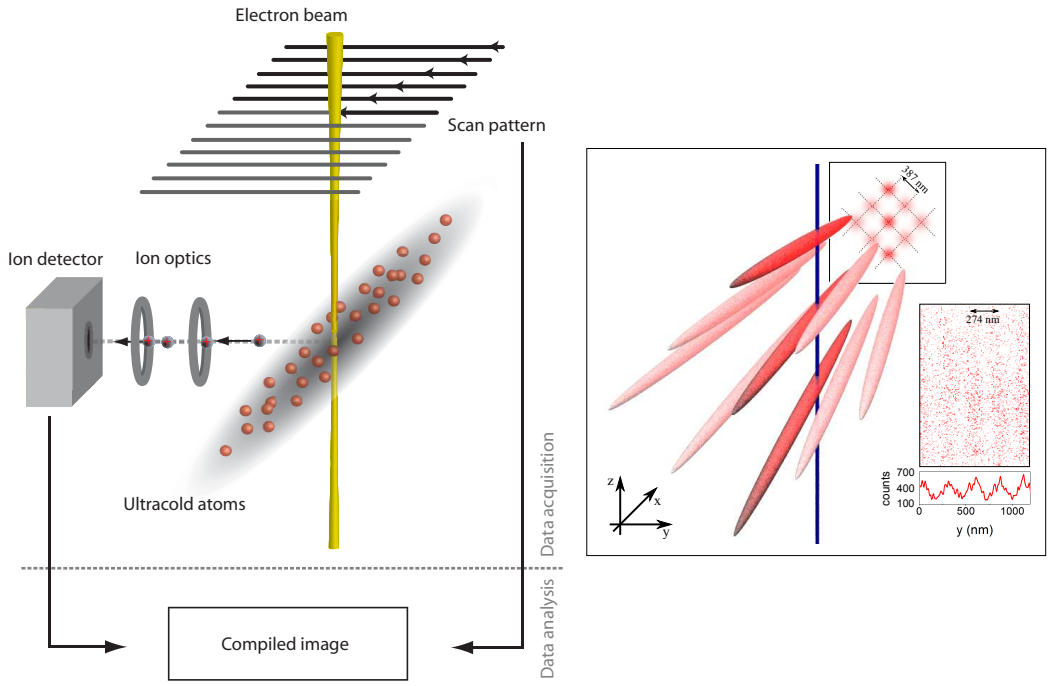

Figure 24: Scheme of the experimental setup. Left: General setup. (Picture taken from [WGL+09]) The scanning of the electron beam is used to measure the global density distribution. Right: To measure time-dependent calculations, an additional optical lattice is imposed on the gas, and the beam is fixed to the central position, intersecting a number of quasi one-dimensional tubes. (Picture taken from [GML+12])

temporal bunching in a three-dimensional rubidium gas has been observed, when heated above the critical temperature of the Bose-Einstein transition. Using an additional optical lattice, see Fig. 24 (right), the experiment can be conducted in the one-dimensional, Lieb-Liniger regime [GML+12], and gives access to time-dependent correlations. The quantity extracted is the correlation in the arrival times of the ions at the detector. It is equivalent to $g^{(2)}(\xi, \tau)$, while for the time being only correlations at the same position, $\xi = 0$, are accessible in the experiment. Additionally one has to take into account, that due to technical limitations of the setup, the electron beam always intersects a row of 8 to 11 one-dimensional systems, each in the shape of an elongated tube, simultaneously. This reduces the overall contrast and requires a suitably weighted average over the single systems, which feature a different density and different Tonks-parameter each.

In the following we will provide calculations of $g^{(2)}(\xi, \tau)$ in the ground state.

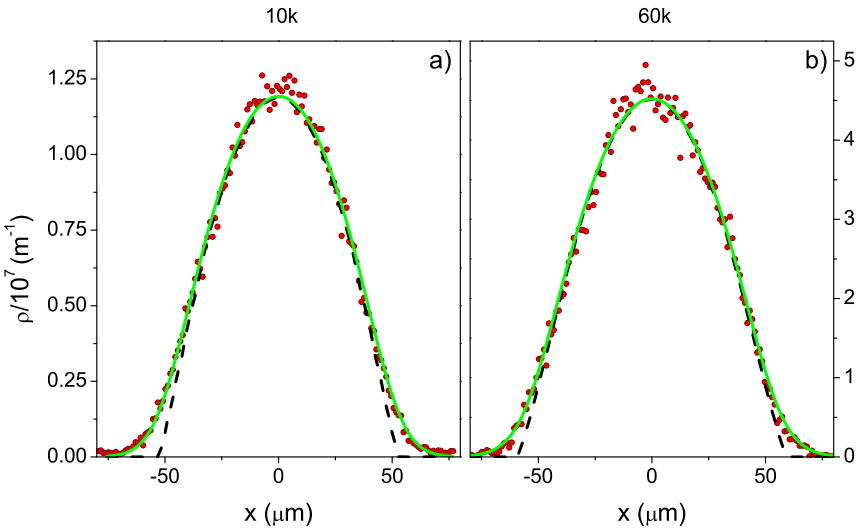

Figure 25: Local density distribution (averaged over all tubes that intersect with the electron beam) measured in the experiment (symbols), compared to a fit using the Yang-Yang solution [YY69] in linear density approximation (green continuous lines). The experiment is performed with two different total numbers of particles: $9.3 \pm 0.7 \cdot 10^3$ ("10k", a) respectively $52 \pm 5 \cdot 10^3$ ("60k", b). The fit yields temperatures well below the degeneracy temperature, such that the results coincide with the zero temperature profile (dashed line), except at the edges of the system, where the degeneracy temperature is small, and the gas is in the high-temperature, non-degenerate regime.

This is sufficient for a comparison to the experiment, because the temperatures are very low there. This was checked by fitting a density profile, calculated using the thermodynamical Bethe ansatz [YY69] and local density approximation, to the measured density profile of the gas [GML+12]. This yields a temperature that confirms that the relevant part of the system, around the center, is well below the degeneracy temperature $T_\mathrm{d} = \rho^2/2$, see Fig. 25. The smallness of the effect of the finite temperature can be seen in $g^{(2)}(0)$, which we calculate from the Hellmann-Feynman theorem [KGDS03] and which differs at most by 1% (for the interaction strength given) between the observed temperature and $T = 0$.

The dynamical density-density correlation function $\sim \langle \hat{\Psi}_t^\dagger \hat{\Psi}_t \hat{\Psi}_{t_0}^\dagger \hat{\Psi}_{t_0} \rangle$ in the Lieb-Liniger model has been calculated from the Bethe ansatz solution [CC06]. However it differs from the correlation function considered here, because it is not time and normal ordered. There is no simple relation between the two, because the commutator between field operators is non-trivial (it contains essentially all the dynamics of the system), and we have to employ an independent calculation.

The numerical procedure will only involve the propagation of quantum states, not

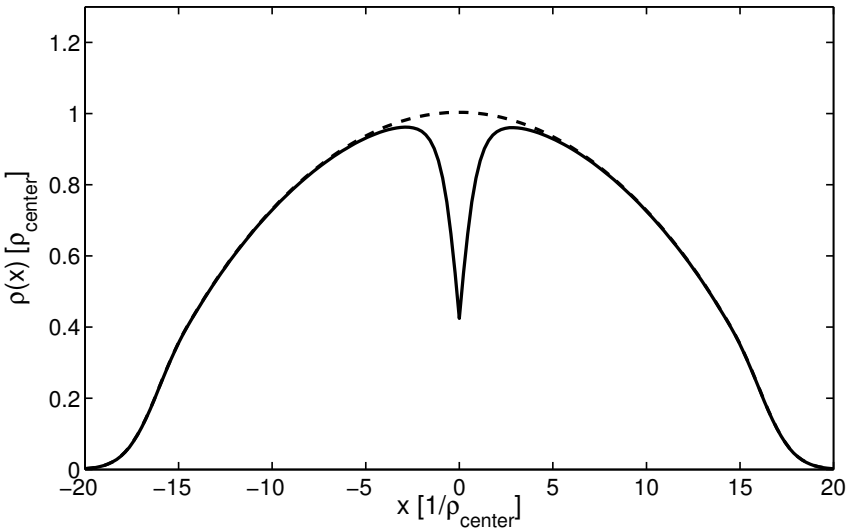

Figure 26: Local density in initial state, $\langle\hat{\Psi}(x_0 = 0)|\hat{\rho}(x)|\hat{\Psi}(x_0 = 0)\rangle$ (continuous line), and in the ground state, $\langle 0|\hat{\rho}(x)|0\rangle$, for comparison (dashed line). ($\gamma = 1.3944$, 25 particles in harmonic trap, generated using imaginary time evolution via TEBD, see also Fig. 8.)

of the field operators. We start with the ground state $|0\rangle$. We apply the field operator at position x_0 and get the state $|\hat{\Psi}(x_0)\rangle = \hat{\Psi}(x_0)|0\rangle$. The correlation function may now be written

$$\begin{aligned} g^{(2)}(\xi,\tau) &= \frac{1}{\rho^2}\langle\hat{\Psi}(x_0)|\hat{\Psi}^\dagger_{t-t_0}(x)\hat{\Psi}_{t-t_0}(x)|\hat{\Psi}(x_0)\rangle \\ &= \frac{1}{\rho^2}\langle\hat{\Psi}(x_0)|\hat{U}^\dagger_{t-t_0}\hat{\rho}(x)\hat{U}_{t-t_0}|\hat{\Psi}(x_0)\rangle \end{aligned} \tag{142}$$

The second form shows, that we can shift the time dependence to the state $|\hat{\Psi}(x_0)\rangle$ instead of propagating the field operators. $g^{(2)}(\xi,\tau)$ is thus equal to the local density at position x in the evolved state $|\hat{\Psi}(x_0)\rangle_{t-t_0} = \hat{U}_{t-t_0}|\hat{\Psi}(x_0)\rangle$. This can be interpreted as follows: At $t = t_0$ a particle is removed from the system, see Fig. 26, corresponding to a detection event in the experiment. The probability to detect another particle is proportional to the local density at the given position, which is time dependent, because the removal of the first particle excites the system.

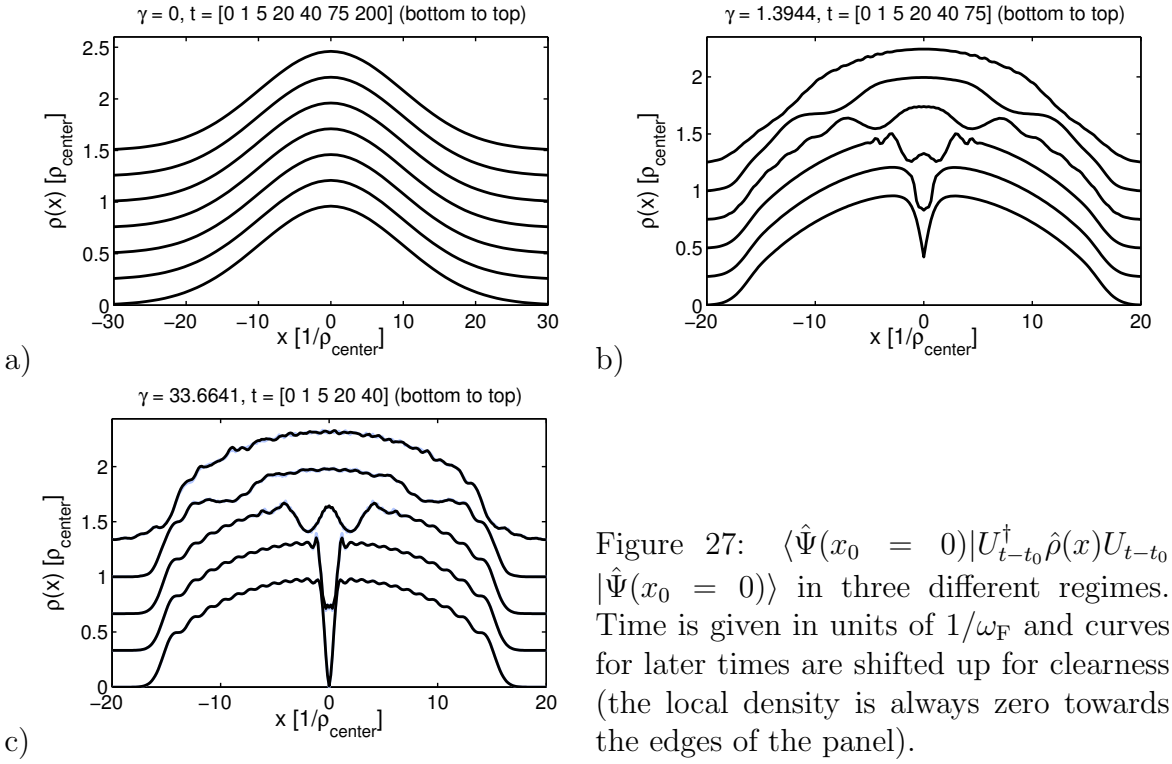

Figure 27: $\langle\hat{\Psi}(x_0 = 0)|U^\dagger_{t-t_0}\hat{\rho}(x)U_{t-t_0}|\hat{\Psi}(x_0 = 0)\rangle$ in three different regimes. Time is given in units of $1/\omega_\mathrm{F}$ and curves for later times are shifted up for clearness (the local density is always zero towards the edges of the panel).

7.1 TEBD numerics

We calculate $g^{(2)}(\xi,\tau)$ numerically using TEBD in the following way: The ground state is calculated for $N = 25$ particles in a harmonic trap as in section 3.5, using a sufficiently small discretization length Δx (and the discretization formula (89), which maps the system to the Bose-Hubbard model). It will turn out, that this system size is large enough, such that finite size effects are not influencing the dynamics on time scales relevant for $g^{(2)}(\xi,\tau)$ at the center of the trap. We can thus identify the results with those of the thermodynamic limit, using the same density as in the center of trap at $x_0 = 0$. In the next step, we prepare $|\hat{\Psi}(x_0 = 0)\rangle$ by acting with the discretized version, $\hat{\Psi}(0) \approx \hat{a}_0/\sqrt{\Delta x}$, on the ground state, see Fig. 26. This is a local operation, which can be easily implemented for MPS. Finally, we evolve the the resulting state, which contains exactly $N-1$ particles, in time. We get $U_{t-t_0}|\hat{\Psi}(x_0 = 0)\rangle$ and calculate the correlation function from the expectation value of the local density

$$g^{(2)}(\xi,\tau) = \frac{1}{\rho^2}\left(\langle\hat{\Psi}(x_0 = 0)|U^\dagger_{t-t_0}\right)\hat{\rho}(x)\left(U_{t-t_0}|\hat{\Psi}(x_0 = 0)\rangle\right). \tag{143}$$

In Fig. 27 we show this density dynamics of the initial state.

The evolution of $g^{(2)}(\xi,\tau)$ is shown in Fig. 27 for different interaction strength. Starting with the uncorrelated state for free bosons, $g^{(2)}(\xi,\tau) = 1 = \text{const.}$ and we

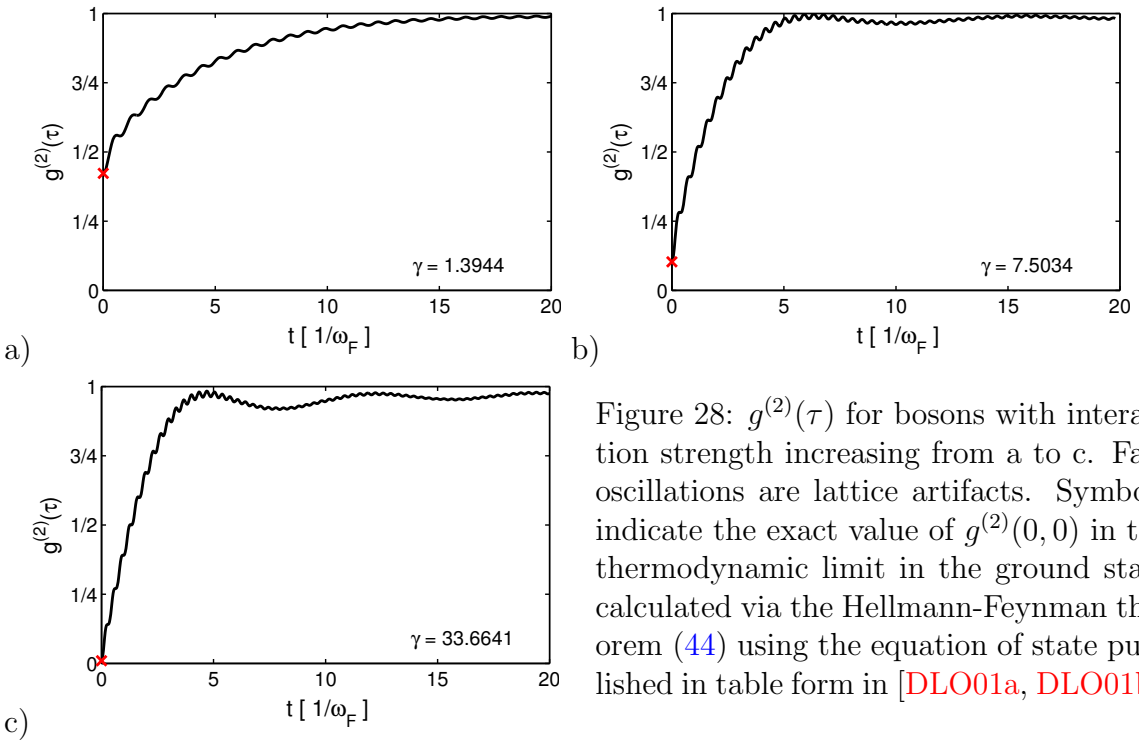

Figure 28: $g^{(2)}(\tau)$ for bosons with interaction strength increasing from a to c. Fast oscillations are lattice artifacts. Symbols indicate the exact value of $g^{(2)}(0,0)$ in the thermodynamic limit in the ground state calculated via the Hellmann-Feynman theorem (44) using the equation of state published in table form in [DLO01a, DLO01b].

see no structure at all. For increasing interaction strength it develops a minimum at $\xi = \tau = 0$ that approaches zero with γ becoming large [LL63]. The dynamics happens on a timescale of $1/\omega_{\mathrm{F}}$. The spatial extension of the hole is initially of the order $1/\rho$ and spreads in the following. The local correlation function $g^{(2)}(\tau)$ is shown in Fig. 28 for different Tonks-parameters. (We will skip the spatial dependence whenever $\xi = 0$.) For higher Tonks parameters, Friedel oscillations are visible, before the function approaches 1 and the particles (and therefore the detection events in the experiment) become uncorrelated. The fast oscillations are a discretization artifacts due to the finite Δx between $1/5\rho$ and $1/7\rho$ for the data shown.

The TEBD calculations presented in this section are actually numerically quite inexpensive. This is because the initial state $|\hat{\Psi}(x_0)\rangle$ is close to an eigenstate, in the sense that they deviate from it only in a small region. We thus expect to have a small number of excitations in the system. This is reflected in the fact, that a bond dimension of $\chi = 50$ was sufficient to generate converged results for all data shown.

7.2 Adaptions to the experimental situation

7.2.1 Finite beam width

In the experiment [GWE+11, GML+12] the detection beam is never perfectly focused, but has a finite width of a fraction of $1/\rho$. The measured correlation function is

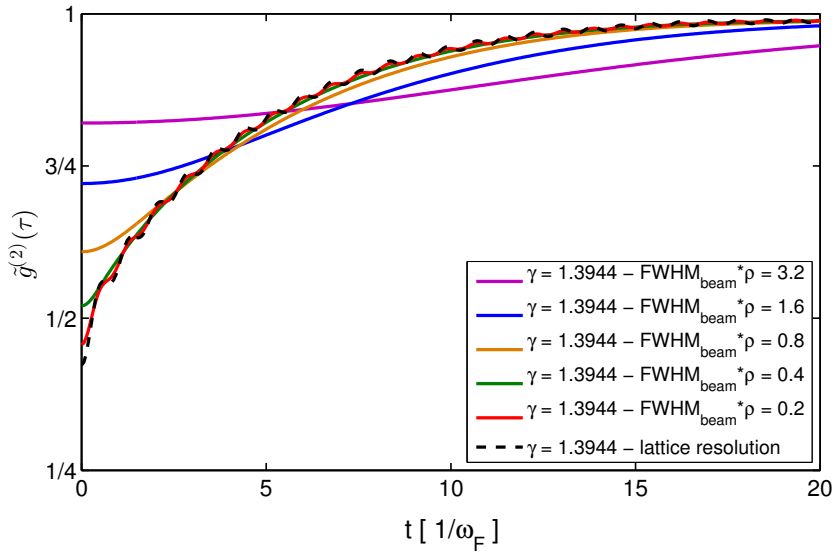

Figure 29: Dependence of $\tilde{g}^{(2)}(\tau)$ on the width $\mathrm{FWHM}_{\mathrm{beam}}$ of the electron beam.

therefore somewhat smeared out. This can be taken into account by

$$\tilde{g}^{(2)}(\tau) = \int_{-\infty}^{\infty} \mathrm{d}x \; W(x) \; \langle \hat{\Psi}(x_0 = 0) | \hat{U}^{\dagger}_{t-t_0} \hat{\rho}(x) \hat{U}_{t-t_0} | \hat{\Psi}(x_0 = 0) \rangle, \tag{144}$$

where $W(x)$ is the normalized Gaussian weighting function

$$W(x) = \frac{\sqrt{2}}{\mathrm{FWHM}_{\mathrm{beam}}} \cdot \sqrt{\frac{\log 2}{\pi}} \cdot 2^{-2\left(\frac{x}{\mathrm{FWHM}_{\mathrm{beam}}}\right)^2}, \tag{145}$$

as shown in Fig. 29 for different width of the beam. Note that the full width (full width half maximum) of $W(x)$ is actually $\sqrt{2}$ times the full width $\mathrm{FWHM}_{\mathrm{beam}}$ of the beam, because both the position of the first and the second particle detected have this uncertainty. In the experiment the beam width is of the order $\mathrm{FWHM}_{\mathrm{beam}} \approx 1/3\rho$. This is larger than the numerical discretization length used. We see from the figure, that consequently the lattice artifacts are concealed. Otherwise the curve is not changed, except for the value at $\tau = 0$ which is most sensitive to the beam width. Only at larger $\mathrm{FWHM}_{\mathrm{beam}}$, which was not used in the experiment, deformations occur. The finite width of the beam, will be taken into account when comparing to the experiment.

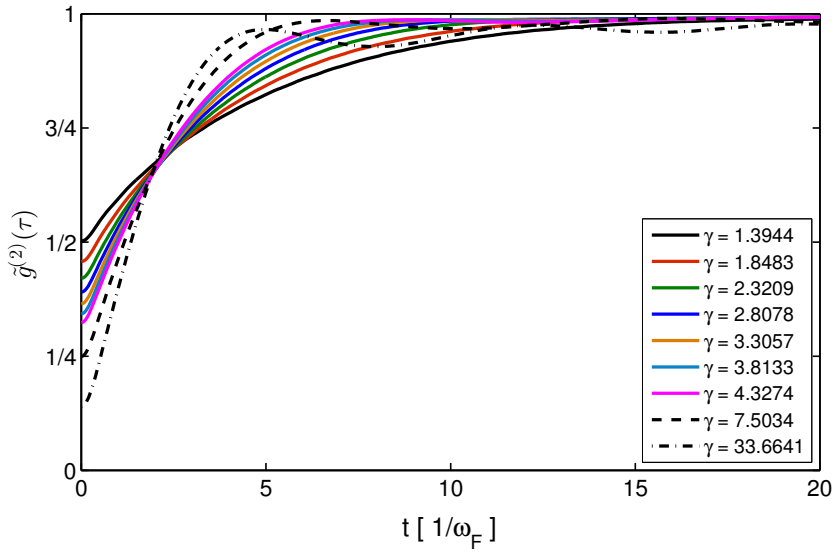

Figure 30: $\tilde{g}^{(2)}(\tau)$ for finite beam width $\mathrm{FWHM}_{\mathrm{beam}} = 1/3\rho$ in the intermediate regime of interactions, as used for comparison with experimental data.

7.2.2 Varying Tonks parameter

As mentioned above, the experiment averages over several independent systems with varying interaction strength. We generate sets of correlation functions for various values of γ. One is shown in Fig. 30 for $\mathrm{FWHM}_{\mathrm{beam}} = 1/3\rho$ and γ in the range of 1.4 to 4.3.

7.2.3 More than two detection events

In the experiment, the system is continuously exposed to the ionizing beam in order to acquire a sufficient number of ionization events to extract correlations. In fact the experiment has to be repeated several thousand times, among other reasons because each ionization event reduces the number of particles in the system, and this depletion must not become noticeable. The correlations between detection events does not distinguish between events that directly follow each other and those with other events in between. Thus, assuming that the system is always in equilibrium when the first particle (of a pair that contributes to the correlation) is detected, is not strictly fulfilled. To estimate the effect of a third detection event, we calculate one of the extreme cases: The fact, that the system is not back to the ground state locally for every measurement will lead to contributions of the form

$$\left\langle \hat{\Psi}^\dagger(t_0)\hat{\Psi}^\dagger(t_0)\hat{\Psi}^\dagger(t)\hat{\Psi}(t)\hat{\Psi}(t_0)\hat{\Psi}(t_0) \right\rangle \tag{146}$$

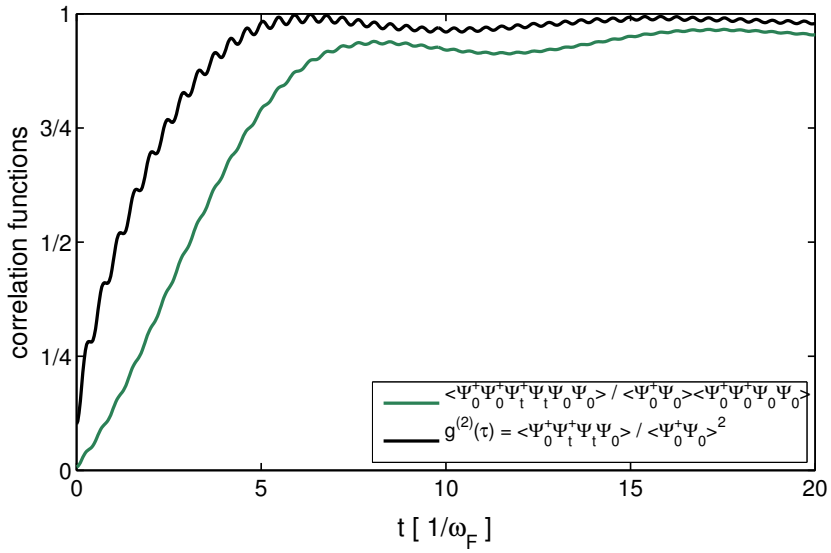

Figure 31: Comparison of $g^{(2)}(\tau)$ to higher correlation functions which contribute as minor corrections to the detection statistics ($\gamma = 7.5034$ here).

to the correlations in the detection events. We can see from Fig. 31, that even for this extreme case, the relaxation of the correlation is only somewhat slower than that of $g^{(2)}(\tau)$. It's contribution to the overall result will also be small, because three events close together are very rare: The average time between detection events is much longer than $1/\omega_{\mathrm{F}}$, such that the anti-bunching can be seen only in the rare pairs of events with small temporal separation. Three events close together are therefore even more rarely observed. (The data acquired are not sufficient to extract meaningful third order correlations.) Accordingly, we will not take into account corrections arising from more than two detection events in the comparison to the experiment.

7.2.4 Local depletion

The presence of the electron beam leads to a significant reduction of the total particle density around its center [Gua] in the experiment. This effect can be taken into account by assuming that the local potential for the particles is the harmonic trapping potential plus a repulsive potential at the position (the trap center at $x_0 = 0$) and with the width of the electron beam, which has a Gaussian profile. Its strength can be adjusted, such that the reduction of the particle density at this position is comparable to that in the experiment. Fig. 32a shows the particle density around the hole, both for the ground state of the resulting potential, as well as after the application of $\hat{\Psi}(x_0 = 0)$, i.e. after the detection of a particle at the trap center, for

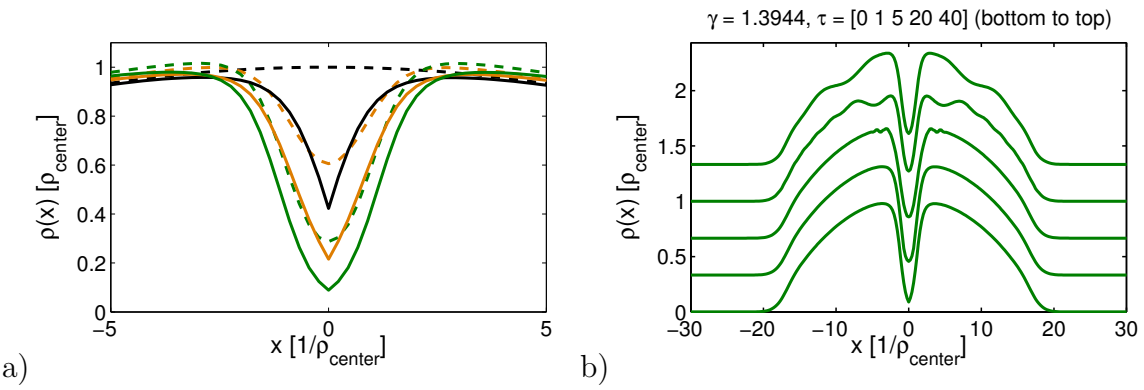

Figure 32: a) Ground state $|0\rangle$ (broken lines) and initial state $|\hat{\Psi}(x_0 = 0)\rangle$ (continuous lines) local density for pure harmonic confinement (black), weak (green) and stronger (blue) Gaussian local potential of FWHM $1/3\rho$. In all cases $\gamma \approx 1.3944$ taking not the local density inside the hole, but in the center of the ground state with only the harmonic confinement as a reference (which is very close to the density surrounding the hole). b) $\langle\hat{\Psi}(x_0 = 0)|U^{\dagger}_{t-t_0}\hat{\rho}(x)U_{t-t_0}|\hat{\Psi}(x_0 = 0)\rangle$ as in Fig. 27 for the stronger case.

two different strength of the local potential imposed by the electron beam. Fig. 32b additionally shows $\langle\hat{\Psi}(x_0 = 0)|\hat{\rho}_{t-t_0}(x)|\hat{\Psi}(x_0 = 0)\rangle$. The behavior is similar to that of the quasi homogeneous case: The density modulations excited by the first detection event propagate away from the center and the density around the electron beam goes back to its ground state value, i.e., the dashed curve in part a of the figure. The propagation is through the region surrounding the beam, which has higher density. This explains, why the time scale is again given by the properties of the region surrounding the beam, i.e. it remains to a large extend unchanged.

Although the beam strongly deforms the local density distribution of the ground state, $g^{(2)}(\tau)$ is only weakly affected, see Fig. 33. Taking the density outside the hole created by the beam as a reference in the definition of ω_{F} and γ one gets a result surprisingly similar to the quasi-homogeneous calculation. We will therefore not take the local depletion into account when comparing to the experiment.

7.2.5 Average over multiple systems

In the experiment the electron beam intersects a number M of independent, and therefore uncorrelated systems, which is of the order 10. The detector is unable to discriminate the origin of the ions. Accordingly the anti-bunching signal in the averaged correlation function $g^{(2)}_{\mathrm{av}}(\tau)$ will be reduced compared to the bare $\tilde{g}^{(2)}(\tau)$ for a single system. The individual systems are not equivalent, but have different density

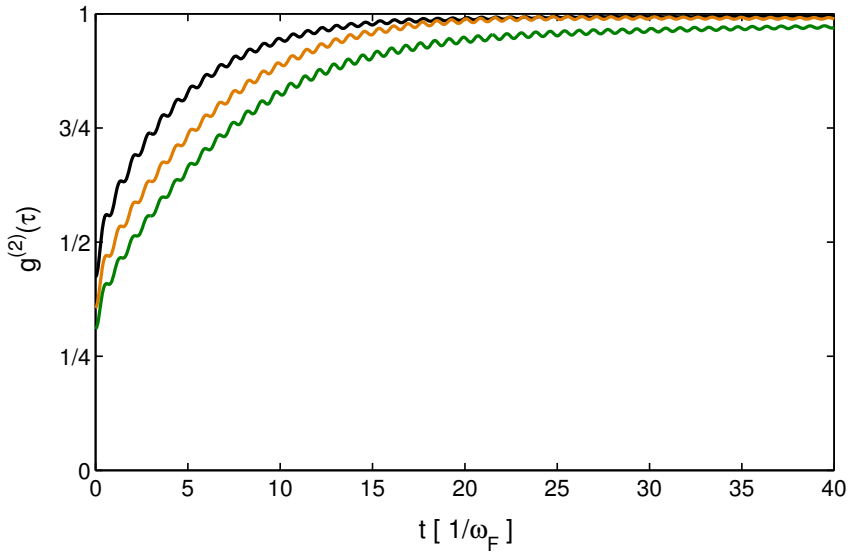

Figure 33: $g^{(2)}(\tau)$ for the three cases shown in Fig. 32. $\gamma \approx 1.3944$ taking not the local density inside the hole, but in the center of the ground state with only the harmonic confinement as a reference (which is very close to the density surrounding the hole). This density also enters in ω_{F}.

ρ_j at $x_0 = 0$, such that the probability for a detected ion to originate from tube j is $p_j = \rho_j/\rho_{\mathrm{tot}}$ with the summed density $\rho_{\mathrm{tot}} = \sum_j \rho_j$. Although the bare interaction strength g can be assumed to be the same in every tube, this results in individually different Tonks parameters and therefore different $\tilde{g}_j^{(2)}(\tau)$. The averaged correlation function is therefore

$$\begin{aligned} g_{\mathrm{av}}^{(2)}(\tau) &= \sum_{i,j=1}^{M} p_i p_j \left(\delta_{i,j}\tilde{g}_j^{(2)}(\tau) + (1-\delta_{i,j})\right) \\ &= 1 - \sum_{j=1}^{M} p_j^2 \left(1 - \tilde{g}_j^{(2)}(\tau)\right). \end{aligned} \tag{147}$$

For example if the tubes were equivalent and the anti-bunching perfect ($\tilde{g}_j^{(2)}(\tau) = 0$), the result would be $g_{\mathrm{av}}^{(2)}(\tau) = 1 - 1/M$, i.e., the contrast in the anti-bunching would be reduced only by a factor of $1/M$. Formula (147) will be used in the comparison to the experimental data below.

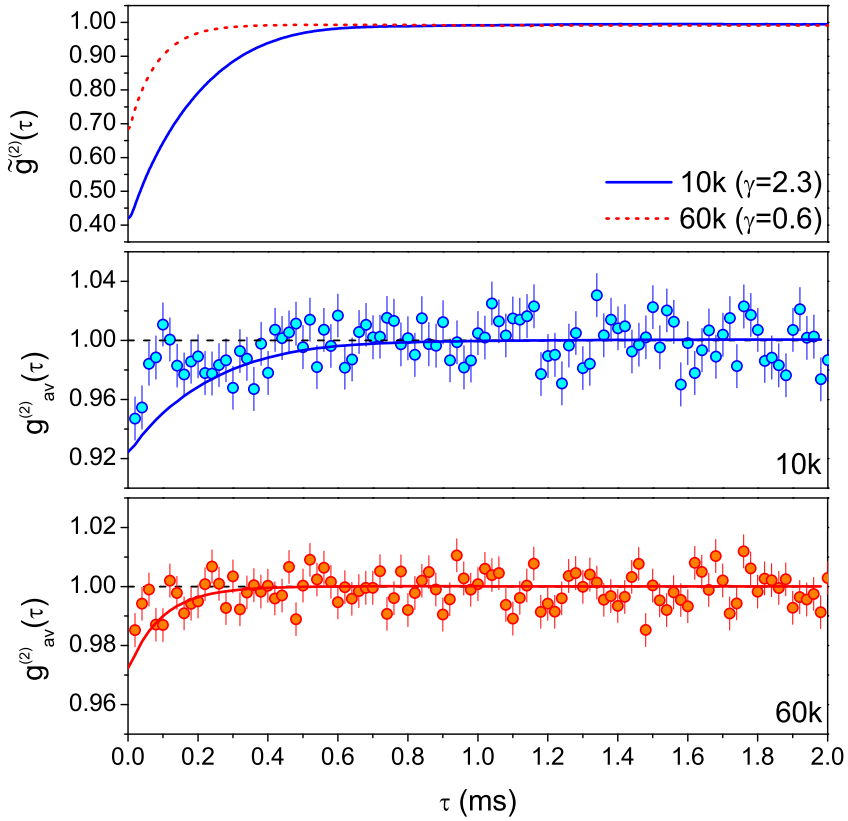

Figure 34: Comparison between theoretical prediction and experimental measurement of two-particle correlations for two experiments with different total particle number (see text). Top panel: Calculated $\tilde{g}^{(2)}(\tau)$ at the trap center for the central tube (which contributes the most and has lowest γ), including the finite width $\mathrm{FWHM}_{\mathrm{beam}} = 1/3\rho$ of the beam. Middle and lower panel: Average $g^{(2)}_{\mathrm{av}}(\tau)$ (147) of the calculated curves (continuous lines) and correlations extracted from the detection events (error-bars).

7.3 Comparison to experimental data

The experiment is performed with two different total numbers of particles: $9.3 \pm 0.7 \cdot 10^3$ ("10k") respectively $52 \pm 5 \cdot 10^3$ ("60k"). This results in different timescales due to different linear density, different total number of tubes ($M = 8$ respectively $M = 11$) and different Tonks parameter ($\gamma = 2.3$ respectively $\gamma = 0.6$ in the central tube). To apply formula (147), various curves for different values of γ have been calculated, such that $\tilde{g}^{(2)}_j(\tau)$ is available for every tube by means of interpolation. The result is shown in Fig. 34: As expected, the anti-bunching is strongly reduced (6% respectively 2%), in spite of the relatively high γ-values, due to the averaging. The statistical errors in the experimental results are quite large. Within this limit, the agreement is quite satisfying, and both the amplitude and the timescale of the

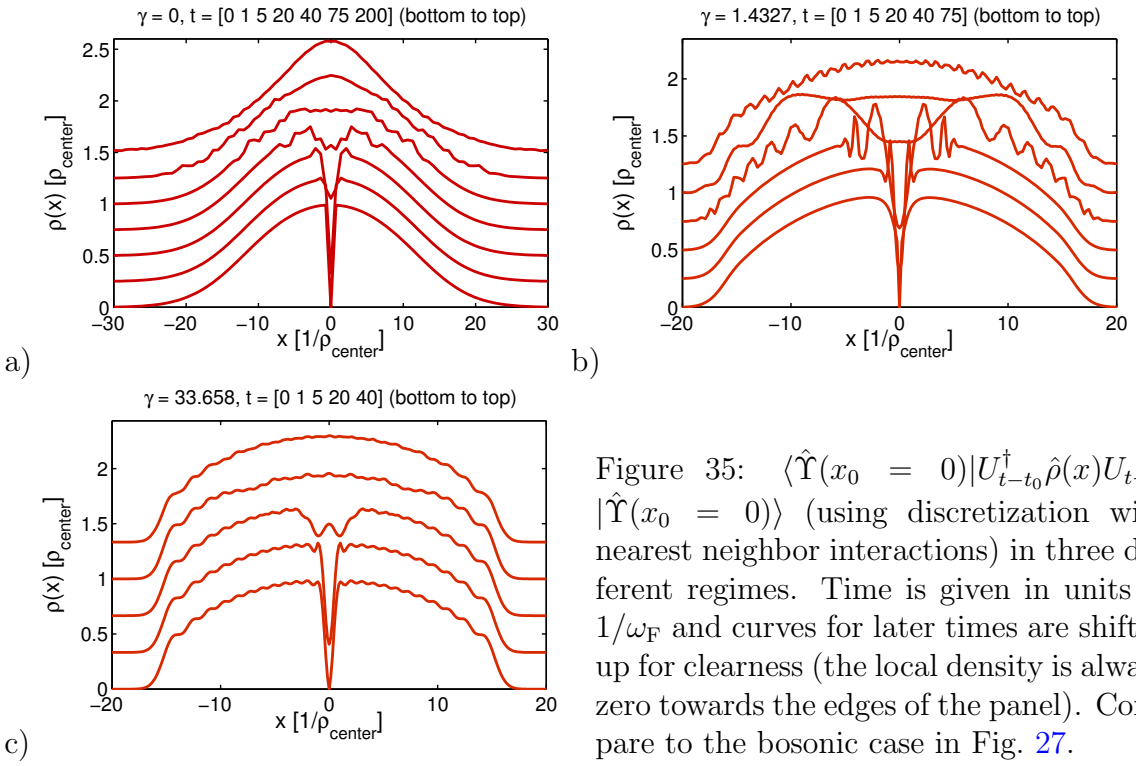

Figure 35: $\langle\hat{\Upsilon}(x_0 = 0)|U^\dagger_{t-t_0}\hat{\rho}(x)U_{t-t_0}|\hat{\Upsilon}(x_0 = 0)\rangle$ (using discretization with nearest neighbor interactions) in three different regimes. Time is given in units of $1/\omega_F$ and curves for later times are shifted up for clearness (the local density is always zero towards the edges of the panel). Compare to the bosonic case in Fig. 27.

correlations are reproduced correctly.

7.4 Dependence on particle statistics

In contrast to the correlation functions of sections 5 and 6, $g^{(2)}(\xi,\tau)$ is sensitive to the statistics of the particles. The above results are only valid for bosons, such as the rubidium atoms used in the experiment. Replacing $\hat{\Psi}$ by $\hat{\Upsilon}$ (21) and using the fermionic Hamiltonian with the corresponding interaction strength (55) does not yield the same correlation function. Thus an experiment should in principle also be able to detect the difference between bosons and spin polarized fermions. This is because $|\hat{\Psi}(x_0)\rangle = \hat{\Psi}(x_0)|0\rangle$ and $|\hat{\Upsilon}(x_0)\rangle = \hat{\Upsilon}(x_0)|0\rangle$ are not the same state, and do not yield the same local density $\langle\hat{\rho(x)}(\tau)\rangle$, except for $\tau = 0$, see Fig. 35 (compare to Fig. 27).

The propagation of the excitation is different for bosons and fermions and in the different regimes of the interaction strength. This becomes most obvious at $\gamma = 0$: For free bosons, applying $\hat{\Psi}$ to the coherent ground state again produces an eigenstate, the ground state for $N-1$ particles, so there is no time dependence. In contrast applying $\hat{\Upsilon}$ to the $\gamma = 0$ ground state (the Fermi-Tonks gas) introduces a pronounced hole[19],

[19] In fact the resulting density must be the same, regardless of whether we eliminate a boson or a fermion, except at the singular point $x = x_0$. The fact that it is visible in Fig. 35a is truly a lattice artifact. The resulting state must contain excitations not because of the discontinuity,

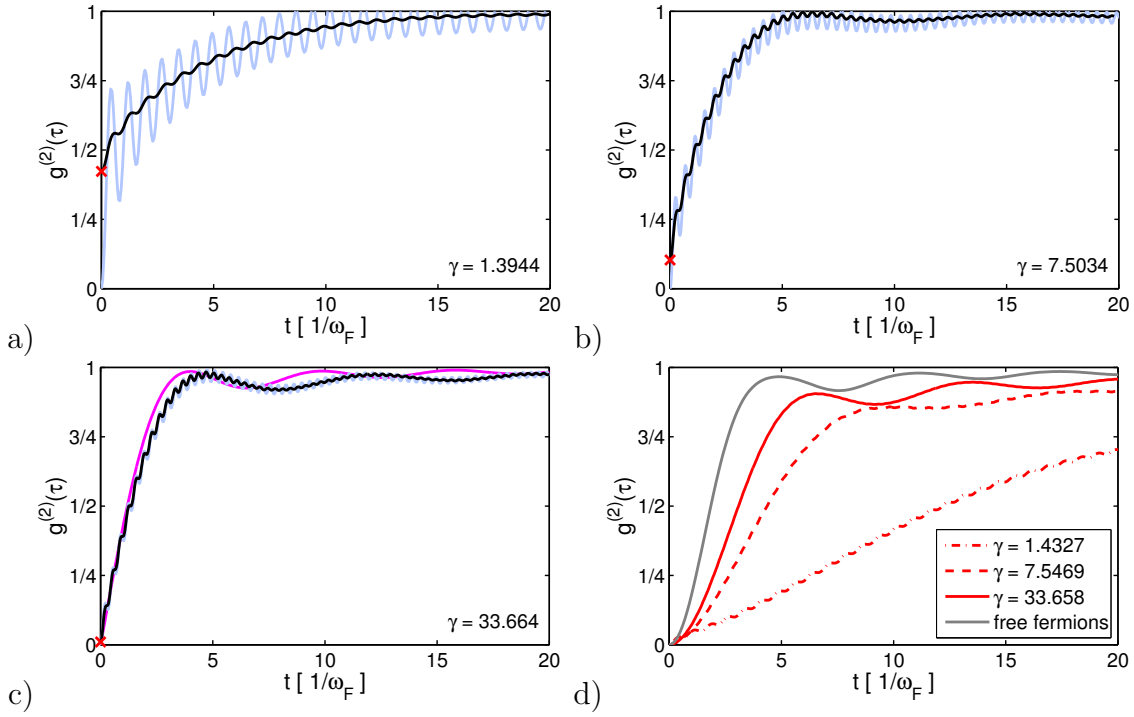

Figure 36: $g^{(2)}(\tau)$ for bosons (a-c) and fermions (d). Fast oscillations are lattice artifacts. For bosons, nearest neighbor interactions (black) produce less pronounced artifacts than discretization via hard core bosons with nearest neighbor interaction (blue). The purple curve in (c) shows the analytic result for the Tonks gas [Ima12] for comparison. The gray curve in (d) shows the analytic result for free fermions for comparison. Symbols as in Fig. 28.

see Fig. 35a. In the Tonks regime the dynamics will also be very different depending on statistics. One reason for this is the very different momentum distribution for the two particle types, see Fig. 3: While $\hat{\Upsilon}$ can only create excitations up to the Fermi energy (for the lack of higher momenta being present in the ground state), this is not true for $\hat{\Psi}$.

The evolution of $g^{(2)}(\tau)$ is shown in Fig. 36. There is the expected large difference between bosons and fermions. As γ is increased, the fermionic correlation function approaches that of free fermions, (259), calculated analytically in appendix F, while the bosonic correlation function approaches that of the Tonks gas [Ima12].

Numerically, both for bosons and fermions one has the choice of using either the bosonic discretization, i.e. on-site interactions, or the fermionic discretization, i.e. hard core particles with nearest neighbor interactions. For ground state calculations

but because of the alternating phases imposed on even respectively odd particle numbers by the fermionic annihilator (21).

we have seen in section 3 that both work equally well. For the dynamical problem discussed here, using the "wrong" discretization of the interaction introduces stronger artifacts. For fermions this is understandable, because the annihilation operator $\hat{\Upsilon}$ is ill defined for more than two particles at the same position (which has finite probability in the ground state calculated from the bosonically discretized interaction). We find that the lattice artifacts are smallest for bosons too, if we use the "canonical" on-site interactions. Fig. 36 shows both for comparison.

Finally note, that in contrast to $g^{(2)}(\xi, \tau)$, the dynamical density-density correlation [CC06] is insensitive to the statistics of the particles.

In conclusion, we have demonstrated in this section, that exact numerical calculations of time dependent correlation functions at zero temperature can be done quite efficiently using TEBD. We have successfully adapted the technique to the situation present in current experiments using ultracold atoms in optical lattices and scanning electron microscopy. The comparison is reasonable within the limits given by the statistical errors in the experimental data. Interestingly, the strong repulsive potential of the electron beam does not introduce as large a deterioration of the measurable correlations from the behavior of homogeneous gas as one might expect. This is because all locally created excitations have to be transported through the surrounding and more dense medium, which is not affected by the repulsion of the beam.

8 Dynamics and evaporation of defects in Mott-insulating clusters of boson pairs[20]

Petrosyan et al. [PSAF07] have studied the many-body dynamics of the repulsively bound dimers of bosons. Due to virtual transitions of the dimer constituent particles, the dimers at neighboring lattice sites strongly attract each other, with the corresponding interaction energy exceeding the dimer tunneling energy by a factor of 4, see section 1.1.2. For multiple dimers on the lattice, it is then energetically favorable to form dynamically stable "droplets", constituting incompressible Mott-insulating clusters with the number of particles per site of exactly $n = 2$. Inevitable imperfections in the preparation process would typically cause such Mott-insulating clusters to contain hole and particle defects corresponding, respectively, to unpaired and excess particles (monomers and trimers). An important question is thus how to purify the system reducing thereby the entropy. In the present section, we discuss a mechanism of self-purification of stable Mott-insulating clusters of dimers surrounded by lattice vacuum. We study the dynamics of defects in a one-dimensional system by analytical calculations and numerical TEBD simulations.

This section is organized as follows: In subsection 8.1 we outline the properties of the pure dimer clusters [PSAF07] and the different types of defects, which display different dynamical properties, see Figure 37. We then introduce in subsection 8.2 an effective theory of scattering of a single particle (hole defect) from a domain wall separating the dimer cluster and the vacuum. The momentum redistribution of a hole defect upon collisions with a particle defect in the lattice with periodic and open boundaries is studied in subsection 8.3. In subsection 8.4 we present the results of many-body numerical simulations for a realistic system with several hole and particle defects in a dimer cluster surrounded by empty lattice. Finally, in subsection 8.5 we discuss the case of two bosonic species, which is more flexible theoretically, but is demanding experimentally. In the limit of infinite intra-species interaction, it contains the special case of the Hubbard model [HMMR+09], since in one-dimension and in the absence of double occupancy, bosons and fermions are equivalent through the Jordan-Wigner transformation. Much of the involved technical details are deferred to Appendices B, C, D and E.

8.1 Clusters of repulsively bound dimers

Throughout this paper, we assume that the on-site interaction is the dominant energy parameter, $U \gg J$. In this regime, the dimers are described by the Hamiltonian (see

[20] This section is based on the publication [MPF12].

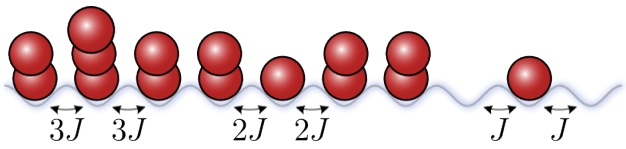

Figure 37: Trimer (particle defect), single hole, single particle, and effective hopping.

section 1.1.2)

$$\hat{H} = -\tilde{J}\sum_j (\hat{c}_j^\dagger \hat{c}_{j+1} + \text{H.a.}) + \tilde{B}\sum_j \hat{c}_j^\dagger \hat{c}_{j+1}^\dagger \hat{c}_{j+1}\hat{c}_j. \tag{15}$$

It can be mapped to the spin-$\frac{1}{2}$ XXZ model [SBE+09, MFS10] with the anisotropy parameter $\Delta = \tilde{B}/2\tilde{J} = 4$. For $\Delta > 1$, we are in the ferromagnetic, Ising-like regime, and a cluster of dimers, corresponding to a lattice domain with maximum magnetization, is dynamically stable. To understand this in terms of dimers, observe that, for any $U(\gg J)$, the maximal kinetic energy $2\tilde{J}$ gained by releasing a dimer from the cluster boundary is small compared to the binding energy $\tilde{B}$ of the dimer to the cluster.

The stability of the dimer cluster is an intrinsic feature of the Bose-Hubbard model. It is rooted in the bosonic amplification of the inter-site hopping of the particles, which in turn enhances the effective (second-order) nearest neighbor interaction $\tilde{B}$. For the fermionic Hubbard model discussed in [HMMR+09] in the context of defect evaporation from a dimer cluster, i.e., a band insulator, we show in subsection 8.5 that $\Delta = 1$ ($\tilde{B} = 2\tilde{J}$), which means that the cluster is unstable and the dimers will diffuse away.

8.1.1 Hole and particle defects

Within the cluster, hole and particle defects can propagate via resonant single-particle hopping with enhanced amplitude, which stems from the bosonic statistics of the surrounding $n = 2$ Mott-insulating environment, see Fig. 37. Outside the cluster, hole defects correspond to free particles. Since their tunneling energy J is much larger than the monomer-dimer interaction energy $\sim J^2/U$ [VPS10], hole defects are not bound to the cluster and can "evaporate". However, the widths of the single particle Bloch band is twice larger inside the cluster than outside of it, therefore only the hole defects with energies in the center of the band can penetrate the cluster boundaries and evaporate into the lattice vacuum. Low- and high-energy hole defects remain in the cluster, because there is no momentum redistribution via two-particle collisions between identical particles in one dimension. We show that the presence of particle defects leads to efficient "thermalization" of the hole defects via momentum

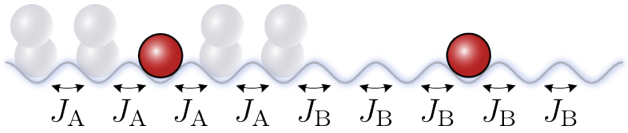

Figure 38: Illustration of the single defect effective theory.

redistributing collisions. Hence, very few such "catalyzing" particle defects can purify the Mott-insulating cluster.

8.2 Single defect model in the strong-interaction limit

The dynamics of dimers is rather slow, as it is governed by the small characteristic energies $\sim J^2/U$, but the dynamics of monomers is much faster, involving the large single-particle hopping rate J. We can thus retain only the contributions on the scale of J, which results in a very simple and transparent effective theory for the monomers. For a monomer in the cluster (hole defect), the bosonic statistics plays an important role: it increases the hopping amplitude of the monomer in the environment of dimers by a factor of 2, see Fig. 37. As a result, the kinetic energy of the monomer inside the dimer cluster is $E_k = -4J\cos(k)$, while in the vacuum it is $E_k = -2J\cos(k)$, where $k \in [-\pi, \pi]$ is the monomer quasi-momentum quantified by the phase change between neighboring lattice sites. Therefore the monomer will be confined to the cluster if its momentum is not inside the transmission region given by

$$k \in (-2\pi/3, -\pi/3) \cup (\pi/3, 2\pi/3), \tag{148}$$

up to a correction due to small interactions of the order of $J^2/U \ll J$ which we neglected.

Consider the scattering of a monomer from the domain wall between the dimer cluster occupying sites $j < 0$ (region A) and the vacuum at sites $j > 0$ (region B), see Fig. 38. The local bare particle number is $n_j = 2$ for $j < 0$ and $n_j = 0$ for $j > 0$. The particle number at $j = 0$ depends on the position i of the monomer $n_i = 1$: inside the cluster $i < 0$ we have $n_0 = 2$, at the boundary $i = 0$ obviously $n_0 = 1$, while outside the cluster (in the vacuum) $i > 0$ leads to $n_0 = 0$. Hence the position of the wall shifts when the monomer crosses the boundary. This needs to be taken into account when considering many defects. The hopping rate of the monomer is $J_A = 2J$ for sites $j \leq 0$ and $J_B = J$ for sites $j > 0$. The effective Hamiltonian for a single monomer then reads

$$\hat{H} = -J_A \sum_{j<0} (\hat{a}_j^\dagger \hat{a}_{j+1} + \text{H.a.}) - J_B \sum_{j\geq 0} (\hat{a}_j^\dagger \hat{a}_{j+1} + \text{H.a.}). \tag{149}$$

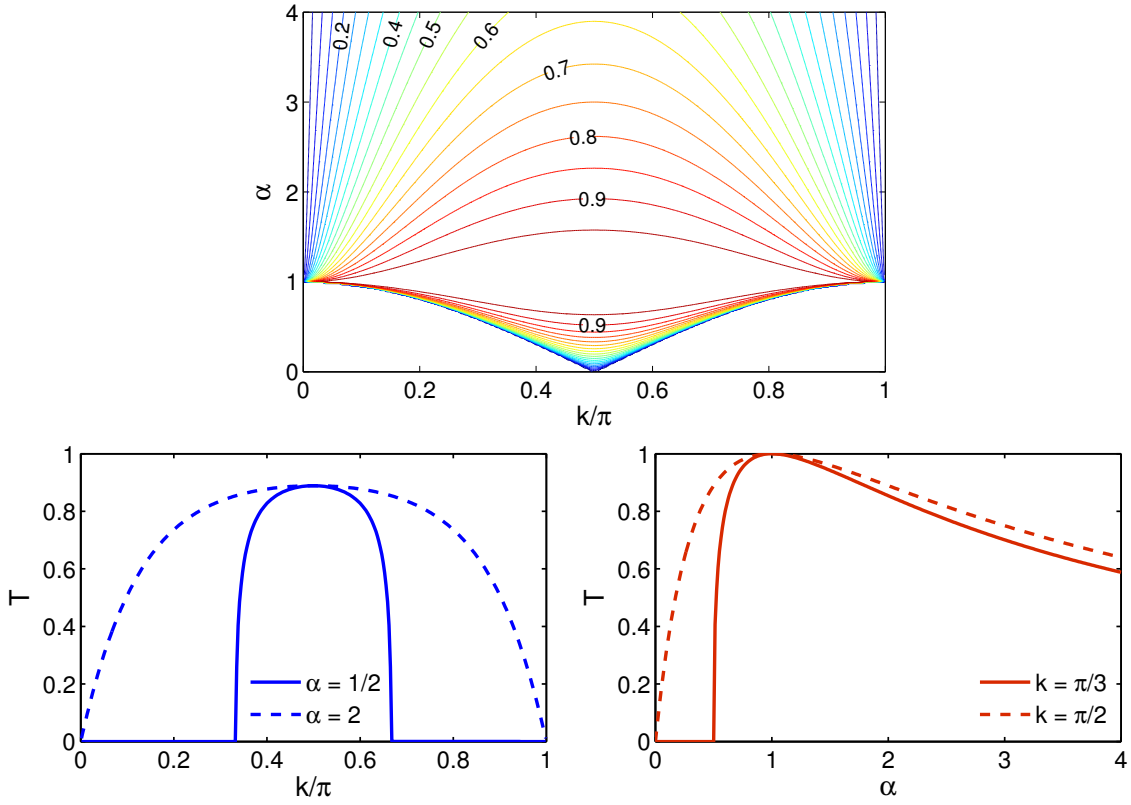

Figure 39: Transmission probability $T(k)$ [cf. Eq. (241)] for various $\alpha = J_B/J_A$.

In Appendix B we calculate the exact transmission probability $T(k)$ of a particle crossing a domain wall in a system described by Hamiltonian (149). The results are illustrated in Fig. 39 for various $\alpha = J_B/J_A$. The values of $\alpha = 1/2$ and $\alpha = 2$ correspond, respectively, to the single particle leaving the dimer cluster and entering it from vacuum.

8.3 Momentum redistribution between the defects

We have seen above that a hole defect can leave the Mott-insulating cluster only if its momentum is within the transmission range of Eq. (148), while a defect with the momentum outside the transmission range will remain in the cluster indefinitely. Hence, to completely purify the cluster of hole defects, their momenta should be continuously redistributed over the entire range of $k \in [-\pi, \pi]$. In two or more dimensions, collisions between identical particles can redistribute the absolute values of their momenta, and we therefore expect the evaporation of all defects through the cluster boundaries after a few collisions. In a one-dimensional lattice, however, collisions of two particles interacting via any finite range potential can only exchange

their quasi-momenta or leave the quasi-momenta unchanged [PM07, VP08, VP09, Val10] (for indistinguishable particles both outcomes are equivalent), provided that the lattice is deep enough so that the band gap precludes interband transitions. Similarly, collisions with the fixed boundaries can only reverse the quasi-momentum of a particle. The simplest momentum redistribution mechanism is then a three particle collision. This happens at a rate proportional to the defect density squared, which is too slow for cold atom experiments.

In the dimer cluster, in addition to hole defects (monomers), we may have particle defects (trimers) with different effective mass. The hopping rates of a monomer and a trimer in the cluster are $J_a = 2J$ and $J_t = 3J$, respectively, Fig. 37. Before collision, their momenta are k_a and k_t, while conservation of momentum, $k_a + k_t = k'_a + k'_t$, and energy, $J_a \cos(k_a) + J_t \cos(k_t) = J_a \cos(k'_a) + J_t \cos(k'_t)$, during the collision determine the new momenta k'_a and k'_t via

$$J_a \cos(k_a) + J_t \cos(k_t) = J_a \cos(k'_a) + J_t \cos(k_a + k_t - k'_a). \tag{150}$$

If there is a collision with the wall, or a third defect of either kind, before this process is reversed, all energetically allowed combinations of k_a, k_t can be assumed, as will be verified below by exact numerical simulations.

8.3.1 Two classical particles

The timescale for momentum redistribution can be calculated from purely classical considerations. A monomer or a trimer moving in the Mott-insulating cluster has a kinetic energy of $E_{k_\mu} = -2J_\mu \cos(k_\mu)$ and the corresponding group velocity of $v_\mu = 2J_\mu \sin(k_\mu)$ $[\mu = a, t]$.

Consider first two wave packets in a periodic lattice of length L. After a collision (the defects can not penetrate each other), their velocities are assumed to be $v_a = 2J_a \sin(k_a) < v_t = 2J_t \sin(k_t)$. The next collision happens after time

$$\frac{t_c}{2} = \frac{L-1}{2} \frac{1}{J_t \sin(k_t) - J_a \sin(k_a)}, \tag{151}$$

and the new momenta are determined by Eq. (150). It follows that the time interval between all subsequent collisions is the same $t_c/2$, since Eq. (150) and

$$\begin{aligned} & \frac{L-1}{2} \frac{1}{J_t \sin(k_t) - J_a \sin(k_a)} \\ = \; & \frac{L-1}{2} \frac{1}{-J_t \sin(k_a + k_t - k'_a) + J_a \sin(k'_a)} \end{aligned}$$

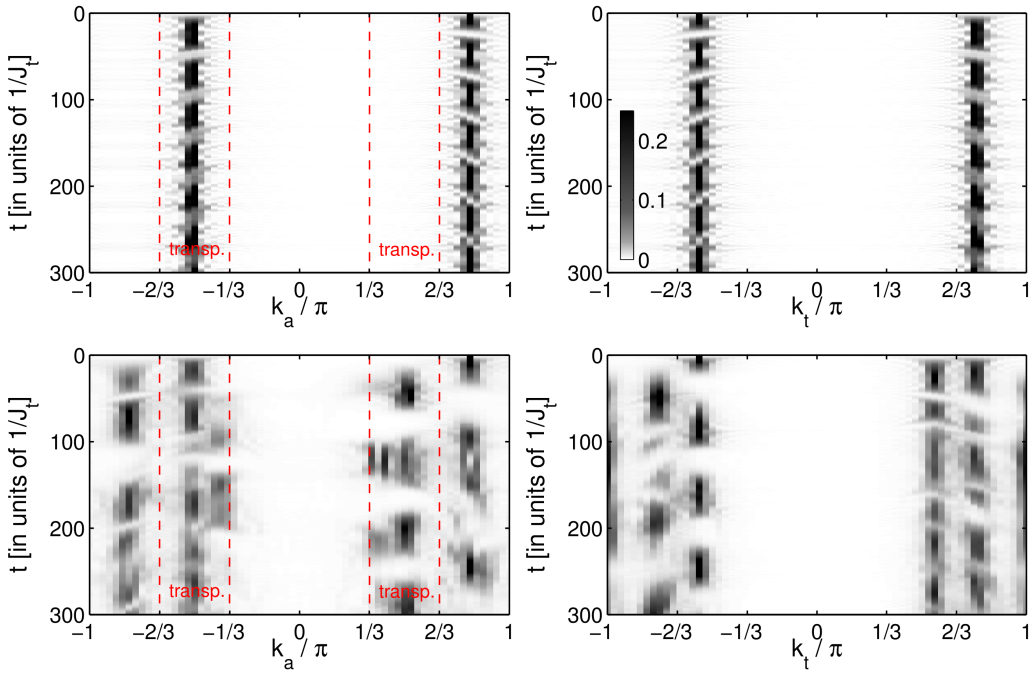

Figure 40: Dynamics of the momentum distribution for the monomer (left column) and trimer (right column) in a lattice of $L = 64$ sites. The initial momenta are $k_a = \pi\frac{13}{16}$ and $k_t = -\pi\frac{9}{16}$. Upper panels correspond to periodic boundary conditions, where the markers on the right indicate multiples of the revival time $t_c \approx 46.63/J_t$. Lower Panels are obtained for open boundary conditions. Dashed vertical lines mark the transmission regions for monomer quasi-momenta as per Eq. (148).

have always a common solution.

In the presence of a wall, or a third defect, the momenta can take any values energetically allowed. A revival is not expected, but now t_c^{-1} is an effective rate of momentum redistribution. It is essentially given by J over the mean free path, i.e., it is proportional to J times the average defect density, which is indeed much faster than the rate of three particle collisions.

8.3.2 Two quantum particles: Numerical simulations

We simulate the quantum dynamics of the hole and particle defects in a dimer cluster using the two-particle Hamiltonian in momentum space, see Appendix C. Each defect is initially prepared in a momentum eigenstate, with the combined state given by

$$|k_a, k_t\rangle = \frac{1}{L}\sum_{j_a,j_t=1}^{L} e^{ik_a j_a} e^{ik_t j_t} \hat{a}^\dagger_{j_a} \hat{t}^\dagger_{j_t} |\text{vac}\rangle, \tag{152}$$

where $\hat{a}_j^\dagger$ creates a monomer and $\hat{t}_j^\dagger$ a trimer at site j of a finite lattice filled with dimers, playing here the role of an effective vacuum $|\text{vac}\rangle$.

Fig. 40 shows the results of our numerical simulations. In the case of periodic boundary conditions, the dynamics is mainly classical; only two values of momentum k are assumed by each particle, and after the classical revival time t_c, the momentum distribution is restored to the initial one. For open boundary conditions, however, we observe fast redistribution of momenta, and already the first revival is hardly noticeable. We may therefore conclude that a single trimer can catalyze the redistribution of momenta of monomers, making the evaporation of almost all hole defects possible, provided that their average kinetic energy is initially close to the center of the band. This will be verified by the following many-body calculations.

8.4 Many-body numerical simulations

To study the dynamics of several defects under experimentally realistic conditions, we use a sufficiently long lattice that can accommodate dimer clusters spanning a few dozen sites. The complete Hilbert space for such a system is too large to be amenable to exact diagonalization treatments. We therefore resort to time-dependent density matrix renormalization group specifically, the TEBD algorithm. Even then, however, simulating the full Bose-Hubbard model is a difficult task. This is due to sizable quantum fluctuations present even in the pure dimer cluster for any finite interaction strengths U/J. These fluctuations contribute to the many-body entanglement and consume much of the computational resources required to simulate the dynamics of the defects. We therefore introduce an effective model for the defects only.

8.4.1 Many defect effective theory in the strong-interaction limit

Since the states with different number of particles per site have energies separated by multiples of $U(\gg J)$, the numbers of monomers, dimers, and trimers in a lattice are, to a good approximation, conserved separately. This allows us to treat the monomers, dimers, and trimers as distinguishable species, each represented by hard-core bosons, Eqs. (16). Furthermore, as discussed in section 8.1, dimers forming stable clusters do not contribute to the dynamics of the system. For our initial conditions, typically containing a single cluster, we can thus reformulate the problem as one of the hole and particle defects moving on the background of dimers or vacuum, with the spatial configuration of the dimer cluster entering the effective Hamiltonian for the defects only as a parameter.

We define a reference system in which the pure dimer cluster occupies certain lattice sites while all the defects are placed at the beginning (left side) of the lattice.

As the defects move in the lattice, the effective hopping rates depend on whether they are inside or outside the Mott-insulating cluster. In turn, the position of the cluster depends on the positions of the defects, since each defect crossing the system from the left to the right shifts the position of the dimers, and the cluster as a whole, by one site to the left. The effective Hamiltonian for the defects can then be cast as

$$\hat{H} = \sum_{j=1}^{L-1} \sum_{\overrightarrow{n}=0}^{N} \hat{H}_j^{[\Theta(j+\overrightarrow{n})]} \otimes \hat{P}_{[j+2,L]}^{\overrightarrow{n}} \equiv \sum_{j=1}^{L-1} \tilde{H}_j, \tag{153}$$

where $\hat{P}_{[j+2,L]}^{\overrightarrow{n}}$ is the projector onto the subspace containing exactly $\overrightarrow{n}$ hole and particle defects on sites $j+2$ to L, while each local operator $\hat{H}_j^{[\Theta]}$ acts on sites j and $j+1$ as

$$\begin{aligned} \hat{H}_j^{[\Theta]} &= -J_{\mathrm{a}}^{[\Theta]}(\hat{a}_j^\dagger \hat{a}_{j+1} + \text{H.a.})\hat{t}_j \hat{t}_{j+1} \hat{t}_{j+1}^\dagger \hat{t}_j^\dagger \\ &\quad -J_{\mathrm{t}}^{[\Theta]}(\hat{t}_j^\dagger \hat{t}_{j+1} + \text{H.a.})\hat{a}_j \hat{a}_{j+1} \hat{a}_{j+1}^\dagger \hat{a}_j^\dagger. \end{aligned} \tag{154}$$

Here $\hat{a}_j^\dagger$ and $\hat{a}_j$ ($\hat{t}_j^\dagger$ and $\hat{t}_j$) are the hard-core bosonic creation and annihilation operators for the monomers (trimers). The function $\Theta(j)$ is initialized for all j with respect to the reference system, and it can take two values: $\Theta(j) = 1$ for site $j+1$ being empty (vacuum) and $\Theta(j) = 2$ for $j+1$ containing a dimer. Then the hopping rates for the monomers are $J_{\mathrm{a}}^{[1]} = J$ and $J_{\mathrm{a}}^{[2]} = 2J$, and for the trimers are $J_{\mathrm{t}}^{[1]} = 0$ (they can not move on an empty lattice in first order in J) and $J_{\mathrm{t}}^{[2]} = 3J$.

Note that since the effective Hamiltonian (154) contains two species of particles with hardcore interactions, it can not be mapped onto a model of free fermions via the Jordan-Wigner transformation (which is possible for identical hardcore bosons). The dynamics is therefore non-trivial and actual calculations require numerical many-body (TEBD) techniques. The practical advantage of the effective model—besides the largely reduced number of particles—is that the fast timescale U^{-1} is eliminated from the system's dynamics and in our numerical simulations we can choose Trotter steps on the time scale $\lesssim J^{-1}$. Further discussion on the effective defect model is given in Appendix D.

8.4.2 Initial states

In our numerical calculations, we use several typical configurations of the defects in the lattice, each configuration described by a pure quantum state. Various coherent and incoherent superpositions of such configurations would represent mixed initial states.

We consider piecewise product states. A Mott-insulating segment of length l

contains a fixed number of particles n at every site ($n = 2$ inside the dimer cluster and $n = 0$ in the vacuum),

$$|\cdot\rangle_l^n = \bigotimes_{j=1}^{l} \frac{(\hat{a}_j^\dagger)^n}{\sqrt{n!}} |\mathrm{vac}\rangle, \tag{155}$$

with $|\mathrm{vac}\rangle$ denoting the true vacuum. Each segment can contain an additional defect. For a defect localized as site j, we use the notation

$$|j_+\rangle_l^n = \frac{\hat{a}_j^\dagger}{\sqrt{n+1}} |\cdot\rangle_l^n, \tag{156a}$$

$$|j_-\rangle_l^n = \frac{\hat{a}_j}{\sqrt{n}} |\cdot\rangle_l^n \quad (n \geq 1), \tag{156b}$$

with $\pm$ corresponding, respectively, to a particle and a hole defect. Similarly, we denote a defect with momentum k, which must be a multiple of $2\pi/l$, as

$$|k\rangle_l^{n+} = \frac{1}{\sqrt{l}} \sum_{j=1}^{l} e^{ikj} |j_+\rangle_l^n, \tag{157a}$$

$$|k\rangle_l^{n-} = \frac{1}{\sqrt{l}} \sum_{j=1}^{l} e^{ikj} |j_-\rangle_l^n \quad (n \geq 1). \tag{157b}$$

We prepare the cluster by joining Mott-insulating segments with and without defects. Since we are only interested in low defect densities, we do not use segments containing multiple defects. In order to perform TEBD simulations, the initial states have to be represented in the MPS form, which is discussed in Appendix E.

8.4.3 Numerical results

Figures 41 and 42 show the time evolution of defects in a $n = 2$ Mott-insulating cluster surrounded by vacuum, obtained from the full Bose-Hubbard model. Hole defects with quasi-momenta at the center of the band can easily leave the cluster after just a few scattering events, Fig. 41. Hole defects prepared at the edges of the band remain trapped in the cluster. An additional particle defect, which itself can not leave the cluster, induces fast momentum redistribution of the hole defects, large fraction of which can now leave the cluster.

The same effect is observed with localized defects, Fig. 42. For hole defects alone, about one third of their population leaves the cluster (note that the localized initial state of each defect has uniform distribution of momentum $k \in [-\pi, \pi]$, and not energy $E_k \in [-4J, 4J]$), while an additional localized particle defect increases this

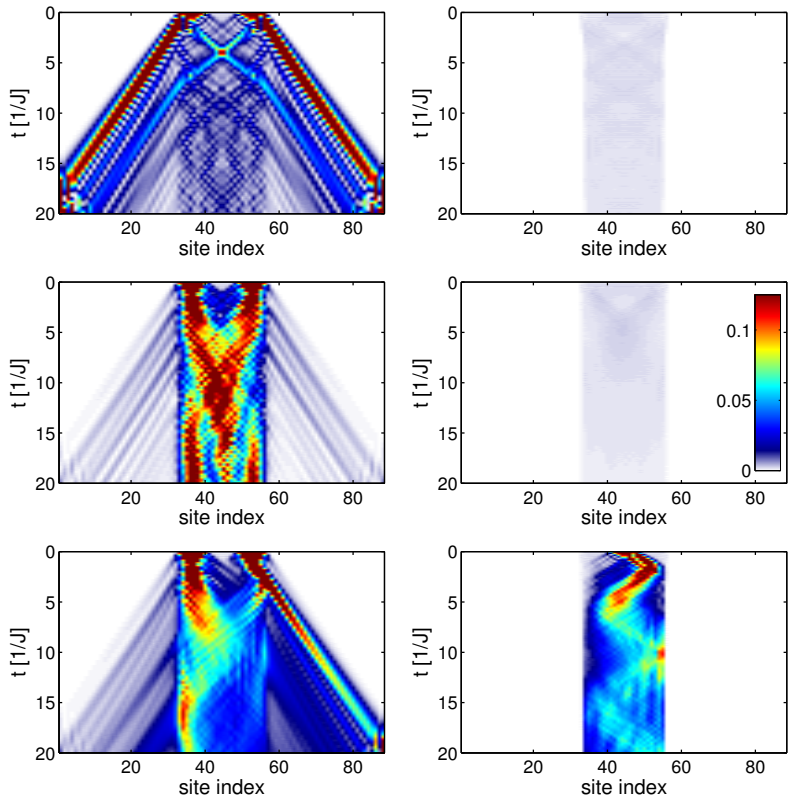

Figure 41: Density of monomers (left column) and trimers (right column) in the $n = 2$ Mott-insulating cluster of 24 sites surrounded by empty lattice, $|\cdot\rangle_{32}^{0}$, on both sides. In the top panels, the initial state of the cluster $|-\pi/2\rangle_8^{2-}|\cdot\rangle_8^2|\pi/2\rangle_8^{2-}$ corresponds to two monomers at the center of the band moving to the left and right. In the central panel, the initial state $|\pi\rangle_8^{2-}|\cdot\rangle_8^2|0\rangle_8^{2-}$ corresponds to two monomers at the upper and lower band edges. In the bottom panel, the initial state $|\pi\rangle_8^{2-}|\pi/2\rangle_8^{2+}|0\rangle_8^{2-}$ is the same as in the central panels plus a particle defect at the center of the band, moving to the right. The interaction strength is $U = 100J$. The density of monomers (trimers) corresponds to the probability of finding exactly one (three) particles at a given site. A TEBD [Vid03] algorithm with bond dimension $\chi = 200$ is used for the time evolution with a fourth order Trotter decomposition and time step size $1/50J$, with particle number conservation explicitly included in the MPS [DCJZ05].

fraction significantly.

In Fig. 43(a) and (b) we show the time evolution of the total population of monomers outside the dimer cluster pertaining to the cases illustrated in Figs. 41 and 42, respectively. Again, hole defects with quasi-momenta in the center of the band easily escape the cluster even without the assistance of a particle defect, Fig. 43(a). Conversely, for the hole defects with quasi-momenta at the edges of the Bloch band in the cluster, very little population is found outside the cluster in the long time

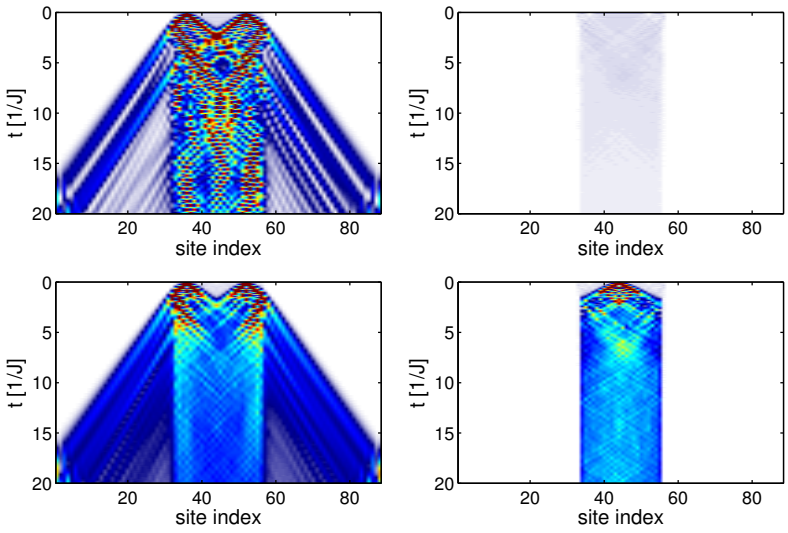

Figure 42: Same as Fig. 41 but for localized initial states: Top panel, $|4_-\rangle_8^2|\cdot\rangle_8^2|4_-\rangle_8^2$, two localized monomers; bottom panel, $|4_-\rangle_8^2|4_+\rangle_8^2|4_-\rangle_8^2$, same plus a localized trimer.

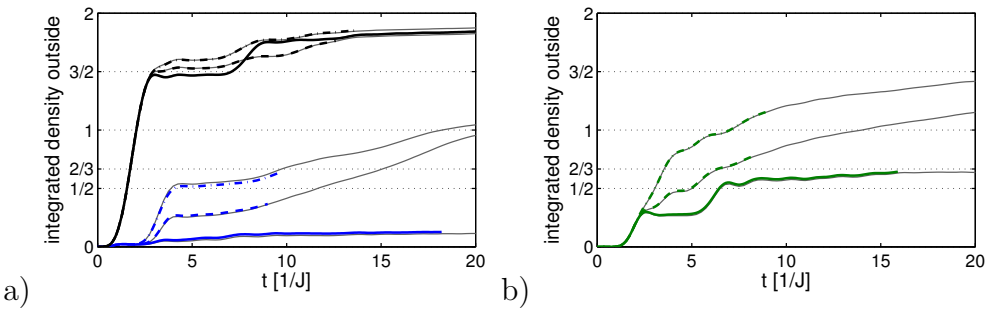

Figure 43: Total population (integrated density, $\sum_{j=1}^{31}\langle\hat{a}_j^\dagger\hat{a}_j\rangle + \sum_{j=58}^{88}\langle\hat{a}_j^\dagger\hat{a}_j\rangle$) of monomers outside the dimer cluster. (a) Initial states of the cluster are: in the upper black branch, $|-\pi/2\rangle_8^{2-}|\cdot\rangle_8^2|\pi/2\rangle_8^{2-}$ (solid line), $|-\pi/2\rangle_8^{2-}|4_+\rangle_8^2|\pi/2\rangle_8^{2-}$ (dashed line), and $|-\pi/2\rangle_8^{2-}|\pi/2\rangle_8^{2+}|\pi/2\rangle_8^{2-}$ (dot-dashed line); in the lower blue branch, $|\pi\rangle_8^{2-}|\cdot\rangle_8^2|0\rangle_8^{2-}$ (solid line), $|\pi\rangle_8^{2-}|4_+\rangle_8^2|0\rangle_8^{2-}$ (dashed line), and $|\pi\rangle_8^{2-}|\pi/2\rangle_8^{2+}|0\rangle_8^{2-}$ (dot-dashed line). (b) Initial states of the cluster are: $|4_-\rangle_8^2|\cdot\rangle_8^2|4_-\rangle_8^2$ (solid line), $|4_-\rangle_8^2|4_+\rangle_8^2|4_-\rangle_8^2$ (dashed line), and $|4_-\rangle_8^2|\pi/2\rangle_8^{2+}|4_-\rangle_8^2$ (dot-dashed line). The interaction strength is $U = 100J$. Numerical parameters are the same as in Figs. 41 and 42, and the curves terminate when the accumulated cut-off error equals 10^{-2}. The gray lines are obtained from the equivalent effective model, with the time step increased to $1/10J$.

limit (the small fraction of monomer population in the vacuum is due to the finite binding energy U of the dimers). Adding a particle defect in the cluster significantly increases the fraction of monomers outside the cluster; we find that the increase is always larger for a particle defect in the center of the band than for a localized one.

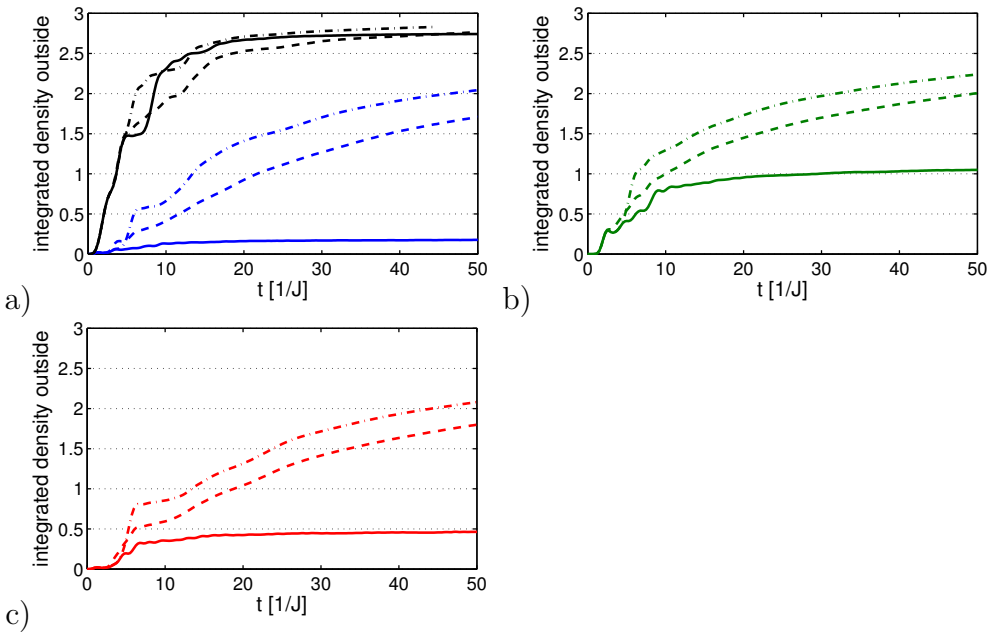

Figure 44: Total population $(\sum_{j=1}^{63}\langle\hat{a}_j^\dagger\hat{a}_j\rangle + \sum_{j=98}^{160}\langle\hat{a}_j^\dagger\hat{a}_j\rangle)$ of monomers outside the dimer cluster of 32 sites surrounded by empty lattice, $|\cdot\rangle_{64}^0$, on both sides. (a) Initial states of the cluster are: in the upper black branch, $|-\pi/2\rangle_8^{2-}|\cdot\rangle_8^2|\pi/2\rangle_8^{2-}|-\pi/2\rangle_8^{2-}$ (solid line), $|-\pi/2\rangle_8^{2-}|4_+\rangle_8^2|\pi/2\rangle_8^{2-}|-\pi/2\rangle_8^{2-}$ (dashed line), and $|-\pi/2\rangle_8^{2-}|\pi/2\rangle_8^{2+}|\pi/2\rangle_8^{2-}|-\pi/2\rangle_8^{2-}$ (dot-dashed line); in the lower blue branch, $|\pi\rangle_8^{2-}|\cdot\rangle_8^2|0\rangle_8^{2-}|\pi\rangle_8^{2-}$ (solid line), $|\pi\rangle_8^{2-}|4_+\rangle_8^2|0\rangle_8^{2-}|\pi\rangle_8^{2-}$ (dashed line), and $|\pi\rangle_8^{2-}|\pi/2\rangle_8^{2+}|0\rangle_8^{2-}|\pi\rangle_8^{2-}$ (dot-dashed line). (b) Initial states of the cluster are: $|4_-\rangle_8^2|\cdot\rangle_8^2|4_-\rangle_8^2|4_-\rangle_8^2$ (solid line), $|4_-\rangle_8^2|4_+\rangle_8^2|4_-\rangle_8^2|4_-\rangle_8^2$ (dashed line), and $|4_-\rangle_8^2|\pi/2\rangle_8^{2+}|4_-\rangle_8^2|4_-\rangle_8^2$ (dot-dashed line). (c) Initial states of the cluster are: $|\pi\rangle_8^{2-}|\cdot\rangle_8^2|0\rangle_8^{2-}|4_-\rangle_8^2$ (solid line), $|\pi\rangle_8^{2-}|4_+\rangle_8^2|0\rangle_8^{2-}|4_-\rangle_8^2$ (dashed line), and $|\pi\rangle_8^{2-}|\pi/2\rangle_8^{2+}|4_-\rangle_8^2|4_-\rangle_8^2$ (dot-dashed line). Simulations were performed with the effective model. Bond dimensions $\chi = 300$ are used, and the time step size is $1/10J$. The curves terminate when the accumulated cut-off error equals 10^{-1}.

For the initially localized hole defects, Fig. 43(b), and without assistance of a particle defect, we find that, as expected, about a third of their total population occupying the center of the Bloch band leaves the cluster in the long-time limit. A particle defect can further increase the portion of escaping population of the hole defects by redistributing their quasi-momenta over the entire band.

Note that the results of numerical simulations for the system with a particle defect are reliable for shorter times as compared to the simulations with the hole defects only, which is due to the larger entanglement created dynamically upon the trimer-monomer collisions.

So far we have been restricted to the treatment of only two monomers and one trimer and for relatively short times, because in the full Bose-Hubbard model the fast

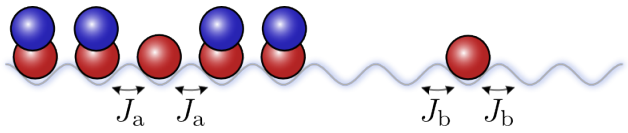

Figure 45: Illustration of the single-defect physics in the two species model.

growing entanglement in the system limits the numerical method. With the effective model containing only the hole and particles defects, we can simulate the dynamics for much longer times with the same numerical accuracy, as can be seen in Fig. 43. The perfect agreement between the full and effective models allows us to employ the effective model for simulating larger systems and for longer times.

Fig. 44 shows numerical results for a system containing initially up to four defects. As expected, the evaporation works for the larger systems as well. Most importantly, in the presence of a particle defects, the number of hole defects left in the cluster in the long-time limit falls well below unity (extrapolating the curves to somewhat larger times than shown in Fig. 44, if necessary).

8.5 Two species Bose-Hubbard model

We have seen in the previous sections that, in the single species Bose-Hubbard model, the hopping amplitudes of a monomer inside an $n = 2$ Mott-insulating cluster and on an empty lattice differ by a fixed factor of 2. More flexibility is offered by the two species Bose-Hubbard model, which we now briefly discuss. The Hamiltonian for the system is

$$\begin{aligned}\hat{H} &= -J_a \sum_j (\hat{a}_j^\dagger \hat{a}_{j+1} + \text{H.a.}) - J_b \sum_j (\hat{b}_j^\dagger \hat{b}_{j+1} + \text{H.a.}) \\ &\quad + \frac{U_a}{2} \sum_j \hat{a}_j^\dagger \hat{a}_j^\dagger \hat{a}_j \hat{a}_j + \frac{U_b}{2} \sum_j \hat{b}_j^\dagger \hat{b}_j^\dagger \hat{b}_j \hat{b}_j \\ &\quad + U_{ab} \sum \hat{a}_j^\dagger \hat{a}_j \hat{b}_j^\dagger \hat{b}_j, \end{aligned} \tag{158}$$

where $\hat{a}_j$ ($\hat{b}_j$) are the bosonic operators for the particles of type a (b) hopping between adjacent sites with the rate J_a (J_b), while U_a, U_b and U_{ab} are the intra- and inter-species on-site interactions.

Assuming the conditions $U_a, U_b, U_{ab}, |U_a + U_b - 2U_{ab}| \gg J_a, J_b$, we first consider the situation where each lattice site is either empty or contains a single a-b dimer, that is, a pair of strongly interacting (via U_{ab}) particles a and b localized on the same site. Upon adiabatic elimination of the non resonant states containing unpaired particles on neighboring sites [SBE+09], we obtain an effective Hamiltonian of the form of

Eq. (15), where now the dimer hopping and nearest-neighbor interaction are given by

$$\tilde{J} = -\frac{2J_\mathrm{a}J_\mathrm{b}}{U_\mathrm{ab}}, \quad \tilde{B} = -2\left(\frac{2J_\mathrm{a}^2}{U_\mathrm{a}} + \frac{2J_\mathrm{b}^2}{U_\mathrm{b}} + \frac{J_\mathrm{a}^2 + J_\mathrm{b}^2}{U_\mathrm{ab}}\right). \tag{159}$$

With all the interactions repulsive, the anisotropy parameter

$$\Delta = \tilde{B}/2\tilde{J} = \frac{J_\mathrm{a}}{J_\mathrm{b}}\left(\frac{1}{2} + \frac{U_\mathrm{ab}}{U_\mathrm{a}}\right) + \frac{J_\mathrm{b}}{J_\mathrm{a}}\left(\frac{1}{2} + \frac{U_\mathrm{ab}}{U_\mathrm{b}}\right) \tag{160}$$

is larger than 1 for any finite $U_\mathrm{a}/U_\mathrm{ab}$ or $U_\mathrm{b}/U_\mathrm{ab}$, and the Mott-insulating cluster of a-b dimers is stable.

Inside the $n = n_\mathrm{a} + n_\mathrm{b} = 2$ ($n_\mathrm{a} = n_\mathrm{b} = 1$) Mott-insulating cluster, a hole defect of type a (unpaired particle b) is created by $\hat{a}_j$, see Fig. 45. The defect hops in the cluster with the rate J_a while outside the cluster its hopping rate is J_b. It must be stable and not resonantly converted into a pair of particles b and a single b-hole (unpaired particle a), which requires that $U_\mathrm{b} - U_\mathrm{ab} \gg J_\mathrm{a}, J_\mathrm{b}$. Neglecting the second-order corrections of the order of $J_\mathrm{a,b}^2/U_\mathrm{a,b,ab}$, we have the effective single-particle Hamiltonian (149) with $J_\mathrm{A} = J_\mathrm{a}$ and $J_\mathrm{B} = J_\mathrm{b}$. Using the results of Appendix B, we can calculate the transmission probability $T(k)$ of the particle through the domain wall separating the regions A and B for various $J_\mathrm{b}/J_\mathrm{a}$, which is shown in Fig. 39. At $J_\mathrm{a} = J_\mathrm{b}$ ($\alpha = 1$) we find an almost perfect transmission for all k, up to a small correction due to finite interactions. The above results equally apply to a hole defect of type b (unpaired particle a) with the replacement a $\leftrightarrow$ b.

We have performed numerical simulations of the dynamics of several defects in a dimer cluster surrounded by vacuum using the full model of Eq. (158). For computational reasons, we truncate the local Hilbert space to three bosons of each species per site, which is justified by the fact that, due to the strong interactions, the occupation of a single site by more particles can safely be neglected.

In Fig. 46 we show the behavior of two unpaired particles b, or a-holes, moving in the cluster with different initial velocities. In the case of $J_\mathrm{a} = J_\mathrm{b}$ (top panel), both defects almost completely leave the cluster upon the first encounter with the walls. For $J_\mathrm{a} \neq J_\mathrm{b}$, only partial transmission of each defect is observed, depending on its initial quasi-momentum, as per Fig. 39. As an example, at $J_\mathrm{a} = 2J_\mathrm{b}$ (central panel) the unpaired particle b with $k = \pi/2$ can exit the cluster, while that with $k = \pi/4$ can not, as its quasi momentum is close to the lower band edge.

Fig. 47 illustrates the results for a pair of initially localized defects of different type. Again, for $J_\mathrm{a} = J_\mathrm{b}$, both defects easily leave the cluster through its walls, but when $J_\mathrm{a} \neq J_\mathrm{b}$, only a fraction of the population of each defect leaves the cluster after the first collision with its wall. Note, however, that since the two types of hole

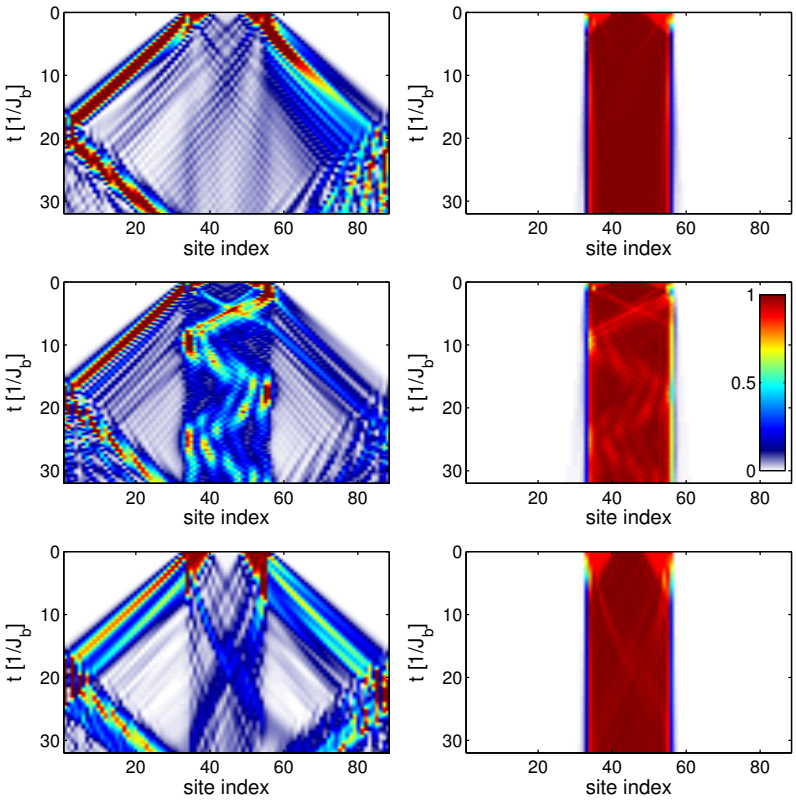

Figure 46: Density of unpaired particles b, or a-holes, in the cluster (left column), and particles a (right column), in the lattice with a Mott-insulating cluster of a-b dimers spanning 24 sites surrounded by empty lattice, $|\cdot\rangle_{32}^{0}$, on both sides. The initial state of the cluster $|-\pi/2\rangle_8^{2-\mathrm{a}}|\cdot\rangle_8^2|\pi/4\rangle_8^{2-\mathrm{a}}$ corresponds to two a-hole defects moving to the left with velocity $2J_\mathrm{a}$, and to the right with velocity $\sqrt{2}J_\mathrm{a}$, respectively, while all particles a are dimerized with particles b (no b-hole defects). The parameters are $U_\mathrm{a} = U_\mathrm{b} = 60J_\mathrm{b}$, $U_\mathrm{ab} = 40J_\mathrm{b}$, and $J_\mathrm{a} = J_\mathrm{b}$ (top panel), $J_\mathrm{a} = 2J_\mathrm{b}$ (central panel), and $J_\mathrm{a} = \frac{1}{2}J_\mathrm{b}$ (bottom panel). A TEBD algorithm with bond dimension $\chi = 100$ is used for the time evolution with a fourth order Trotter decomposition and time step size $1/50J_\mathrm{b}$, with the particle number conservation for each species explicitly included in the MPS.

defects have different effective mass, their collisions with each other and the walls of the cluster can effectively redistribute their momenta, and no trimer defects are required to purify the Mott-insulating cluster.

8.5.1 Fermionic Hubbard model

A related work [HMMR+09] deals with fermionic dimers described by the Hubbard model. After preparing a cold atomic gas with filling of $n \simeq 2$ in the trap center, followed by turning off the trap, the hole defects will simply tunnel out of the cluster

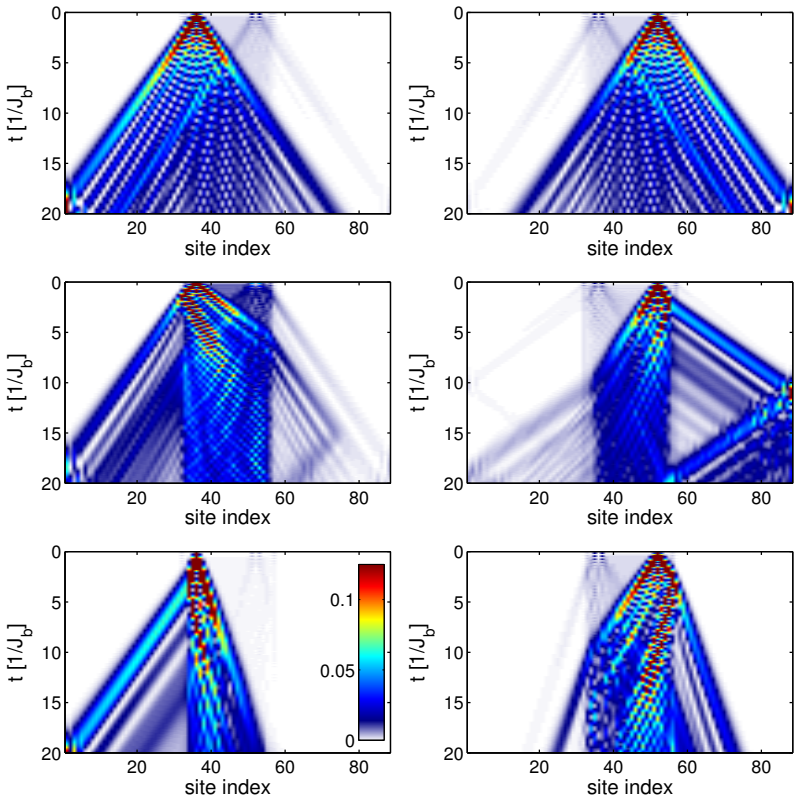

Figure 47: Dynamics of an initially localized unpaired particle b, or a-hole, in the cluster (left column), and an unpaired particle a, b-hole, in the cluster (right column), for the initial cluster state $|4_{-\mathrm{a}}\rangle_8^2|\cdot\rangle_8^2|4_{-\mathrm{b}}\rangle_8^2$. All parameters are as in Fig. 46, and the bond dimension of the TEBD is $\chi = 200$.

into the vacuum. In one dimension, this is equivalent to the two-species bosonic model discussed above, for $U_\mathrm{a} = U_\mathrm{b}$ and $U_\mathrm{a}/U_\mathrm{ab}.U_\mathrm{b}/U_\mathrm{ab} \to \infty$, i.e., if double occupancies by a single species is completely suppressed, as in the fermionic case. In this case however, according to (160), the effective attraction between two pairs approaches its minimum, because the effective second-order tunneling of the on-site pairs is not restrained by the interaction between the pairs. This corresponds to the critical value $\Delta = 1$ for the anisotropy and the dimer cluster is unstable. Thus, although the transmissibility is perfect in this case, i.e., the hole defects are not effected at all by the boundaries, the cluster also dissolves on a time scale U_ab/J^2. A numerical study using the Heisenberg model and an initial product state cluster as in our case, but without any defects, has been published recently [KMT11]. It shows the decay of the cluster and also the different velocities of paired and unpaired particles.

To conclude, in one-dimensional Mott-insulating clusters of repulsively bound dimers of bosons [PSAF07], hole defects (unpaired particles, or monomers) can evap-

orate through the cluster boundaries, taking away the entropy of the system. In the case of dimers of identical bosons, only part of the monomer population can leave the cluster unassisted. Complete evaporation of the hole defects is possible in the presence of catalyzing particle defects (trimers), which efficiently thermalize the hole defects via momentum redistributing collisions. The particle defects themselves can not leave the cluster, due to the large energy mismatch $2U$ between a single excess particle on top of the $n = 2$ Mott-insulating cluster and on an empty lattice.

In the case of dimers composed of two different bosonic species, the defect evaporation proceeds by itself, without the need of any catalyzing species.

Part IV
t-DMRG in the Heisenberg picture

White's DMRG and it's more recent generalizations to time evolution using TEBD or t-DMRG algorithms are indispensable tools in the numerical simulation of one-dimensional quantum many body systems. They permit high-accuracy calculations, provided that the entanglement between any two complementary partitions remains small. For finite-range interactions this is the case for the ground state [VC06]. However in real time evolution the entanglement often grows linear in time, limited only by the Lieb-Robinson upper bound [LR72, BHV06, EO06]. Very often the actual time evolution of the entanglement entropy is indeed linear. For example for the spin-$\frac{1}{2}$ XY chain the evolution of the entanglement entropy was investigated in [FC08] showing explicitly the linear growth in time.

However the evolved state contains a lot of information which is of little interest. Experimental measurements as well as theories are almost solely concerned with few particle properties, i.e., quantities that can be expressed in terms of expectation values of only a small number of elementary operators. This suggests to go to the Heisenberg picture instead, and to simulate the dynamics of these operators. Prosen et al. [PŽ07, PP07] where the first to pursue this approach. They observed an exponential speed up in numerical simulations of local operators for integrable systems. So far there is however no general understanding of why this is the case and whether or not integrability is crucial. In the present part of this thesis we have a closer look at this question. In section 9 we first introduce matrix product operators (MPO), which are used to represent operators in the Heisenberg picture TEBD. In section 10 we first provide an explanation of the speed-up for integrable models that can be mapped to free fermions. We also argue that integrability is not necessary and that the existence of a conservation law may suffice for the efficient simulation of the dynamics of local operators that constitute the conserved quantity. We will discuss the spin-$\frac{1}{2}$ and spin-1 XXZ models as specific examples supporting and illustrating our arguments. In section 11 we discuss in detail how to take conserved quantities into account for the construction of matrix product operators, and what simplifications and advantages arise from this.

9 Matrix product operators

MPOs can be understood as a generalization of product operators in the same way as shown in (70) for MPS,

$$\hat{O} \;=\; \mathrm{Tr}\left[\bigotimes_m \left(\sum_j A^{[m],j}\hat{o}_j\right)\right]. \tag{161}$$

The $\hat{o}_j$ form an orthogonal basis of the local operator space of single site, normalized according to the Hilbert-Schmidt norm,

$$\mathrm{Tr}\left[\hat{o}_j^\dagger \hat{o}_{j'}\right] = \delta_{j,j'}. \tag{162}$$

The space of operators can be mapped to a "super-space" of kets via

$$\hat{O} = \sum_{\vec{i},\vec{j}} o_{\vec{i},\vec{j}} |\vec{i}\rangle\langle\vec{j}| \;\longmapsto\; |\hat{O}\rangle = \sum_{\vec{i},\vec{j}} o_{\vec{i},\vec{j}} \left|\begin{smallmatrix}\vec{j}\\ \vec{i}\end{smallmatrix}\right\rangle. \tag{163}$$

Again the $\vec{i}$ and $\vec{j}$ are vectors of occupation numbers for every lattice site, thus corresponding to a Fock state. In these terms we talk about an upper in- and a lower out-chain. ("In" and "out" refer to the original operator acting as a function.) An MPO is then equivalent to an MPS representation of such a "super-state". E.g., the Schmidt decomposition at two neighboring bonds reads

$$|\hat{O}\rangle = \sum_{\alpha,\beta=1}^{\chi} \sum_{i=0}^{d-1}\sum_{j=0}^{d-1} \lambda_\alpha^{[m-1]}\Gamma_{\alpha,\beta}^{[m]i,j}\lambda_\beta^{[m]} \left|\begin{smallmatrix} j\\ i\end{smallmatrix}\right\rangle_m \otimes |\alpha\rangle_\mathrm{A} \otimes |\beta\rangle_\mathrm{B}. \tag{164}$$

The structure of the Γ tensors for certain symmetric operators will be discussed in sections 11.1 and 11.2. Note that the local Hilbert space dimension d in general has to be restricted to some reasonable value, usually by allowing for a maximum on-site number d of states (e.g. by allowing for a maximum occupation number of $d-1$). This is because otherwise certain operators (even such basic ones as a particle annihilator or even unity) would have non-vanishing contributions from infinitely many states (particle numbers) and in general can not even be normalized.

The relevant measure for the resources required to approximate an operator well by an MPO is now the entanglement in operator space, a possible measure being the operator space entanglement entropy [PP07] (OSEE) which is defined just as the entanglement entropy (75) for MPS. It must not be confused with the systems statistical entropy when interpreting $\hat{O}$ as a density matrix: As a striking example, the

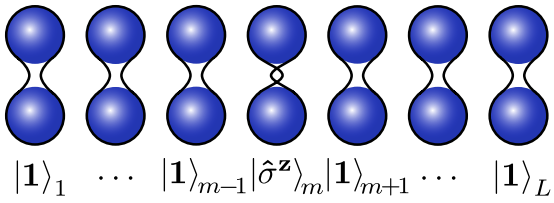

Figure 48: In the grand canonical Hilbert space a product operator can be interpreted as a state on a double chain, which can be in general maximally entangled locally, but not at all along the chain.

infinite temperature density matrix $\mathbf{1}/d^L$ has maximal statistical entropy of $L \log_2(d)$ but it is clearly a product operator and therefore the OSEE is 0. On the other hand a projector $|\Psi\rangle\langle\Psi|$ is always pure and has statistical entropy 0 while its OSEE is just the entanglement entropy of the state $|\Psi\rangle$ which can be as large as $L \log_2(d)/2$, in which case there will be no efficient approximation by an MPO.

We observe that a product operator always maps to a product state, i.e., with bond dimension $\chi = 1$, and therefore with no entanglement between the sites:

$$\bigotimes_m \hat{O}^{[m]} = \bigotimes_m \left(\sum_{i,j} o^{[m]}_{j,i} |i\rangle_m \langle j|_m \right) \longmapsto \bigotimes_m \left(\sum_{i,j} o^{[m]}_{j,i} \Big| \begin{matrix} j \\ i \end{matrix} \Big\rangle_m \right). \tag{165}$$

Product operators, and eventually sums of a small number of those, e.g. correlators, form the majority of physically interesting quantities, namely those which are potentially measurable in real many body systems. What makes a Heisenberg picture dynamical simulation a promising approach, is the fact that we find no entanglement in them initially, i.e., at time $t = 0$.This is illustrated in Fig. 48.

The Heisenberg equation of motion for the operators, $i\partial_t \hat{O} = \left[\hat{O}, \hat{H}\right]$, gives rise to a Schrödinger type equation of motion for the "super-states", $i\partial_t |\hat{O}\rangle = \tilde{H}|\hat{O}\rangle$, with the new Hamiltonian

$$\tilde{H} = \mathbf{1} \otimes \hat{H} - \hat{H} \otimes \mathbf{1}. \tag{166}$$

Thus this "super-Hamiltonian" acts on the in- and out-chains independently. (In general the dynamics is however not just the dynamics of two independent chains, because the initial operator will be mapped to a state with strong entanglement between the in- and out-chain, equation (163).)

10 Dynamical simulation of integrable and non-integrable models in the Heisenberg picture[21]

In order to do Heisenberg picture simulations using e.g. the TEBD scheme, the operator $\hat{O}(t)$ at time t is expressed in terms of a matrix product operator (MPO). For typical observables this is straightforward for the initial time $t = 0$. Time evolution is then calculated by updating the matrices according to the Heisenberg equation of motion using a Trotter decomposition. Because this corresponds to a Schrödinger type equation of motion in the super space, efficient simulation again requires that the bond dimension of the MPO is limited to a maximum value χ. We restrict ourselves to open boundary conditions here, but this is not an issue for local operators as long as the time is shorter than time required to reach the boundaries, which is essentially given by system size over the finite speed at which information can spread through the system [LR72]. This means that only the χ largest Schmidt values in the Hilbert space of operators are kept, corresponding to a small operator-space entanglement between any two complementary partitions of the lattice. To quantify the entanglement of an operator $\hat{O}(t)$, which, as discussed in the previous section, can be viewed as state vector in operator space, we use the operator space Rényi entropies (OSRE):

$$S_\alpha = \frac{\log_2 \mathrm{Tr}\ \hat{\kappa}^\alpha}{1-\alpha} \geq S_\beta, \quad \beta > \alpha > 0 \tag{167}$$

Here $\hat{\kappa}$ is the corresponding reduced density matrix in operator space resulting from tracing out the left or right partition of the in- and out-doublechain at a given bond. In the limit $\alpha \to 1$, S_α is the well known von Neumann entropy, which is a good measure of bi-partite entanglement. For $\alpha \to 0$, S_α gives the dimension of the Hilbert space. Clearly for an MPO of bond dimension χ, the maximum for all Rényi entropies is $\log_2 \chi$. Although it is not yet fully established when a quantum state or an operator is faithfully represented by a matrix product with finite bond dimension, one can employ the results of Schuch et al. [SWVC08a] to show that efficient simulation is impossible if the Rényi entropies with $\alpha > 1$ scale faster than logarithmically with time. If $S_{\alpha>1}$ grows linearly in time, we must expect that the computational cost required to reach a certain accuracy, which is polynomial in χ, will grow exponentially with time (note that this is not necessarily true for S_α with $\alpha \leq 1$ [SWVC08a]). In fact for the time evolution of typical state vectors in the Schrödinger picture this is very often the case [SWVC08b]. On the other hand an at most logarithmic growth of $S_{\alpha>1}$ is a necessary condition for an efficient simulability. Although not sufficient, it also gives good indication when such a simulation is possible. In the following we

[21] This section is based on the publication [MUF11].

will discuss the time evolution of the OSRE for a generic model, the XXZ chain,

$$\hat{H} = -\frac{1}{2}\sum_j \left(\hat{\sigma}_j^x \hat{\sigma}_{j+1}^x + \hat{\sigma}_j^y \hat{\sigma}_{j+1}^y + \Delta \hat{\sigma}_j^z \hat{\sigma}_{j+1}^z\right), \tag{168}$$

where $\hat{\sigma}^{x,y,z}$ denote the Pauli matrices in the spin-$\frac{1}{2}$ case and the spin-1 matrices (eigenvalues $-1, 0, 1$) in the spin-1 case respectively. The spin-$\frac{1}{2}$ case is integrable for any value of the anisotropy Δ and maps to interacting fermions using the Jordan-Wigner transformation (99). For the special case of $\Delta = 0$ (spin-$\frac{1}{2}$ XX model) it can be mapped to free fermions.

10.1 Integrable models equivalent to free fermions

Let us consider the spin-$\frac{1}{2}$ XXZ model as a generic example of a 1D integrable model. We have calculated the time evolution of the OSRE S_2 for different types of simple operators using the TEBD scheme with open boundary conditions and a fourth order Trotter decomposition [SS99]. The restriction to open boundary conditions is not an issue for local operators as long as the time is shorter than the propagation time to reach the boundaries [LR72]. Although not shown the operator space von-Neumann entropy S_1 has the same scaling behavior. One clearly notices that the OSRE of all operators scales at most logarithmically in time, an observation made already by Prosen et al. for other integrable models [PP07, PP09]. In the special case of $\Delta = 0$ the entropy even saturates at a finite value for some operators like $\hat{\sigma}^z$ or products of operators at a small number of different lattice sites.

In the following we will provide an explanation of the entropy scaling for the case of the XX-model, i.e., for $\Delta = 0$, which can be mapped to free fermions. This will be done by reexpressing the XXZ model in terms of Majorana-fermion operators [Pro08]:

$$\begin{aligned} \hat{w}_{2j-1} &= \left(\prod_{l<j} \hat{\sigma}_l^z\right)\hat{\sigma}_j^x \\ \hat{w}_{2j} &= \left(\prod_{l<j} \hat{\sigma}_l^z\right)\hat{\sigma}_j^y. \end{aligned} \tag{169}$$

The Majorana operators are Hermitian and fulfill anti-commutation relations $\{\hat{w}_j, \hat{w}_l\} = 2\delta_{jl}$. The three types of interactions in the XXZ-model can be reexpressed as

$$\begin{aligned} \hat{\sigma}_j^x \hat{\sigma}_{j+1}^x &= -i\hat{w}_{2j}\hat{w}_{2(j+1)-1}, \\ \hat{\sigma}_j^y \hat{\sigma}_{j+1}^y &= i\hat{w}_{2j-1}\hat{w}_{2(j+1)}, \\ \hat{\sigma}_j^z \hat{\sigma}_{j+1}^z &= -\hat{w}_{2j-1}\hat{w}_{2j}\hat{w}_{2(j+1)-1}\hat{w}_{2(j+1)}. \end{aligned} \tag{170}$$

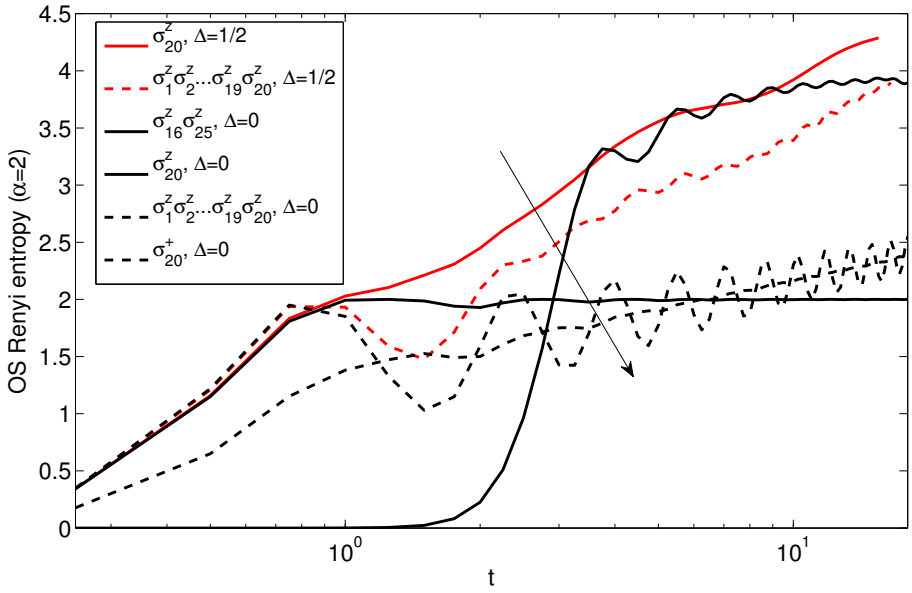

Figure 49: OSRE dynamics for the 40 site spin-$\frac{1}{2}$ XXZ model for a split in the center. The legend gives initial operator and anisotropy in the order in which the arrow cuts the graphs. Dashed lines mark infinite index operators (see text). $\chi = 1000$ is used in all cases and the numerical error is negligible on the time scale shown.

A complete basis in the operator space is given by

$$\hat{P}_\alpha = \prod_j \hat{w}_{2j-1}^{\alpha_{2j-1}} \hat{w}_{2j}^{\alpha_{2j}}, \tag{171}$$

where $\alpha \equiv (\alpha_1, \alpha_2, \dots)$ and $\{\alpha_l\} \in \{0,1\}^N$. We can now define adjoint-fermion annihilators and creators via

$$\begin{aligned} \hat{a}_j |\hat{P}_\alpha\rangle &= \alpha_j |\hat{w}_j \hat{P}_\alpha\rangle, \\ \hat{a}_j^\dagger |\hat{P}_\alpha\rangle &= (1-\alpha_j) |\hat{w}_j \hat{P}_\alpha\rangle, \end{aligned} \tag{172}$$

with $\{\hat{a}_j, \hat{a}_l^\dagger\} = \delta_{jl}$. Associating the adjoint vacuum $|\hat{P}_0\rangle$ with the unity operator $\mathbf{1}$, i.e., $|\mathbf{1}\rangle = |\hat{P}_0\rangle$, we can express all operators in terms of adjoint-fermion excitations [PP09]:

$$|\hat{P}_\alpha\rangle = \prod_j \left(\hat{a}_{2j-1}^\dagger\right)^{\alpha_{2j-1}} \left(\hat{a}_{2j}^\dagger\right)^{\alpha_{2j}} |\mathbf{1}\rangle. \tag{173}$$

Mapping the Heisenberg equation then gives a Schrödinger like equation for the evolution in operator space,

$$i\frac{d}{dt}\hat{P}_\alpha = \left[\hat{P}_\alpha, \hat{H}\right] \;\mapsto\; i\frac{d}{dt}|\hat{P}_\alpha\rangle = \left|\left[\hat{P}_\alpha, \hat{H}\right]\right\rangle =: \hat{\mathcal{H}}|\hat{P}_\alpha\rangle. \tag{174}$$

with a "super"-Hamiltonian $\hat{\mathcal{H}}$. Explicitly calculating the terms in the commutator for the XX-model via

$$\begin{aligned} |[\hat{P}_\alpha, \hat{\sigma}_j^x \hat{\sigma}_{j+1}^x]\rangle &= 2i\big(\hat{a}_{2j}^\dagger \hat{a}_{2(j+1)-1} - \text{h.a.}\big)|\hat{P}_\alpha\rangle, \text{ and} \\ |[\hat{P}_\alpha, \hat{\sigma}_j^y \hat{\sigma}_{j+1}^y]\rangle &= -2i\big(\hat{a}_{2j-1}^\dagger \hat{a}_{2(j+1)} - \text{h.a.}\big)|\hat{P}_\alpha\rangle \end{aligned} \tag{175}$$

yields the XX super-Hamiltonian

$$\hat{\mathcal{H}}_{XX} = i \sum_j \Big(\hat{a}_{2j}^\dagger \hat{a}_{2j+1} + \hat{a}_{2j-1}^\dagger \hat{a}_{2j+2} - \text{h.a.} \Big) \tag{176}$$

This Hamiltonian corresponds to two uncoupled chains of free fermions. The total number of adjoint fermions, $\sum_{m=1}^{2N} \hat{a}_m^\dagger \hat{a}_m$, is conserved. Note that the anisotropy Δ in the original XXZ Hamiltonian would introduce recombination and pair creation of adjoint fermions across the chains. Although the above mapping is non-local, operators acting only left of a given site j will be mapped to fermions that are again only left of the pair $\{2j-1, 2j\}$ of sites. So the OSRE of the original XX-model will be the same as the corresponding state vector Rényi entropy of two uncoupled chains of free fermions. Thus we have to calculate the entanglement dynamics of the two uncoupled chains with an initial state given by the operator in questions to get the OSRE in the XX model. The key point is that local operators are equivalent to very special, simple initial states in the corresponding fermion chains. We here have to distinguish between finite index operators (those that involve only a finite number of adjoint fermions after the mapping) and infinite index operators (involving a number proportional to the system size L). An example of the first kind is

$$|\hat{\sigma}_j^z\rangle = -i\hat{a}_{2j-1}^\dagger \hat{a}_{2j}^\dagger |\mathbf{1}\rangle \text{ (finite index)}. \tag{177}$$

Examples of the second kind arise either from local operators like

$$|\hat{\sigma}_j^x\rangle = i^{j-1} \left(\prod_{l=1}^{2(j-1)} \hat{a}_l^\dagger \right) \hat{a}_{2j-1}^\dagger |\mathbf{1}\rangle \text{ (infinite index)} \tag{178}$$

or non-local ones like

$$|\hat{F}\rangle = \left| \prod_{l=1}^{j-1} \hat{\sigma}_l^z \right\rangle = i^{j-1} \left(\prod_{l=1}^{2(j-1)} \hat{a}_l^\dagger \right) |\mathbf{1}\rangle \text{ (infinite index)}. \tag{179}$$

We proceed by showing that the bi-partite Rényi entropy S_2 for a system of free

fermions in 1D is strictly related to the number fluctuations in any one of the two partitions assuming a fixed total number. We can assume that the initial state of the fermions corresponding to the local operators of interest is a Gaussian state. Due to the free evolution it remains Gaussian and can be transformed into a product form $\hat{\rho} = \bigotimes_j \hat{\rho}_j$ where the $\hat{\rho}_j$ correspond to site j and have eigenvalues $\frac{1\pm\eta_j}{2}$, $|\eta_j| \leq 1$. The square of the variance of the total particle number in each partition is then [Kli06]

$$\Delta N_A^2 = \sum_{j\in A}(1-\eta_j^2)/4 = \Delta N_B^2. \tag{180}$$

On the other hand

$$\begin{aligned} S_2 &= -\log_2 \mathrm{Tr}\hat{\rho}^2 \\ &= -\sum_j \log_2\Big(1-(1-\eta_j^2)/2\Big). \end{aligned} \tag{181}$$

Using $\frac{2}{\ln 2}\frac{x}{2-x} \leq -\log_2(1-x) \leq \frac{1}{\ln 2}\frac{x}{1-x}$, where $0 \leq x \leq \frac{1}{2}$, one obtains

$$\frac{4}{\ln 2}\Delta N^2 \geq S_2 \geq \frac{2}{\ln 2}\Delta N^2. \tag{182}$$

For finite index operators we find saturation as can be seen in Fig. 49. This reflects the fact, that there is only a finite number M of free particles present in both chains together. Thus a finite χ of 2^M yields the exact solution [CPH+10, HPCP09] for all times[22]. For infinite index operators we observe logarithmic growth of the OSRE, see Fig. 49. While the infinite number of involved adjoint fermions may suggest a linear growth of ΔN^2, this is not the case as can be understood in the following way: The super state corresponding to an infinite index operator like $|\hat{F}\rangle$ (a finite size example of which is shown in Fig. 49) is filled up completely with fermions in the left part of the chains. Inside these regions the Pauli principle prevents hopping of fermions and thus only particles at the edge where the effective band-insulator is connected to the vacuum can move and fill the empty parts of the double chain. For the half filled chain Antal et al. have shown that $\Delta N^2 \cong (\ln t + D)/2\pi^2$ in the limit of large t with a known constant $D > 0$ [AKR08]. Other infinite index operators that result in an initial occupation of the two chains different from that of $|\hat{F}\rangle$ only on a finite number of sites show the same logarithmic long time behavior of the OSRE, see $|\hat{\sigma}^+\rangle$ at a single site, also shown in Fig. 49. This explains the logarithmical growth of the OSRE in the XX model as a generic example of an integrable model that can be

[22] S_2 remains finite also because $\Delta N^2 \xrightarrow{t\to\infty} \frac{M}{4}$ as the probability for a particle of being left or right becomes equal.

mapped to free fermions.

10.2 Non-integrable models

We now show that there is another class of systems and operators which may allow an efficient simulation of dynamics in the Heisenberg picture. We construct an upper bound for the OSRE S_α, $\alpha > 1$, in terms of the infinite-temperature auto-correlation function (ITAC). Without loss of generality we assume a normalized operator

$$\frac{1}{d^L}\mathrm{Tr}\left[\hat{O}^\dagger \hat{O}\right] = 1, \tag{183}$$

where d is the local dimension of the chain. With respect to a splitting of the chain of length L into two parts here and below all $\hat{A}$ act on the sub chain A of length L_A and all $\hat{B}$ on B of length L_B. Any operator can be represented as

$$\hat{O}\left(t\right) = \sum_{m,n} \Lambda_{mn}\left(t\right) \hat{A}_m \otimes \hat{B}_n \tag{184}$$

with orthonormal bases $\frac{1}{d^{L_\mathrm{A}}}\mathrm{Tr}\left[\hat{A}_n{}^\dagger \hat{A}_m\right] = \frac{1}{d^{L_\mathrm{B}}}\mathrm{Tr}\left[\hat{B}_n^\dagger \hat{B}_m\right] = \delta_{nm}$. Λ is a matrix and its singular values $\sqrt{\lambda_n}$, ($\lambda_1 \geq \lambda_2 \geq \ldots$ are the eigenvalues of the reduced density matrix in operator space $\hat{\kappa}$) are coefficients of a Schmidt decomposition $\hat{O}(t) = \sum_{n=1}^{\chi} \sqrt{\lambda_n}\hat{\mathcal{A}}_n(t) \otimes \hat{\mathcal{B}}_n(t)$. The Schmidt rank χ is at most $d^{2\min(L_\mathrm{A},L_\mathrm{B})}$. This allows to express the infinite-temperature auto-correlation function in terms of Schmidt coefficients. We find for $\alpha > 1$

$$\begin{aligned}
\left|\left\langle \hat{O}^\dagger(t)\hat{O}\right\rangle_{T=\infty}\right| &= \left|\mathrm{Tr}\left[\Lambda^\dagger\left(t\right)\Lambda\left(0\right)\right]\right| \\
&\leq \sum_{k=1}^{\chi} \sqrt{\lambda_k \lambda_k\left(0\right)} && (185) \\
&\leq \mathrm{Tr}\sqrt{\hat{\kappa}(0)} \left(\sum_{k=1}^{\chi} \frac{\sqrt{\lambda_k(0)}}{\mathrm{Tr}\sqrt{\hat{\kappa}(0)}} \lambda_k^{\frac{\alpha}{2}}\right)^{\frac{1}{\alpha}} && (186) \\
&= \left(\mathrm{Tr}\sqrt{\hat{\kappa}(0)}\right)^{1-\frac{1}{\alpha}} \left(\sum_{k=1}^{\chi} \lambda_k^\alpha\right)^{\frac{1}{2\alpha}} && (187)
\end{aligned}$$

In (185) we made use of von Neumann's trace inequality (see e.g. [Gan59]). Furthermore Jensen's inequality can be used because $x^{\frac{1}{\alpha}}$ is a concave function in x. Finally (187) is true by the Cauchy-Schwarz inequality. We thus obtain the following estimate for Rényi entropies, assuming an initial product operator, $\mathrm{Tr}\sqrt{\hat{\kappa}(0)} = 1$, for

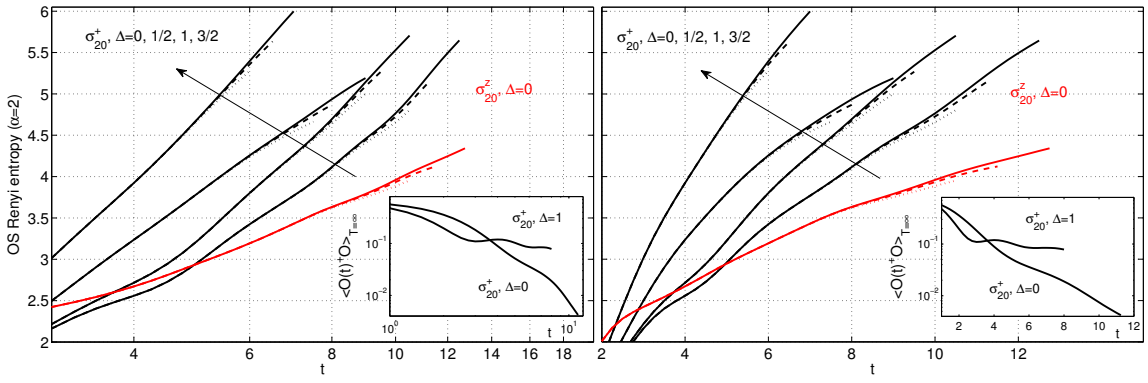

Figure 50: OSRE dynamics for the 40 site spin-1 XXZ model for a split in the center. Dotted, dashed, and solid lines indicate simulations using $\chi = 300$, $\chi = 500$, and $\chi = 1000$ respectively. The left panel features a logarithmic, the right panel a linear time scale. The curves show clear indication of the predicted long-time scaling. The insets show two corresponding ITAC curves for $\hat{\sigma}^+_{20}$ (note the logarithmic vertical scaling).

simplicity:

$$S_\alpha \leq \frac{2\alpha}{1-\alpha} \log_2 \left| \left\langle \hat{O}^\dagger(t)\hat{O} \right\rangle_{T=\infty} \right| \quad \text{for } \alpha > 1. \tag{188}$$

If the ITAC decays with a power law or even slower in time, S_α will grow at most logarithmically for $\alpha > 1$. The ITAC has been studied over decades in condensed matter physics as it is measured in nuclear magnetic resonance and neutron scattering experiments in magnetic spin chains. While not proved rigorously, it is believed that the Bloembergen-de Gennes conjecture [Blo49, DG58, KM63] of spin diffusion holds: If $\sum_{j=1}^{L} \hat{O}_j$ is a conserved quantity, then the ITAC of $\hat{O}_j$ will show diffusive behavior (i.e. scale as $\sim 1/\sqrt{t}$ in 1D). To our knowledge there is no counter example except for integrable models, where this diffusive behavior can turn into a ballistic one (i.e. $\sim 1/t$ in 1D) [FM98, Sir06]. Nevertheless it always remains slower than exponential. We conclude that in the Heisenberg picture TEBD we can expect S_2 to grow at most logarithmically in time, even if the model is non-integrable, if the initial operator belongs to a conservation law (for integrable systems there is an infinite number of those, but one is sufficient). This in turn indicates that for this special operator an efficient classical simulation should be possible for large times.

The spin-1 XXZ chain is an example of a non-integrable system, although extension to additional higher-order nonlinear terms may turn it into an integrable one [BT86, Sog84]. However the total z-magnetization $\sum_{j=1}^{L} \hat{\sigma}^z_j$ is conserved, where $\hat{\sigma}^z_j$ is now the z-component of the spin at lattice site j with eigenvalues $-1, 0, 1$. This conservation law will lead to a logarithmic scaling of S_2 for $\hat{\sigma}^z$. Fig. 50 shows numerical

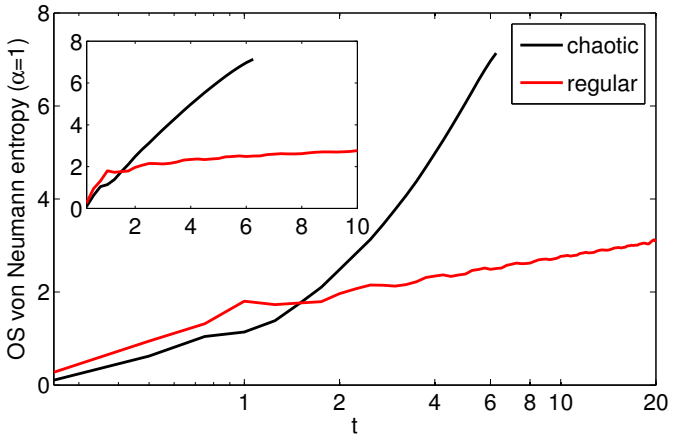

Figure 51: Operator space von Neumann entropy dynamics for the 40 site Ising model (189) for a split in the center. The initial operator is $\hat{\sigma}^x_{20}$. The time axis has logarithmic scale, while the insert shows the same curves with a linear time scale. The curves show clear indication of the predicted long-time scaling. Due to the lack of exploitable conserved quantities, in TEBD calculations we are limited to a block dimension of $\chi = 400$. The curves end where the cutoff error reaches $5 \cdot 10^{-3}$.

indication for this. It should be noted that the spin-1 model is computationally much harder than the spin-$\frac{1}{2}$ model since the local Hilbert space dimension is increased. Although we do observe logarithmic scaling of the OSRE corresponding to $\hat{\sigma}^z$, the matrix dimension χ up to the point where the cutoff error reaches 10^{-2}. A clear tendency is visible: On the logarithmic scale S_2 approaches a straight line, while in the linear plot a sub-linear scaling is evident. This is consistent with the expected logarithmic scaling of the OSRE. For $\hat{\sigma}^+$ Fig. 50 shows logarithmic scaling of S_2 only for $\Delta = 1$ because only then the total x- and y-magnetization are also conserved. Otherwise it indicates linear growth of S_2 with time. We can understand this now as a direct consequence of the Bloembergen-de Gennes conjecture, which predicts a power law rather than an exponentially decaying ITAC in the isotropic case (see insets of Fig. 50).

From the numerical results we can also extract the von Neumann entropy as a function of time. It scales exactly as S_2 in the spin-$\frac{1}{2}$ model for all operators we looked at. The results are not conclusive in the spin-1 case however, since the dependence on the matrix dimension χ used in the simulations is much stronger. At least they do not contradict the presumption, that again the scaling is the same as for S_2.

As another example the von Neumann entropy can be calculated using Heisenberg picture TEBD for the regular and chaotic Hamiltonians used in the work of Prosen and Žnidarič [PŽ07]. As representative regular (chaotic) model these authors

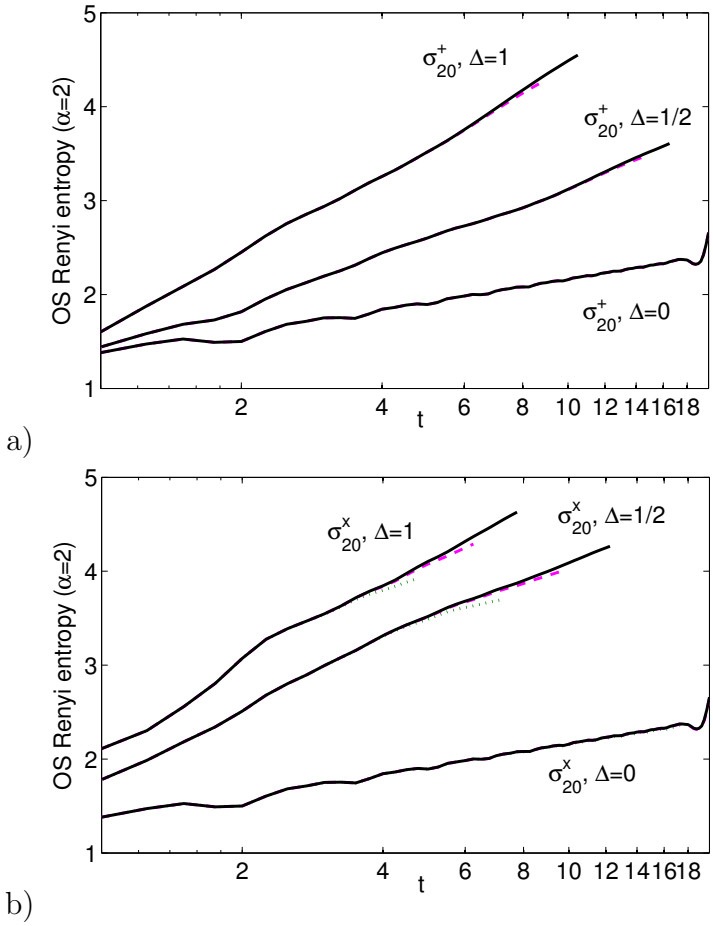

Figure 52: OSRE dynamics for the 40 site spin-1/2 XXZ model for a split in the center. a) $\hat{\sigma}^+_{20}$ – purple dashed and black solid lines indicate simulations using $\chi = 500$ and $\chi = 1000$ respectively. b) $\hat{\sigma}^x_{20}$ – green dotted, purple dashed, and black solid lines indicate simulations using $\chi = 100$, $\chi = 200$, and $\chi = 400$ respectively. The matrix dimension can be chosen larger for $\hat{\sigma}^+$ than for $\hat{\sigma}^x$, because the latter does not commute with the total particle number N and the resulting more efficient MPS representation, see section 11.1, can not be used. Note that although both operators are equivalent here ($\hat{\sigma}^z = \hat{\sigma}^+ + (\hat{\sigma}^+)^\dagger$) and therefore show the same logarithmic scaling of S_2, the prefactor is smaller in the $\hat{\sigma}^+$ case.

considered the quantum Ising model in a longitudinal (tilted) field,

$$\hat{H} = -\sum_j \left(\hat{\sigma}^x_j \hat{\sigma}^x_{j+1} + B_x \hat{\sigma}^x_j + B_z \hat{\sigma}^z_j \right), \tag{189}$$

with $B_x = 0$ and $B_z = 2$ ($B_x = B_z = 1$). We plotted the numerically calculated OSRE in Fig. 51. It shows the expected time dependence, i.e. logarithmic scaling in the regular and linear scaling in the chaotic case.

Finally note, that there are cases where the OSEE scales logarithmically with time, but this behavior can not be directly explained by the arguments presented in the present section: Fig. 52 shows S_2 for $\hat{\sigma}^+$ on a single site in the spin-1/2 XXZ model (and for $\hat{\sigma}^x$ which does not contain any additional information in this model because $\hat{\sigma}^x = \hat{\sigma}^+ + (\hat{\sigma}^+)^\dagger$). The scaling is logarithmic independently of the value of Δ. However a direct mapping to free fermions is only possible for an anisotropy of $\Delta = 0$. The operators are directly connected to conserved densities only for $\Delta = 1$. The logarithmic scaling for other values of the anisotropy can be ascribed to the integrability of the model, given that it is not observed in the spin-1 case above. However this connection can not be made directly via the arguments given here.

In summary, in this section we have given a simple explanation of the at most logarithmic time dependence of the OSRE S_2 for the spin-1/2 XX model as a generic integrable model that can be mapped to free fermions. The operator dynamics in that model is equivalent to two uncoupled chains of free fermions with an initial state corresponding to the operator under consideration. For local operators these initial states are rather simple. E.g. an operator $\hat{\sigma}_j^z$ corresponds to a single fermion in each chain. We have shown that the bi-partite OSRE S_2 is strictly related to the fluctuations of the fermion number in the two partitions, which in turn allowed a simple understanding of the entropy dynamics. We have shown furthermore that for any model, integrable or not, S_2 in operator space can be bound by the infinite-temperature auto-correlation function of the considered operator. This in turn means that for systems and observables for which the Bloembergen-de Gennes conjecture of spin diffusion holds, an at most logarithmic growth of the operator space entanglement is expected. The latter applies e.g. for local operators that constitute a global conservation law.

11 Particle number conservation in quantum many-body simulations with matrix product operators[23]

Particle number conservation is present in many non-relativistic model systems. It results from a global U(1) symmetry, i.e. the Hamiltonian is invariant under the transformation

$$\hat{a}_j \;\mapsto\; \hat{a}' = e^{i\phi}\hat{a}_j, \tag{190}$$

where ϕ is any real number. Particle number conservation is implemented in MPS algorithms routinely. Its explicit implementation is necessary if one wants to calculate ground state (section 3.5) or dynamical (sections 5 and 6) properties in the low filling limit, where the average number of particles per lattice site is small compared to 1, as it results e.g. from the discretization of a continuous model, section 3.

In DMRG-like dynamical simulations matrix product *operators* naturally arise either as density-operators at non-zero-temperature [VGRC04, ZV04] or in open systems [VGRC04, ZV04, HPCP09, PŽ09] or as general operators in the Heisenberg picture, see [PŽ07] and the preceding section. (The Hamiltonian itself can also be conveniently expressed [McC07] as an MPO of small bond dimension in the case of short-range interactions, which gives rise to elegant formulations of the algorithm [Sch11].) In this section we will focus on operators in the Heisenberg picture. Most of the results are however equally valid in the context of finite temperature calculations.

The purpose of the present work is to show how symmetries can be imposed on MPOs in general and to discuss the computational benefits and penalties. For simplicity, we will restrict the discussion to particle number conservation. It can be incorporated into MPOs on two levels: The first option reduces the Hilbert space dimension only halfway, as the operator is not projected onto a certain symmetry sector. It only requires the operator to annihilate (or create) a fixed number ΔN of particles (which might be zero),

$$\hat{O} = \sum_N \hat{P}_{N-\Delta N}\hat{O}\hat{P}_N, \tag{191}$$

where $\hat{P}_N$ is the projectors onto the N particle Hilbert space. This property is conserved under time-evolution with a particle-number conserving Hamiltonian. The operator is not restricted to any particular input particle number. We will therefore refer to this as the grand-canonical method[24]. The way the symmetry is imposed is

[23] This section is based on the publication [Mut11].

[24] We do however not require the operator to actually be a density matrix, which would imply

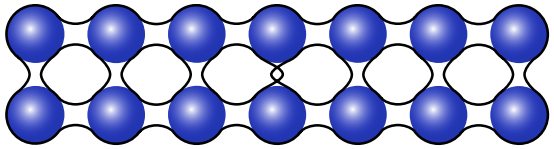

Figure 53: In the grand canonical Hilbert space a product operator can be interpreted as a state on a double chain, which can be in general maximally entangled locally, but not at all along the chain, see Fig. 48. If the operator is however projected to a certain particle number, the corresponding double-chain state gets entangled also along the chain. This entanglement can overcompensate the benefits from shrinking the Hilbert space, depending on the actual particle number in question.

then equivalent to the usual way of adjoining good quantum numbers to an MPO [Sch11]. This approach has already proven useful in practical calculations [MUF11] and introduces no entanglement overhead. With the second option, we however go a step further: The Hilbert space dimension is reduced further by projecting onto a symmetry sector. This second method of using the conservation law for MPOs restricts the operator to a particular input particle number. We will therefore refer to it as the canonical method. This approach however introduces additional entanglement in the MPO, as illustrated in Fig. 53. If the filling (number of particles per lattice site) is sufficiently low this is not a problem. However it can make the method less useful in the generic case.

In sections 11.1 and 11.2 we will discuss the two distinct ways of imposing particle number conservation onto MPOs in detail. Section 11.3 will give details on how to construct the projected operator in practice and gives exact results on the entanglement overhead introduced. Section 11.4 gives example calculations, which illustrate how the two methods and also the "brute force" method, where no symmetry is taken into account, perform in comparison.

11.1 Unprojected operators

To introduce the first method, which works in the grand-canonical Hilbert space, we observe that, because $\hat{H}$ conserves the total particle number, $\tilde{H}$ conserves the number *difference* between the in- and out- chains:

$$\left[\tilde{H}, \hat{N} \otimes \mathbf{1} - \mathbf{1} \otimes \hat{N}\right] = 0 \tag{192}$$

If we consider operators (191) which annihilate (or create) a fixed number of

$\Delta N = 0$

particles ΔN (like, e.g., the particle annihilation and creation operators $\hat{a}_m$ or $\hat{a}_m^\dagger$ at some given site m, and products of those) they will map to an eigenstates of this difference. (If $\hat{O}$ is a density matrix, $[\hat{O}, \hat{N}] = 0$ and therefore it is such an operator and $\Delta N = 0$.) Note that the identity on the whole Hilbert space,

$$\mathbf{1} = \bigotimes_m \mathbf{1}^{[m]} = \sum_N \hat{P}_N, \tag{193}$$

is a prototype of an operator of the form given in equation (191). ΔN now is a conserved quantity in the super-space. The Heisenberg dynamics will then take place only in a specific symmetry sector (with a fixed ΔN) and the MPO can be restricted accordingly. This can be done in exactly the same way as for MPS when the total number itself is conserved:

Consider the canonical form of the MPO and the Schmidt decomposition at two neighboring bonds, equation (164). If $|\hat{O}\rangle$ is a particle number difference eigenstate, then also the Schmidt vectors $|\alpha\rangle_\mathrm{A}$ and $|\beta\rangle_\mathrm{B}$ must be eigenstates of the particle number difference in their respective subsystems. By the notation used in (164), the local particle number difference $\Delta N_\mathrm{local} = \Delta N - \Delta N_\mathrm{A} - \Delta N_\mathrm{B} = j - i$ is thus determined from j, α and β alone,

$$j + \Delta N_\mathrm{B} = i - \Delta N_\mathrm{A} + \Delta N. \tag{194}$$

In an actual implementation (with no further local degrees of freedom) there is no second physical index i necessary in the Γ tensor. This particular form of the MPS can be kept during time evolution, using the scheme discussed in section 2.1. For details we refer the reader to the literature [DCJZ05, McC07, SZV10].

This grand-canonical method gives great advantage [MUF11] over the plain approach which works for general systems without conservation laws. A comparison for an example case will be given in section 11.4.

Before we continue to the second method, we take a look at the entanglement in this first approach. Therefore we give an explicit construction of the initial MPO in two steps. The first step is the construction of an MPO for the identity operator. This task is trivial, but we take a route that can be conveniently generalized in section 11.2: Given a state $\sum_{\vec{j}} c_{\vec{j}} |\vec{j}\rangle$, that is a superposition of Fock states, the mapping

$$|j\rangle_m \longmapsto |j\rangle_m \langle j|_m, \tag{195}$$

which is applied locally at every site m simultaneously, maps it to a superposition $\sum_{\vec{j}} c_{\vec{j}} |\vec{j}\rangle\langle\vec{j}|$ of projectors onto these Fock states. We get the identity matrix by su-

perimposing *all* Fock states with amplitude $c_{\vec{j}} = 1$,

$$\sum_{\vec{j}} |\vec{j}\rangle = \bigotimes_m \left(\sum_{j=0}^{d-1} |j\rangle_m \right) \longmapsto \bigotimes_m \left(\sum_{j=0}^{d-1} |j\rangle_m \langle j|_m \right) = \sum_{\vec{j}} |\vec{j}\rangle\langle\vec{j}| = \mathbf{1}. \tag{196}$$

It's MPO representation,

$$|\mathbf{1}\rangle \;=\; \sum_{\vec{j}} |\begin{smallmatrix}\vec{j}\\ \vec{j}\end{smallmatrix}\rangle = \bigotimes_m \left(\sum_{j=0}^{d-1} \left| \begin{smallmatrix} j \\ j \end{smallmatrix} \right\rangle_m \right) \tag{197}$$

thus has large entanglement between the two chains. The entanglement is however contained *within* the matrices themselves. There is no entanglement between different lattice sites, thus a bond dimension of $\chi = 1$ suffices. The matrices of the MPO are simply 1.

In the second step we get the MPO representation of $\hat{O}$ by *applying* $\hat{O}$ itself only to the out-chain of $|\mathbf{1}\rangle$,

$$|\hat{O}\rangle = \sum_{\vec{i},\vec{j}} o_{\vec{i},\vec{j}} \left| \begin{smallmatrix} \vec{j} \\ \vec{i} \end{smallmatrix} \right\rangle = \left(\mathbf{1} \otimes \hat{O} \right) |\mathbf{1}\rangle. \tag{198}$$

A typical observable will be reasonably simple, e.g., a two point correlator $\hat{a}^\dagger_m \hat{a}_m \hat{a}^\dagger_{m'} \hat{a}_{m'}$ which is a product operator. Another one is a local current $i \left(\hat{a}^\dagger_j \hat{a}_{j+1} - \hat{a}^\dagger_{j+1} \hat{a}_j \right)$ for which $\chi = 2$. Then its MPO will also have a simple form. This will change dramatically however, if we project the operator to the subspace of a given particle number, as discussed in the next section.

11.2 Projected operators

This method works in the canonical Hilbert space. $\tilde{H}$ does of course not only conserve the number difference between the two chains, but also the total numbers in the in-chain, $\hat{N}^{(\mathrm{in})} = \hat{N} \otimes \mathbf{1}$, and in the out-chain, $\hat{N}^{(\mathrm{out})} = \mathbf{1} \otimes \hat{N}$, *separately*:

$$\left[\tilde{H}, \hat{N} \otimes \mathbf{1} \right] = \left[\tilde{H}, \mathbf{1} \otimes \hat{N} \right] = 0 \tag{199}$$

However MPO representations for general operators (191) are not eigenstates of any of these. Taking into account particle number conservation in each chain separately therefore only applies to operators that are nonzero only in a given symmetry sector. If we project the operator to a given input particle number N, i.e., take only one of

the summands in (191),

$$\hat{O}_N = \hat{P}_{N-\Delta N}\hat{O}\hat{P}_N, \tag{200}$$

we find an eigenstate of the total particle number in the upper *and* in the lower chain simultaneously. Thus when working in the canonical Hilbert space, particle number conservation can be used twice:

If in (164) $|\hat{O}\rangle$ is a particle number eigenstate in both chains, then also the Schmidt vectors $|\alpha\rangle_\mathrm{A}$ and $|\beta\rangle_\mathrm{B}$ must be eigenstates of the particle number in both chains in their respective subsystems. The local particle numbers i and j are thus determined from α and β alone,

$$\begin{aligned} N_\mathrm{A}^{(\mathrm{in})} + j + N_\mathrm{B}^{(\mathrm{in})} &= N \\ N_\mathrm{A}^{(\mathrm{out})} + i + N_\mathrm{B}^{(\mathrm{out})} &= N - \Delta N. \end{aligned} \tag{201}$$

In an actual implementation (with no further local degrees of freedom) there are no physical indices i and j at all necessary in the Γ tensor. This particular form of the MPS can again be kept during time evolution. Thereby the T tensor, equation (81), will break up into even smaller blocks, speeding up the calculation of it's singular value decomposition even more than in the grand-canonical method.

We get the MPO representation of $\hat{O}_N$ by applying $\hat{O}$ itself to the out-chain of the MPO representation of $\hat{P}_N$,

$$|\hat{O}_N\rangle = |\hat{P}_{N-\Delta N}\hat{O}\hat{P}_N\rangle = \left(\mathbf{1}\otimes\hat{O}\right)|\hat{P}_N\rangle. \tag{202}$$

$\hat{P}_N$ is now the identity *only in the sector of particle number* N. It vanishes in the remains of the grand canonical Hilbert space. $\hat{P}_N$ takes the role as a prototype of a projected operator, analogous to the identity in (198). The difficulty of the second approach results from the fact that $\hat{P}_N$ is clearly not a product operator, but entangled between sites, as illustrated in Fig. 53. We will construct it explicitly in section 11.3.

Working with the canonical method has the advantage, that we do not have to limit the local dimension explicitly to d, as $d < N$ is automatically fulfilled, which comes in handy, e.g., for bosonic models.

Of course $\hat{O}$ and $\hat{O}_N$ are not equivalent. But in certain cases this is not relevant, e.g. if $\hat{O}$ is an observable (which implies $\Delta N = 0$), and we evolve $\hat{O}$ in time using Heisenberg t-DMRG in order to find the dynamics of its expectation value. Then the result is the same using $\hat{O}_N$ if the state $|\Psi_0\rangle$ of the system for which we want to calculate the expectation value is a particle number eigenstate, $\hat{N}|\Psi_0\rangle = N|\Psi_0\rangle$:

$$\langle\Psi_0|\hat{O}_t|\Psi_0\rangle = \langle\Psi_0|\hat{P}_N\hat{O}_t\hat{P}_N|\Psi_0\rangle = \langle\Psi_0|\left(\hat{P}_N\hat{O}\hat{P}_N\right)_t|\Psi_0\rangle \tag{203}$$

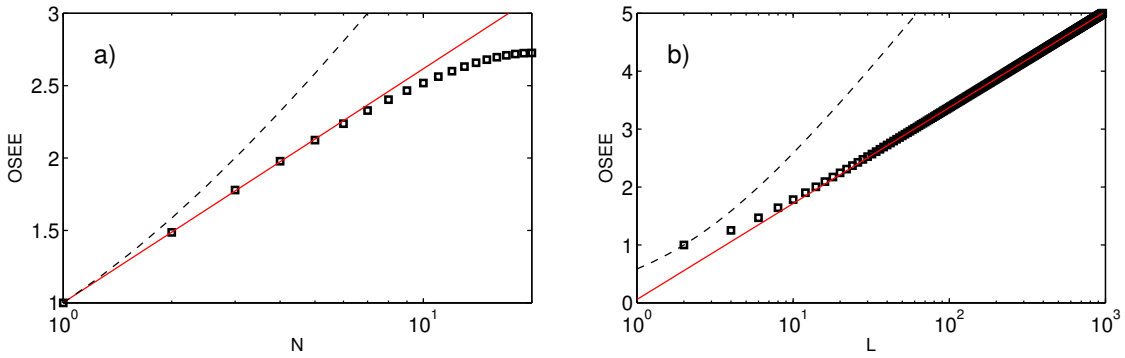

Figure 54: Logarithmic scaling of the OSEE of the projector $\hat{P}_N$ at the center of the chain with particle number N and system size L. We show $S^{[L/2]}$ in a system of fermions ($d = 2$) on a lattice, a) as a function of N for fixed system size $L = 40$. (Note that as $N > L/2$ the entropy goes down again due to the Pauli principle and particle hole symmetry.) b) as a function of L for a fixed filling of $N/L = 1/2$. – Symbols are from the numerical evaluation of (205). Straight lines show fits to these. Dashed lines show the upper limit (210). We checked numerically, that also for a higher local dimension d the prefactor of the logarithmic scaling actually stays much below this limit.

An example of this type is given for a bosonic model at the end of section 11.4.

11.3 Preparing the projector onto the subspace of a fixed particle number

What is left is the construction of the MPO representation of $|\hat{P}_N\rangle$. Following the arguments in section 11.1 for the construction of $|\mathbf{1}\rangle$, this reduces to preparing an MPS that is a superposition of all Fock states *with total particle number* N, which will be discussed in the following. The operationally simple mapping (195) together with (163) will transform it to $|\hat{P}_N\rangle$.

Let us denote the normalized, equal superposition of all N-particle Fock states which are locally constrained to a maximum particle number of $d-1$ by $|N\rangle$. If we want to work without a local constraint, we set $d = N + 1$. Given a bi-partition of our lattice we note that its Schmidt decomposition is

$$|N\rangle = \sum_{l=0}^{N} \lambda_l^{[m]} |l\rangle_{\mathrm{A}} \otimes |N-l\rangle_{\mathrm{B}}. \tag{204}$$

The sub-chain A comprises sites 1 to m, the sub-chain B comprises sites $m+1$ to L. This shows that the MPS will have bond dimension $\chi = N + 1$. ${\lambda_l^{[m]}}^2$ is the

probability of finding l particles left of bond m:

$$\lambda_l^{[m]\,2} = \frac{\Omega_d\,(l,m)\,\Omega_d\,(N-l,L-m)}{\Omega_d\,(N,L)}. \tag{205}$$

Here $\Omega_d(n,L)$ is the number of possibilities to distribute n indistinguishable particles among L sites in such a way that no site is occupied by more than $d-1$ particles, given by the recursion formula [Fre56]

$$\Omega_d(n,L) = \sum_{j=0}^{\min(n,d-1)} \Omega_d(n-j,L-1); \quad \Omega_d(n,0) = \delta_{n0}. \tag{206}$$

For $d=2$ this reduces to $\Omega_2(n,L) = \binom{L}{n}$, for $d>n$ it reduces to $\Omega_{d>n}(n,L) = \binom{L+n-1}{n}$.

We continue with the Schmidt decomposition at the following bond. (Repeating it for all bonds leads to the canonical form of the MPS.) Here the remaining task is to determine the coefficients of

$$|N\rangle = \sum_{l=0}^{N}\sum_{r=0}^{N} \lambda_l^{[m]}\Gamma_{lr}^{[m+1]}\lambda_r^{[m+1]}|l\rangle_{\mathrm{A}} \otimes |r-l\rangle_{m+1} \otimes |N-r\rangle_{\mathrm{B}'}. \tag{207}$$

The λ tensors are already known from (205). The sub-chain B′ comprises sites $m+2$ to L. Thus $\Gamma_{lr}^{[m+1]\,2}\,\lambda_r^{[m+1]\,2}$ is the probability of finding $N-r$ particles at the right side of bond $m+1$ *provided that there are already l particles at the left of bond m*:

$$\begin{aligned}\Gamma_{lr}^{[m+1]\,2}\,\lambda_r^{[m+1]\,2} &= \frac{\Omega_d(r-l,1)\Omega_d(N-(r-l),L-1)}{\Omega_d(N,L)} \times \\ &\times \frac{\Omega_d(l,m)\Omega_d(N-r,L-m-1)}{\Omega_d(N-(r-l),L-1)} \times \frac{1}{\lambda_l^{[m]\,2}}.\end{aligned} \tag{208}$$

Equations (205) and (208) determine the Γ and λ tensors completely. Thus we can calculate the coefficients of the MPS exactly. By means of (195) and (163) this also yields the MPO representation of $\hat{P}_N$:

$$|N\rangle \overset{(195)}{\longmapsto} \frac{\hat{P}_N}{\sqrt{\Omega_d(N,L)}} \overset{(163)}{\longmapsto} \frac{|\hat{P}_N\rangle}{\sqrt{\Omega_d(N,L)}}. \tag{209}$$

The Γ matrices do not have physical indices explicitly, because the local particle numbers are given by the bond indices (due to particle number conservation), l and r here. Note that in this particular case, the value of the bond index has a physical

meaning[25], namely the particle number at the left side of the bond m considered. The absence of physical indices is especially useful for bosonic systems, because the local Hilbert space dimension must not artificially be cut-off.

This construction shows the main difficulty of going to the canonical version of the MPO: Even the trivial operator $\hat{P}_N$ has an extensive bond dimension of $\chi = N + 1$. The initial entanglement, even of a local operator, is no longer only between the chains but also along the chain, see the illustration in Fig. 53 and the example in Fig. 56. Although computations can be done with a higher bond dimension here, this advantage is often overcompensated by the initial entanglement. However a linear growth of the matrix dimension does not imply, that the algorithm is inefficient. In contrast, the required matrix dimension in general grows exponentially with *time*[CC05], which is a more severe limitation. Here, a linear scaling of the matrix dimension implies that the OSEE scales only logarithmically with system size,

$$S^{[m]} = -\sum_{l=0}^{L} {\lambda_l^{[m]}}^2 \log_2 \left({\lambda_l^{[m]}}^2 \right) \leq \log_2(N+1), \tag{210}$$

which is favorable[26]. This entropy is minor compared to the entropy which has to be added on top for time evolution. Beyond that, for a low over all particle number N, the entropy that can be generated dynamically is bounded or at least drastically reduced. Longer times can then be reached as we will see in the example of the next section.

In fact the upper bound (210) is not even tight, as shown in Fig. 54. For details on the relation between the scaling of the entropy and the efficiency of an MPS see [SWVC08a].

11.4 Examples

As first example we take the spin-$\frac{1}{2}$ XXZ chain

$$\hat{H} = -\frac{1}{2} \sum_{\langle m,n \rangle} \left(\hat{\sigma}_m^x \hat{\sigma}_n^x + \hat{\sigma}_m^y \hat{\sigma}_n^y + \Delta \hat{\sigma}_m^z \hat{\sigma}_n^z \right), \tag{211}$$

where the $\hat{\sigma}$ denote the Pauli matrices and the sum runs over all nearest neighbors. The U(1) symmetry (rotation around the z-axis) of the system implies conservation

[25] I.e., here we have a one to one correspondence between index and good quantum number.

[26] Actually the polynomial scaling of the matrix dimension can be taken as the definition of efficient. The nontrivial problem in general is to show that from the logarithmic scaling of the entanglement entropy one can conclude that there exist efficient approximations by MPS, see, e.g. [VC06].

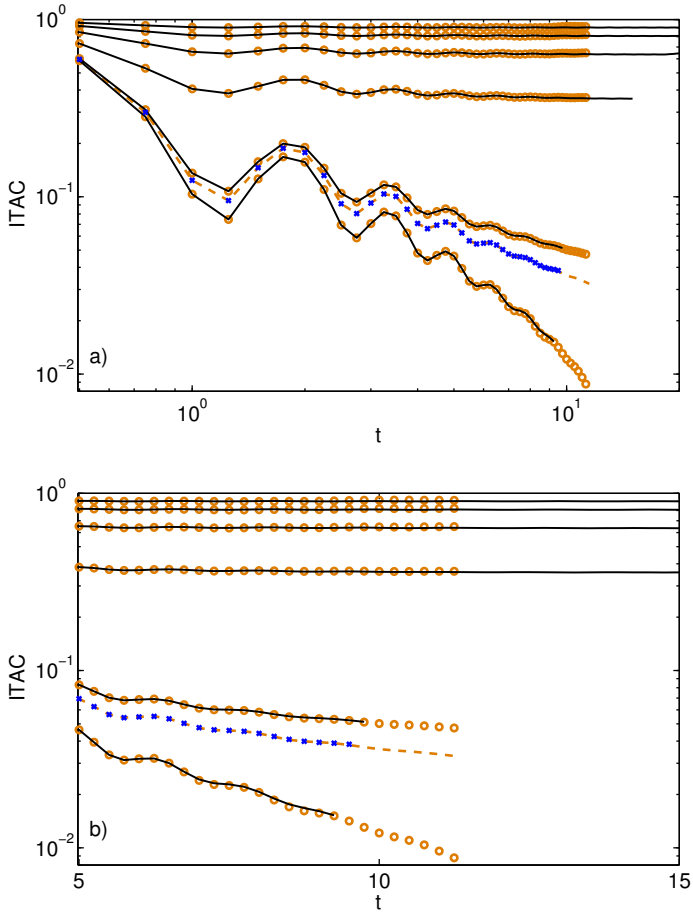

Figure 55: Spin-$\frac{1}{2}$ XXZ-chain of length $L = 40$ at $\Delta = 0.8$, time evolution in the Heisenberg picture. ITAC at site $m = 20$: $\mathfrak{Re}\,[C_N(t)]$ ($N = 1, 2, 4, 8, 16, 20$ from top down, calculated using the canonical (solid line) and the grand-canonical method (orange circles)) and $\mathfrak{Re}\,[G(t)]$ calculated from the unprojected (dashed orange) and a "brute force" method (blue crosses) the latter ignoring particle number conservation completely. a) double logarithmic plot to emphasize the power law behavior of the ITAC. b) same data as a), but linear time axis for better visibility of the difference in time reached by the different methods (and in the different symmetry sectors in case of the projected method). Bond dimensions used where $\chi = 4000$ in the canonical calculations, $\chi = 1000$ for the grand-canonical example, and $\chi = 500$ in the "brute force" calculation. All curves end at the point where the accumulated cut-off error reaches 10^{-2}. The TEBD algorithm is used with time step size $1/4$ in all cases. Curves are shown only up to $t = 20$. At later times boundary effects show up, because the excitations have propagated to the end of the chain.

of the total magnetization $\hat{M}_z = \sum_m \hat{\sigma}^z_m$. Via a Wigner-Jordan transformation this transforms into particle number conservation in the equivalent fermion lattice model.

The properties of the model depend strongly on the anisotropy Δ. E. g., in the

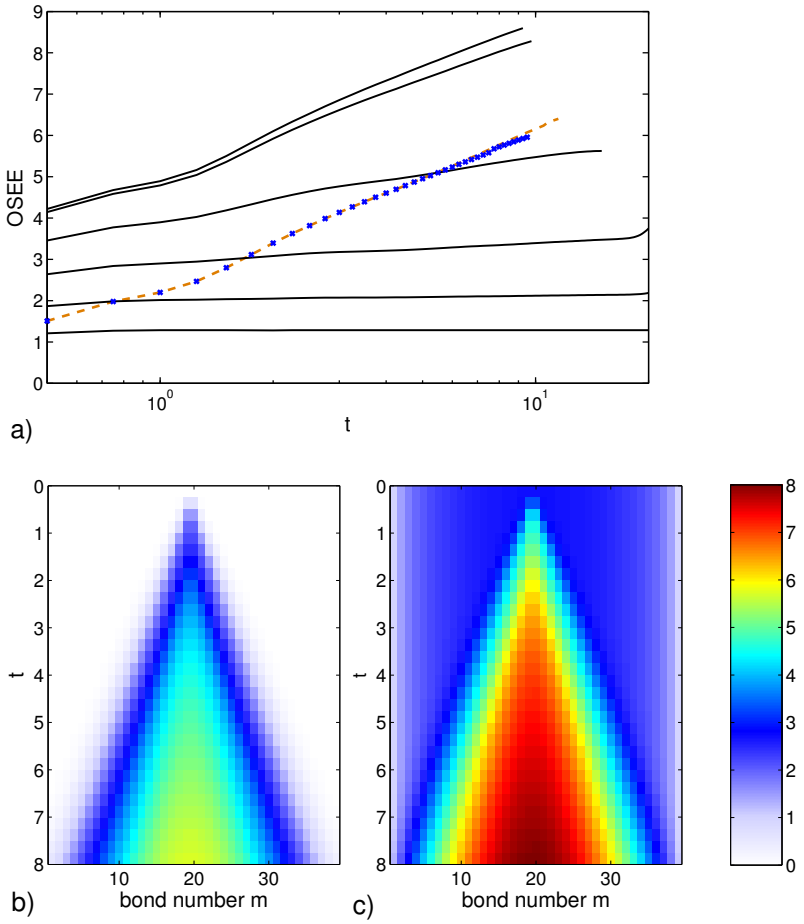

Figure 56: Spin-$\frac{1}{2}$ XXZ-chain of length $L = 40$ at $\Delta = 0.8$, time evolution in the Heisenberg picture. a) OSEE $S^{[20]}(t)$ of $\hat{P}_N \hat{\sigma}^z_{20} \hat{P}_N$ (solid, $N = 1, 2, 4, 8, 16, 20$ from bottom up) and $\hat{\sigma}^z_{20}$ (dashed: from canonical, crosses: from "brute force" calculation without taking symmetry constraints into account at all). Panels b) and c) both show the OSEE $S^{[m]}(t)$ between sites m and $m+1$. Initial operators are b) $\hat{\sigma}^z_{20}$ (calculated using the grand-canonical method) and c) $\hat{P}_{16} \hat{\sigma}^z_{20} \hat{P}_{16}$ (calculated using the canonical method). The same data sets as in Fig. reffig:delta08 are used.

critical regime, $|\Delta| < 1$, spin transport is believed to be ballistic, while in the gapped regime $|\Delta| > 1$ it seems diffusive [PŽ09]. A quantity of interest in this context is the infinite temperature auto-correlation function (ITAC)

$$\langle \hat{O}_l^\dagger \hat{O} \rangle_{T=\infty} = \mathrm{Tr}\left[\hat{O}_l^\dagger \hat{O} \hat{\rho}_{T=\infty} \right] \tag{212}$$

for $\hat{O} = \hat{\sigma}^z_m$ at a given lattice site m. The expectation value is taken at infinite temperature, which makes it straight forward to calculate it from the Heisenberg

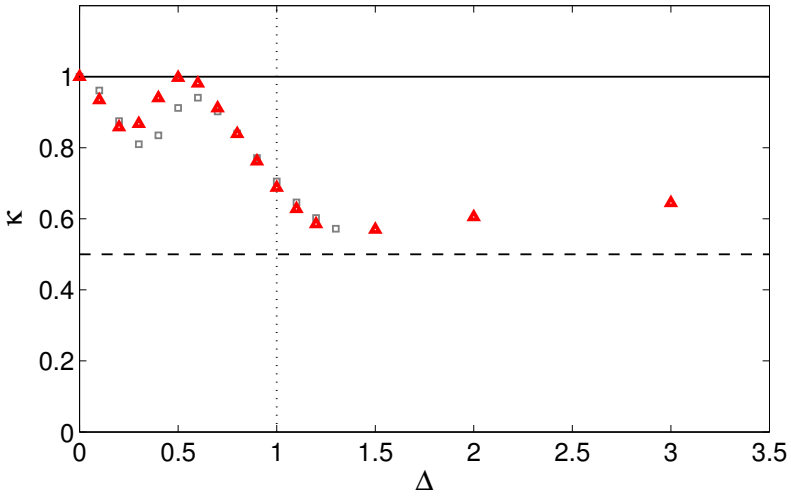

Figure 57: Exponent κ of the decay of the ITAC in ths spin-$\frac{1}{2}$ XXZ model as a function of the anisotropy parameter Δ. Red triangles show TEBD calculations using unprojected operators with the same parameters as in Fig. 55. The gray boxes indicate the original results [FM98] using exact diagonalization. In Both cases the exponent is extracted using the fitting function (213).

picture time evolution[27]. In general it decays as $t^{-1/2}$, an observation usually called spin diffusion.

In the spin-$\frac{1}{2}$ chain this behavior has been confirmed numerically for $\Delta \gtrsim 1$. Around $\Delta = 1$ there is a change towards a t^{-1} power law, which is the exact asymptotic behavior at $\Delta = 0$. However the exponents are hard to extract numerically, especially for Δ around 1 and larger, because of the limited timescales accessible. In the grand canonical ensemble there exist exact diagonalization [FM98], as well as transfer matrix DMRG [Sir06] studies. The Heisenberg picture t-DMRG results using unprojected operators presented here reproduce these results, see Fig. 57. The timescale accessible with Heisenberg picture t-DMRG is somewhat larger. For the value of $\Delta = 0.8$ we find an exponent for the decay of $\kappa \approx -0.83$ from the data shown

[27]Note that the infinite temperature density matrix of any system is proportional to the unity operator. Therefore from the definition of the ITAC, we see that in order to calculate it we have to do the same in the Schrödinger picture (take $\mathrm{Tr}\left[\hat{O}^\dagger \cdot \hat{U}_t \hat{O} \mathbf{1} \hat{U}_t^\dagger\right]$, where $\hat{U}_t$ is the full propagator) and in the Heisenberg picture (take $\mathrm{Tr}\left[\hat{U}_t^\dagger \hat{O}^\dagger \mathbf{1} \hat{U}_t \cdot \hat{O}\right]$). In fact this is an example where the requirement of using a mixed state in the Schrödinger picture makes it exactly as demanding as the Heisenberg picture calculation.

in Fig. 55 using an empirical fitting function proposed in [FM98],

$$\langle \hat{O}_t^\dagger \hat{O} \rangle_{T=\infty} \approx t^\kappa \left[A + B e^{-\gamma(t-t_0)} \cos\left(\Omega(t-t_0)\right) \right], \tag{213}$$

applied in a least squares fit to the data in the range $t = 3$ to $t = 11.5$. Although this value for the exponent is slightly closer to -1 than in previous calculations [FM98, Sir06], a decisive conclusion whether there is a sudden change of the exponent at $\Delta = 1$ can not be drawn.

We calculate the ITAC here to compare the power of the different methods discussed above. In Fig. 55 we show Heisenberg picture t-DMRG results for the normalized ITAC at $\Delta = 0.8$ both in the grand canonical ensemble,

$$G(t) = \langle (\hat{\sigma}_m^z)_t \, \hat{\sigma}_m^z \rangle_{T=\infty} = \mathrm{Tr}[(\hat{\sigma}_m^z)_t \, \hat{\sigma}_m^z]/2^L, \tag{214}$$

as well as in the canonical ensemble,

$$C_N(t) = \langle (\hat{\sigma}_m^z)_t \, \hat{\sigma}_m^z \rangle_{T=\infty} = \mathrm{Tr}\left[\left(\hat{P}_N \hat{\sigma}_m^z \hat{P}_N \right)_t \hat{\sigma}_m^z \right] \Big/ \binom{L}{N}. \tag{215}$$

Because $\mathrm{Tr}\left[\left(\hat{P}_M \hat{O} \hat{P}_N \right)_t \hat{O} \right] = \mathrm{Tr}\left[\hat{P}_M \hat{O}_t \hat{P}_N \hat{O} \right] = \mathrm{Tr}\left[\hat{O}_t \hat{P}_N \hat{O} \hat{P}_M \right]$ we can calculate the latter from both the projected, time-evolved or the unprojected, time-evolved $\hat{\sigma}_m^z$. The behavior in the canonical ensemble is as expected: For low filling, $C_N(t)$ decays only to a finite value. (From combinatorial arguments we find that $1 - C_N(t) \leq 4N/L$.) Therefore at half filling $C_N(t)$ has to be smaller than $G(t)$, because the latter is the weighted average

$$G(t) = \frac{1}{2^L} \sum_{n=0}^{N} \binom{L}{n} C_n(t). \tag{216}$$

Fig. 55 shows, that for low filling the canonical approach is clearly superior. However for generic filling ($N = L/2$ corresponds to a total magnetization of 0) longer times can be reached with the grand-canonical algorithm. All curves shown are calculated using about the same computational resources. In order to propagate $\hat{P}_N \hat{\sigma}_{20}^z \hat{P}_N$ for half filling up to the same point in time with the same accuracy as $\hat{\sigma}_{20}^z$ an increase of computation time and memory by an order of magnitude would be required. The reason becomes apparent in Fig. 56a. The OSEE scales logarithmically both in the grand-canonical and the canonical picture for generic filling. This is expected from [PŽ07, MUF11]. In fact the OSEE looks the same for both $\hat{\sigma}_{20}^z$ and $\hat{P}_N \hat{\sigma}_{20}^z \hat{P}_N$, but the latter is shifted by the entanglement present in the initial MPO. The cut-off error in the algorithm therefore grows faster and the calculation breaks down earlier. In this example the higher bond dimension available for fixed particle number does not

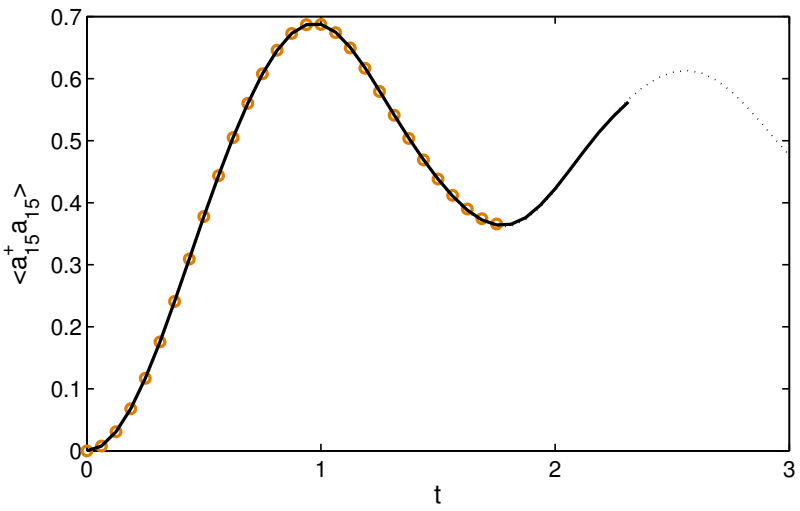

Figure 58: Expectation value of the local density at site 15 on a Bose Hubbard lattice (restricted to local dimension $d = 4$) of length $L = 30$ at $U = 10$ initially prepared in the state $|0101\ldots0101\rangle$, calculated using the projected (solid, black) and the unprojected method (orange circles). Bond dimensions used where $\chi = 2000$ in the canonical calculations, $\chi = 500$ in the grand canonical. Both curves end at the point where the accumulated cut-off error reaches 10^{-3}. The dashed line shows the result of a Schrödinger picture calculation which can be regarded exact, as the cut-off error is numerically zero at this time scale. The TEBD algorithm is used with time step size 1/16 in all three cases.

quite make up for this. Vice versa, to propagate $\hat{\sigma}^z_{20}$ up to $t = 20$, as can be done easily for $\hat{P}_N\hat{\sigma}^z_{20}\hat{P}_N$ for low filling, would also require an increase of computational resources by orders of magnitude.

The OSEE as a function of both lattice position and time is shown in Fig. 56b-c. The light cone like appearance is imposed by causality[28]. It confirms that there will be no finite size effects in the center of the system before times close to 20. The projected operator is distinguished from the unprojected mainly by the fact, that there is initial entanglement away from the center (which is where $\hat{\sigma}^z_{20}$ acts nontrivial), compare to the illustration given in Figs. 48 and 53. It is constant in time, as $|\hat{P}_N\rangle$ is an eigenstate of $\tilde{H}$. The entanglement generated dynamically seems to merely add.

Fig. 55 also shows a "brute force" calculation for $G(t)$, that does not take into account particle number conservation at all. It is clearly inferior to the unprojected method, section 11.1. Again a huge increase in computational resources would be required to reach the same accuracy.

[28]More rigorous result[BHV06, EO06] of this reasoning have been provided in terms of Lieb-Robinson bounds.

As a second example we take the Bose Hubbard model,

$$\hat{H} = -J \sum_{\langle m,n \rangle} \left(\hat{a}_m^\dagger \hat{a}_n + h.a. \right) + \frac{U}{2} \sum_m \hat{a}_m^\dagger \hat{a}_m^\dagger \hat{a}_m \hat{a}_m. \tag{217}$$

The $\hat{a}^\dagger$ and $\hat{a}$ operators are bosonic creation and annihilation operators. The first sum is again over nearest neighbors. For convenience, we set the hopping parameter $J = 1$. Recently there is a lot of interest in the thermalization of far-from equilibrium states (not only in this model). Cramer et al. [CFM+08] investigated the dynamics of the "anti-ferromagnetic" state $|\Psi_0\rangle = |0101 \ldots 0101\rangle$ using Schrödinger picture t-DMRG. They propose an experimental setup to prepare this state and observe its dynamics in an experiment using ultracold atoms in optical lattices. First measurements have been reported recently [TCF+11].

Fig. 58 shows the dynamics of the local density at site $m = 15$ in a system of total length $L = 30$. Again the size has been chosen large enough, such that there are no boundary effects arriving at the center for the times shown. The figure shows the expectation value in the state $|\Psi_0\rangle$ (where site 15 is empty) calculated using both the unprojected, $\langle \Psi_0 | \left(\hat{a}_{15}^\dagger \hat{a}_{15} \right)_t | \Psi_0 \rangle$, and the projected method, $\langle \Psi_0 | \left(\hat{P}_{15} \hat{a}_{15}^\dagger \hat{a}_{15} \hat{P}_{15} \right)_t | \Psi_0 \rangle$. Since $|\Psi_0\rangle$ is a particle number eigenstate, both expectation values are identical and coincide with a Schrödinger picture calculation, $\langle \Psi_0 |_t \hat{a}_{15}^\dagger \hat{a}_{15} | \Psi_0 \rangle_t$.

Again both curves are calculated using approximately the same numerical resources. For performance purposes, we restrict the local Hilbert space to $d = 4$. We find that using the projected operator we can calculate up to considerably larger times. So here the canonical method is ahead of the grand-canonical, *even* if the particle number N is of the order of $L/2$, in contrast to the first example. While the canonical method is only moderately affected by a higher local dimension $d > 4$ ($d = 16$ being the largest meaningful number here), the unprojected one breaks down as the Hilbert space dimension increases (not shown in the figure).

Although the timescales reachable are not large enough to see the local density equilibrate at $\frac{1}{2}$ for any of the methods, a Schrödinger picture calculation is actually the method of choice in this example, as the timescale reachable is still significantly larger[CFM+08] than in the Heisenberg picture. This is true in spite of the fact, that the local density is a conserved density and in the Heisenberg picture we therefore expect much better scaling of the OSEE with time[MUF11]. It can be explained by the overhead of having to include high local occupation numbers in the Heisenberg picture (in contrast to the above spin-$\frac{1}{2}$ example), which are actually not populated dynamically for the given initial state. This is a quite general drawback of the Heisenberg picture calculation whenever the local degree of freedom is large, not necessarily

because the particles are bosons, but also, e.g., for higher spin models. In the case of a highly entangled or mixed initial state, the two pictures might compare differently. Another overhead introduced by allowing for higher local occupation numbers is the introduction of higher energy scales, because the maximum local interaction energy in the truncated Bose Hubbard model is $\frac{U}{2}(d-1)(d-2)$. Therefore time steps Δt must be reduced as d^{-2} if a Suzuki Trotter expansion is used, to keep track of the time evolution correctly.

The two different approaches to include particle number conservation into an MPO have quite different effects on the performance of a Heisenberg-picture t-DMRG. The grand-canonical method brings the advantages known from ordinary (t-)DMRG, namely, the reduction of the Hilbert space dimension without introducing any additional entanglement. It is the method of choice in the presence of an appropriate symmetry. The Hilbert space dimension can be further reduced by projecting the MPO to a certain symmetry-sector. The effect then is quite counter-intuitive. Although the projected operators do only contain a small subset of the information present in the grand-canonical MPO, their propagation in time is not always easier. This is due to the entanglement introduced by fixing the total particle number. (The identity is not a product operator if projected to a symmetry sector.) In the low filling case, the reduction of the Hilbert space dimension is more important and we gain access to longer times. For generic filling however, the grand-canonical method remains superior.

Appendices

A Free bosons quenched in a periodic system

In this appendix we employ the Gaudin transformation [Gau83, KBI93, JPGB08, BPG08] to study an interaction quench in the Lieb-Liniger models starting from the ground state of free bosons. It will turn out, that it does not work in general, because the resulting, transformed wave function can not be normalized.

We assume a ring of length $L = 1$ with N identical bosons initially in a coherent superposition, $\Phi_0(x_1, \ldots, x_N) = 1$. We work in the fundamental sector $R_1 : x_1 < x_2 < \cdots < x_N$. We decompose

$$\Phi_0(x_1, \ldots, x_N) = 1 = \sum_{k_1 < \cdots < k_N} a_{k_1,\ldots,k_N} \Psi_{k_1,\ldots,k_N}(x_1, \ldots, x_N) \tag{218}$$

into eigenfunctions of N free fermions on the ring,

$$\Psi_{k_1,\ldots,k_N}(x_1, \ldots, x_N) = \frac{1}{\sqrt{N!}} \left| \left\{ e^{i \cdot 2\pi \cdot k_l x_m} \right\}_{ml} \right|, \tag{219}$$

$k_1, k_2, \ldots, k_N \in \mathbb{Z}$.

We get the free fermionic wave function at finite time t as

$$\Psi(x_1, \ldots, x_N; t) \;=\; \sum_{k_1 < \cdots < k_N} a_{k_1,\ldots,k_N} e^{it \sum_{j=1}^N \frac{(2\pi)^2 k_j^2}{2}} \Psi_{k_1,\ldots,k_N}(x_1, \ldots, x_N). \tag{220}$$

Clearly we get an exact revival for $2\pi t \in \mathbb{Z}$.

The Gaudin transformation yields the bosonic wave function for finite interaction strength c. In R_1 it reads

$$\begin{aligned}
\Phi(x1, \ldots, x_N; t) &= \mathcal{N}_{c,\Psi} \mathcal{O}_c \Psi(x_1, \ldots, x_N; t) \\
&= \mathcal{N}_{c,\Psi} \prod_{1 \le m < n \le N} \left[1 + \frac{1}{c} (\partial_n - \partial_m) \right] \Psi(x_1, \ldots, x_N; t) \\
&= \mathcal{N}_{c,\Psi} \sum_{k_1 < \cdots < k_N} a_{k_1,\ldots,k_N} e^{it \sum_{j=1}^N \frac{(2\pi)^2 k_j^2}{2}} \times \\
&\quad \times \underbrace{\prod_{1 \le m < n \le N} \left[1 + \frac{1}{c} (\partial_n - \partial_m) \right] \Psi_{k_1,\ldots,k_N}(x_1, \ldots, x_N)}_{= \mathcal{O}_c \Psi_{k_1,\ldots,k_N}(x_1,\ldots,x_N)},
\end{aligned} \tag{221}$$

with a normalizing factor $\mathcal{N}_{c,\Psi}$ that depends on the interaction strength c as well as on the wave function transformed. At $t = 0$ we do get back the initial bosonic wave function Φ_0 as required. The construction of a fermionic wave function that maps to

the initial bosonic wave function under the Gaudin transformation is usually a tricky task, but not here, because the derivatives in $\mathcal{O}_c$ all vanish.

To find the normalizing factor, we calculate

$$\begin{aligned}\mathcal{O}_c\Psi_{k_1,\ldots,k_N}(x_1,\ldots,x_N) &= \frac{1}{\sqrt{N!}}\sum_{p\in\mathbb{P}(\{1,\ldots,N\})}(-1)^p\mathcal{O}_c\prod_{j=1}^{N}e^{i2\pi k_{p(j)}x_j}\\ &= \frac{1}{\sqrt{N!}}\sum_{p\in\mathbb{P}(\{1,\ldots,N\})}(-1)^p\times\\ &\quad\times\left[\prod_{1\le m<n\le N}\left(1+\frac{2\pi i}{c}(k_{p(n)}-k_{p(m)})\right)\right]\prod_{j=1}^{N}e^{i2\pi k_{p(j)}x_j}\end{aligned} \tag{222}$$

Note that the plain waves are eigenfunctions of $\mathcal{O}_c$ and while the phase of the eigenvalue depends on the permutation, its absolute value does not, and we get explicitly (see also [KBI93])

$$\sqrt{\|\mathcal{O}_c\Psi_{k_1,\ldots,k_N}(x_1,\ldots,x_N)\|^2} =: \frac{1}{\mathcal{N}_{c,k_1,k_2,\ldots,k_N}} = \prod_{1\le m<n\le N}\sqrt{1+\left(\frac{2\pi}{c}\right)^2(k_n-k_m)^2}. \tag{223}$$

Using the fact, that $\mathcal{O}_c\Psi_{k_1,\ldots,k_N}$ does again form an orthogonal set with respect to the ks, we get

$$\frac{1}{\mathcal{N}_{c,\Psi}} = \sqrt{\sum_{k_1<\cdots<k_N}\left(\frac{a_{k_1,\ldots,k_N}}{\mathcal{N}_{c,k_1,\ldots,k_N}}\right)^2}. \tag{224}$$

As shown explicitly for three particles below, this sum does in general not converge for $c<\infty$ and our choice of initial conditions $\Phi_0=1$. This fact is reflected in the very discontinuous character of the fermionic wave function at finite t, as illustrated in Fig. 59.

A.1 Explicit calculation for three particles

In the case $N=3$ we have

$$\begin{aligned}a_{k_1<k_2<k_3} &= \sum_{p\in\mathbb{P}(\{1,2,3\})}\iiint_{R_1}dx^3\; e^{-i\cdot2\pi\left(k_{p(1)}x_1+k_{p(2)}x_2+k_{p(3)}x_3\right)}\\ &= \delta(k_2)\delta(k_1+k_3)\frac{i\sqrt{6}}{\pi}\eta(k_3) = a_{k_3>0},\end{aligned} \tag{225}$$

where we use

$$\eta(k) = \begin{cases} 0 & k = 0 \\ \frac{1}{k} & k \neq 0 \end{cases} \quad \text{and} \quad \delta(k) = \begin{cases} 1 & k = 0 \\ 0 & k \neq 0 \end{cases} . \tag{226}$$

We get the free fermionic wave function at finite time t as

$$\Psi(x_1, \ldots, x_N; t) = \sum_{k_3>0} a_{k_3} e^{it(2\pi)^2 k_3^2} \Psi_{k_3}(x_1, \ldots, x_N). \tag{227}$$

The symmetry of the a coefficients allows us to restrict ourselves to use only the fermionic wave functions where $k_3 > 0$, $k_2 = 0$, and $k_1 = -k_3$:

$$\begin{aligned} \Psi_{k_3}(x_1, \ldots, x_N) &= 2i[\sin(2\pi k_3(x_3 - x_1)) - \\ &\quad - \sin(2\pi k_3(x_2 - x_1)) - \sin(2\pi k_3(x_3 - x_2))] \end{aligned} \tag{228}$$

The bosonic wave function then follows as

$$\begin{aligned} \Phi(x1, \ldots, x_3; t) &= \mathcal{N}_c \sum_{k_3>0} a_{k_3} e^{it(2\pi)^2 k_3^2} \prod_{1 \leq m < n \leq N} \left[1 + \frac{1}{c}(\partial_n - \partial_m)\right] \Psi_{k_3}(x_1, \ldots, x_N) \\ &= \mathcal{N}_c \sum_{k_3>0} a_{k_3} e^{it(2\pi)^2 k_3^2} \Phi_{k_3}(x_1, \ldots, x_N), \end{aligned} \tag{229}$$

with the unnormalized bosonic wave function

$$\begin{aligned} \Phi_{k_3}(x_1, \ldots, x_3) = -\frac{1}{\sqrt{6}} \frac{2i}{c^3} \Big\{ & \quad c(c^2 + 4k_3^2\pi^2) \left[\sin(2\pi k_3(x_2 - x_1)) + \sin(2\pi k_3(x_3 - x_2))\right] \\ & + \; c(20k_3^2\pi^2 - c^2) \sin(2\pi k_3(x_3 - x_1)) \\ & + \; 4k_3\pi(c^2 + 4k_3^2\pi^2) \left[\cos(2\pi k_3(x_2 - x_1)) + \cos(2\pi k_3(x_3 - x_2))\right] \\ & + \; 8k_3\pi(2k_3^2\pi^2 - c^2) \cos(2\pi k_3(x_3 - x_1)) \Big\}. \end{aligned} \tag{230}$$

Using

$$\frac{1}{\mathcal{N}_{c,k_3}} = \sqrt{1 + \left(\frac{2\pi}{c}\right)^2 (2k_3)^2} \left[1 + \left(\frac{2\pi}{c}\right)^2 k_3^2\right]. \tag{231}$$

the normalizing constant reads

$$\begin{aligned}
\frac{1}{\mathcal{N}_c^2} &= \sum_{k_k>0} \left(\frac{a_{k_3}}{\mathcal{N}_{c,k_3}}\right)^2 \\
&= \sum_{k_3>0} \left|\frac{i\sqrt{6}}{\pi k_3}\right|^2 \left\{\sqrt{1+\left(\frac{2\pi}{c}\right)^2 (2k_3)^2}\left[1+\left(\frac{2\pi}{c}\right)^2 k_3^2\right]\right\}^2 \\
&\geq \frac{6}{\pi^2}\sum_{k_3>0} \frac{\left[1+\left(\frac{2\pi}{c}\right)^2 k_3^2\right]^3}{k_3^2} = \begin{cases} 1 & c=\infty \\ \infty & 0<c<\infty \end{cases}
\end{aligned} \tag{232}$$

So we can not directly sum up (229) numerically. This might be connected to the fact, that there are no singularities in the Bethe ansatz solution of the Lieb-Liniger model, except at $\gamma = 0$ [LL63, Lie63], which we have taken as initial condition here. A look at the fermionic wave function, Fig. 59, shows that it appears to have an infinite number of singularities, and the derivatives in $\mathcal{O}_c$ yield no useful results.

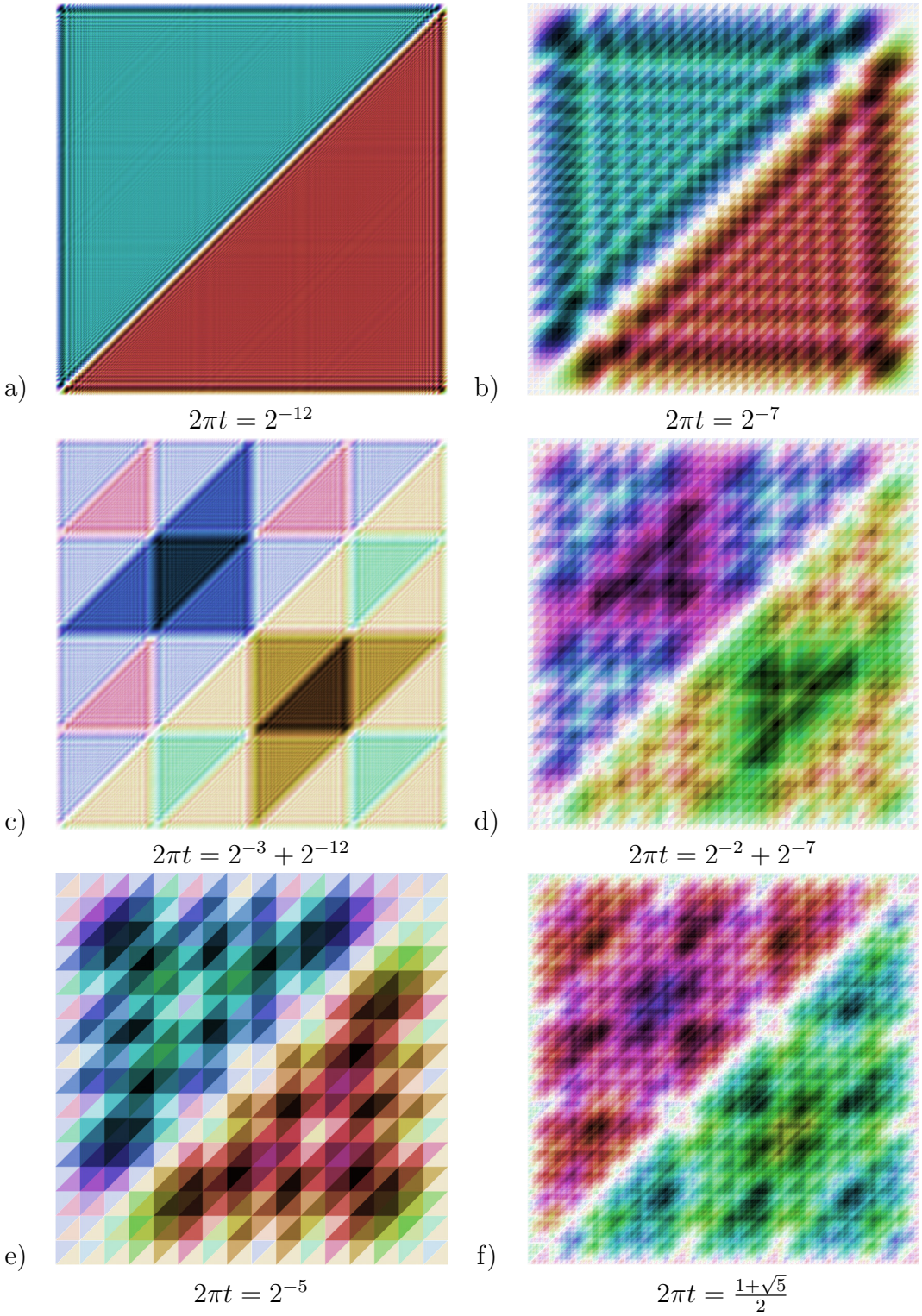

Figure 59: Fermionic wave function $\Psi(0, x_2, x_3; t)$ at different times (darkness = absolute value, hue = phase). Note the interference effects, resulting in the duality of wave fronts made out of triangles (b) and triangles made out of wave fronts (c), the regular but discontinuous structure for times where $2\pi t$ is a ratio of two small integers (e), and the fractal structure for irrational $2\pi t$ such as the golden ratio (f).

B Transmission of a particle through a domain wall

Here we calculate the probability of transmission of a particle with quasi-momentum k through a domain wall, as per Eq. (149). For the particle incident from the left, we solve the stationary Schrödinger equation using the standard scattering ansatz for the wave function,

$$\psi_j = \begin{cases} e^{ikj} + \rho e^{-ikj} & j \leq 0 \\ \tau e^{ik'j} & j \geq 0 \end{cases}, \tag{233}$$

where ρ and τ are the complex reflection and transmission amplitudes. The energy eigenvalue is $E_k = E_k^{(\mathrm{A})} = -2J_\mathrm{A}\cos(k) = -2J_\mathrm{B}\cos(k') = E_{k'}^{(\mathrm{B})}$, and therefore the refraction is given by

$$k' = \cos^{-1}\left(\frac{\cos(k)}{\alpha}\right). \tag{234}$$

Thus the transmission vanishes if $\cos(k) \geq \alpha$, where $\alpha = J_\mathrm{B}/J_\mathrm{A}$. (In this thesis we are primarily concerned with the case of $\alpha = 1/2$, except for section 8.5.)

Continuity at $j = 0$ implies $1 + \rho = \tau$, which together with the Schrödinger equation at $j = 0$,

$$(\hat{H}\psi)_0 = -J_\mathrm{A}\psi_{-1} - J_\mathrm{B}\psi_1 = E_k\psi_0, \tag{235}$$

yields

$$\rho = \frac{J_\mathrm{B}e^{ik'} + J_\mathrm{A}e^{-ik} - 2J_\mathrm{A}\cos(k)}{-J_\mathrm{B}e^{ik'} - J_\mathrm{A}e^{ik} + 2J_\mathrm{A}\cos(k)}. \tag{236}$$

The current density in the two parts of the system is given by

$$f_j = \begin{cases} f_j^{(\mathrm{A})} = -iJ_\mathrm{A}(\psi_j^*\psi_{j+1} - \psi_j\psi_{j+1}^*) & j < 0 \\ f_j^{(\mathrm{B})} = -iJ_\mathrm{B}(\psi_j^*\psi_{j+1} - \psi_j\psi_{j+1}^*) & j \geq 0 \end{cases}. \tag{237}$$

One can readily verify that

$$\frac{\mathrm{d}}{\mathrm{d}t}\psi_j^*\psi_j = (-i\hat{H}\psi)_j^*\psi_j + \psi_j^*(-i\hat{H}\psi)_j = -(f_j - f_{j-1}). \tag{238}$$

For the state of Eq. (233), we have

$$f_\mathrm{in} = 2J_\mathrm{A}\sin(k), \tag{239a}$$

$$f_\mathrm{ref} = -2J_\mathrm{A}\sin(k)\rho^*\rho, \tag{239b}$$

$$f_\mathrm{trans} = 2J_\mathrm{B}\sin(k')\tau^*\tau, \tag{239c}$$

so that the reflection and transmission probabilities are

$$R = \left|\frac{f_{\rm ref}}{f_{\rm in}}\right| = \rho^*\rho, \tag{240}$$

$$T = \left|\frac{f_{\rm trans}}{f_{\rm in}}\right| = \alpha\frac{\sin(k')}{\sin(k)}\tau^*\tau. \tag{241}$$

On can verify that $T + R = 1$ as it should.

C Two particle Hamiltonian in momentum space

We consider a pair of distinguishable, locally interacting particles on a lattice described by Hamiltonian

$$\begin{aligned}\hat{H} = & -J_a\left(\sum_{j=1}^{L-1}\hat{a}_j^\dagger\hat{a}_{j+1} + \gamma\hat{a}_L^\dagger\hat{a}_1 + \text{H.a.}\right)\\ & -J_t\left(\sum_{j=1}^{L-1}\hat{t}_j^\dagger\hat{t}_{j+1} + \gamma\hat{t}_L^\dagger\hat{t}_1 + \text{H.a.}\right)\\ & +U\sum_{j=1}^{L}\hat{a}_j^\dagger\hat{a}_j\hat{t}_j^\dagger\hat{t}_j,\end{aligned} \tag{242}$$

where the periodic and open boundary conditions correspond, respectively, to $\gamma = 1$ and $\gamma = 0$. The operators $\hat{a}_j^\dagger$ and $\hat{t}_j^\dagger$ create soft-core particles interacting via U, which is convenient for the exact numerical simulations presented in section 8.3.2.

In momentum representation, $k = 2\pi\nu/L$ ($\nu = \lfloor -\frac{L}{2} + 1\rfloor \ldots \lfloor\frac{L}{2}\rfloor$), we have $\hat{a}_k^\dagger = \frac{1}{\sqrt{L}}\sum_{j=1}^{L} e^{ikj}\hat{a}_j^\dagger$ and $\hat{t}_k^\dagger = \frac{1}{\sqrt{L}}\sum_{j=1}^{L} e^{ikj}\hat{t}_j^\dagger$ and the two particles have probability L^{-1} to be on the same site. The Hamiltonian then reads

$$\begin{aligned}&\hat{H} =\\ &-2J_a\sum_k \cos(k)\hat{a}_k^\dagger\hat{a}_k + \frac{(1-\gamma)J_a}{L}\sum_{k,k'}\hat{a}_k^\dagger\hat{a}_{k'}(e^{ik} + e^{-ik'})\\ &-2J_t\sum_k \cos(k)\hat{t}_k^\dagger\hat{t}_k + \frac{(1-\gamma)J_t}{L}\sum_{k,k'}\hat{t}_k^\dagger\hat{t}_{k'}(e^{ik} + e^{-ik'})\\ &+\frac{U}{L}\sum_{k,k',k''}\hat{a}_k^\dagger\hat{a}_{k'}\hat{t}_{k''}^\dagger\hat{t}_{(k+k''-k')}.\end{aligned} \tag{243}$$

D Effective theory for monomers and trimers

The non-locality of the effective theory presented in section 8.4.1 might seem surprising at first sight. From the point of view of quantum information theory, however, the Hamiltonian (153) is still local, in the sense that the commutator $[\tilde{H}_j, \tilde{H}_{j'}]$ vanishes except for $j' = j \pm 1$, despite the fact that the support of any two $\tilde{H}_j, \tilde{H}_{j'}$ has a large overlap. This property should always be conserved in any effective theory, since it guarantees that correlations in the model system travel with the same maximal velocity as in the full system [BHV06, EO06]. This property also permits the application of the TEBD numerical method, in conjunction with the conservation of the total particle number, to the effective model. For then all the basis states used in the TEBD (eigenstates of the reduced density matrices for all bi-partitions of the lattice) are, by construction, the eigenstates of the total particle number in the corresponding subsystem. Since the total particle number is the only observable that enters Hamiltonian (153) via $\hat{P}_j^{\vec{n}}$, this type of non-locality does not introduce additional difficulties in the use of the TEBD method.

The effective model can also be extended to higher orders in perturbation theory. In second order, this introduces nearest neighbor interactions, local potentials and effective exchange between monomers and trimers. All these terms are of the order of J^2/U and depend on Θ, which can now assume four different values depending on the type of bond between sites j and $j+1$. Another term of the same order describes hole defect hopping to the next-nearest neighbor site in the cluster. As this is spanning three sites, it also depends on the state of the central site and requites more values of Θ. The presence of such a longer-range term would necessitate a more general numerical simulation algorithm than TEBD. We have verified, however, that the effective Hamiltonian (154) containing only the terms first order in J already captures all the essential physics discussed in this paper.

In Fig. 60 we compare the dynamics of hole defects obtained from the full and effective models, which agree very well for large interaction strength $U \gg J$. Observe, however, that a local theory neglecting the motion of the cluster boundaries, Fig. 60(d), and therefore violating the conservation of the total number of dimers and bare particles, does not describe the dynamics quantitatively correct.

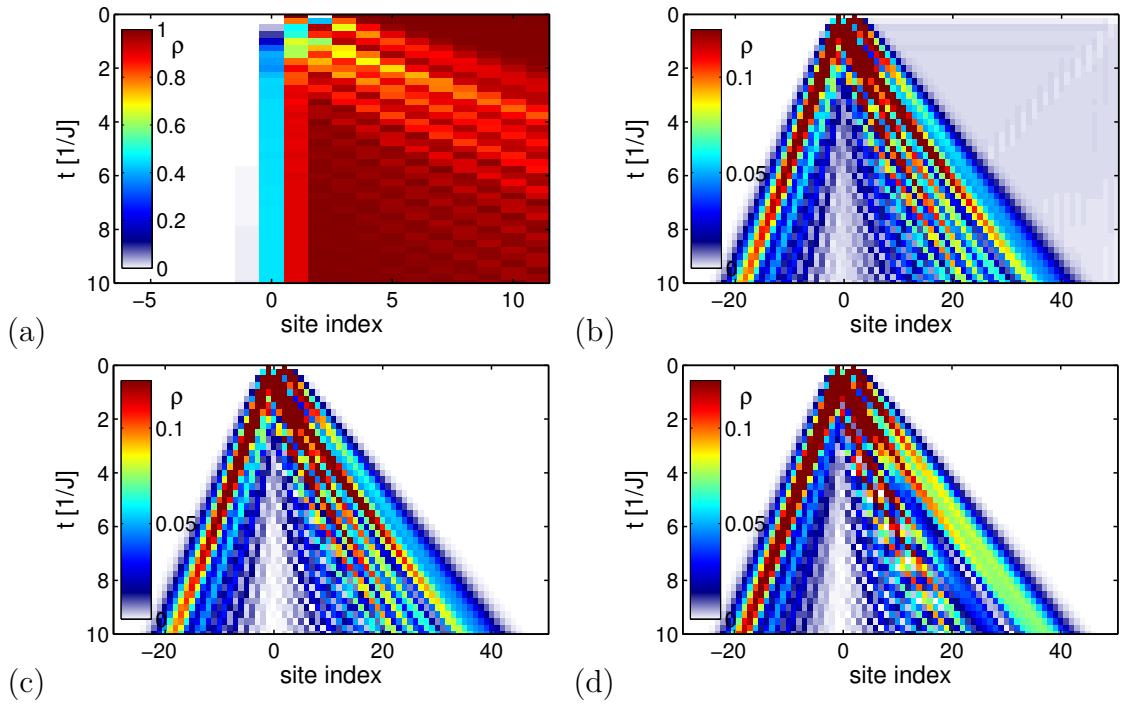

Figure 60: (Color online) Comparison of the full Bose-Hubbard dynamics, Eq. (13) with $U = 100J$, (a) and (b), with the effective model, Eq. (153), (c). The initial state contains a MI cluster of dimers on sites $j \geq 1$ and localized monomers at sites $j = -1$ and $j = 2$. The density of dimers is shown in (a), and the density of monomers in (b)-(d). Note that the cluster boundary is shifted upon particle crossing, which manifests in (a) as a smoothing of step in the dimer density. The effective Hamiltonian without moving boundaries, $\hat{H} = \sum_{j=1}^{L-1} \hat{H}_j^{[\Theta(j)]}$, yields the dynamics of (d).

E MPS representation of a state with particles in a given single particle state

Here we show how to construct an exact MPS representation for a lattice containing a fixed number of bosons each in a certain single particle state. The resulting MPS will be in the canonical representation [PGVWC07] and symmetric [Sch11], i.e., it will be an eigenstate of the total particle number by construction. The construction is analogous to that of matrix product operators for fixed total particle number [Mut11], see section 11.3.

The single particle state is given by a normalized wave-function ϕ_j. In the examples of section 8.4.2, we have $\phi_j = \frac{1}{\sqrt{L}} e^{ikj}$ with fixed momentum k, while for the harmonic oscillator ground state used in section 5 ϕ_j would be a discretized version of a Gaussian function, but what follows is really general. The corresponding state $|\Psi^1\rangle = \sum_{j=1}^{L} \phi_j \hat{a}_j^\dagger |0\rangle$ can be written as

$$|\Psi^1\rangle = \left(\sqrt{q_m}\hat{a}_\mathrm{A}^\dagger + \sqrt{1-q_m}\hat{a}_\mathrm{B}^\dagger\right)|0\rangle_\mathrm{A} \otimes |0\rangle_\mathrm{B}, \tag{244}$$

where sub-lattice A spans sites 1 to m and sub-lattice B is from $m+1$ to L, while $q_m = \sum_{j=1}^{m} \phi_j^* \phi_j$ is the single particle probability of being in A. The bosonic creation operators $\hat{a}_\mathrm{A}^\dagger$ and $\hat{a}_\mathrm{B}^\dagger$ are defined by

$$\hat{a}_\mathrm{A}^\dagger = \frac{1}{\sqrt{q_m}} \sum_{j=1}^{m} \phi_j \hat{a}_j^\dagger, \quad \hat{a}_\mathrm{B}^\dagger = \frac{1}{\sqrt{1-q_m}} \sum_{j=m+1}^{L} \phi_j \hat{a}_j^\dagger. \tag{245}$$

The many-particle state of the lattice with N particles in the same single particle state can then be expressed as

$$\begin{aligned} |\Psi^N\rangle &= \frac{1}{\sqrt{N!}}\left(\sqrt{q_m}\hat{a}_\mathrm{A}^\dagger + \sqrt{1-q_m}\hat{a}_\mathrm{B}^\dagger\right)^N |0\rangle_\mathrm{A} \otimes |0\rangle_\mathrm{B} \\ &= \frac{1}{\sqrt{N!}} \sum_{l=0}^{N} \binom{N}{l} \\ &\quad \times \left(\sqrt{q_m}\hat{a}_\mathrm{A}^\dagger\right)^l \left(\sqrt{1-q_m}\hat{a}_\mathrm{B}^\dagger\right)^{N-l} |0\rangle_\mathrm{A} \otimes |0\rangle_\mathrm{B}, \end{aligned} \tag{246}$$

and the density matrix of the system is

$$\begin{aligned}
&|\Psi^N\rangle\langle\Psi^N| \\
&= \frac{1}{N!}\sum_{l,l'=0}^{N}\binom{N}{l}\binom{N}{l'} \\
&\times\left(\sqrt{q_m}\hat{a}_{\mathrm{A}}^{\dagger}\right)^{l}|0\rangle_{\mathrm{A}}\langle 0|_{\mathrm{A}}\left(\sqrt{q_m}\hat{a}_{\mathrm{A}}\right)^{l'} \\
&\otimes\left(\sqrt{1-q_m}\hat{a}_{\mathrm{B}}^{\dagger}\right)^{N-l}|0\rangle_{\mathrm{B}}\langle 0|_{\mathrm{B}}\left(\sqrt{1-q_m}\hat{a}_{\mathrm{B}}\right)^{N-l'}.
\end{aligned} \tag{247}$$

The density matrix of subsystem A is

$$\begin{aligned}
\rho_{\mathrm{A}} &= \mathrm{Tr}_{\mathrm{B}}\left[|\Psi^{\mathrm{N}}\rangle\langle\Psi^{\mathrm{N}}|\right] \\
&= \frac{1}{N!}\sum_{l=0}^{N}\binom{N}{l}^2(N-l)!\,(1-q_m)^{N-l} \\
&\quad\times\left(\sqrt{q_m}\hat{a}_{\mathrm{A}}^{\dagger}\right)^{l}|0\rangle_{\mathrm{A}}\langle 0|_{\mathrm{A}}\left(\sqrt{q_m}\hat{a}_{\mathrm{A}}\right)^{l}.
\end{aligned} \tag{248}$$

Note that ρ_{A} has at most $\chi = N+1$ nonzero eigenvalues, one for each possible distribution of the N particles between A and B. With $\hat{P}_l^{[\mathrm{A}]}$ the projector onto the l particle sector of subsystem A, the probability of finding l particles in A is

$$\begin{aligned}
\mathrm{Tr}_{\mathrm{A}}\left[\rho_{\mathrm{A}}\hat{\mathrm{P}}_{\mathrm{l}}^{[\mathrm{A}]}\right] &= \frac{1}{N!}\sum_{l=0}^{N}\binom{N}{l}^2(N-l)!\;l!\;(1-q_m)^{N-l}(q_m)^l \\
&= \sum_{l=0}^{N}\binom{N}{l}(1-q_m)^{N-l}(q_m)^l \\
&= B_{q_m}(l|N),
\end{aligned} \tag{249}$$

which is a binomial distribution.

We can now construct $|\Psi^N\rangle$ as a matrix product state in the canonical [PGVWC07] form. Given a bi-partition of the lattice, its Schmidt decomposition is

$$|\Psi^N\rangle = \sum_{l=0}^{N}\lambda_l^{[m]}|\Psi^l\rangle_{\mathrm{A}}\otimes|\Psi^{N-l}\rangle_{\mathrm{B}}, \tag{250}$$

with $|\Psi^l\rangle_{\mathrm{A}} = \frac{1}{\sqrt{l!}}(\hat{a}_{\mathrm{A}}^{\dagger})^l|0\rangle_{\mathrm{A}}$ and $|\Psi^{N-l}\rangle_{\mathrm{B}} = \frac{1}{\sqrt{(N-l)!}}(\hat{a}_{\mathrm{B}}^{\dagger})^{(N-l)}|0\rangle_{\mathrm{B}}$. The MPS will have bond dimension of $\chi = N+1$. The probability of finding l particles to the left of bond m is

$$\left(\lambda_l^{[m]}\right)^2 = B_{q_m}(l|N). \tag{251}$$

We then continue with the Schmidt decomposition at the following bond. The remaining task is to determine the coefficients of

$$\begin{aligned} |\Psi^N\rangle &= \sum_{l=0}^{N}\sum_{r=l}^{N} \lambda_l^{[m]}\Gamma_{lr}^{[m+1]}\lambda_r^{[m+1]} \\ &\quad \times |\Psi^l\rangle_{\mathrm{A}} \otimes |\Psi^{r-l}\rangle_{m+1} \otimes |\Psi^{N-r}\rangle_{\mathrm{B}'}. \end{aligned} \tag{252}$$

The λ tensors are already known from (251). The sub-chain B′ comprises sites $m+2$ to L. Thus $\left(\lambda_l^{[m]}\right)^2\left|\Gamma_{lr}^{[m+1]}\right|^2\left(\lambda_r^{[m+1]}\right)^2$ is the probability of finding $N-r$ particles on the right of bond $m+1$ *and* l particles on the left of bond m, resulting in

$$\begin{aligned} \left|\Gamma_{lr}^{[m+1]}\right|^2 &= \frac{B_{\frac{q_m}{q_{m+1}}}(l|r)}{B_{q_m}(l|N)} \\ &= \frac{r!\,(N-l)!}{(r-l)!\,N!} q_{m+1}^{-r}\left(q_{m+1}-q_m\right)^{r-l}\left(1-q_m\right)^{l-N}. \end{aligned} \tag{253}$$

For the phase to be correct, we obviously have to set

$$\arg\left(\Gamma_{lr}^{[m+1]}\right) = (r-l)\,\arg\left(\phi_{m+1}\right). \tag{254}$$

Equations (251), (253), and (254) completely determine the tensors Γ and λ. Note that in this particular case, the value of the bond index of $\lambda^{[m]}$ has a physical meaning of the number of particles to the left of bond m. The resulting MPS is an eigenstate of the total particle number, which can be used in TEBD implementations that take advantage of particle number conservation explicitly, as in this paper.

The construction is more complicated when one intends to prepare N_α particles in different single particle states $\alpha = 1, 2, \ldots, M$. From simple combinatorial considerations, we deduce that the Schmidt rank will be $\chi = \prod_\alpha (1+N_\alpha)$, i.e., exponentially large in the number M of different single particle states. (This implies that, as a starting point for dynamical simulations, one can construct an exact MPS for the ground state of non-interacting bosons, as done in [MSF10], but not for non-interacting fermions.) The exact expression in terms of the $q_{m,\alpha}$ will contain overlaps between the different single particle states, which in general are finite in any subsystem even if the single particle states are orthogonal on the entire lattice.

F Two particle time dependent correlations in a non interacting, homogeneous, spin polarized, one-dimensional Fermi gas

We calculate $g^{(2)}(\tau = t_0 - t)$ in the ground state in the thermodynamic limit, where all momentum eigenstates in $[-\hbar k_\mathrm{F}, \hbar k_\mathrm{F}]$ are occupied and all other states empty. $k_\mathrm{F} = \pi\rho$ is the Fermi momentum. Calculating

$$g^{(2)}(t_0 = 0, t)\rho^2 = \left\langle \hat{\Psi}_0^\dagger(x)\hat{\Psi}_t^\dagger(x)\hat{\Psi}_t(x)\hat{\Psi}_0(x) \right\rangle \tag{255}$$

$$= \frac{1}{4\pi^2} \int \mathrm{d}k^4 \; e^{i(k_1+k_2-k_3-k_4)x} e^{i\frac{\hbar k_2^2 - \hbar k_3^2}{2m}t} \left\langle \hat{\Psi}_0^\dagger(k_1)\hat{\Psi}_0^\dagger(k_2)\hat{\Psi}_0(k_3)\hat{\Psi}_0(k_4) \right\rangle \tag{256}$$

$$= \frac{1}{4\pi^2} \int_{-k_\mathrm{F}}^{k_\mathrm{F}} \mathrm{d}k_2 \; \mathrm{d}k_3 \; \left(1 - e^{i\frac{\hbar k_2^2 - \hbar k_3^2}{2m}t} \right) \tag{257}$$

$$= \rho^2 \left(1 - \frac{1}{4} \left| \int_{-1}^{1} \mathrm{d}u \; e^{iu^2 \frac{\hbar k_\mathrm{F}^2 t}{2m}} \right|^2 \right), \tag{258}$$

shows that

$$g^{(2)}(\tau) = 1 - \frac{1}{4} \left[\int_{-1}^{1} \mathrm{d}u \; \cos\left(u^2 \frac{\hbar k_\mathrm{F}^2 (t - t_0)}{2m} \right) \right]^2. \tag{259}$$

This function is shown in Fig. 36d.

References

[ABCG05] G. E. Astrakharchik, J. Boronat, J. Casulleras and S. Giorgini, "Beyond the Tonks-Girardeau gas: Strongly correlated regime in quasi-one-dimensional Bose gases", *Phys. Rev. Lett.* **95**, 190407 (2005) [DOI:10.1103/PhysRevLett.95.190407].

[AEM+95] M. H. Anderson, J. R. Eensher, M. R. Matthews, C. E. Wieman and E. A. Cornell, "Observation Of Bose-Einstein Condensation In A Dilute Atomic Vapor", *Science* **269**, 198–201 (1995) [DOI:10.1126/science.269.5221.198].

[AKR08] T. Antal, P. L. Krapivsky and A. Rakos, "Logarithmic current fluctuations in nonequilibrium quantum spin chains", *Phys. Rev. E* **78**, 061115 (2008) [DOI:10.1103/PhysRevE.78.061115].

[AM76] N. W. Ashcroft and N. D. Mermin, *Solid state physics*, Holt, Rinehart and Winston (1976).

[Bax78] R. J. Baxter, "Variational Approximations For Square Lattice Models In Statistical-mechanics", *J. Stat. Phys.* **19**, 461–478 (1978) [DOI:10.1007/BF01011693].

[BB82] P. Bak and R. Bruinsma, "One-dimensional Ising-model and the Complete Devils Staircase", *Phys. Rev. Lett.* **49**, 249–251 (1982) [DOI:10.1103/PhysRevLett.49.249].

[BBP93] N. M. Bogoliubov, R. K. Bullough and G. D. Pang, "Exact Solution of A Q-boson Hopping Model", *Phys. Rev. B* **47**, 11495–11498 (1993) [DOI:10.1103/PhysRevB.47.11495].

[BBW04] J. Berges, S. Borsanyi and C. Wetterich, "Prethermalization", *Phys. Rev. Lett.* **93**, 142002 (2004) [DOI:10.1103/PhysRevLett.93.142002].

[BCH11] M. C. Bañuls, J. I. Cirac and M. B. Hastings, "Strong and Weak Thermalization of Infinite Non-integrable Quantum Systems", *Phys. Rev. Lett.* **106**, 050405 (2011) [DOI:10.1103/PhysRevLett.106.050405].

[BCOT11] B. Bauer, P. Corboz, R. Orus and M. Troyer, "Implementing global Abelian symmetries in projected entangled-pair state algorithms", *Phys. Rev. B* **83**, 125106 (2011) [DOI:10.1103/PhysRevB.83.125106].

[BDZ08] I. Bloch, J. Dalibard and W. Zwerger, "Many-body physics with ultracold gases", *Rev. Mod. Phys.* **80**, 885 (2008) [DOI:10.1103/RevModPhys.80.885].

[BEG05] S. A. Bender, K. D. Erker and B. E. Granger, "Exponentially decaying correlations in a gas of strongly interacting spin-polarized 1D fermions with zero-range interactions", *Phys. Rev. Lett.* **95**, 230404 (2005) [DOI:10.1103/PhysRevLett.95.230404].

[Bet31] H. Bethe, "Zur Theorie der Metalle", *Z. Physik* **71**, 205 (1931).

[BGP+09] W. S. Bakr, J. I. Gillen, A. Peng, S. Fölling and M. Greiner, "A quantum gas microscope for detecting single atoms in a Hubbard-regime optical lattice", *Nature* **462**, 74–77 (2009) [DOI:10.1038/nature08482].

[BHV06] S. Bravyi, M. B. Hastings and F. Verstraete, "Lieb-robinson bounds and the generation of correlations and topological quantum order", *Phys. Rev. Lett.* **97**, 050401 (2006) [DOI:10.1103/PhysRevLett.93.050401].

[BIK98] N. M. Bogoliubov, A. G. Izergin and N. A. Kitanine, "Correlation functions for a strongly correlated boson system", *Nucl. Phys. B* **516**, 501–528 (1998) [DOI:10.1016/S0550-3213(98)00038-8].

[Blo49] N. Blombergen, "On the interaction of nuclear spins in a crystalline lattice", *Physika* **15**, 386 (1949).

[BPCS09] F. J. Burnell, M. M. Parish, N. R. Cooper and S. L. Sondhi, "Devil's staircases and supersolids in a one-dimensional dipolar Bose gas", *Phys. Rev. B* **80**, 174519 (2009) [DOI:10.1103/PhysRevB.80.174519].

[BPG08] H. Buljan, R. Pezer and T. Gasenzer, "Fermi-Bose transformation for the time-dependent Lieb-Liniger gas", *Phys. Rev. Lett.* **100**, 080406 (2008) [DOI:10.1103/PhysRevLett.100.080406].

[BPG+09] P. Barmettler, M. Punk, V. Gritsev, E. Demler and E. Altman, "Relaxation of Antiferromagnetic Order in Spin-1/2 Chains Following a Quantum Quench", *Phys. Rev. Lett.* **102**, 130603 (2009) [DOI:10.1103/PhysRevLett.102.130603].

[BPT+10] W. S. Bakr, A. Peng, M. E. Tai, R. Ma, J. Simon, J. I. Gillen, S. Fölling, L. Pollet and M. Greiner, "Probing the Superfluid-to-Mott Insulator Transition at the Single-Atom Level", *Science* **329**, 547–550 (2010) [DOI:10.1126/science.1192368].

[BSTH95] C. C. Bradley, C. A. Sackett, J. J. Tollett and R. G. Hulet, "Evidence of Bose-einstein Condensation In An Atomic Gas With Attractive Interactions", *Phys. Rev. Lett.* **75**, 1687–1690 (1995) [DOI:10.1103/PhysRevLett.75.1687].

[BT86] H. M. Babujian and A. M. Tsvelick, "Heisenberg Magnet With An Arbitrary Spin and Anisotropic Chiral Field", *Nucl. Phys. B* **265**, 24–44 (1986).

[Büc11] H. P. Büchler, "Crystalline phase for one-dimensional ultra-cold atomic bosons", *New J. Phys.* **13**, 093040 (2011) [DOI:10.1088/1367-2630/13/9/093040].

[Caz04] M. A. Cazalilla, "Bosonizing one-dimensional cold atomic gases", *J. Phys. B: At., Mol. Opt. Phys.* **37**, S1–S47 (2004) [DOI:10.1088/0953-4075/37/7/051].

[Caz06] M. A. Cazalilla, "Effect of suddenly turning on interactions in the Luttinger model", *Phys. Rev. Lett.* **97**, 156403 (2006) [DOI:10.1103/PhysRevLett.97.156403].

[CC05] P. Calabrese and J. Cardy, "Evolution of entanglement entropy in one-dimensional systems", *J. Stat. Mech.*, P04010 (2005) [DOI:10.1088/1742-5468/2005/04/P04010].

[CC06] J. S. Caux and P. Calabrese, "Dynamical density-density correlations in the one-dimensional Bose gas", *Phys. Rev. A* **74**, 031605 (2006) [DOI:10.1103/PhysRevA.74.031605].

[CCR11] A. C. Cassidy, C. W. Clark and M. Rigol, "Generalized Thermalization in an Integrable Lattice System", *Phys. Rev. Lett.* **106**, 140405 (2011) [DOI:10.1103/PhysRevLett.106.140405].

[CDEO08] M. Cramer, C. M. Dawson, J. Eisert and T. J. Osborne, "Exact relaxation in a class of nonequilibrium quantum lattice systems", *Phys. Rev. Lett.* **100**, 030602 (2008) [DOI:10.1103/PhysRevLett.100.030602].

[CDPO+08] R. Citro, S. De Palo, E. Orignac, P. Pedri and M. L. Chiofalo, "Luttinger hydrodynamics of confined one-dimensional Bose gases with dipolar interactions", *New J. Phys.* **10**, 045011 (2008) [DOI:10.1088/1367-2630/10/4/045011].

[CDV08] G. M. Crosswhite, A. C. Doherty and G. Vidal, "Applying matrix product operators to model systems with long-range interactions", *Phys. Rev. B* **78**, 035116 (2008) [DOI:10.1103/PhysRevB.78.035116].

[CFM+08] M. Cramer, A. Flesch, I. P. McCulloch, U. Schollwöck and J. Eisert, "Exploring local quantum many-body relaxation by atoms in optical superlattices", *Phys. Rev. Lett.* **101**, 063001 (2008) [DOI:10.1103/PhysRevLett.101.063001].

[CGM+08] D. E. Chang, V. Gritsev, G. Morigi, V. Vuletic, M. D. Lukin and E. A. Demler, "Crystallization of strongly interacting photons in a nonlinear optical fibre", *Nat. Phys.* **4**, 884–889 (2008) [DOI:10.1038/nphys1074].

[CGYH10] S. Chen, L. Guan, X. Yin and X. Hao Y.and Guan, "Transition from a Tonks-Girardeau gas to a super-Tonks-Girardeau gas as an exact many-body dynamics problem", *Phys. Rev. A* **81**, 031609 (2010) [DOI:10.1103/PhysRevA.81.031609].

[CM02] M. A. Cazalilla and J. B. Marston, "Time-dependent density-matrix renormalization group: A systematic method for the study of quantum many-body out-of-equilibrium systems", *Phys. Rev. Lett.* **88**, 256403 (2002) [DOI:10.1103/PhysRevLett.88.256403].

[COPC07] R. Citro, E. Orignac, S. D. Palo and M. L. Chiofalo, "Evidence of Luttinger-liquid behavior in one-dimensional dipolar quantum gases", *Phys. Rev. A* **75**, 051602(R) (2007) [DOI:10.1103/PhysRevA.75.051602].

[CP00] M. C. Chung and I. Peschel, "Density-matrix spectra for two-dimensional quantum systems", *Phys. Rev. B* **62**, 4191–4193 (2000) [DOI:10.1103/PhysRevB.62.4191].

[CPH+10] S. R. Clark, J. Prior, M. J. Hartmann, D. Jaksch and M. B. Plenio, "Exact matrix product solutions in the Heisenberg picture of an open quantum spin chain", *New J. Phys.* **12**, 025005 (2010) [DOI:10.1088/1367-2630/12/2/025005].

[CS98] T. Cheon and T. Shigehara, "Realizing discontinuous wave functions with renormalized short-range potentials", *Phys. Lett. A* **243**, 111–116 (1998) [DOI:10.1016/S0375-9601(98)00188-1].

[CS99] T. Cheon and T. Shigehara, "Fermion-Boson duality of one-dimensional quantum particles with generalized contact interactions", *Phys. Rev. Lett.* **82**, 2536–2539 (1999) [DOI:10.1103/PhysRevLett.82.2536].

[CSZ06a] V. V. Cheianov, H. Smith and M. B. Zvonarev, "Exact results for three-body correlations in a degenerate one-dimensional Bose gas", *Phys. Rev. A* **73**, 051604 (2006) [DOI:10.1103/PhysRevA.73.051604].

[CSZ06b] V. V. Cheianov, H. Smith and M. B. Zvonarev, "Three-body local correlation function in the Lieb-Liniger model: bosonization approach", *J. Stat. Mech.*, P08015 (2006) [DOI:10.1088/1742-5468/2006/08/P08015].

[CWBD11] D. Chen, M. White, C. Borries and B. DeMarco, "Quantum Quench of an Atomic Mott Insulator", *Phys. Rev. Lett.* **106**, 235304 (2011) [DOI:10.1103/PhysRevLett.106.235304].

[DCJZ05] A. J. Daley, S. R. Clark, D. Jaksch and P. Zoller, "Numerical analysis of coherent many-body currents in a single atom transistor", *Phys. Rev. A* **72**, 043618 (2005) [DOI:10.1103/PhysRevA.72.043618].

[DG58] P. G. De Gennes, "Inelastic Magnetic Scattering of Neutrons At High Temperatures", *J. Phys. Chem. Solids* **4**, 223–226 (1958).

[DKSV04] A. J. Daley, C. Kollath, U. Schollwöck and G. Vidal, "Time-dependent density-matrix renormalization-group using adaptive effective Hilbert spaces", *J. Stat. Mech.*, P04005 (2004) [DOI:10.1088/1742-5468/2004/04/P04005].

[DLO01a] V. Dunjko, V. Lorent and M. Olshanii, "Bosons in cigar-shaped traps: Thomas-Fermi Tonks-Girardean regime, and in between", *Phys. Rev. Lett.* **86**, 5413–5416 (2001) [DOI:10.1103/PhysRevLett.86.5413].

[DLO01b] V. Dunjko, V. Lorent and M. Olshanii, "Table of $f(\gamma)$ for those values of γ for which the asymptotic expansions do not give good results", *http://physics.usc.edu/~olshanii/DIST/1D_gases/e_f.dat* (2001).

[DMA+95] K. B. Davis, M. O. Mewes, M. R. Adrews, N. J. Vandruten, D. S. Durfee, D. M. Kurn and W. Ketterle, "Bose-Einstein Condensation In A Gas Of Sodium Atoms", *Phys. Rev. Lett.* **75**, 3969–3973 (1995) [DOI:10.1103/PhysRevLett.75.3969].

[DPZ10] M. Dalmonte, G. Pupillo and P. Zoller, "One-Dimensional Quantum Liquids with Power-Law Interactions: The Luttinger Staircase", *Phys. Rev. Lett.* **105**, 140401 (2010) [DOI:10.1103/PhysRevLett.105.140401].

[DSG+09] P. Deuar, A. G. Sykes, D. M. Gangardt, M. J. Davis, P. D. Drummond and K. V. Kheruntsyan, "Nonlocal pair correlations in the one-dimensional Bose gas at finite temperature", *Phys. Rev. A* **79**, 043619 (2009) [DOI:10.1103/PhysRevA.79.043619].

[EO06] J. Eisert and T. J. Osborne, "General entanglement scaling laws from time evolution", *Phys. Rev. Lett.* **97**, 150404 (2006) [DOI:10.1103/PhysRevLett.97.150404].

[ES12] T. Enss and J. Sirker, "Light cone renormalization and quantum quenches in one-dimensional Hubbard models", *New J. Phys.* **14**, 023008 (2012) [DOI:10.1088/1367-2630/14/2/023008].

[FC08] M. Fagotti and P. Calabrese, "Evolution of entanglement entropy following a quantum quench: Analytic results for the XY chain in a transverse magnetic field", *Phys. Rev. A* **78**, 010306(R) (2008) [DOI:10.1103/PhysRevA.78.010306].

[FCM+08] A. Flesch, M. Cramer, I. P. McCulloch, U. Schollwöck and J. Eisert, "Probing local relaxation of cold atoms in optical superlattices", *Phys. Rev. A* **78**, 033608 (2008) [DOI:10.1103/PhysRevA.78.033608].

[Fey39] R. P. Feynman, "Forces in molecules", *Phys. Rev.* **56**, 340–343 (1939) [DOI:10.1103/PhysRev.56.340].

[FM96] J. K. Freericks and H. Monien, "Strong-coupling expansions for the pure and disordered Bose-Hubbard model", *Phys. Rev. B* **53**, 2691–2700 (1996) [DOI:10.1103/PhysRevB.53.2691].

[FM98] K. Fabricius and B. M. McCoy, "Spin diffusion and the spin-1/2 XXZ chain at T=infinity from exact diagonalization", *Phys. Rev. B* **57**, 8340–8347 (1998) [DOI:10.1103/PhysRevB.57.8340].

[Fre56] J. E. Freund, "Restricted Occupancy Theory - A Generalization of Pascal's Triangle", *Am. Math. Mon.* **63**, 20–27 (1956).

[FRNDS08] A. E. Feiguin, E. Rezayi, C. Nayak and S. Das Sarma, "Density matrix renormalization group study of incompressible fractional quantum Hall states", *Phys. Rev. Lett.* **100**, 166803 (2008) [DOI:10.1103/PhysRevLett.100.166803].

[FW71] A. L. Fetter and J. D. Walecka, *Quantum theory of many particle systems*, McGraw-Hill (1971).

[FWGF89] M. P. A. Fisher, P. B. Weichman, G. Grinstein and D. S. Fisher, "Boson Localization And The Superfluid-Insulator Transition", *Phys. Rev. B* **40**, 546–570 (1989) [DOI:10.1103/PhysRevB.40.546].

[GA10] M. D. Girardeau and G. E. Astrakharchik, "Wave functions of the super-Tonks-Girardeau gas and the trapped one-dimensional hard-sphere Bose gas", *Phys. Rev. A* **81**, 061601 (2010) [DOI:10.1103/PhysRevA.81.061601].

[Gan59] F. R. Gantmacher, *Applications of the theory of matrices*, Interscience Publ. (1959).

[Gau83] M. Gaudin, *La Fonction d'Onde de Bethe*, Paris: Masson (1983).

[Gia03] T. Giamarchi, *Quantum Physics in One Dimension, International Series of Monographs in Physics*, Oxford University Press (2003).

[Gir60] M. Girardeau, "Relationship Between Systems Of Impenetrable Bosons And Fermions In One Dimension", *J. Math. Phys.* **1**, 516–523 (1960) [DOI:10.1063/1.1703687].

[GKSS05] D. Gobert, C. Kollath, U. Schollwöck and G. Schütz, "Real-time dynamics in spin-1/2 chains with adaptive time-dependent density matrix renormalization group", *Phys. Rev. E* **71**, 036102 (2005) [DOI:10.1103/PhysRevE.71.036102].

[GM96] M. P. Grabowski and P. Mathieu, "The structure of conserved charges in open spin chains", *J. Phys. A: Math. Gen.* **29**, 7635–7650 (1996) [DOI:10.1088/0305-4470/29/23/024].

[GM06] M. D. Girardeau and A. Minguzzi, "Bosonization, pairing, and superconductivity of the fermionic Tonks-Girardeau gas", *Phys. Rev. Lett.* **96**, 080404 (2006) [DOI:10.1103/PhysRevLett.96.080404].

[GME+02] M. Greiner, O. Mandel, T. Esslinger, T. W. Hansch and I. Bloch, "Quantum phase transition from a superfluid to a Mott insulator in a gas of ultracold atoms", *Nature* **415**, 39–44 (2002) [DOI:10.1038/415039a].

[GML+12] V. Guarrera, D. Muth, R. Labouvie, A. Vogler, G. Barontini, M. Fleischhauer and H. Ott, "Spatio-temporal Fermionization of Strongly Interacting 1D Bosons", *arXiv:1201.5015* (2012).

[GO04] M. D. Girardeau and M. Olshanii, "Theory of spinor Fermi and Bose gases in tight atom waveguides", *Phys. Rev. A* **70**, 023608 (2004) [DOI:10.1103/PhysRevA.70.023608].

[GR06] J. J. Garcia-Ripoll, "Time evolution of Matrix Product States", *New J. Phys.* **8**, 305 (2006) [DOI:10.1088/1367-2630/8/12/305].

[Gruon] F. Grusdt, "Fraktionaler Quanten Hall Effekt mit Rydberg-Polaritonen", *thesis*, Fachbereich Physik, TU Kaiserslautern (in preparation).

[GS03] D. M. Gangardt and G. V. Shlyapnikov, "Stability and Phase Coherence of Trapped 1D Bose Gases", *Phys. Rev. Lett.* **90**, 010401 (2003).

[GSM+05] K. Gunter, T. Stoferle, H. Moritz, M. Kohl and T. Esslinger, "p-Wave interactions in low-dimensional fermionic gases", *Phys. Rev. Lett.* **95**, 230401 (2005) [DOI:10.1103/PhysRevLett.95.230401].

[Gua] V. Guarrera, *private communication.*

[GUHO06] T. Gericke, C. Utfeld, N. Hommerstad and H. Ott, "A scanning electron microscope for ultracold atoms", *Laser Phys. Lett.* **3**, 415–419 (2006) [DOI:10.1002/lapl.200610028].

[GWE+11] V. Guarrera, P. Würtz, A. Ewerbeck, A. Vogler, G. Barontini and H. Ott, "Observation of Local Temporal Correlations in Trapped Quantum Gases", *Phys. Rev. Lett.* **107**, 160403 (2011) [DOI:10.1103/PhysRevLett.107.160403].

[Hal81] F. D. M. Haldane, "Effective Harmonic-Fluid Approach To Low-Energy Properties Of One-Dimensional Quantum Fluids", *Phys. Rev. Lett.* **47**, 1840–1843 (1981) [DOI:10.1103/PhysRevLett.47.1840].

[Hel33] H. Hellmann, "Zur Rolle der kinetischen Elektronenenergie für die zwischenatomaren Kräfte", *Z. Physik* **85**, 180–190 (1933) [DOI:10.1007/BF01342053].

[HGM+09] E. Haller, M. Gustavsson, M. J. Mark, J. G. Danzl, R. Hart, G. Pupillo and H. C. Nägerl, "Realization of an Excited, Strongly Correlated Quantum Gas Phase", *Science* **325**, 1224–1227 (2009) [DOI:10.1126/science.1175850].

[HLF+07] S. Hofferberth, I. Lesanovsky, B. Fischer, T. Schumm and J. Schmiedmayer, "Non-equilibrium coherence dynamics in one-dimensional Bose gases", *Nature* **449**, 324–327 (2007) [DOI:10.1038/nature06149].

[HMMR+09] F. Heidrich-Meisner, S. R. Manmana, M. Rigol, A. Muramatsu, A. E. Feiguin and E. Dagotto, "Quantum distillation: Dynamical generation of low-entropy states of strongly correlated fermions in an optical lattice", *Phys. Rev. A* **80**, 041603(R) (2009) [DOI:10.1103/PhysRevA.80.041603].

[HPCP09] M. J. Hartmann, J. Prior, S. R. Clark and M. B. Plenio, "Density Matrix Renormalization Group in the Heisenberg Picture", *Phys. Rev. Lett.* **102**, 057202 (2009) [DOI:10.1103/PhysRevLett.102.057202].

[Hub78] J. Hubbard, "Generalized Wigner Lattices In One Dimension and Some Applications To Tetracyanoquinodimethane (TCNQ) Salts", *Phys. Rev. B* **17**, 494–505 (1978) [DOI:10.1103/PhysRevB.17.494].

[ILGG10] A. Imambekov, A. A. Lukyanov, L. I. Glazman and V. Gritsev, "Exact Solution for 1D Spin-Polarized Fermions with Resonant Interactions", *Phys. Rev. Lett.* **104**, 040402 (2010) [DOI:10.1103/PhysRevLett.104.040402].

[Ima12] A. Imambekov, "Notes on time dependences of (x, t) correlators in 1D and their relation to beyond Luttinger physics", unpublished (2012).

[JBC+98] D. Jaksch, C. Bruder, J. I. Cirac, C. W. Gardiner and P. Zoller, "Cold bosonic atoms in optical lattices", *Phys. Rev. Lett.* **81**, 3108–3111 (1998) [DOI:10.1103/PhysRevLett.81.3108].

[JPGB08] D. Jukić, R. Pezer, T. Gasenzer and H. Buljan, "Free expansion of a Lieb-Liniger gas: Asymptotic form of the wave functions", *Phys. Rev. A* **78**, 053602 (2008) [DOI:10.1103/PhysRevA.78.053602].

[KBI93] V. E. Korepin, N. M. Bogoliubov and A. G. Izergin, *Quantum Inverse Scattering Method and Correlation Functions*, Cambridge University Press (1993).

[KCI12] M. Kormos, Y. Chou and A. Imambekov, "Exact three-body local correlations for arbitrary excited states of the 1D Bose gas", *Phys. Rev. Lett.* **107**, 230405 (2012) [DOI:10.1103/PhysRevLett.107.230405].

[KE08] M. Kollar and M. Eckstein, "Relaxation of a one-dimensional Mott insulator after an interaction quench", *Phys. Rev. A* **78**, 013626 (2008) [DOI:10.1103/PhysRevA.78.013626].

[KGDS03] K. V. Kheruntsyan, D. M. Gangardt, P. D. Drummond and G. V. Shlyapnikov, "Pair correlations in a finite-temperature 1D Bose gas", *Phys. Rev. Lett.* **91**, 040403 (2003) [DOI:10.1103/PhysRevLett.91.040403].

[KGJ06] T. Kohler, K. Goral and P. S. Julienne, "Production of cold molecules via magnetically tunable Feshbach resonances", *Rev. Mod. Phys.* **78**, 1311–1361 (2006) [DOI:10.1103/RevModPhys.78.1311].

[Kli06] I. Klich, "Lower entropy bounds and particle number fluctuations in a Fermi sea", *J. Phys. A: Math. Gen.* **39**, L85–L91 (2006) [DOI:10.1088/0305-4470/39/4/L02].

[KM63] L. P. Kadanoff and P. C. Martin, "Hydrodynamic Equations and Correlation Functions", *Ann. Phys. (New York)* **24**, 419–469 (1963) [DOI:10.1016/0003-4916(63)90078-2].

[KMT09] M. Kormos, G. Mussardo and A. Trombettoni, "Expectation Values in the Lieb-Liniger Bose Gas", *Phys. Rev. Lett.* **103**, 210404 (2009) [DOI:10.1103/PhysRevLett.103.210404].

[KMT11] J. Kajala, F. Massel and P. Torma, "Expansion Dynamics in the One-Dimensional Fermi-Hubbard Model", *Phys. Rev. Lett.* **106**, 206401 (2011) [DOI:10.1103/PhysRevLett.106.206401].

[KW41] H. A. Kramers and G. H. Wannier, "Statistics of the two-dimensional ferromagnet Part II", *Phys. Rev.* **60**, 263–276 (1941).

[KWW04] T. Kinoshita, T. Wenger and D. S. Weiss, "Observation of a one-dimensional Tonks-Girardeau gas", *Science* **305**, 1125–1128 (2004) [DOI:10.1126/science.1100700].

[KWW06] T. Kinoshita, T. Wenger and D. S. Weiss, "A quantum Newton's cradle", *Nature* **440**, 900–903 (2006) [DOI:10.1038/nature04693].

[Lau12] A. Lauer, "Optisch angeregte Rydberggase und Rydbergpolaritonen", *thesis*, Fachbereich Physik, TU Kaiserslautern (2012).

[LBH10] A. M. Läuchli, E. J. Bergholtz and M. Haque, "Entanglement scaling of fractional quantum Hall states through geometric deformations", *New J. Phys.* **12**, 075004 (2010) [DOI:10.1088/1367-2630/12/7/075004].

[Lee71a] D. K. Lee, "Ground State of A 1-dimensional Many-boson System", *Phys. Rev. A* **3**, 345 (1971) [DOI:10.1103/PhysRevA.3.345].

[Lee71b] D. K. Lee, "Theory of Many-boson Systems In Weak Coupling Limit", *Phys. Lett. A* **37**, 49 (1971) [DOI:10.1016/0375-9601(71)90326-4].

[LH08] H. Li and F. D. M. Haldane, "Entanglement spectrum as a generalization of entanglement entropy: Identification of topological order in non-Abelian fractional quantum Hall effect states", *Phys. Rev. Lett.* **101**, 010504 (2008) [DOI:10.1103/PhysRevLett.101.010504].

[Lie63] E. H. Lieb, "Exact Analysis Of An Interacting Bose Gas II: Excitation Spectrum", *Phys. Rev.* **130**, 1616–1624 (1963) [DOI:10.1103/PhysRev.130.1616].

[LL63] E. H. Lieb and W. Liniger, "Exact Analysis Of An Interacting Bose Gas I: General Solution And Ground State", *Phys. Rev.* **130**, 1605–1616 (1963) [DOI:10.1103/PhysRev.130.1605].

[LMFon] A. Lauer, D. Muth and M. Fleischhauer, "Melting of Rydberg crystals on a 1D lattice" (in preparation).

[LP94] S. D. Liang and H. B. Pang, "Approximate Diagonalization Using the Density-matrix Renormalization-group Method - A 2-dimensional-systems Perspective", *Phys. Rev. B* **49**, 9214–9217 (1994) [DOI:10.1103/PhysRevB.49.9214].

[LR72] E. H. Lieb and D. W. Robinson, "The finite group velocity of quantum spin systems", *Commun. Math. Phys.* **28**, 251–257 (1972) [DOI:10.1007/BF01645779].

[LSA+07] M. Lewenstein, A. Sanpera, V. Ahufinger, B. Damski, A. Sen(De) and U. Sen, "Ultracold atomic gases in optical lattices: mimicking condensed matter physics and beyond", *Adv. Phys.* **56**, 243–379 (2007) [DOI:10.1080/00018730701223200].

[LSY98] R. B. Lehoucq, D. C. Sorensen and C. Yang, *ARPACK Users' Guide: Solution of Large Scale Eigenvalue Problems with Implicitly Restarted Arnoldi Methods*, SIAM (1998).

[LXW03] H. G. Luo, T. Xiang and X. Q. Wang, "Comment on "Time-dependent density-matrix renormalization group: A systematic method for the study of quantum many-body out-of-equilibrium systems"", *Phys. Rev. Lett.* **91**, 049701 (2003) [DOI:10.1103/PhysRevLett.91.049701].

[MABC08] F. Mazzanti, G. E. Astrakharchik, J. Boronat and J. Casulleras, "Ground-state properties of a one-dimensional system of hard rods", *Phys. Rev. Lett.* **100**, 020401 (2008) [DOI:10.1103/PhysRevLett.100.020401].

[McC07] I. P. McCulloch, "From density-matrix renormalization group to matrix product states", *J. Stat. Mech.*, P10014 (2007) [DOI:10.1088/1742-5468/2007/10/P10014].

[McC08] I. P. McCulloch, "Infinite size density matrix renormalization group, revisited", *arXiv:0804.2509* (2008).

[McG64] J. B. McGuire, "Study of Exactly Soluble One-Dimensional N-Body Problems", *J. Math. Phys.* **5**, 622–636 (1964) [DOI:10.1063/1.1704156].

[MF10] D. Muth and M. Fleischhauer, "Dynamics of pair correlations in the attractive Lieb-Liniger gas", *Phys. Rev. Lett.* **105**, 150403 (2010) [DOI:10.1103/PhysRevLett.105.150403].

[MFS10] D. Muth, M. Fleischhauer and B. Schmidt, "Discretized versus continuous models of p-wave interacting fermions in one dimension", *Phys. Rev. A* **82**, 013602 (2010) [DOI:10.1103/PhysRevA.82.013602].

[MG02] I. P. McCulloch and M. Gulacsi, "The non-Abelian density matrix renormalization group algorithm", *Europhys. Lett.* **57**, 852–858 (2002) [DOI:10.1209/epl/i2002-00393-0].

[MG06] A. Minguzzi and M. D. Girardeau, "Pairing of a harmonically trapped fermionic Tonks-Girardeau gas", *Phys. Rev. A* **73**, 063614 (2006) [DOI:10.1103/PhysRevA.73.063614].

[MMF08] D. Muth, A. Mering and M. Fleischhauer, "Ultracold bosons in disordered superlattices: Mott insulators induced by tunneling", *Phys. Rev. A* **77**, 043618 (2008) [DOI:10.1103/PhysRevA.77.043618].

[Mos08] J. Mossel, "Dynamics of the antiferromagnetic Heisenberg spin-1/2 chain", *thesis*, Universiteit van Amsterdam, Instituut voor Theoretische Fysica (2008).

[MPF12] D. Muth, D. Petrosyan and M. Fleischhauer, "Dynamics and evaporation of defects in Mott-insulating clusters of boson pairs", *Phys. Rev. A* **85**, 013615 (2012) [DOI:10.1103/PhysRevA.85.013615].

[MS98] J. G. Muga and R. F. Snider, "Solvable three-boson model with attractive delta-function interactions", *Phys. Rev. A* **57**, 3317–3329 (1998) [DOI:10.1103/PhysRevA.57.3317].

[MS09] I. E. Mazets and J. Schmiedmayer, "Restoring integrability in one-dimensional quantum gases by two-particle correlations", *Phys. Rev. A* **79**, 061603 (2009) [DOI:10.1103/PhysRevA.79.061603].

[MSF10] D. Muth, B. Schmidt and M. Fleischhauer, "Fermionization dynamics of a strongly interacting one-dimensional Bose gas after an interaction quench", *New J. Phys.* **12**, 083065 (2010) [DOI:10.1088/1367-2630/12/8/083065].

[MUF11] D. Muth, R. G. Unanyan and M. Fleischhauer, "Dynamical Simulation of Integrable and Nonintegrable Models in the Heisenberg Picture", *Phys. Rev. Lett.* **106**, 077202 (2011) [DOI:10.1103/PhysRevLett.106.077202].

[Mut08] D. Muth, "TEBD Simulation von 1D Quantengasen", *thesis*, Fachbereich Physik, TU Kaiserslautern (2008).

[Mut11] D. Muth, "Particle number conservation in quantum many-body simulations with matrix product operators", *J. Stat. Mech.*, P11020 (2011) [DOI:10.1088/1742-5468/2011/11/P11020].

[NJGN02] S. Nishimoto, E. Jeckelmann, F. Gebhard and R. M. Noack, "Application of the density matrix renormalization group in momentum space", *Phys. Rev. B* **65**, 165114 (2002) [DOI:10.1103/PhysRevB.65.165114].

[OD03] M. Olshanii and V. Dunjko, "The short-distance first-order correlation function of the interacting one-dimensional Bose gas", *New J. Phys.* **5**, 98 (2003) [DOI:10.1088/1367-2630/5/1/398].

[OLMFon] J. Otterbach, A. Lauer, D. Muth and M. Fleischhauer (in preparation).

[Ols98] M. Olshanii, "Atomic scattering in the presence of an external confinement and a gas of impenetrable bosons", *Phys. Rev. Lett.* **81**, 938–941 (1998) [DOI:10.1103/PhysRevLett.81.938].

[PGVWC07] D. Perez-Garcia, F. Verstraete, M. M. Wolf and J. I. Cirac, "Matrix product state representations", *Quant. Inf. Comp.* **7**, 401–430 (2007).

[PM07] R. Piil and K. Molmer, "Tunneling couplings in discrete lattices, single-particle band structure, and eigenstates of interacting atom pairs", *Phys. Rev. A* **76**, 023607 (2007) [DOI:10.1103/PhysRevA.76.023607].

[PP07] T. Prosen and I. Pižorn, "Operator space entanglement entropy in a transverse Ising chain", *Phys. Rev. A* **76**, 032316 (2007) [DOI:10.1103/PhysRevA.76.032316].

[PP09] I. Pižorn and T. Prosen, "Operator space entanglement entropy in XY spin chains", *Phys. Rev. B* **79**, 184416 (2009) [DOI:10.1103/PhysRevB.79.184416].

[Pro08] T. Prosen, "Third quantization: a general method to solve master equations for quadratic open Fermi systems", *New J. Phys.* **10**, 043026 (2008) [DOI:10.1088/1367-2630/10/4/043026].

[PSAF07] D. Petrosyan, B. Schmidt, J. R. Anglin and M. Fleischhauer, "Quantum liquid of repulsively bound pairs of particles in a lattice", *Phys. Rev. A* **76**, 033606 (2007) [DOI:10.1103/PhysRevA.76.033606].

[PU78] V. L. Pokrovsky and G. V. Uimin, "Properties of Monolayers of Adsorbed Atoms", *J. Phys. C: Solid State Phys.* **11**, 3535–3549 (1978) [DOI:10.1088/0022-3719/11/16/022].

[PWE10] P. Pippan, S. R. White and H. G. Evertz, "Efficient matrix-product state method for periodic boundary conditions", *Phys. Rev. B* **81**, 081103 (2010) [DOI:10.1103/PhysRevB.81.081103].

[PWM+04] B. Paredes, A. Widera, V. Murg, O. Mandel, S. Fölling, I. Cirac, G. V. Shlyapnikov, T. W. Hänsch and I. Bloch, "Tonks-Girardeau gas of ultracold atoms in an optical lattice", *Nature* **429**, 277–281 (2004) [DOI:10.1038/nature02530].

[PŽ07] T. Prosen and M. Žnidarič, "Is the efficiency of classical simulations of quantum dynamics related to integrability?", *Phys. Rev. E* **75**, 015202(R) (2007) [DOI:10.1103/PhysRevE.75.015202].

[PŽ09] T. Prosen and M. Žnidarič, "Matrix product simulations of non-equilibrium steady states of quantum spin chains", *J. Stat. Mech.*, P02035 (2009) [DOI:10.1088/1742-5468/2009/02/P02035].

[RDO08] M. Rigol, V. Dunjko and M. Olshanii, "Thermalization and its mechanism for generic isolated quantum systems", *Nature* **452**, 854–858 (2008) [DOI:10.1038/nature06838].

[RDYO07] M. Rigol, V. Dunjko, V. Yurovsky and M. Olshanii, "Relaxation in a completely integrable many-body quantum system: An ab initio study of the dynamics of the highly excited states of 1D lattice hard-core bosons", *Phys. Rev. Lett.* **98**, 050405 (2007) [DOI:10.1103/PhysRevLett.98.050405].

[Rig09] M. Rigol, "Breakdown of Thermalization in Finite One-Dimensional Systems", *Phys. Rev. Lett.* **103**, 100403 (2009) [DOI:10.1103/PhysRevLett.103.100403].

[RMO06] M. Rigol, A. Muramatsu and M. Olshanii, "Hard-core bosons on optical superlattices: Dynamics and relaxation in the superfluid and insulating regimes", *Phys. Rev. A* **74**, 053616 (2006) [DOI:10.1103/PhysRevA.74.053616].

[Rou09] G. Roux, "Quenches in quantum many-body systems: One-dimensional Bose-Hubbard model reexamined", *Phys. Rev. A* **79**, 021608 (2009) [DOI:10.1103/PhysRevA.79.021608].

[SBE+09] B. Schmidt, M. Bortz, S. Eggert, M. Fleischhauer and D. Petrosyan, "Attractively bound pairs of atoms in the Bose-Hubbard model and antiferromagnetism", *Phys. Rev. A* **79**, 063634 (2009) [DOI:10.1103/PhysRevA.79.063634].

[Sch05] U. Schollwöck, "The density-matrix renormalization group", *Rev. Mod. Phys.* **77**, 259–315 (2005) [DOI:10.1103/RevModPhys.77.259].

[Sch09] B. Schmidt, "Exact numerical simulations of strongly interacting atoms in 1D trap potentials and optical lattices", *dissertation*, Fachbereich Physik, TU Kaiserslautern (2009).

[Sch11] U. Schollwöck, "The density-matrix renormalization group in the age of matrix product states", *Ann. Phys. (New York)* **326**, 96–192 (2011) [DOI:10.1016/j.aop.2010.09.012].

[SDV06] Y. Y. Shi, L. M. Duan and G. Vidal, "Classical simulation of quantum many-body systems with a tree tensor network", *Phys. Rev. A* **74**, 022320 (2006) [DOI:10.1103/PhysRevA.74.022320].

[Seb86] P. Seba, "The Generalized Point Interaction In One Dimension", *Czech. J. Phys.* **36**, 667–673 (1986).

[SF07] B. Schmidt and M. Fleischhauer, "Exact numerical simulations of a one-dimensional trapped Bose gas", *Phys. Rev. A* **75**, 021601(R) (2007) [DOI:10.1103/PhysRevA.75.021601].

[Sir06] J. Sirker, "Spin diffusion and the anisotropic spin-1/2 Heisenberg chain", *Phys. Rev. B* **73**, 224424 (2006) [DOI:10.1103/PhysRevB.73.224424].

[SK05] J. Sirker and A. Klumper, "Real-time dynamics at finite temperature by the density-matrix renormalization group: A path-integral approach", *Phys. Rev. B* **71**, 241101 (2005) [DOI:10.1103/PhysRevB.71.241101].

[Sog84] K. Sogo, "Ground-state and Low-lying Excitations in the Heisenberg XXZ Chain of Arbitrary Spins", *Phys. Lett. A* **104**, 51–54 (1984) [DOI:10.1016/0375-9601(84)90588-7].

[SPF05] B. Schmidt, L. I. Plimak and M. Fleischhauer, "Stochastic simulation of a finite-temperature one-dimensional Bose gas: From the Bogoliubov to the Tonks-Girardeau regime", *Phys. Rev. A* **71**, 041601(R) (2005) [DOI:10.1103/PhysRevA.71.041601].

[SS99] A. T. Sornborger and E. D. Stewart, "Higher-order methods for simulations on quantum computers", *Phys. Rev. A* **60**, 1956–1965 (1999) [DOI:10.1103/PhysRevA.60.1956].

[Suz76] M. Suzuki, "Generalized Trotters Formula and Systematic Approximants of Exponential Operators and Inner Derivations With Applications To Many-body Problems", *Commun. Math. Phys.* **51**, 183–190 (1976) [DOI:10.1007/BF01609348].

[SW06] U. Schollwöck and S. R. White, "Methods for time dependence in DMRG", in: G. G. Batrouni and D. Poilblanc (ed.), *Effective models for low-dimensional strongly correlated systems*, 155–185, American Institute of Physics (2006).

[SWE+10] J. F. Sherson, C. Weitenberg, M. Endres, M. Cheneau, I. Bloch and S. Kuhr, "Single-atom-resolved fluorescence imaging of an atomic Mott insulator", *Nature* **467**, 68–72 (2010) [DOI:10.1038/nature09378].

[SWVC08a] N. Schuch, M. M. Wolf, F. Verstraete and J. I. Cirac, "Entropy scaling and simulability by matrix product states", *Phys. Rev. Lett.* **100**, 030504 (2008) [DOI:10.1103/PhysRevLett.100.030504].

[SWVC08b] N. Schuch, M. M. Wolf, K. G. H. Vollbrecht and J. I. Cirac, "On entropy growth and the hardness of simulating time evolution", *New J. Phys.* **10**, 033032 (2008) [DOI:10.1088/1367-2630/10/3/033032].

[SZV10] S. Singh, H. Q. Zhou and G. Vidal, "Simulation of one-dimensional quantum systems with a global SU(2) symmetry", *New J. Phys.* **12**, 033029 (2010) [DOI:10.1088/1367-2630/12/3/033029].

[TCF+11] S. Trotzky, Y. Chen, A. Flesch, I. P. McCulloch, U. Schollwöck, J. Eisert and I. Bloch, "Probing the relaxation towards equilibrium in an isolated strongly correlated 1D Bose gas", *arXiv:1101.2659* (2011).

[TZS08] E. Tempfli, S. Zollner and P. Schmelcher, "Excitations of attractive 1D bosons: binding versus fermionization", *New J. Phys.* **10**, 103021 (2008) [DOI:10.1088/1367-2630/10/10/103021].

[UMF10] R. G. Unanyan, D. Muth and M. Fleischhauer, "Short-time versus long-time dynamics of entanglement in quantum lattice models", *Phys. Rev. A* **81**, 022119 (2010) [DOI:10.1103/PhysRevA.81.022119].

[Val10] M. Valiente, "Lattice two-body problem with arbitrary finite-range interactions RID E-1668-2011", *Phys. Rev. A* **81**, 042102 (2010) [DOI:10.1103/PhysRevA.81.042102].

[VC04] F. Verstraete and J. I. Cirac, "Renormalization algorithms for Quantum-Many Body Systems in two and higher dimensions", *arXiv:cond-mat/0407066* (2004).

[VC06] F. Verstraete and J. I. Cirac, "Matrix product states represent ground states faithfully", *Phys. Rev. B* **73**, 094423 (2006) [DOI:10.1103/PhysRevB.73.094423].

[VGRC04] F. Verstraete, J. J. Garcia-Ripoll and J. I. Cirac, "Matrix product density operators: Simulation of finite-temperature and dissipative systems", *Phys. Rev. Lett.* **93**, 207204 (2004) [DOI:10.1103/PhysRevLett.93.207204].

[Vid03] G. Vidal, "Efficient classical simulation of slightly entangled quantum computations", *Phys. Rev. Lett.* **91**, 147902 (2003) [DOI:10.1103/PhysRevLett.91.147902].

[Vid04] G. Vidal, "Efficient simulation of one-dimensional quantum many-body systems", *Phys. Rev. Lett.* **93**, 040502 (2004) [DOI:10.1103/PhysRevLett.93.040502].

[Vid07a] G. Vidal, "Classical simulation of infinite-size quantum lattice systems in one spatial dimension", *Phys. Rev. Lett.* **98**, 070201 (2007) [DOI:10.1103/PhysRevLett.98.070201].

[Vid07b] G. Vidal, "Entanglement renormalization", *Phys. Rev. Lett.* **99**, 220405 (2007) [DOI:10.1103/PhysRevLett.99.220405].

[Vid10] G. Vidal, "Entanglement Renormalization: An Introduction", in: L. Carr (ed.), *Understanding Quantum Phase Transitions*, Taylor and Francis (2010).

[vOvdSS01] D. van Oosten, P. van der Straten and H. T. C. Stoof, "Quantum phases in an optical lattice", *Phys. Rev. A* **63**, 053601 (2001) [DOI:10.1103/PhysRevA.63.053601].

[VP08] M. Valiente and D. Petrosyan, "Two-particle states in the Hubbard model", *J. Phys. B: At., Mol. Opt. Phys.* **41**, 161002 (2008) [DOI:10.1088/0953-4075/41/16/161002].

[VP09] M. Valiente and D. Petrosyan, "Scattering resonances and two-particle bound states of the extended Hubbard model", *J. Phys. B: At., Mol. Opt. Phys.* **42**, 121001 (2009) [DOI:10.1088/0953-4075/42/12/121001].

[VPC04] F. Verstraete, D. Porras and J. I. Cirac, "Density matrix renormalization group and periodic boundary conditions: A quantum information perspective", *Phys. Rev. Lett.* **93**, 227205 (2004) [DOI:10.1103/PhysRevLett.93.227205].

[VPS10] M. Valiente, D. Petrosyan and A. Saenz, "Three-body bound states in a lattice", *Phys. Rev. A* **81**, 011601(R) (2010) [DOI:10.1103/PhysRevA.81.011601].

[WES+11] C. Weitenberg, M. Endres, J. F. Sherson, M. Cheneau, P. Schauss, T. Fukuhara, I. Bloch and S. Kuhr, "Single-spin addressing in an atomic Mott insulator", *Nature* **471**, 319–324 (2011) [DOI:10.1038/nature09827].

[WF04] S. R. White and A. E. Feiguin, "Real-time evolution using the density matrix renormalization group", *Phys. Rev. Lett.* **93**, 076401 (2004) [DOI:10.1103/PhysRevLett.93.076401].

[WGL+09] P. Würtz, T. Gericke, T. Langen, A. Koglbauer and H. Ott, "Probing Bose-Einstein Condensates by Electron Impact Ionization", *J. Phys.: Conf. Ser.* **141**, 012020 (2009) [DOI:10.1088/1742-6596/141/1/012020].

[Whi92] S. R. White, "Density-Matrix Formulation For Quantum Renormalization-Groups", *Phys. Rev. Lett.* **69**, 2863–2866 (1992) [DOI:10.1103/PhysRevLett.69.2863].

[Whi93] S. R. White, "Density-matrix Algorithms For Quantum Renormalization-groups", *Phys. Rev. B* **48**, 10345–10356 (1993) [DOI:10.1103/PhysRevB.48.10345].

[WLG+09] P. Würtz, T. Langen, T. Gericke, A. Koglbauer and H. Ott, "Experimental Demonstration of Single-Site Addressability in a Two-Dimensional Optical Lattice", *Phys. Rev. Lett.* **103**, 080404 (2009) [DOI:10.1103/PhysRevLett.103.080404].

[WLPB08] H. Weimer, R. Löw, T. Pfau and H. P. Büchler, "Quantum Critical Behavior in Strongly Interacting Rydberg Gases", *Phys. Rev. Lett.* **101**, 250601 (2008) [DOI:10.1103/PhysRevLett.101.250601].

[WTL+06] K. Winkler, G. Thalhammer, F. Lang, R. Grimm, J. Hecker Denschlag, A. J. Daley, A. Kantian, H. P. Büchler and P. Zoller, "Repulsively bound atom pairs in an optical lattice", *Nature* **441**, 853–856 (2006) [DOI:10.1038/nature04918].

[Xia96] T. Xiang, "Density-matrix renormalization-group method in momentum space", *Phys. Rev. B* **53**, 10445–10448 (1996) [DOI:10.1103/PhysRevB.53.R10445].

[Yan62] C. N. Yang, "Concept Of Off-Diagonal Long-Range Order And Quantum Phases Of Liquid He And Of Superconductors", *Rev. Mod. Phys.* **34**, 694–704 (1962) [DOI:10.1103/RevModPhys.34.694].

[YG05] V. I. Yukalov and M. D. Girardeau, "Fermi-Bose mapping for one-dimensional Bose gases", *Laser Phys. Lett.* **2**, 375–382 (2005) [DOI:10.1002/lapl.200510011].

[YY69] C. N. Yang and C. P. Yang, "Thermodynamics Of A One-Dimensional System Of Bosons With Repulsive Delta-Function Interaction", *J. Math. Phys.* **10**, 1115 (1969) [DOI:10.1063/1.1664947].

[ZNP97] X. Zotos, F. Naef and P. Prelovsek, "Transport and conservation laws", *Phys. Rev. B* **55**, 11029–11032 (1997) [DOI:10.1103/PhysRevB.55.1102].

[ZSH11] J. Z. Zhao, D. N. Sheng and F. D. M. Haldane, "Fractional quantum Hall states at 1/3 and 5/2 filling: Density-matrix renormalization group calculations", *Phys. Rev. B* **83**, 195135 (2011) [DOI:10.1103/PhysRevB.83.195135].

[ZV04] M. Zwolak and G. Vidal, "Mixed-state dynamics in one-dimensional quantum lattice systems: A time-dependent superoperator renormalization algorithm", *Phys. Rev. Lett.* **93**, 207205 (2004) [DOI:10.1103/PhysRevLett.93.207205].

[Zvo10] M. Zvonarev, "Notes on Bethe Ansatz", *http://cmt.harvard.edu/demler/TEACHING/Physics284/LectureZvonarev.pdf* (2010).